The Mathematics and Biology of the Biodistribution of Radiopharmaceuticals – A Clinical Perspective

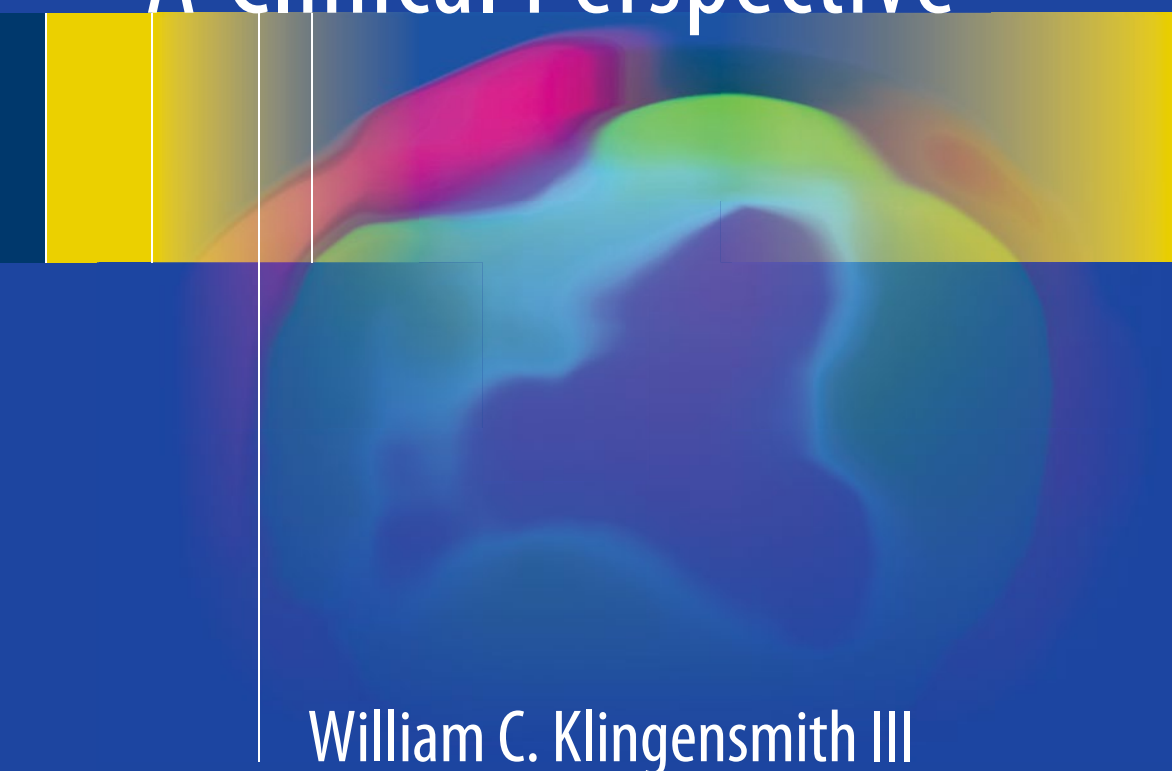

William C. Klingensmith III

Springer

The Mathematics and Biology of the Biodistribution of Radiopharmaceuticals- A Clinical Perspective

William C. Klingensmith III

The Mathematics and Biology of the Biodistribution of Radiopharmaceuticals- A Clinical Perspective

Springer

William C. Klingensmith III
Cherry Hills Village
Colorado
USA

ISBN 978-3-319-26702-9 ISBN 978-3-319-26704-3 (eBook)
DOI 10.1007/978-3-319-26704-3

Library of Congress Control Number: 2016931336

Springer Cham Heidelberg New York Dordrecht London

Printed on acid-free paper

Springer International Publishing AG Switzerland is part of Springer Science+Business Media (www.springer.com)

To the memory of Henry N. Wagner, Jr., M.D. –
Working with Henry was exciting, fun, and intellectually rewarding,
His dedication to science and the scientific method never wavered,
And his ability to reason conceptually and by analogy was exceptional.
It would be hard to imagine a better academic mentor.

Preface

The title of this book, *The Mathematics and Biology of the Biodistribution of Radiopharmaceuticals - A Clinical Perspective*, requires some explanation. The efficacy of every diagnostic and therapeutic nuclear medicine procedure is critically dependent on the biodistribution over time of the radiopharmaceutical in question. This book explores the mathematics and biology of the biodistribution of radiopharmaceuticals following their introduction into the body, but it does so primarily from a clinical perspective – from the point of view of interpretation of images and any associated image-derived quantification.

To this end, the mathematics is different from the traditional approach of using compartmental analysis because compartmental analysis requires data that are not available in the clinical setting. For an equation to be included in this book, it must (1) relate directly to the biodistribution of radiopharmaceuticals and (2) be clinically useful, either conceptually or by quantifying a biological parameter, e.g., renal clearance. In particular, the more complex equations in this book are not meant to be solved, but instead are intended to provide a conceptual basis for the analysis of clinical images, especially difficult or unusual images.

The general mathematical analysis provides a framework for the biologic discussion that follows. The examination of the biology of the biodistribution of radiopharmaceuticals focuses on the physiology and molecular biology that accounts for (1) the movement of a radiopharmaceutical from the site of administration to other parts of the body, (2) the uptake or clearance of the radiopharmaceutical into an organ, tissue, or lesion (in most studies), and (3) the subsequent transport of the radiopharmaceutical through an organ and into an excretory system (in a few studies).

The equation, diagrams, and images in the figure below summarize the meaning of the title and intent of the book.

$$A\ (\mu Ci/gm) = F\ (mL/min\text{-}gm) \bullet EE \bullet P_{NI}/P_{Aa} \bullet \int_0^T C(t)\,dt\ (\mu Ci\text{-}min/mL)$$

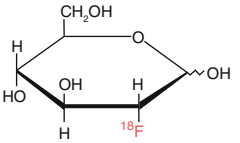

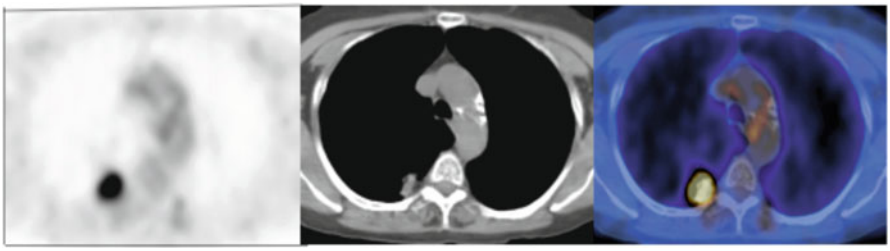

PET CT Fused

The equation indicates that there are four factors that determine the clearance of a radiopharmaceutical from blood. The chemical diagram depicts the radiopharmaceutical F-18-fluorodeoxyglucose (FDG), an analog of glucose. The three serial drawings of a portion of a cell membrane show a molecule of glucose entering the cell by facilitated diffusion via a transmembrane glucose transporter protein (GLUT-1). And finally, the PET-CT images demonstrate a focus of increased glucose metabolism in the posterior right lung in a PET image, a mass in the posterior right lung in the corresponding CT image, and confirmation that the increased glucose metabolism localizes to the lung mass in the fused image.

Of the four factors in the clearance equation, the most likely ones to explain the moderate to marked increased glucose metabolism in the lung mass are increased blood flow (1st factor) and/or increased extraction efficiency (second factor) secondary to an increased expression of glucose transporter receptors. A decrease in competing substances (third factor), e.g., hypoglycemia, and a higher concentration of F-18-fluorodeoxyglucose in the blood flowing to the mass compared to other tissues (fourth factor) are unlikely. The most likely etiologies are cancer and infection. Both are associated with increased blood flow and an increased extraction efficiency. The patient had severe emphysema, but also was from Southeast Asia. The lesion was a tuberculoma.

This book is divided into three parts. Part I: Introductory Concepts contains just two chapters. The first chapter, "General Concepts in Nuclear Medicine," presents a series of concepts and facts related to nuclear medicine that serve as a general background for what follows. The second chapter, "Quantitative versus Visual Interpretation of Images," specifically examines the advantages and disadvantages of quantitative versus visual interpretation of images and when to use or not use quantification. Both introductory chapters lend support to the importance of having a mathematical and conceptual framework for the analysis and

interpretation of the biodistribution of radiopharmaceuticals as depicted in clinical images.

Part II: Mathematics of the Biodistribution of Radiopharmaceuticals consists of eight chapters that focus on the mathematics that describe the biodistribution of radiopharmaceuticals and that conceptually inform image interpretation or that allow quantification of biologic parameters. The first chapter gives an overview of the content and approach of each of the following chapters. The subsequent chapters introduce various equations that describe the time-dependent biodistribution of radiopharmaceuticals within the body. Different equations are required for different studies depending on (1) where the radiopharmaceutical is introduced, (2) how the radiopharmaceutical is cleared, and (3) whether the radiopharmaceutical is excreted. In cases in which an equation is not widely known, the equation is derived.

In general, mathematics that are related to nuclear medicine, but that do not involve biologic processes and that are not directly related to the time-dependent biodistribution of radiopharmaceuticals, are not covered in this book. Examples include the equations and algorithms for radioactive decay, image reconstruction (SPECT and CT), correction for cross talk, etc. These subjects are adequately covered in textbooks of medical physics.

Part III: Quantitative Evaluation in Nuclear Medicine Studies consists of 10 chapters. The first chapter is an overview of the content and approach of the following chapters. The subsequent chapters systematically look at the diagnostic procedures that are used clinically from the point of view of how the equations discussed in Part II: (1) inform the design of an optimal study protocol and (2) can assist in the interpretation of clinical images. In addition, Part III summarizes the literature with respect to what is known of the physiologic or molecular biologic mechanism(s) that primarily determine the biodistribution of each radiopharmaceutical. This mechanism usually, but not always, involves the extraction or clearance of the radiopharmaceutical from blood into tissue. While the focus of the book is on diagnostic imaging procedures, the mathematics, biology, and associated concepts apply equally well to the biodistribution of radiopharmaceuticals in the corresponding therapeutic procedures.

Nuclear medicine studies have many variables and there are multiple approaches to the performance and interpretation of almost every nuclear medicine procedure. The approaches presented in this book reflect the experience and preferences of the author, but it is recognized that other valid approaches exist.

Despite the fact that this book is written from a clinical point of view and is primarily intended for nuclear medicine physicians, it should also prove useful to radiochemists who are involved in the design of novel radiopharmaceuticals, as well as medical physicists, radiation biologists, and other scientists working in the field of nuclear medicine.

Colorado, USA William C. Klingensmith III

Contents

Part I

Introductory Concepts

General Concepts in Nuclear Medicine

1

Introduction

Nuclear medicine is fundamentally based on radiopharmaceuticals whose biodistribution in health and disease result in either images that are diagnostically useful or local irradiation of tissue that is therapeutically beneficial. In this book we examine the physiologic and molecular biologic processes that account for the biodistribution of radiopharmaceuticals and the mathematics that describes and, to some extent, clarifies these physiologic and molecular biologic processes. This approach to the biodistribution of radiopharmaceuticals provides the nuclear medicine physician with a conceptual framework for the evaluation of clinical images that can be complementary to pattern recognition.

In this first chapter of Part I, we briefly examine several general nuclear medicine facts and concepts that help set the stage for what follows. Then in Chap. 2, Quantitative vs. Visual Evaluation of Images, we evaluate the advantages and disadvantages of quantitative vs visual interpretation of images. Next in Part II, Mathematics of the Biodistribution of Radiopharmaceuticals, we evaluate the mathematics that applies to the biodistribution of radiopharmaceuticals. And last in Part III, Quantitative Evaluation of Nuclear Medicine Studies, we systematically look at the degree to which the mathematical equations and concepts apply to the physiology and molecular biology that determine the biodistribution of radiopharmaceuticals in each of the clinically useful nuclear medicine studies.

General Nuclear Medicine Facts and Concepts

The Place of Nuclear Medicine Within the Realm of Science

Figure 1.1 shows the place of the discipline of nuclear medicine within the general realm of science, starting from science as a whole and proceeding to ever more specific entities.

W.C. Klingensmith III, *The Mathematics and Biology of the Biodistribution of Radiopharmaceuticals-A Clinical Perspective*,
DOI 10.1007/978-3-319-26704-3_1

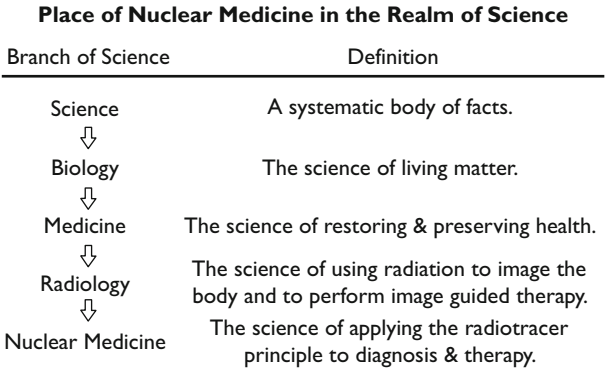

Fig. 1.1 Place of nuclear medicine in the realm of science

Table 1.1 The scientific discoveries underlying nuclear medicine

1896	Henri Becquerel	Discovery of radioactivity in uranium
1899	Ernst Rutherford	Discovery of alpha and beta particles
1900	Paul Villard	Discovery of gamma rays
1905	Albert Einstein	Equation for conversion of mass to energy
1911	Ernst Rutherford	Discovery of protons
1913	George de Hevesy	Discovery of the radiotracer principle
1931	Ernst Lawrence	Invention of the cyclotron
1936	Carl Anderson	Discovery of positrons (antimatter)
1939	Segre and Seaborg	Discovery of Tc-99m
1942	Enrico Fermi	First sustained release of nuclear energy

As Table 1.1 indicates, nuclear medicine is based on the radiotracer principle, which was discovered by Georg de Hevesy in 1913. The radiotracer principle allows the study of a wide variety of processes in a noninvasive way that does not disturb the system under study. De Hevesy was awarded the Noble Prize in Chemistry for his discovery of the radiotracer principle in 1943.

Scientific Discoveries That Made Nuclear Medicine Possible

Table 1.1 is a somewhat arbitrary list of critical discoveries (and year of discovery) that underlie the discipline of nuclear medicine. Of interest, all but Paul Villard's discovery of gamma rays resulted in a Noble Prize. There may be no other medical specialty that is enabled by so many Noble Prize winning discoveries, particularly in physics. While there have been many Nobel Prizes in physiology or medicine that contribute to the foundation of medicine, they contribute to all of the specialties in medicine.

Attributes That Make Imaging Useful

Every hospital has a radiology department, including nuclear medicine, but why? The answer lies in two attributes, regional and noninvasive. The diagnostic

information that images provide is inherently of a regional nature and it is obtained in a noninvasive fashion. By contrast surgery gives a regional effect, but it does so in an invasive fashion. Similarly, laboratory medicine provides noninvasive information, e.g., elevated blood parathormone level, but it does not tell you which parathyroid gland is hyperactive, i.e., no regional information.

The same attributes apply to therapy. Both interventional radiology and nuclear medicine therapy procedures cause a regional therapeutic effect in a relatively noninvasive manner. In Fig. 1.2 Graves disease is used to illustrate how the attributes of regional and noninvasive apply to therapy. Graves disease can be treated medically with antithyroid medication such as propylthiouracil, surgically with a partial thyroidectomy or with radiotherapy with I-131.

Medical therapy is noninvasive, but it is not completely regional in that the antithyroid medication has side effects in other organs, i.e., the liver and bone marrow. And surgery gives regional therapy but is invasive.

Role of Nuclear Medicine in Diagnostic Imaging

Figure 1.3 shows the various imaging modalities categorized according to whether they depict predominately anatomy or function. All of the modalities in radiology primarily demonstrate anatomy except for nuclear medicine. Nuclear medicine primarily demonstrates function while the other modalities cannot for many reasons (Table 1.2). Figure 1.4 demonstrates why, unlike many radiographic, CT and MR

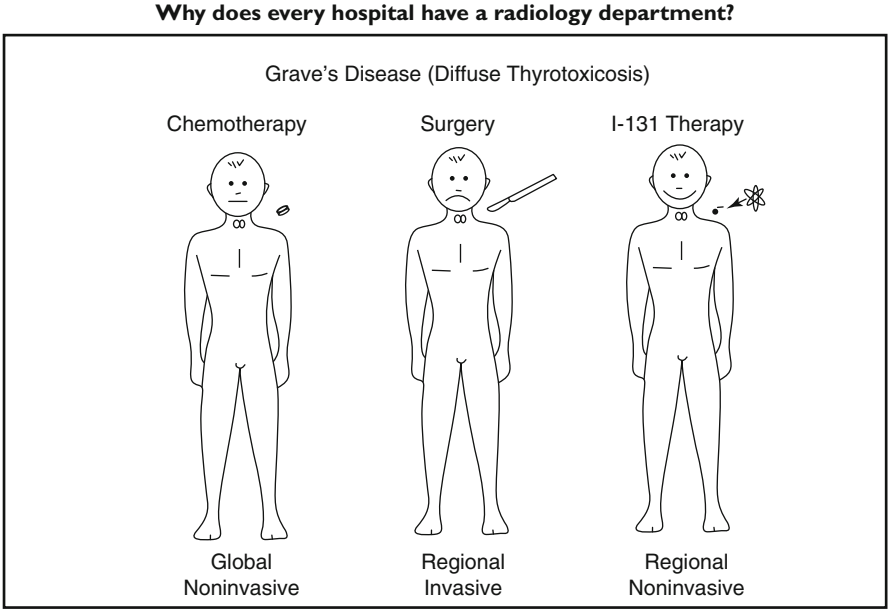

Fig. 1.2 Combination of regional and noninvasive attributes. The power of radiology arises from its ability to obtain regional information or to give a regional effect in a noninvasive fashion

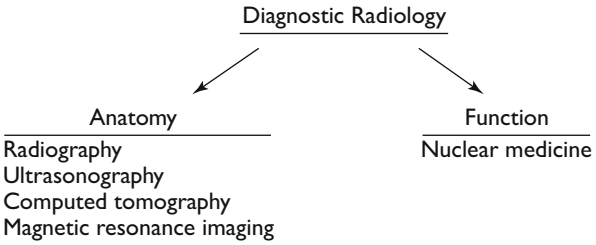

Fig. 1.3 Anatomic vs. functional modalities in radiology. All but 1 modality gives mainly anatomic information. Nuclear medicine is the only modality that provides mainly functional information

Table 1.2 Reasons nuclear medicine can image function

Parameter	Explanation
High contrast	Before injection of the radiopharmaceutical, there is no radioactivity in the body. The ratio of radioactivity in the target to adjacent tissue can be very high
High sensitivity	Nuclear medicine imaging machines can detect a single photon from a single molecule. Other modalities cannot detect a single molecule, even in a vacuum
High specificity	When a nuclear medicine machine detects a signal, it is certain which atom or molecule it comes from This is not true for any other modality
High spatial resolution	Nuclear medicine machines with built in CT give nuclear medicine images the spatial resolution of CT by way of co-registration
Inherently quantitative	Each gamma photon that passes from within the patient to the imaging machine is individually counted

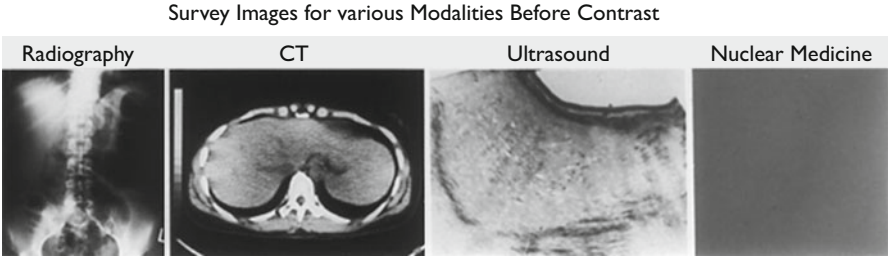

Fig. 1.4 Survey images for various modalities. There is no radioactivity in the body to begin with so survey images are usually not obtained in nuclear medicine

studies, no initial survey image is obtained prior to injection of the radiopharmaceutical in nuclear medicine studies.

Importance of PET in Nuclear Medicine

As indicated in Fig. 1.5 under "Function" nuclear medicine can be divided into two parts: (1) conventional nuclear medicine with gamma cameras, when studies were

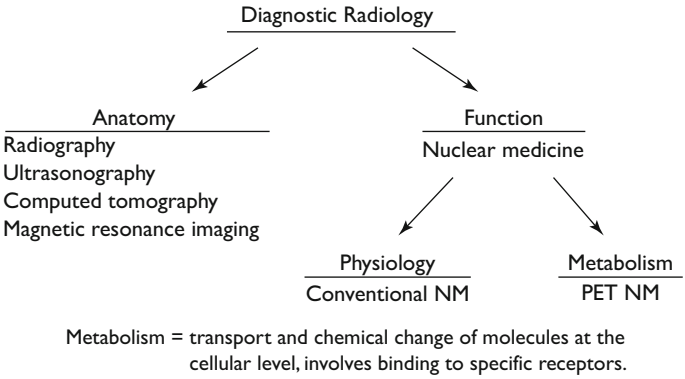

Fig. 1.5 Conventional vs. PET nuclear medicine. In general, conventional nuclear medicine with gamma cameras was not able to image metabolism

limited primarily to imaging physiology, and (2) modern nuclear medicine after clinical PET became available, which made it possible for nuclear medicine to image metabolism.

By physiology we mean the work of organs, not directly involving chemical reactions. By metabolism we mean the transport and chemical change of molecules at the cellular level that involves binding to receptors and enzymes.

So why can PET image metabolism and gamma cameras cannot? The answer is shown in Fig. 1.6 and Table 1.3. Figure 1.6 shows the periodic table with the common elements in biology colored purple and the trace elements colored green.

Table 1.3 shows the "Elements of life" in the first column: oxygen, carbon, hydrogen, and nitrogen. Together these four elements make up more than 96 % of the body by weight. In order to image metabolism with a gamma camera, you need radioisotopes of one or more of the four elements of life that emits a gamma ray with an appropriate energy and a reasonable half-life. Unfortunately, when we look at the chart of the nuclides, there are none, so it is impossible to image small metabolically important molecules with a gamma camera.

On the other hand, if we repeat this exercise and look at the chart of the nuclides for positron-emitting radioisotopes of the elements of life, we find useable positron emitters of oxygen, carbon, and nitrogen, but none for hydrogen. However, fluorine-18 can serve as a workable substitute for hydrogen because it has the same valence state in its outer electron shell and a similar atomic radius because of its nearly full outer electron shell. This striking advantage of PET, the ability to image the elements of life, meant that the introduction of PET into clinical nuclear medicine opened all of molecular biology to imaging.

Ultimate Nuclear Medicine Imaging Machine

The most recent advance in nuclear medicine imaging is the integration of an anatomic machine, e.g., a CT scanner, into PET machines (Figs. 1.7 and 1.8).

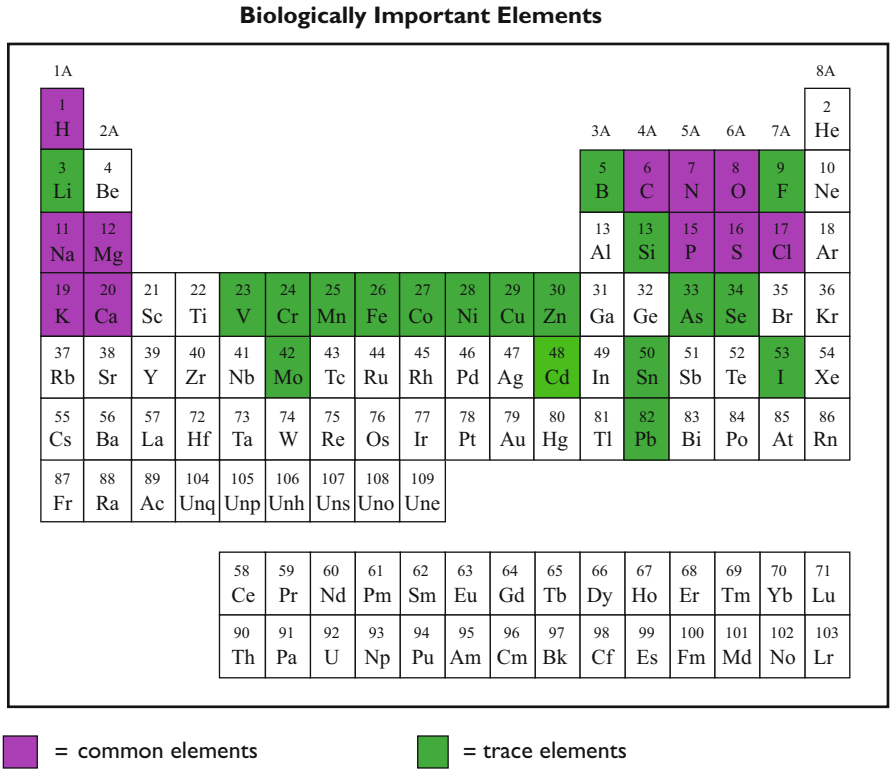

Fig. 1.6 Biologically important elements. Elements in *purple* are common in biological systems while those in *green* are present in trace amounts

Table 1.3 Conventional NM vs. positron imaging

Elements of life	Biologic abundance	Conventional equivalent	Positron equivalent
Oxygen-16	65 %	–	O-15
Carbon-12	18 %	–	C-11
Hydrogen-1	10 %	–	F-18
Nitrogen-14	3 %	–	N-13
	96 %		

Since PET scanners can image physiology as well as metabolism and have higher spatial resolution as well as other advantages, most nuclear medicine studies in the future will be done with PET-CT machines. The PET-CT machine is arguably the most sophisticated clinical imaging machine to date.

The Spatial Resolution of PET

Nonnuclear medicine physicians frequently ask what the spatial resolution of a PET scanner is. The standard method of determining the spatial resolution of an imaging

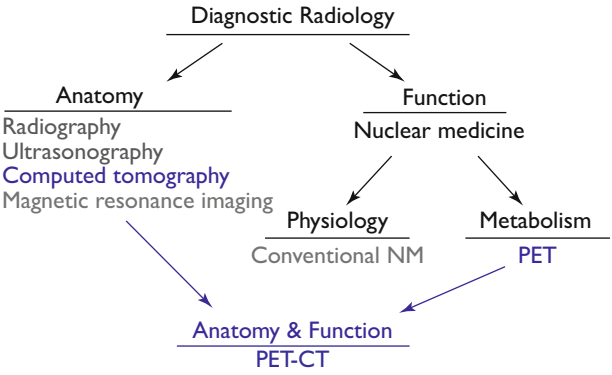

Fig. 1.7 Integration of PET and CT. Hybrid PET and CT machines give the best of both worlds, function and anatomy

Fig. 1.8 Commercial PET-CT machine. This is arguably the most powerful medical imaging machine to date (GE Medical Systems)

system is to measure how close together you can bring two appropriate objects and still distinguish them as two objects instead of one. The current answer for a PET scanner is about 4 mm. However, it can be argued that there are other kinds of spatial resolution that are pertinent.

Figure 1.9 demonstrates two other types of PET and PET-CT resolution. The images show PET, CT, and PET-CT (fused) images of a straight pin whose head was dipped in F-18 before it was stuck into the bottom of an upside-down Styrofoam cup.

The PET image shows a clear focus of activity despite the fact that the activity is distributed over a distance of only 1 mm on the head of a straight pin, below the spatial resolution of a PET scanner. The activity looks larger than 1 mm because the spatial resolution of the PET scanner is only 4 mm. However, the activity is clearly detected. In fact, there is no theoretical lower limit for detection resolution. With current PET scanners and current radiopharmaceuticals, the smallest clinical structure that can be seen is probably a 3 mm nodal metastasis of melanoma labeled with F-18-fluorodeoxyglucose (FDG) located in subcutaneous fatty tissue, which takes up very little FDG.

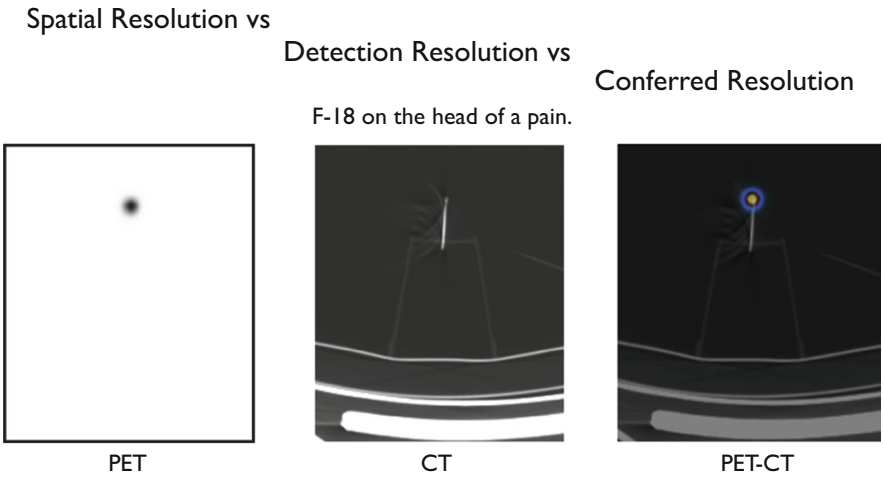

Fig. 1.9 Spatial vs. detection vs. conferred PET resolution. The PET scanner inherently has a spatial resolution and a detection resolution. The CT scanner adds a third, a conferred resolution

Figure 1.9 also demonstrates conferred resolution, which is the resolution conferred on the PET scanner by the attached CT scanner. For analysis of conferred resolution, we start with evaluation of the PET image, then move to the PET-CT image and then to the CT image. In Fig. 1.9 we would first note the focus of activity in the PET image, then look at the PET-CT image to see where it is anatomically, and finally look at the unobscured CT image to see that the activity corresponds to the 1 mm head of a straight pin. In fact, this sequence is what nuclear medicine physicians do all the time when interpreting PET-CT studies. Thus, the presence of a CT scanner confers CT spatial resolution, i.e., submillimeter, onto the PET scanner.

A Suboptimal Radiotracer Can Be an Optimal Radiopharmaceutical

The ideal radiotracer by definition passes through the same pathway as the molecule under study without perturbing the system under study. However, sometimes a radiotracer that does not completely follow the molecule under study makes a better radiopharmaceutical than a perfect radiotracer would. An example is FDG, a radiotracer of native glucose. Figure 1.10 shows glucose and FDG interacting with a cell that has expressed glucose transporters (GLUT) in the cell membrane.

Although the chemical structure of FDG does not exactly match the glucose molecule that it is tracing, FDG does bind to the receptor site on the GLUT receptor and is transported into the cell. Within the cell FDG and glucose both bind to the

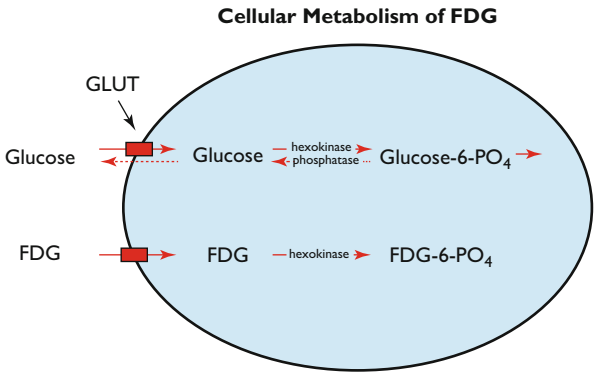

Fig. 1.10 Cellular uptake of glucose vs. FDG. Most transmembrane glucose transport proteins bind to glucose and FDG equally. In addition, the hexokinase enzyme binds to and phosphorylates glucose and FDG equally well. However, the next enzyme in the glycolytic pathway binds phosphorylated glucose, but not phosphorylated FDG

hexokinase that phosphorylates the molecules, a process which prevents the molecules from passing back out through the cell membrane.

At this point the fates of FDG and glucose diverge. FDG does not bind to any other enzyme and remains within the cell. However, glucose continues through the glycolytic pathway and its metabolites pass back out through the cell membrane. In addition, a small amount of phosphorylated glucose is dephosphorylated by a phosphatase and passes out of the cell. The fact that the F-18 radioactive label on FDG stays within the cell results in a higher target to background ratio in images.

Another difference in the interaction of FDG and glucose with the body is that FDG is filtered in the kidney but not reabsorbed, whereas glucose is reabsorbed. Thus, the blood level of FDG drops faster than it otherwise would, which also contributes to a higher target to background ratio.

PET as the Imaging Component of Molecular Medicine

> Chemistry is the language of health and disease, and if the definition of disease is molecular, diagnosis becomes molecular.
>
> Henry N. Wagner, Jr.

Essentially all of biology is based on chemistry, which in turn is based on atoms and molecules. With the rapid advances in molecular biology over the past few decades, medicine has more and more become molecular medicine. Figure 1.11 shows a protein interaction map of a representative cell, as of 2003; yellow is the cell wall, blue the cytoplasm, and green the nucleus.

The dots represent known cellular proteins, the location of the dots indicates where the proteins are found within the cell, the color of the dots codes for the organelle to which the proteins are attached, and the connecting lines indicate

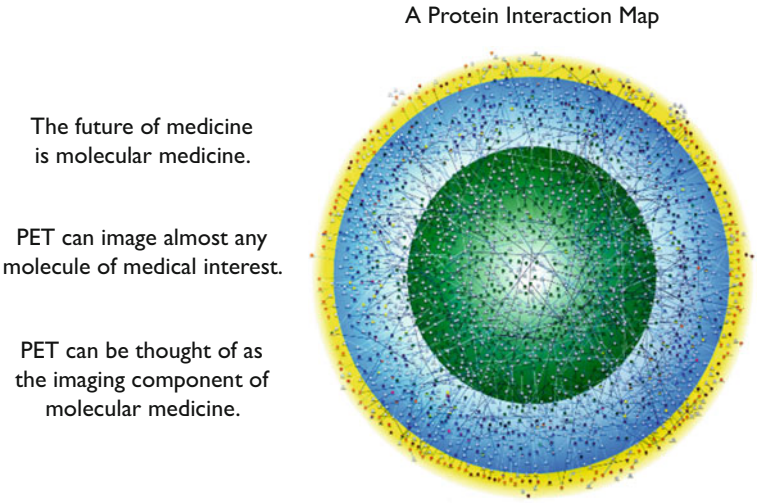

Fig. 1.11 PET as the imaging component of molecular medicine. This protein interaction map emphasizes the growing knowledge of cell structure and function at the molecular level. PET is capable of imaging almost any molecule of biologic interest (Giot L, et al.: *Science* 302:1727–36, 2003)

known interactions between proteins. From an imaging point of view, only PET is capable of imaging almost any molecule of biomedical significance. Thus, PET can be thought of as the imaging component of molecular medicine.

Relative Scope of Practice of Nuclear Medicine

It is of interest to compare the scope of practice of nuclear medicine to the other divisions of radiology. In Table 1.4 the divisions of radiology are listed in the first column and various parameters are listed across the top. The modalities are listed from top to bottom in order of increasing scope of practice. The entries in the matrix are conceptual and not strictly literal, i.e., breast imaging is listed as pertaining only to females.

It can be seen that the division of breast imaging has the narrowest scope of practice: one organ, one disease, only anatomy, only diagnosis, only adults, and only females. At the other end of the spectrum nuclear medicine has the greatest scope of practice: all organs, all diseases, anatomy and function, diagnosis and therapy, all ages, and both males and females. In addition, every time a new clinically useful radiopharmaceutical is developed, nuclear medicine gets a new study, e.g., the Striatal Dopamine Transporter Study with I-123-ioflupane. In fact, there is no other specialty or subspecialty in medicine, not just radiology, with such a complete scope of practice.

Table 1.4 Scope of practice of various divisions of radiology

Division	Organ(s)	Disease(s)	Anatomy/function[a]	Diagnosis/therapy[a]	Age	Sex	
Breast imaging	Breast	Cancer	Anatomy	Diagnosis	Adult	F	Scope ↓
Musculoskeletal	MSK	All	Anatomy	Diagnosis/therapy	All	M/F	
Neuroradiology	CNS	All	Anatomy	Diagnosis	All	M/F	
Abdominal imaging	Abdomen	All	Anatomy	Diagnosis	All	M/F	
Chest imaging	Chest	All	Anatomy	Diagnosis	All	M/F	
Interventional radiology	All	Vascular, infection	Anatomy	Therapy/diagnosis	All	M/F	
Pediatrics	All	All	Anatomy/function	Diagnosis/therapy	Pediatric	M/F	
Nuclear medicine	All	All	Anatomy/function	Diagnosis/therapy	All	M/F	

Quantitative vs. Visual Interpretation of Images

2

Introduction

> Accurate reckoning. The entrance into the knowledge of all existing things and all obscure secrets.
>
> *Rhind Mathematical Papyrus*, ~1650 BCE [1]

> Measure the measurable and try to render measurable what is not yet.
>
> Galileo Galilei (1564–1642)

> When you can measure what you are speaking about, and express it in numbers, you know something about it; but when you cannot measure it, when you cannot express it in numbers, your knowledge is of a meagre and unsatisfactory kind; it may be the beginning of knowledge, but you have scarcely in your thoughts advanced to the state of Science, whatever the matter may be.
>
> Lord Kelvin, 1893

Members of the public are generally impressed by quantitation and numbers; and scientists, in particular, show great reverence for measurements and quantitative analysis. Relatively simple well-defined parameters of basic qualities such as a person's height and weight can be easily measured in an accurate and reproducible fashion. The person's height and weight can also be estimated visually by a human observer, but the estimate will be neither as accurate nor as reproducible.

At the other end of the spectrum of complexity are images such as the human face and medical images. These images consist of multiple parameters, lack sharp borders or geometric shapes, have variable signal intensity within a single structure, and cannot be easily measured. Yet these images hold very useful information. The question is not a simple one such as height or weight but whether a face is that of specific person, from any projection and in any mood, or whether a medical image is consistent with a certain medical condition or is pathognomonic of a particular disease.

In addition, the details of a pattern for any given disease will vary from patient to patient because of variations in the size, shape, and age of the patient and the

W.C. Klingensmith III, *The Mathematics and Biology of the Biodistribution of Radiopharmaceuticals-A Clinical Perspective*,
DOI 10.1007/978-3-319-26704-3_2

location, extent, and duration of the disease. The possible variation in details of the same disease from patient to patient and from time to time is endless. And, there is essentially no equivalent to a discrete scientific quality that can be measured that would summarize the useful information in the image.

Evolutionary pressures have resulted in a human eye-brain complex which has extraordinary abilities for analyzing images and recognizing patterns (Fig. 2.1). As an example, radiologists refer to a typical pattern of a disease or condition in a medical image that can be immediately recognized once you have seen it before as an "Aunt Minnie." Aunt Minnie patterns have certain features that can be described and listed, but there is no substitute for having seen an image of the disease or condition before.

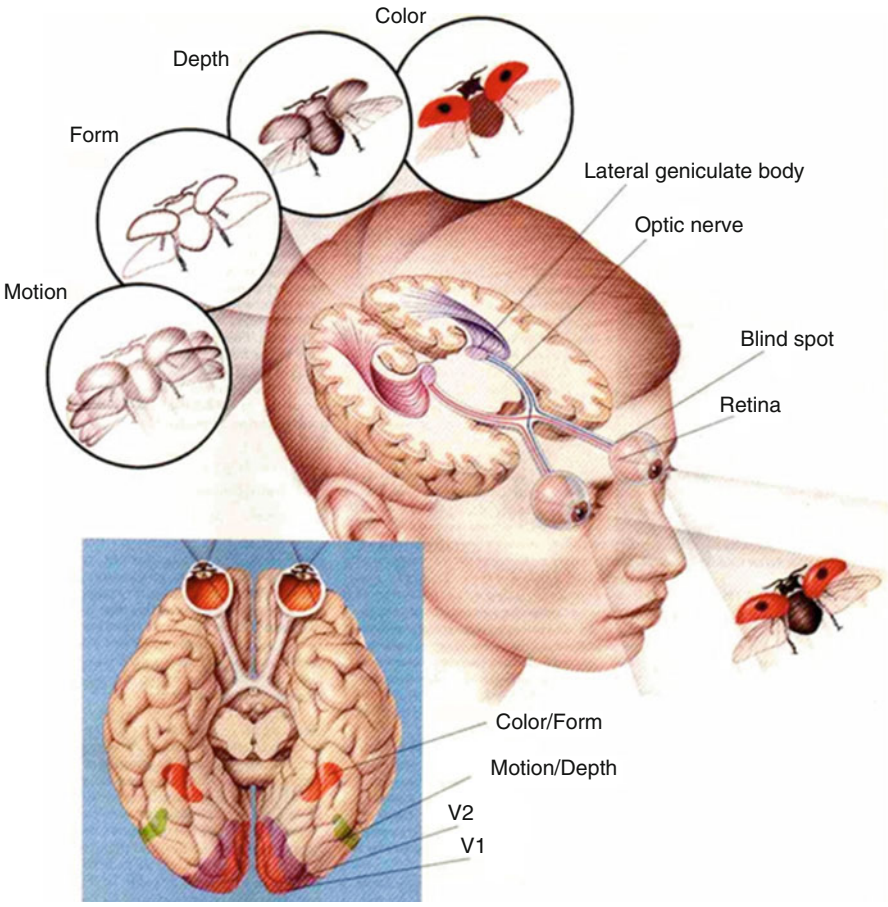

Fig. 2.1 The eye-brain complex. The eye-brain complex, in almost real time, breaks down an image into multiple different parameters, evaluates each one separately, and then synthesizes the data into a coherent result [2]

The same phenomenon applies to faces as the label suggests. Imagine a lineup of your Aunt Minnie and four other older women who were chosen because they look like your Aunt Minnie: same height, weight, hair color, eye color, dress, etc. Since you know your Aunt Minnie, you can visually analyze the faces and immediately pick out your Aunt Minnie. Now imagine that you have to create an algorithm for a colleague, who doesn't know your Aunt Minnie, that will enable your colleague to pick her out of the group. You could specify hair and eye color, distance between eyes and nostrils, a pleasant disposition, etc., but your colleague most likely will do little better than chance. A related dictum in radiology is "A radiologist with a ruler (or electronic calipers) is a radiologist in trouble." The point is that if the radiologist does not recognize the abnormality from previous experience, resorting to a series of measurements is not likely to provide the answer.

> The brain is the last and grandest frontier, the most complex thing we have yet discovered in our universe. It contains hundreds of billions of cells interlinked through trillions of connections. The brain boggles the mind.
>
> James D. Watson

Another critical capability of the eye-brain complex is its ability to recognize a pattern that has been significantly distorted (Fig. 2.2) [3]. This image of Abraham Lincoln from a cover of Science has been digitized at low spatial resolution, but an American eye-brain complex can still recognize who it is almost instantly. The original cover of Science had three additional images of Lincoln with increasing amounts of smoothing, which in turn made the image progressively easier to recognize. Here only the most distorted version is shown.

The ability of the eye-brain complex to recognize distorted images is also demonstrated by the widely used method, CAPTCHA (Completely Automated Public Turing test to tell Computers and Humans Apart) (Fig. 2.3). CAPTCHA is a challenge-response test that is used on the internet to determine if the entity on the other end of the connection is a human or a computer software application [4]. Another aspect of the eye-brain complex is demonstrated in Fig. 2.4. Panel a is a matrix of Hounsfield units from a medical image. Every digital image has an underlying matrix of numbers that corresponds to the intensity of the gray scale in each cell of the matrix. Yet the numbers alone, while very quantitative, are essentially uninterpretable to the eye-brain complex. The information must be converted to a gray or color scale before it can be analyzed by the eye-brain complex (panel b).

> Everything that can be counted does not necessarily count;
> everything that counts cannot necessarily be counted.
>
> Albert Einstein

Despite the exquisite sophistication of the eye-brain complex for evaluating patterns, it must be stated that there is no theoretical reason why a computer cannot be programmed to analyze patterns in images, as reflected in a matrix of numbers, as well as, or better than, the eye-brain complex [5]. However, currently the ability of

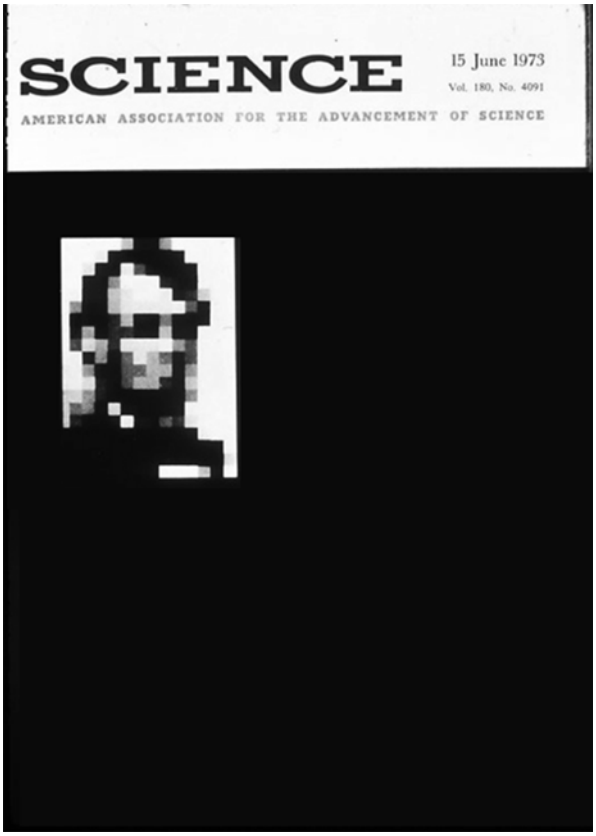

Fig. 2.2 Abraham Lincoln. The original cover of Science showed four digitized images of Abraham Lincoln with increasing degrees of smoothing. Three of them have been removed for clarity. The point is that despite significant distortion of the remaining image, those familiar with Lincoln's face have no trouble recognizing him [3]

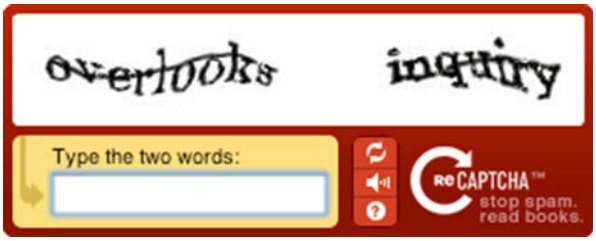

Fig. 2.3 CAPTCHA. CAPTCHA tests consist of distorted letters or figures. Humans can easily determine what the symbols represent, but computer algorithms, in general, are unable to decipher them [4]

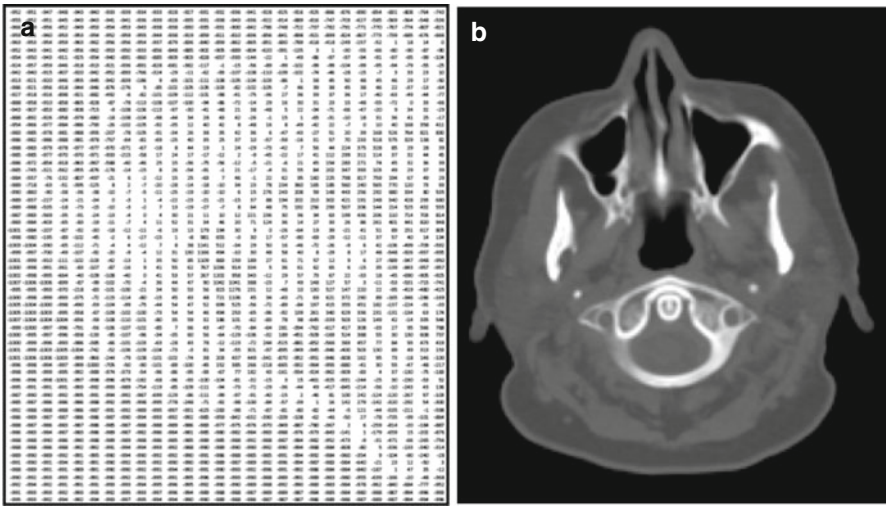

Fig. 2.4 Digital medial image. Panel (**a**) is a matrix of numbers, which in this case are Hounsfield units from a CT image. Although the information is very quantitative, the eye-brain complex is unable to interpret the information until the numbers are converted to a gray scale (Panel **b**)

computers to analyze digital images created by medical imaging machines is quite limited. Because of the inability of computer search engines to make sense of images, beyond their labels, online images have been called the "dark matter of the digital age" [6]. Presumably, it will be a long time before computers or some more advanced analytic device matches the pattern recognition capabilities of the eye-brain complex.

Generating Numbers: General

There are a total of 39 diagnostic nuclear medicine studies included in this book (Appendix A). Sixteen of them routinely involve the explicit generation of one or more numbers, which are integrated with the visual evaluation of the images to form the overall interpretation of the study. In addition, quantification is performed in a number of other studies as an optional maneuver. In the 16 studies, in which a number is generated routinely, visual evaluation is directly involved in the quantitative process either by determining when activity reaches a certain anatomic structure or by determining the appropriate anatomic boundaries of one of more regions of interest (ROIs). This concept even applies to the thyroid uptake measurement with I-123 in that correct placement of the thyroid probe depends on visual assessment of the patient's neck and thigh although here the visual evaluation is done by the nuclear medicine technologist. In addition, visual interpretation should always be used to evaluate all of the images in a study whether there is any quantitation involved or not.

As will be mentioned below and discussed in detail in Part II, Mathematics of the Biodistribution of Radiopharmaceuticals, and Part III, Quantitative Evaluation of Nuclear Medicine Studies, the numbers that are generated by the various quantitative processes are subject to a number of errors [7–9]. Whenever the visual appearance of the structures involved in generating numbers does not agree with the number, the various steps in the quantitative process, especially the placement of ROI(s), should be reviewed. In general, the nuclear medicine physician should not let a number override his/her visual interpretation.

We will now look at three different types of quantitation as examples of how quantitation in nuclear medicine studies can be conceptually categorized. These three categories are (1) measurement of transit time by visual evaluation of a sequence of images; (2) measurement of relative function, in terms of either time or clearance; and (3) measurement of absolute function in terms of clearance. Each of these categories, as well as others, will be discussed more extensively in Parts II and III of this book.

Generating Numbers: Transit Times

Table 2.1 lists the five nuclear medicine studies in which visual evaluation is used to directly determine a number, the leading edge transit time, through a flowing system. This works because the beginning and end points are operationally well defined and/or easily identified in the images. Because of laminar flow, the leading edge transit time will always be faster than the mean transit time (see Chap. 5, Mean Transit Time: Central Volume Principle).

In the case of the Cisternography Study, the start time is the time of injection of the tracer into the lumbar subarachnoid space and the end time is the time at which the tracer reaches the region of the superior sagittal sinus. Normally, the tracer reaches the convexity of the brain by 24 h after intrathecal injection in the lumbar region. Blockage of the subarachnoid space and enlargement of the cerebrospinal fluid space are two causes of a prolonged leading edge transit time.

Table 2.1 Studies that measure leading edge transit times visually

Study	Radiopharmaceutical	Parameter	Upper limit of normal
Cisternography	In-111-DTPA	Subarachnoid space: lumbar to superior sagittal sinus	24 h
Cardiac Gated Blood Pool Study	Tc-99m-red blood cells	Vascular space: right ventricle to left ventricle	6 s
Hepatobiliary Study	Tc-99m-trimethylbromo-IDA	Biliary tract: hepatocytes to extrahepatic bile ducts	10 min
Renal Glomerular Filtration Study	Tc-99m-DTPA	Tubular lumens: glomeruli to calyces	5 min
Renal Tubular Secretion Study	Tc-99m-MAG3	Tubular lumens: tubular cells to calyces	5 min

In the case of the Cardiac Gated Blood Pool Study with Tc-99m-red blood cells, the leading edge transit time through the pulmonary vasculature is defined as the time it takes for the leading edge of the tracer to pass from the right ventricle to the left ventricle. Visually this is the time difference between when the tracer is first seen in the right ventricle and when the tracer is first seen in the left ventricle. The serial images during the first circulation of the Tc-99m-red blood cells are acquired in the left anterior oblique projection in order to provide good separation between the right and left ventricles.

The normal leading edge pulmonary transit time is 6 s or less. Any disease or condition that decreases cardiac output (flow) or increases the blood volume of the lungs will increase the leading edge pulmonary transit time (see Chap. 5, Mean Transit Time: Central Volume Principle). Left ventricular failure both decreases cardiac output and increases pulmonary blood volume and is the most common cause of a prolonged pulmonary leading edge transit time.

In the case of the Hepatobiliary Study with Tc-99m-trimethylbromo-IDA, Renal Glomerular Filtration Study with Tc-99m-DTPA, and the Renal Tubular Secretion Study with Tc-99m-MAG3, the start time is the time of injection even though the parameter being measured starts with extraction of the tracer from blood into the liver or kidneys. However, the time from site of injection to the liver or kidneys is short compared to the parenchymal transit time, the injection time is convenient, and the start of the clearance is not easy to identify. The end times are the times at which the tracers leave the organ in question and appear in the intrahepatic ducts for the Hepatobiliary Study and in the calyces for the two renal studies. The upper limit of normal is 10 min for the Hepatobiliary Study and 5 min for the renal studies. The upper limit of normal is longer for the Hepatobiliary Study than for the kidneys presumably because the liver is larger than the kidneys and has longer pathways. The most common cause of a prolonged leading edge transit time in both organs is acute disease of any kind, possibly because the acute process causes edema and constriction of the intrahepatic bile ducts or renal tubular lumens.

Generating Numbers: Relative Measurements

Table 2.2 lists the 14 studies that routinely include generation of a number in relative terms. Quantitative values in relative terms are measurements that compare two values at two different locations in one or more images measured at the same point in time or two values at the same location in more than one image measured at the different times. For any given comparison, the attenuation of activity between the images is usually similar and in some cases can be ignored. However, background correction is always performed unless the images are tomographic (SPECT or PET) or there is no activity outside of the organ of interest. The amount of activity introduced to perform the study, i.e., the dose, is not part of the calculation.

The visual component in generating these numbers is the placement of the ROIs. The position, size, and shape of each ROI are important because misplacement can result in large numerical errors. The ROI should always be recorded on the pertinent

Table 2.2 Studies with relative quantitation

Procedure	Radiopharmaceutical	Functional parameter	Image type	Attenuation correction	Background subtraction
Cardiovascular system					
Cardiac Gated Blood Pool Study	Tc-99m-red blood cells	Ejection fraction	Planar	No	Background ROI
Myocardial Perfusion Study	N-13-ammonia	Myocardial perfusion	PET-CT	CT density map	Tomography
Myocardial Perfusion Study	Rb-82 as rubidium chloride	Myocardial perfusion	PET-CT	CT density map	Tomography
Myocardial Perfusion Study	Tc-99m-sestamibi	Myocardial perfusion	SPECT	Comparison to normal range	Tomography
Myocardial Perfusion & Viability Study	Tl-201 as thallous chloride	Myocardial perfusion and viability	SPECT	Comparison to normal range	Tomography
Myocardial Viability Study	F-18-FDG	Myocardial viability	PET-CT	CT density map	Tomography
Central nervous system					
Ventricular Shunt Study	Tc-99m-DTPA	Washout time	Planar	No	No background activity
Gastrointestinal system					
Esophageal Motility Study	Tc-99m-sulfur colloid	Transit time	Planar	No	No background activity
Gastric Emptying Study	Tc-99m-sulfur colloid	Transit time	Planar	Geometric mean of opposing images	No background activity
Hepatic Artery Perfusion Study	Tc-99m-MAA	Hepatic artery perfusion	Planar	Geometric mean of opposing images	No background activity
Hepatobiliary Study	Tc-99m-trimethylbromo-IDA	Gallbladder ejection fraction	Planar	No	Background ROI
Genitourinary system					
Renal Glomerular Filtration Study	Tc-99m-DTPA	Half-time of peak renal activity	Planar	No	Background ROI
Renal Tubular Excretion Study	Tc-99m-MAG3	Half-time of peak renal activity	Planar	No	Background ROI
Renal Tubular Function Study	Tc-99m-DMSA	Renal tubular clearance	Planar	No	Background ROI

image, submitted for review at the time of interpretation, and saved permanently as part of the study record.

In the section above, Generating Numbers: Transit Times, the clinical aspects of the studies were discussed as examples of putting everything together and because there are only five studies. However, in this section, because there are so many studies with relative quantitative measurements, the clinical details will be deferred until Part III, Quantitative Evaluation in Nuclear Medicine Studies.

Generating Numbers: Absolute Measurements

Table 2.3 lists four studies that routinely include generation of a number in absolute terms. The list has been arbitrarily limited to quantitative processes that measure a function rather than just an amount. All four studies achieve absolute quantification of a function by forming a ratio of the activity in the organ or lesion of interest in the numerator divided by the amount of activity that was administered to the patient in the denominator. In addition, the issues of attenuation, background activity, and field of view of the imaging or measuring device must be normalized for the numerator and denominator.

There is one other study that involves a routine absolute measurement, but not of a bodily function: the Cystogram with Tc-99m-DTPA quantitates the post-void residual volume of urine in the bladder in absolute terms. In addition, there is a study that involves an absolute measurement, but not on a routine basis: the Cisternogram with In-111-DTPA occasionally quantitates the amount of leakage of tracer into the nasal cavity in absolute terms. These two studies are discussed in Chap. 10, Other Quantitative Techniques, at the end of Part II.

The visual component in generating the absolute quantitation of function is the placement of the ROIs. As stated above for relative measurements, the position, size, and shape of each ROI are important because misplacement can result in large numerical errors. The ROI should always be recorded on the pertinent image, submitted for review at the time of interpretation, and saved permanently as part of the study.

In absolute measurements, in which activity in an organ or lesion in the body is compared to the administered dose, there are even more possibilities for error than in relative measurements. As an example, a partial extravasation of the injected dose of a radiopharmaceutical will decrease the amount of tracer in the blood that is available for clearance into the organ or lesion and will result in a spuriously low measurement from the organ or lesion. But in a relative measurement, the effect of the extravasation has a proportional effect in the two or more ROIs that are involved and the errors cancel.

An important step in the interpretation of all studies is to evaluate the images for artifacts and in the case of studies that have quantitative measurements to look for findings that might render the measurements invalid. Table 2.4 (modified from reference [8]) is a partial summary of the large number of potential sources of error in the commonly used standard uptake value (SUV) in the Tumor Glucose Metabolism Study with F-18-fluorodeoxyglucose [8]. These errors are discussed in greater detail in Chap. 20, Tumor Imaging, in Part III.

Table 2.3 Studies with absolute quantitation

Procedure	Radiopharmaceutical	Functional parameter	Image type	Attenuation correction	Background subtraction	Absolute reference measurement
Endocrine system						
Thyroid Uptake Measurement	!-123	Thyroid uptake (clearance)	Probe	Neck phantom	Similar shaped structure without thyroid: Thigh	Measure dose in phantom with probe
Genitourinary system						
Renal Glomerular Filtration Study	Tc-99m-DTPA	Glomerular filtration (clearance)	Planar	Estimated from height, weight, and age	Background ROI	Measure dose with gamma camera and collimator
Renal Tubular Excretion Study	Tc-99m-MAG3	Tubular excretion (clearance)	Planar	Estimated from height, weight, and age	Background ROI	Measure dose with gamma camera and collimator
Tumor imaging						
Tumor Glucose Metabolism Study	F-18-FDG	Glucose metabolism (clearance)	PET-CT	CT density map	Tomography	Measure dose in dosimeter

Table 2.4 Causes of inaccurate SUV measurements (partial list)

Category/problem	Explanation	Effect	Usual range (maximum effect)
Technical errors			
Relative calibration between PET scanner and dose calibrator	Can create an incorrect calibration factor	Increases or decreases SUV	−10 to 10 % (±50 %)
Residual activity in syringe or administration system	Decreases administered dose	Decreases SUV	0–5 % (typically <15 %)
Dose calibrator and PET scanner clocks not synchronized	–	Increases or decreases SUV	−10 to 10 % (21 %)
Dose calibrator inaccurate	Affects denominator of SUV equation	Increases or decreases SUV	Unknown
Injection vs. calibration time	Inaccurate decay correction	Increases or decreases SUV	−10 to 10 % (unknown)
Extravasation of dose	Decreases blood tracer concentration	Decreases SUV	0–50% (or more)
Biologic factors			
Elevated blood glucose level	Increases competition for clearance of FDG	Decreases SUV	0–15 % (−75 %)
Prolonged FDG uptake time	Increases FDG available for clearance	Increases SUV	0–15 % (30 %)
Patient motion or breathing	Spreads FDG activity into greater number of pixels	Decreases SUV	0–30 % (60 %)
Nontumorous tissue competing for blood FDG	FDG taken out of blood by normal structures, e.g., myocardium, brown fat, muscle	Decreases SUV	Unknown
Decreased extraction efficiency	Down regulation of glucose receptors secondary to elevated blood glucose level	Decrease SUV	Large
Obesity	Attenuation not fully corrected	Decreases SUV	Unknown
Inflammation	Tumors frequently contain white blood cells	Increases SUV	Unknown
Physical factors			
Scan acquisition parameters	Lower SNR causes increase in SUV	Increases SUV	0–15 % (15 %)
Image reconstruction parameters	Insufficient convergence lowers SUV	Decreases SUV	−30 to 0 % (−30 %)
ROI	SUV strongly affected by ROI	Increases or decreases SUV	−30 to 30 % (−50 %)

(continued)

Table 2.4 (continued)

Category/problem	Explanation	Effect	Usual range (maximum effect)
Normalization method	SUV varies with method: weight, surface area, lean mass	Increases or decreases SUV	Trivial
Changing blood CT contrast levels during PET scanning	Inaccurate attenuation of PET data	Increases SUV	0–15 % (50 %)
Spatial resolution of PET scanner	Partial volume effect when lesion under 1.5 cm	Decreases SUV	−50 to 0 % (−100 %)

Conclusion

The approach to any imaging study is to first determine whether the protocol was followed and whether there are any artifacts. Then the images should be evaluated visually. In any study that includes quantitation with ROIs, the ROIs should be evaluated for correct placement. Then the quantitative numbers are assessed. If the numbers do not agree with the visual interpretation, the quantitative process should be scrutinized for errors.

Quantitation can improve the precision and accuracy of the final interpretation and convey useful information to the referring clinician, but the quantitative results should be used as a "consultant" and should not override the visual appearance [10]. For the foreseeable future, quantitation should inform the eye-brain complex, but not replace it.

References

1. Chace AB. Rhind mathematical papyrus; 1927. p. 27. National Council of Teachers of Mathematics, 1979; ISBN 0-87353-133-7.
2. Internet: Extraordinary design in the eye, 2016. http://www.designanduniverse.com/articles/design_in_the_eye.php
3. Harmon LD, Julesz B. Masking in visual recognition: effects of two-dimensional filtered noise. Science. 1973;180:1194.
4. von Ahn L, Maurer B, McMillen C, et al. reCAPTCHA: human-based character recognition via web based security measures. Science. 2008;321:1465–8.
5. Bohannon J. Unmasked: facial recognition software could soon ID you in any photo. Science. 2015;347:492–4.
6. Quote from Fei-Fei Li. In: Beyond the turing test. Science. 2015;347:116.
7. Keyes JW. SUV: standard uptake or silly useless value? J Nucl Med. 1995;36:1836–9.
8. Boellaard R. Standards for PET image acquisition and quantitative data analysis. J Nucl Med. 2009;50:11S–20.
9. Kumar V, Nath K, Berman CG, et al. Variance of SUVs for FDG-PET-CT is greater in clinical practice than under ideal study settings. Clin Nucl Med. 2013;38:175–82.
10. Coleman RE, Graham MM. Is quantitation necessary for oncological PET studies? Eur J Nucl Med. 2002;29:133–5.

Part II

Mathematics of the Biodistribution of Radiopharmaceuticals

Overview of Part II: Mathematics of the Biodistribution of Radiopharmaceuticals

3

In general, nuclear medicine physicians are fully aware of the essential role that the biodistribution of radiopharmaceuticals plays in determining the success of diagnostic and therapeutic nuclear medicine procedures. In addition, they appreciate the importance of the biologic mechanisms that determine the biodistribution of the various radiopharmaceuticals. However, often they are unfamiliar with the mathematics that describe these physiologic or molecular biologic processes or they are unaware of the degree to which a conceptual understanding of the relevant mathematics can inform the interpretation of clinical studies.

Stated differently, the simplest approach to image interpretation is pattern recognition (Aunt Minnie), a more sophisticated approach adds an understanding of the biologic processes that determine the biodistribution of the radiopharmaceutical, and the most complete approach includes a conceptual knowledge of the mathematical equations that describe the quantitative relationships among the various biologic parameters. In this book the mathematics is presented before the biology of the biodistribution of radiopharmaceuticals because each one of a relatively small number of equations applies to many nuclear medicine studies.

The next six chapters cover the mathematics that pertain to (1) the movement of radiopharmaceuticals through the vascular system during the first circulation; (2) the clearance of radiopharmaceuticals from the vascular space into organs, tissue, and lesions; (3) the passage of radiopharmaceuticals through parenchymal excretory systems; (4) the movement of radiopharmaceuticals through compartments; and (5) the calculation of relative and absolute functional measurements. The last chapter in Part II discusses a few miscellaneous mathematical techniques.

It is important to note that the more complex equations are never solved for any of the applicable nuclear medicine studies but that a conceptual knowledge of the structure of the equations can provide insights that may assist in the interpretation of images. Some of the simpler equations are utilized by the technologist in a formulaic fashion, but it is important for nuclear medicine physicians to have an understanding of these equations for purposes of quality control and interpretation.

W.C. Klingensmith III, *The Mathematics and Biology of the Biodistribution of Radiopharmaceuticals-A Clinical Perspective*,
DOI 10.1007/978-3-319-26704-3_3

Noticeable by its absence is compartmental analysis. Unfortunately, the use of compartmental analysis to model the biodistribution of radiopharmaceuticals as a function of time requires creation of an accurate model of the system under study, use of rate constants to describe the movement of the radiopharmaceutical between compartments (often bidirectional), measurement of an input function (ideally arterial), measurement of the amount of radiopharmaceutical in tissues and compartments as a function of time, and calculus for obtaining the solution in terms of rate constants [1–3]. Because these requirements are, in general, never met in nuclear medicine studies, compartmental analysis is not used in the clinical setting.

For an equation to be included in the chapters of Part II, Mathematics of the Biodistribution of Radiopharmaceuticals, it must (1) relate to the biodistribution of radiopharmaceuticals and (2) be clinically useful, either conceptually or by quantifying a biological parameter, e.g., renal clearance. At the same time, equations that relate to nuclear medicine but are not directly related to the biodistribution of radiopharmaceuticals, such as radioactive decay, modulation transfer function, image reconstruction (SPECT and CT), correction for cross talk, etc., are not included. These equations and algorithms are adequately discussed in textbooks of medical physics.

The first mathematical chapter, Chap. 4, Evaluation of Clearance, discusses the equation for clearance of a radiopharmaceutical out of a flowing system, usually from blood. Most, but not all, nuclear medicine studies involve clearance. Of the 39 nuclear medicine studies discussed in this book, 30 involve clearance. Twenty-seven of the 30 involve clearance of the radiopharmaceutical from blood, one involves clearance from lymph flow, and two involve clearance from flowing air, i.e., ventilation. The clearance equation consists of four factors, which are simply multiplied together. How this equation can be used conceptually to assist in image interpretation is discussed and demonstrated. The chapter on the evaluation of clearance is presented first in Part II because of the importance of the clearance process in a large proportion of nuclear medicine studies.

Chapter 5, Mean Transit Time: Central Volume Principle, discusses the relatively simple relationship between the volume of a compartment or region, the flow of blood or other fluids through the compartment or region, and the mean transit time through the compartment or region. This relationship is known as the "central volume principle." The mean transit time and the related leading edge transit time are used as relatively independent indicators of disease in a number of nuclear medicine studies. In all but one of them, clearance is also measured.

Chapter 6, Blood Flow: First Circulation Time-Activity Curves, discusses the information content of rapid serial images acquired during the first circulation of a radiopharmaceutical following intravenous injection. There are five nuclear medicine studies that routinely include first circulation images. In four of these studies, there are paired structures of interest, and in two of these four studies, paired time-activity curves are generated from the symmetrical structures. An understanding of the information content of paired time-activity curves from a mathematical point of view informs the visual interpretation of both the first circulation images and any time-activity curves that might be generated. The paired time-activity curves are not routinely quantitated.

Chapter 7, Regional Transit Times: Convolution Analysis, discusses the situation in which one is interested in the passage of a bolus of radiopharmaceutical through a region, often the parenchyma of an excretory organ such as the kidney. Evaluating the resulting serial images and any time-activity curve(s) generated from the images is relatively easy if the tracer enters the region in question as a discrete instantaneous bolus.

However, usually the incoming bolus is spread out over a considerable distance and enters the region of interest (ROI) over time. The resulting time-activity curve from a ROI is the result of the frequency distribution of transit times through the ROI convolved by the shape of the incoming time-activity curve. This happens routinely in studies of excretory organs like the kidneys and hepatobiliary system. This chapter looks at the underlying mathematics of the convolution process.

Chapter 8, Quantitation of Function: Relative Measurements, discusses the common situation in which activity in two paired organs is compared at one point in time or the activity in one organ is compared at different points in time. The Renal Tubular Secretion Study with Tc-99m-MAG3 includes examples of both: measurement of the percent of total renal function in each kidney is an example of relative comparison at one point in time, and measurement of the change in activity in the renal parenchyma over time is an example of relative comparison at multiple points in time. A defining characteristic of relative quantitative measurements is that the amount of administered dose is not part of the equation.

Relative measurements, particularly in planar images, are relatively simple compared to absolute measurements because attenuation correction is unnecessary. Attenuation will be essentially the same when measurements at two or more different time points are compared from the same ROI and will be nearly the same when measurements from symmetrical structures like the two kidneys are compared at the same time point.

Chapter 9, Quantitation of Function: Absolute Measurements, discusses measurements of function that are made in absolute terms, i.e., relative to the amount of radiopharmaceutical that was administered. Examples include renal clearance in the Renal Tubular Secretion Study with Tc-99m-MAG3, thyroid uptake in the Thyroid Uptake Measurement with I-123, and the SUV (standard uptake value) in the Tumor Glucose Metabolism Study with F-18-fluorodeoxyglucose. In all measurements of absolute function, there has to be an unbroken series of quantitative links from the counts in the ROI in the image back to the amount of administered activity in units of millicuries. In addition, when function is quantified in absolute terms, photon attenuation must be corrected for.

Chapter 10, Other Quantitative Techniques, discusses three nuclear medicine studies with quantitative measurements that do not fit in the preceding chapters. These are the Cystogram – Direct Study with Tc-99m-DTPA, which includes the measurement of post-void residual bladder volume; the Cisternogram with In-111-DTPA, which may include quantification of cerebrospinal fluid leaks into the nasal cavity; and the GLOFIL® Study with I-125-iothalamate that measures renal clearance with blood samples rather than images. In addition, the Body Surface Area Normalization assessment algorithm, which is a general method to determine whether an equation that measures a biologic function needs to be normalized for

body surface area (BSA), is discussed [4]. (The GLOFIL® Study, a non-imaging study, is not widely performed and is not in the Nuclear Medicine Procedure Manual but is included in this book because it fits well in Chap. 10.)

These chapters in Part II, Mathematics of the Biodistribution of Radiopharmaceuticals, cover all of the mathematics that relates to extracting functional measurements from and applying quantitative concepts to nuclear medicine images. In turn, these mathematical methods will be integrated with the physiology and molecular biology that determine the biodistribution of radiopharmaceuticals in Part III, Quantitative Evaluation in Nuclear Medicine Studies.

References

1. Compartmental systems. In: Goris ML, editor. Nuclear medicine application and their mathematical basis. New Jersey: World Scientific; 2011. p. 197–228.
2. Pharmacokinetics and modeling. In: Vallabhajosula S, editor. Molecular imaging: radiopharmaceuticals for PET and SPECT. Berlin: Springer; 2009. p. 205–14.
3. Radiopharmacokinetics. In: Theobald T, editor. Sampson's textbook of radiopharmacy. London: Pharmaceutical Press; 2011. p. 219–49.
4. Klingensmith WC. Tc-99m-MAG3 camera based measurement of renal clearance: should the result be normalized for body surface area? J Nucl Med Technol. 2013;41:279–82.

Evaluation of Clearance

4

Introduction

All nuclear medicine procedures are fundamentally dependent on the optimal biodistribution of the radiopharmaceutical in question either for obtaining physiologic or metabolic information from images in diagnostic studies or for delivering a maximally tolerated therapeutic dose of radiation to tumor in therapeutic procedures. In turn, in most procedures the biodistribution is primarily dependent on clearance of the radiopharmaceutical from the blood into organs, tissues, or lesions.

The Nuclear Medicine Procedure Manual lists 49 diagnostic studies in the 2012–2014 edition [1]. Thirty-nine of them are included in this book (see Appendix A). Of those 39 studies, 27 involve clearance of the radiopharmaceutical from blood into organs, tissues, or lesions. In all of these studies, images are included that are timed to optimally depict the results of clearance (twenty-six of the 27 studies involve direct injection of the radiopharmaceutical into the blood, and one, the Thyroid Imaging and Uptake Study, involves administration of the I-123 orally followed by absorption into the blood). These 27 studies are listed alphabetically in Table 4.1 within the organ systems plus infection and tumor.

Seven of the 27 studies are entitled perfusion studies but in fact measure clearance (Table 4.2). In these seven studies, the clearance of the radiopharmaceuticals usually parallels blood flow and perfusion, but not always. The graph in Fig. 4.1 shows the correlation between coronary blood flow and the amount of uptake (clearance) of the various radiopharmaceuticals used in myocardial perfusion studies [2]. None of the radiopharmaceuticals that are used to measure myocardial perfusion or blood flow show a one to one correspondence to coronary blood flow.

In five of the 27 nuclear medicine studies that show clearance following an intravenous injection, there is routine imaging of one or more physiologic parameters in addition to clearance such as blood flow, parenchymal transit, and excretion (Table 4.3).

W.C. Klingensmith III, *The Mathematics and Biology of the Biodistribution of Radiopharmaceuticals-A Clinical Perspective*,
DOI 10.1007/978-3-319-26704-3_4

Table 4.1 Nuclear medicine studies in which the radiopharmaceutical is cleared from the blood

Procedure	Radiopharmaceutical	Cleared by	Other parameters imaged
Cardiovascular system			
Myocardial Perfusion Study	N-13-ammonia	Myocardium	No
Myocardial Perfusion Study	Rb-82 as rubidium chloride	Myocardium	No
Myocardial Perfusion Study	Tc-99m-sestamibi	Myocardium	No
Myocardial Perfusion and Viability Study	Tl-201-thallous chloride	Myocardium	Yes
Myocardial Viability Study	F-18-fluorodeoxyglucose	Myocardium	No
Central nervous system			
Brain Glucose Metabolism Study	F-18-fluorodeoxyglucose	Brain	No
Brain Perfusion Study	Tc-99m-HMPAO	Brain	No
Striatal Dopamine Transporter Study	I-123-ioflupane [DaTscan]	Striatum	No
Endocrine system			
Neuroectodermal Imaging	I-123-MIBG	Neuroectoderm	No
Parathyroid Study	I-123 & Tc-99m-sestamibi	Thyroid and thyroid + adenoma	No
Thyroid Imaging and Uptake Study	I-123	Thyroid	No
Thyroid Metastases Study	I-123/I-131	Thyroid tissue	No
Gastrointestinal system			
Hepatic Artery Perfusion Study	Tc-99m-MAA	Liver	No
Hepatobiliary Study	Tc-99m-trimethylbromo-IDA	Liver	Yes
Liver-Spleen Study	Tc-99m-sulfur colloid	Liver and spleen	No
Meckel's Diverticulum Study	Tc-99m-pertechnetate	Gastric mucosa	No
Genitourinary system			
Renal Glomerular Filtration Study	Tc-99m-DTPA	Kidneys	Yes
Renal Tubular Function Study	Tc-99m-DMSA	Kidneys	No
Renal Tubular Excretion Study	Tc-99m-MAG3	Kidneys	Yes

(continued)

Table 4.1 (continued)

Procedure	Radiopharmaceutical	Cleared by	Other parameters imaged
Infection imaging			
White Blood Cell Activation Study	F-18-fluorodeoxyglucose	Activated WBCs	No
White Blood Cell Migration Study	In-111-white blood cells	WBC localization	No
Pulmonary system			
Lung Perfusion Study	Tc-99m-MAA	Capillary beds	No
Skeletal system			
Bone Mineral Study	F-18 sodium fluoride	Bone mineral hydroxyapatite	No
Bone mineral Study	Tc-MDP/HMDP	Bone mineral	Yes
Tumor imaging			
B-Cell Lymphoma Imaging Study	In-111-ibritumomab tiuxetan	CD 20	No
Neuroendocrine Tumor Study	In-111-pentetreotide	Somatostatin receptors	No
Tumor Glucose Metabolism Study	F-18-fluorodeoxyglucose	Glucose receptors	No

Table 4.2 Nuclear medicine studies that use clearance as a proxy for blood flow

Study	Radiopharmaceutical	Structure
Myocardial Perfusion Study	N-13-ammonia	Myocardium
Myocardial Perfusion Study	Rb-82 as rubidium chloride	Myocardium
Myocardial Perfusion Study	Tc-99m-sestamibi	Myocardium
Myocardial Perfusion Study	Tl-201 as thallous chloride	Myocardium
Brain Perfusion Study	Tc-99m-HMPAO	Brain
Hepatic Artery Perfusion Study	Tc-99m-MAA	Liver
Lung Perfusion Study	Tc-99m-MAA	Lung

These studies are labeled perfusion studies, but the radiopharmaceuticals localize by clearance

There are three additional nuclear medicine studies in which the radiopharmaceutical is introduced by a route other than intravenous injection, but clearance is the primary parameter of interest (Table 4.4). In the Lymphoscintigraphy Study, filtered Tc-99m-sulfur colloid is injected into the interstitial space and is carried with the flow of lymph to the sentinel node(s) where it is cleared by phagocytosis into sinusoidal macrophages. In the Lung Aerosol Ventilation Study and the Lung Ventilation Study, Tc-99m-DTPA aerosol and Xe-133 gas, respectively, are inhaled

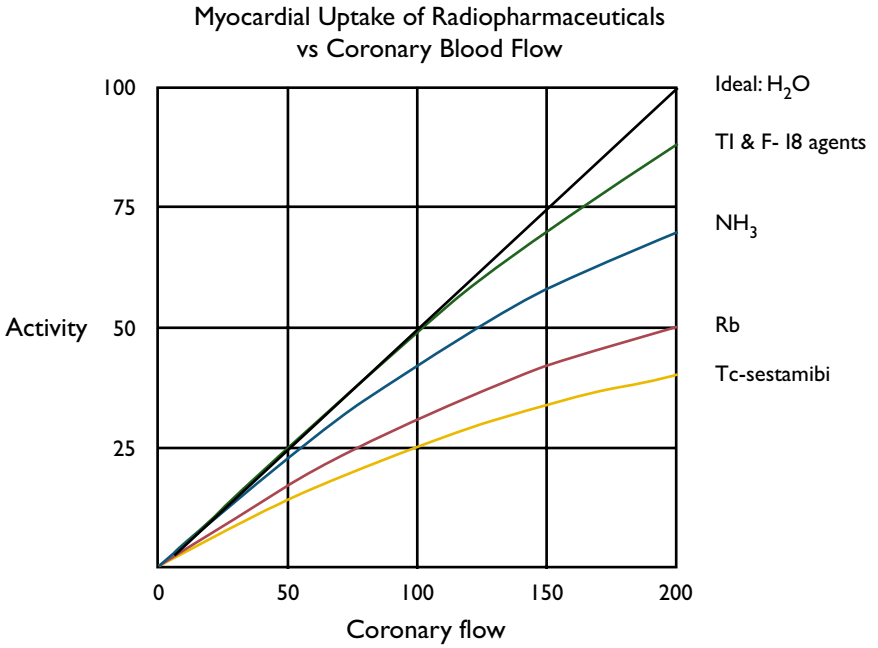

Fig. 4.1 Myocardial uptake (clearance) of radiopharmaceuticals. Clearance of radiopharmaceuticals is often used as a proxy for perfusion, or blood flow, but the correlation between clearance and blood flow is often not one to one [2]

Table 4.3 Nuclear medicine studies with parameters in addition to clearance

Study	Radiopharmaceutical	Structure	Other parameters
Myocardial Perfusion and Viability Study	Tl-201 chloride	Myocardium	Viability
Hepatobiliary Study	Tc-99m-trimethylbromo-IDA	Hepatobiliary tract	Parenchymal transit and excretion
Renal Glomerular Filtration Study	Tc-99m-DTPA	Renal tubules	Blood flow, parenchymal transit, and excretion
Renal Tubular Secretion Study	Tc-99m-MAG3	Renal tubules	Blood flow, parenchymal transit, and excretion
Bone Mineral Study (Three Phase)	Tc-99m-MDP	Bone mineral	Blood flow and extracellular space

and flow through the bronchial tree by the process of ventilation. The Tc-99m-DTPA aerosol is cleared by adherence to mucous in the terminal bronchi and the Xe-133 gas is cleared by confinement in the alveoli.

Table 4.4 Nuclear medicine studies in which the radiopharmaceutical is cleared, but not from blood

Procedure	Radiopharmaceutical	Route of administration
Cardiovascular system		
Lymphoscintigraphy	Filtered Tc-99m-sulfur colloid	Intradermal
Pulmonary system		
Lung Aerosol Ventilation Study	Tc-DTPA aerosol	Inhalation
Lung Ventilation Study	Xe-133 gas	Inhalation

Table 4.5 Nuclear medicine studies with intravenous injection of the radiopharmaceutical, but without clearance from the blood

Procedure	Radiopharmaceutical	Image other parameters
Cardiovascular system		
Cardiac Gated Blood Pool Study	Tc-99m-red blood cells	Yes
Central nervous system		
Brain Death Study	Tc-99m-DTPA	Yes
Gastrointestinal system		
Gastrointestinal Bleeding Study	Tc-99m-red blood cells	Optional
Hemangioma Study	Tc-99m-red blood cells	Yes

There are four other nuclear medicine studies that involve an intravenous injection of the radiopharmaceutical, but there is no clearance of the radiopharmaceutical from the blood in the organ of interest (Table 4.5). The radiopharmaceutical in three of the four studies is Tc-99m-RBCs. The images in these studies depict blood flow and blood volume, but not clearance. The radiopharmaceutical in the fourth study, Tc-99m-DTPA, is cleared in the kidneys by glomerular filtration but not in the brain, the organ that is imaged.

Compartmental Analysis for Describing the Biodistribution of Radiopharmaceuticals

In the research setting, the biodistribution of radiopharmaceuticals as a function of time, including clearance, is sometimes evaluated mathematically with compartmental analysis [3–7]. However, compartmental analysis requires creation of a relatively accurate model of the system (or systems) under study, designation of rate constants to describe the movement of the radiopharmaceutical between compartments (often bidirectional), measurement of an input function (ideally arterial), measurement of the amount of radiopharmaceutical in tissues as a function of time, and employment of calculus for obtaining the solution in terms of rate constants. Unfortunately, in the clinical setting, the model(s) under study is often unknown and the input data is not available. For these and other practical reasons, compartmental analysis is not applicable in the clinical setting.

A Clearance Equation for Evaluating the Biodistribution of Radiopharmaceuticals

In general, nuclear medicine images are interpreted visually based on image patterns. However, there is an underlying biologic process involving several factors or parameters that determines the initial clearance and biodistribution of the radiopharmaceutical. Here we will construct an equation in physiologic terms that can be used conceptually, without quantitation, to assist in image evaluation, particularly in images without a readily recognizable pattern.

The degree to which an intravenously injected radiopharmaceutical is cleared from blood by a specific organ, tissue, or lesion depends on four factors, which multiplied together determine the amount of radiopharmaceutical that localizes in tissue at a given time after injection [8]. First, there must be a factor accounting for delivery of the radiopharmaceutical from the injection site to the clearance site by blood flow on a per gram basis, F (mL/min-g).

Second, there must be a factor that accounts for the clearance or movement of the radiopharmaceutical from blood into tissue. This factor is the extraction efficiency, EE (no units), of the cells or tissue for the radiopharmaceutical in question. The extraction efficiency will be determined primarily by the extraction mechanism. The extraction mechanism depends on more than the physical and chemical properties of the radiopharmaceutical itself, but also on how the radiopharmaceutical interacts with the components of blood, e.g., whether it binds to protein. The renal imaging radiopharmaceutical Tc-99m-MAG3 is a small molecule that would be easily filtered through the renal glomerulus, but most of it is protein bound so that it is cleared mainly by tubular secretion instead [9].

In addition, the term clearance as applied to radiopharmaceutical clearance must be defined more broadly than the removal of a radiopharmaceutical from blood and the vascular space. In order to encompass all mechanisms of clearance, clearance needs to be defined as clearance from "flowing blood." For example, Tc-99m-macroaggregated albumin is cleared by embolization into arterioles; this process results in the removal of the radiopharmaceutical from flowing blood, but not from the vascular space.

Furthermore, because there are situations in which the radiopharmaceutical may move back out of cells and into the vascular space, extraction efficiency should be thought of as net extraction efficiency. Experience suggests that in most cases disease affects the clearance of radiopharmaceutical into tissue in rough proportion to any effect on the movement from tissue back into blood so that the net change in localization of tracer in tissue will approximately parallel change in severity of disease.

Third, a factor is needed to account for competing substances if the extraction mechanism can be saturated. Any atoms, molecules, or substances that compete for extraction with the radiopharmaceutical are accounted for by including a ratio of the normal concentration or pool of such atoms, molecules, or substances,

P_{Nl} (mole/mL), divided by the actual concentration of such atoms, molecules, or substances, P_{Act} (mole/mL). The units cancel.

The second and third factors multiplied together define the overall extraction efficiency, but it is useful to keep them separate because the effect of competing substances can be evaluated separately from extraction efficiency, which increases the specificity of diagnosis.

The first three factors multiplied together equal the clearance rate for the substance being traced in terms of mL/min per gram of tissue, but they do not determine the amount of radiopharmaceutical that will localize in tissue by a given time after injection.

So, a fourth factor is needed to account for the concentration of the radiopharmaceutical in blood, C (μCi/mL), as a function of time from the time of injection, 0 (min), until the time of the end of acquisition of the clearance or localization image, T (min), $\int_0^T C(t)\,dt\,(\mu\text{Ci-min/mL})$.

These four factors multiplied together give a final equation for clearance of a radiopharmaceutical by an extraction mechanism over a specified amount of time that can or cannot be saturated in terms of radioactivity per gram of tissue, A (μCi/g),

$$A(\mu\text{Ci/g}) = F(\text{mL/min-g}) \times \text{EE} \times P_{Nl}/P_{Act} \times \int_0^T C(t)\,dt\,(\mu\text{Ci-min/mL}) \tag{4.1}$$

Table 4.6 provides some additional analysis of Eq. 4.1 in terms of the biologic meaning of the individual factors and various subsets of factors.

If the extraction mechanism for a radiopharmaceutical is non-saturable, then the extraction efficiency will not be affected by the presence of competing atoms, molecules, or substances and the factor P_{Nl}/P_{Act} can be excluded. Equation 4.1 simplifies to,

$$A(\mu\text{Ci/g}) = F(\text{mL/min-g}) \times \text{EE} \times \int_0^T C(t)\,dt\,(\mu\text{Ci-min/mL}) \tag{4.2}$$

In addition, Eq. 4.1 can be used in ratio form to evaluate the relative clearance or localization in two different sites in one image or in a set of images,

$$\frac{A(\mu\text{Ci/g})}{A(\mu\text{Ci/g})} = \frac{F(\text{mL/min-g}) \times \text{EE} \times P_{Nl}/P_{Act} \times \int_0^T C(t)\,dt\,(\mu\text{Ci-min/mL})}{F(\text{mL/min-g}) \times \text{EE} \times P_{Nl}/P_{Act} \times \int_0^T C(t)\,dt\,(\mu\text{Ci-min/mL})} \tag{4.3}$$

Since the ratio of the normal and actual pools of atoms, molecules, or substances that behave the same relative to the extraction mechanism, P_{Nl}/P_{Act}, and the ratio of

Table 4.6 Analysis of clearance equation

Factors	Mathematical equivalent	Biologic description
$F\ (\mathrm{mL/min\text{-}g}) \times \mathrm{EE} \times P_{\mathrm{Nl}}/P_{\mathrm{Act}} \times \int_0^T C(t)\,\mathrm{d}t\ (\mu\mathrm{Ci-min/mL})$	A (μCi/g)	Radiopharmaceutical cleared per gram of tissue through time "T"
F (mL/min-gm)	Same	Blood flow per gram of tissue
EE	Same	Extraction efficiency for substance being traced
$P_{\mathrm{Nl}}/P_{\mathrm{Act}}$	Same	Normal concentration of traced substance/actual concentration of traced substance
$\int_0^T C(t)\ \mathrm{d}t\ (\mu\mathrm{Ci\text{-}min/mL})$	Same	Concentration of radiopharmaceutical per mL of blood integrated from time of injection to end of image acquisition, T
EE * $P_{\mathrm{Nl}}/P_{\mathrm{Act}}$	Same	Overall extraction efficiency
F (mL/min-g) * EE * $P_{\mathrm{Nl}}/P_{\mathrm{Act}}$	Cl (mL/min-g)	Clearance rate per gram of tissue
$F\ (\mathrm{mL/min\text{-}g}) \times \int_0^T C(t)\,\mathrm{d}t\ (\mu\mathrm{Ci\text{-}min/mL})$	A_{A} (μCi/g)	Radiopharmaceutical available to be cleared per gram of tissue, A_{A}, through time "T"

the concentration of radiopharmaceutical in the blood, $\int_0^T C(t)\,\mathrm{d}t\ (\mu\mathrm{Ci\text{-}min/mL})$, are almost always the same at a given time in any two sites within one study, they will cancel giving,

$$\frac{A\ (\mu\mathrm{Ci/gm})}{A\ (\mu\mathrm{Ci/gm})} = \frac{F\ (\mathrm{mL/min\text{-}gm}) \times \mathrm{EE}}{F\ (\mathrm{mL/min\text{-}gm}) \times \mathrm{EE}} \tag{4.4}$$

Thus, in most cases the relative biodistribution of the radiopharmaceutical, saturable or non-saturable, following initial clearance will depend on only two factors or parameters, blood flow and net extraction efficiency.

The diagnostic procedures listed in the Nuclear Medicine Procedure Manual [1] were used to construct tables of studies according to whether clearance of the radiopharmaceutical requires all four factors, Eq. 4.1, or just three factors, Eq. 4.2. In creating the tables, studies in which the radiopharmaceutical is not cleared from blood, e.g., Lymphoscintigraphy with filtered Tc-99m-sulfur colloid, Gastric Emptying Study with Tc-99m-sulfur colloid-labeled instant oatmeal, and Lung Aerosol Ventilation Study with Tc-99m-DTPA aerosol, or are injected intravenously but are not extracted or cleared, e.g., Cardiac Gated Blood Pool Study with Tc-99m-RBCs and Gastrointestinal Bleeding Study with Tc-99m-RBCs, were not considered.

Table 4.7 Nuclear medicine studies that require the full clearance equation (the extraction mechanism is saturable)

Myocardial Viability Study (F-18-fluorodeoxyglucose)	Thyroid Metastases Imaging Study (I-123 as sodium iodide, I-131 as sodium iodide)
Brain Glucose Metabolism Study (F-18-fluorodeoxyglucose)	Thyroid Uptake Measurement (I-123 as sodium iodide)
Striatal Dopamine Transporter Study (I-123-ioflupane [DatScan])	Hepatobiliary Imaging Study (Tc-99m-trimethylbromo-IDA)
Neuroectodermal Imaging Study (I-123-MIBG)	Tumor Glucose Metabolism Study (F-18-fluorodeoxyglucose)
Thyroid Imaging Study (I-123 as sodium iodide)	

The tables of examples of studies that fall into various clearance categories must be viewed as tentative because the extraction mechanism and the factors that affect the extraction mechanism are not fully understood for many radiopharmaceuticals.

Table 4.7 lists nuclear medicine studies in which the radiopharmaceutical is thought to clear by an extraction mechanism that is saturable. This phenomenon is well recognized for radioiodide radiopharmaceuticals, e.g., I-123 and I-131. The most common competing atom or molecule is nonradioactive iodide from recently administered intravenous CT contrast material. The effect of an increased blood glucose concentration on the extraction efficiency of F-18-fluorodeoxyglucose (FDG) is probably more complicated [10]. Change in the blood glucose concentration may affect the expression of glucose receptors, which would affect the extraction efficiency. Tc-99m-trimethylbromo-IDA binds to the same hepatocyte receptor that extracts bilirubin so elevated blood levels of bilirubin will compete with Tc-99m-trimethylbromo-IDA and decrease its extraction efficiency [11].

Table 4.8 lists nuclear medicine studies in which the radiopharmaceutical is thought to clear by an extraction mechanism that is non-saturable under most circumstances. Examples include radiopharmaceuticals that do not bind to a receptor and whose extraction depend on mechanical mechanisms such as the extraction of Tc-99m-macroaggregated albumin by embolization into arterioles (normally an extraction efficiency of 100 %) and the extraction of Tc-99m-DTPA in the kidneys by glomerular filtration (normally an extraction efficiency of 20 %). The technetium-99m bone mineral radiopharmaceuticals also do not bind to a receptor, but are chemisorbed onto hydroxyapatite with little evidence that the extraction efficiency is easily affected by most other atoms, molecules, or substances [12]. The extraction mechanism for Tc-99m-MAG3 can be saturated under experimental conditions, but it is uncertain whether this happens clinically [9].

Table 4.9 lists the four factors that make up the clearance equation across the top and three parameters related to those four factors in the first column. The idea is to explore the role that each of the four factors plays in determining the initial biodistribution or localization of an intravenously injected radiopharmaceutical. The first parameter, "approximate range encountered clinically," estimates the range of the values that may be encountered clinically relative to normal, N, for each of the four

Table 4.8 Nuclear medicine studies that require only the simplified clearance equation (the extraction mechanism is non-saturable)

Myocardial Perfusion Study (N-13-ammonia)	Renal Glomerular Filtration Study (Tc-99m-DTPA)
Myocardial Perfusion Study (Rb-82 as sodium chloride)	Renal Tubular Excretion Study (Tc-99m-MAG3)
Myocardial Perfusion Study (Tc-99m-sestamibi)	White Blood Cell Activation Study (F-18-fluorodeoxyglucose)
Myocardial Perfusion & Viability Study (Tl-201 as thallous chloride)	White Blood Cell Migration Study (In-111-WBCs, Tc-99m-WBCs)
Brain Perfusion Study (Tc-99m-HMPAO, Tc-99m-ECD)	Lung Perfusion Study (Tc-99m-macroaggregated albumin)
Parathyroid Imaging Study (Tc-99m-sestamibi)	Bone Mineral Study (F-18 as sodium fluoride)
Hepatic Artery Perfusion Study (Tc-99m-macroaggregated albumin)	Bone Mineral Study (Tc-99m-methylene diphosphonate)
Liver-Spleen Study (Tc-99m-sulfur colloid)	

Table 4.9 Conditions that affect the four clearance factors

Parameter	F	EE	P_{NI}/P_{Act}	$\int_0^T C(t)\,dt$
Approximate range encountered clinically	0 to >10 N	0–10 N	~0 to 1.3 N	N to >10 N
Example of a condition at lower end of range	Necrosis, distal to arterial occlusion	FDG: Down regulation of GLUTs from hyperglycemia	l-123: Recent CT contrast material	–
Example of a condition at upper end of range	Arteriovenous malformation (AVM)	FDG: Upgrade regulation of GLUTs in high-grade tumor	l-123: Low-iodine diet	Embolus from injection site

N Normal value, *F* Flow (mL/min-g), *EE* extraction efficiency, P_{NI}/P_{Act} pool (normal)/pool (actual), $\int_0^T C(t)\,dt$ integral of concentration of radiopharmaceutical in the blood from time of injection until the end of the time of image acquisition (μCi-min/mL)

factors. The second and third parameters "Example of a condition at lower end of range" and "Example of a condition at upper end of range" give examples of conditions that may result in changes toward the lower and upper ends of the ranges listed in the first row for each factor. Notice that the clinical range for blood flow, F, ranges from zero in the case of an arterial occlusion to greater than 10 times normal with an arteriovenous malformation. The estimated range for extraction efficiency, EE, is similar. The competing substance correction ratio, P_{NI}/P_{Act}, again ranges as low as zero but does not extend much above normal. In general, it is difficult to

markedly reduce the level of a normally circulating molecule or substance, P_{Act}. Finally, the amount of radiopharmaceutical per milliliter that is available for clearance, $\int_0^T C(t)\,dt$, is usually unaffected by pathologic conditions, but a thrombus that forms at the injection site, is impregnated with concentrated radiopharmaceutical, and then embolizes to the lungs will result in a focus of intense increased activity in the lung. The cause is that the flowing blood that contained the embolus has a much higher concentration of activity than other blood.

Equivalence of the Traditional Physiologic Clearance Equation and the Nuclear Medicine Clearance Equation (as Presented in This Chapter)

The traditional non-nuclear medicine clearance equation specifies the physiologic capacity of an organ to clear a substance from the blood. We will use the creatinine clearance equation as an example of a traditional clearance equation,

$$\mathrm{Cl}(\mathrm{mL/min}) = \frac{U(\mathrm{mg/min})}{P(\mathrm{mg/mL})} \tag{4.5}$$

Here "Cl" is clearance in traditional physiologic terms with units of mL/min, "U" is the amount of creatinine in a 24 h urine collection on a per minute basis with units of mg/min, and "P" is the plasma concentration of creatinine with units of mg/mL. The initial step of multiplying the concentration of creatinine in the 24 h urine collection times the urine volume has been omitted. Also, the factor that normalizes the result for body surface area has been left out for simplification. Notice that the traditional physiologic clearance equation determines a rate that describes the capacity of the kidneys to clear creatinine from the blood. The clearance rate, Cl, does not give any specific information about the plasma creatinine concentration or the amount of creatinine in the urine, only the ratio of the two.

In the nuclear medicine setting, the goal is to understand the factors that determine the biodistribution of the radiopharmaceutical, which is reflected in the images. We will start with the nuclear medicine equation for the amount of cleared substance as developed above (see Eq. 4.1).

Now we will show how the nuclear medicine clearance equation, initially expressed in terms of an amount rather than a rate, is equivalent to the traditional physiologic clearance equation. It will be assumed that the nuclear medicine study is the Renal Glomerular Filtration Study with Tc-99m-DTPA since Tc-99m-DTPA is primarily restricted to plasma and interacts with the kidney in a manner similar to creatinine.

It is useful to explain the reason why the two equations are equivalent in words and then, secondarily, in mathematical steps. The left-hand side of the nuclear medicine clearance equation is the amount of test substance that has been cleared from the blood in the allotted time, A (μCi/g), and is, therefore, equivalent to the amount of creatinine that is cleared by the kidney in 24 h, U (mg/min), in the traditional physiologic clearance equation. In addition, in the nuclear medicine clearance equation, the amount of tracer available for clearance is the integral of blood concentration of the tracer from the time of injection to the time of image acquisition, $\int_0^T C(t)\,\mathrm{d}t\,(\mu\mathrm{Ci\text{-}min/mL})$, and is, therefore, equivalent to "P (mg/mL)" in the traditional physiologic clearance equation. Then, if we divide both sides of the nuclear medicine clearance equation by "$\int_0^T C(t)\,\mathrm{d}t\,(\mu\mathrm{Ci\text{-}min/mL})$" and reverse the left- and right-hand sides of the equation, we get,

$$F\,(\mathrm{mL/min\text{-}g}) \times \mathrm{EE} \times P_{\mathrm{NI}}/P_{\mathrm{Act}} = \frac{A\,(\mu\mathrm{Ci/g})}{\int_0^T C(t)\,\mathrm{d}t\,(\mu\mathrm{Ci\text{-}min/mL})} \tag{4.6}$$

The factors "EE" and "$P_{\mathrm{NI}}/P_{\mathrm{Act}}$" together determine the full extraction efficiency. However, when the extraction mechanism cannot be saturated as is the case with glomerular filtration, the factor "$P_{\mathrm{NI}}/P_{\mathrm{Act}}$" can be deleted. In addition, initially the nuclear medicine clearance equation was expressed on a per gram basis and the creatinine clearance equation is implied to be on a per kidneys basis. The "per gram" in the nuclear medicine equation can be replaced by an understood "per kidney" to give,

$$F\,(\mathrm{mL/min}) \times \mathrm{EE} = \frac{A\,(\mu\mathrm{Ci})}{\int_0^T C(t)\,\mathrm{d}t\,(\mu\mathrm{Ci\text{-}min/mL})} \tag{4.7}$$

In the case of the creatinine clearance equation, it is assumed that the concentration of creatinine in plasma, and therefore blood, is constant so that the units can be expressed on a per minute basis rather than a 24 h basis. In addition, "EE" for Tc-99m-DTPA and glomerular filtration will be 20 %, which converts blood flow to the lesser amount of blood volume that would be completely cleared of test substance in the same time, i.e., the same value as "Cl (mL/min)" in the creatinine clearance equation. Thus, the traditional physiologic clearance equation and the nuclear medicine clearance equation are essentially equivalent.

The factor for normalizing the creatinine clearance equation for body surface area could have been carried along with no effect on the mathematical argument. Despite the mathematical equivalence between the creatinine clearance equation and the nuclear medicine clearance equation, there is a significant difference. The creatinine clearance equation is designed to be evaluated and to produce a numerical answer. But the nuclear medicine clearance equation discussed above is meant

to be used on a conceptual basis only and, in particular, to evaluate relative clearance or uptake in images.

However, there are two other nuclear medicine clearance equations for renal clearance with either Tc-99m-DTPA or Tc-99m-MAG3 that are clearance rates in absolute terms, i.e., the amount of cleared radiopharmaceutical is compared to the amount injected into the blood. These absolute nuclear medicine clearance equations yield a quantitative clearance result in terms of a rate of clearance, mL/min, and are discussed in Chap. 9, Quantitation of Function: Absolute Measurements.

Clinical Applications of the Nuclear Medicine Equation for Clearance

In this section we give examples of how Eqs. 4.1, 4.2, and 4.4 can be used to analyze clearance conceptually and in physiologic and molecular biologic terms. Table 4.10 lists a variety of conditions that affect one or more of the four factors that comprise the general clearance or uptake equation that in turn determines the initial biodistribution of an intravenously injected radiopharmaceutical, A (μCi/gm). The conditions are listed in column one, the radiopharmaceuticals in column two, and the various components of the clearance equation in the remaining columns.

In the first example, infection results in increased localization of F-18-fluorodeoxyglucose (FDG) from both increased blood flow and increased extraction efficiency by activated white blood cells [12] with no change in the competing substance pool or local blood concentration of the radiopharmaceutical. In the second example, a pulmonary anatomic arteriovenous malformation results in markedly decreased clearance of Tc-99m-macroaggregated albumin because, even though the

Table 4.10 Conditions and their effect on factors affecting radiopharmaceutical biodistribution

Condition	Radiopharmaceutical	A	F	EE	P_{NI}/P_{Act}	$\int_0^T C(t)\,dt$
Infection	F-18-FDG	↑↑	↑↑↑	↑↑	–	–
Lung AVM	Tc-99m-MAA	↓↓	↑↑	↓↓	–	–
Subacute viral thyroiditis	1-123, 1-131	↓	↑	↓↓	–	–
Graves disease	1-123	↑↑	↑	↑	–	–
Recent CT contrast	1-123, 1-131	↓↓	–	–	↓↓	–
Low iodine diet	1-131	↑	–	–	↑	–
Injection embolus	Tc-99m-MAA	↑↑	–	–	–	↑↑
Injection embolus	F-18-FDG	↑↑	–	–	–	↑↑
Tumor, diabetic, glucose ↑↑	F-18-FDG	↓↓	↑	↓↓	↓↓	–

A activity (μCi/g), F flow (mL/min-g), EE extraction efficiency, P_{NI}/P_{Act} pool (normal)/pool (actual), $\int_0^T C(t)\,dt$ integral of concentration of radiopharmaceutical in the blood from time of injection until the end of the time of image acquisition (μCi-min/mL)

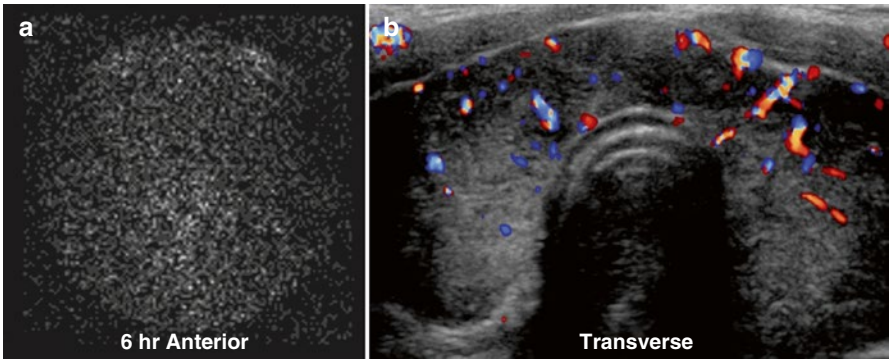

Fig. 4.2 Subacute viral thyroiditis. A 38-year-old female with symptoms of hyperthyroidism, depressed blood thyroid-stimulating hormone level, and a history of a recent pharyngitis. (**a**) Pinhole nuclear medicine image shows very little I-123 in the thyroid gland. The 6 h I-123 thyroid uptake value was markedly decreased at 2.1 % (normal range: 7–20 %). (**b**) Transverse ultrasound image of the neck shows a moderately enlarged thyroid gland with a nonhomogenous echo pattern and moderately increased blood flow by color Doppler

blood flow will be markedly increased, the extraction efficiency will be essentially zero and, thus, clearance will be essentially zero. Of interest, this example demonstrates that most nuclear medicine procedures that are labeled as depicting blood flow or perfusion actually reflect clearance.

In the third example, subacute viral thyroiditis results in significantly decreased uptake of I-123 despite an increase in blood flow because of a markedly decreased extraction efficiency secondary to depressed blood levels of thyroid-stimulating hormone (Fig. 4.2).

In the fourth example, Graves disease results in increased uptake of I-123 in the thyroid from increased blood flow and extraction efficiency. In the fifth example, the recent intravenous administration of CT contrast causes a marked decrease in thyroid uptake of I-123 secondary to a marked increase in competing atoms, i.e., nonradioactive iodine. In the sixth example, a low-iodine diet causes a small increase in thyroid uptake of I-123 secondary to a small decrease in the nonradioactive iodine blood pool.

In the seventh and eighth examples, Tc-99m-macroaggregated albumin or FDG, respectively, adheres to a small thrombus at the injection site, which then embolizes to the lungs resulting in a focus of significantly increased radiopharmaceutical secondary to a significantly increased concentration of radiopharmaceutical in the blood containing the embolus that flowed to the particular area of lung in question (Fig. 4.3). Interestingly, in the case of FDG, the adherence of FDG to the thrombus changes the extraction mechanism from binding to glucose receptors on cell membranes to microembolization.

In the ninth example, a patient with lung cancer demonstrates widespread metastases in a baseline study (Fig. 4.4a). Post therapy the metastases appear to have resolved, but there is also no uptake in the brain (Fig. 4.4b). The patient was determined to have unrecognized diabetes with an elevated blood glucose level.

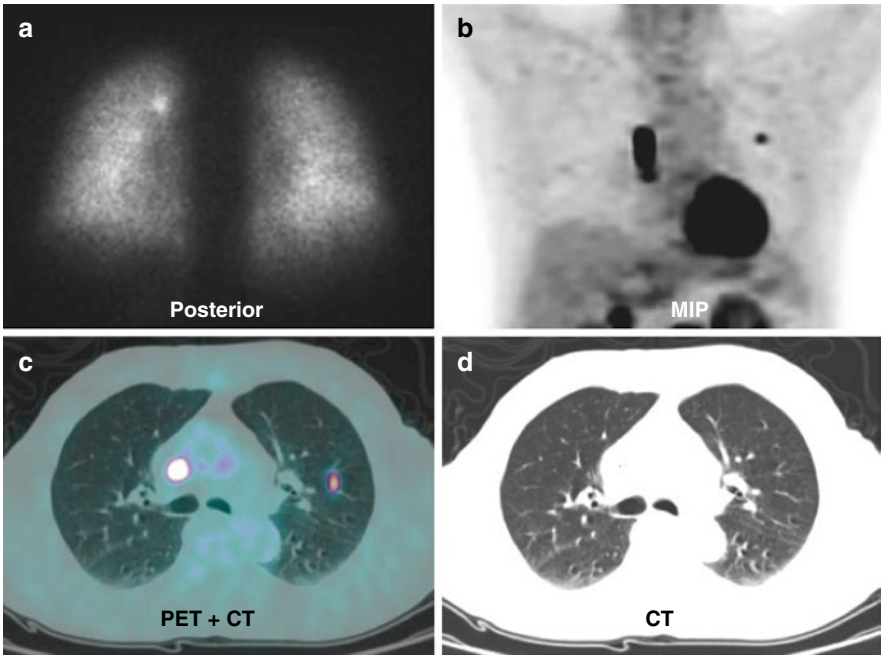

Fig. 4.3 Injection-related microembolus. (**a**) Posterior image from a Tc-99m-macroaggregated albumin lung perfusion study for possible pulmonary embolus shows a focus of increased activity in the medial superior left lung. This finding is most likely secondary to Tc-99m-macroaggregated albumin that adhered to a microthrombus that formed at the injection site and then embolized to the lung. (**b**–**d**) Maximum intensity projection (*MIP*) and tomographic images from a FDG PET-CT study show a focus of increased FDG in the left lung without a CT correlate. This finding is most likely secondary to FDG that adhered to a microthrombus that formed at the end of the superior vena caval catheter and then embolized to the lung

A few days later, after the hyperglycemia had been treated, a repeat study demonstrated progressive metastatic disease and normal brain uptake (Fig. 4.4c). The absent uptake in the first post-therapy study probably cannot be fully explained by the increased nonradioactive glucose pool and suggests a possible downregulation of cell membrane glucose receptors resulting in a decreased extraction efficiency [10].

Many other examples of common or unusual areas of increased or decreased localization or clearance of radiopharmaceutical could be analyzed in this same fashion. However, these nine examples illustrate how the clearance equation can be used conceptually to help clarify the pathophysiology, and in some cases the etiology, of image findings.

Again, the clearance equation is meant to be used conceptually, without quantitation, to assist in the evaluation of nuclear medicine images, particularly those that do not demonstrate a readily recognizable pattern. The equation is in physiologic terms and is designed to describe the initial clearance and biodistribution of an intravenously injected radiopharmaceutical from the blood into organs, tissues, and lesions. Because

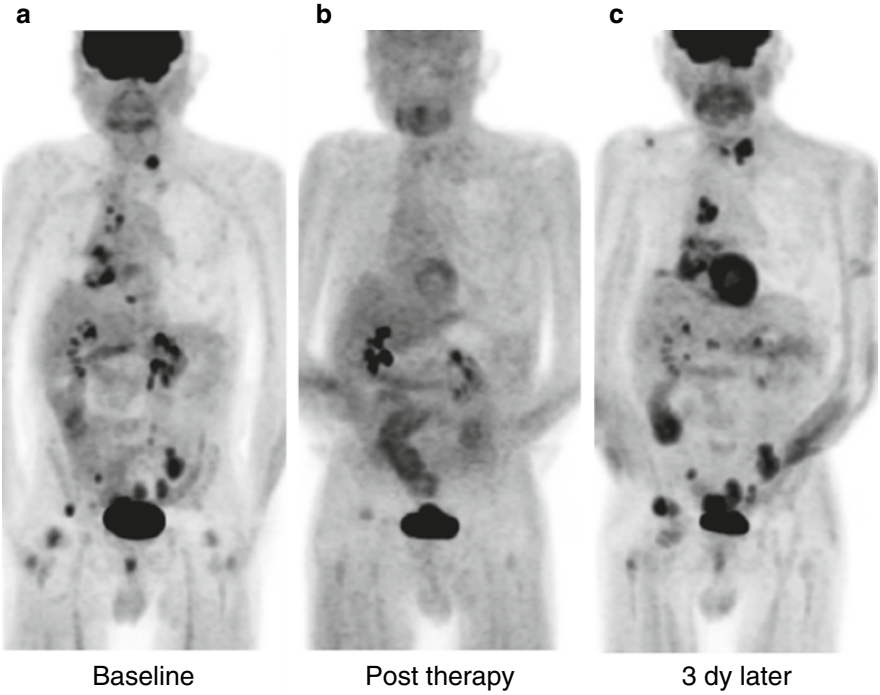

Fig. 4.4 A 76-year-old male with lung cancer. Anterior MIP (maximum intensity projection) images from sequential FDG PET-CT studies. (**a**) The baseline study shows widespread metastases. The blood glucose was 105 mg/dL. (**b**) Post therapy (11 weeks later), the metastases appear to have resolved. Of note, there is very little FDG uptake in the brain. The patient was not known to be a diabetic, but the blood glucose was 260 mg/dL. (**c**) The patient was sent to his physician for treatment of newly diagnosed diabetes. Three days later the blood glucose was 76 mg/dL and the study was repeated. The repeat study demonstrates progressive metastatic disease and normal brain uptake. The elevated blood glucose level at the time of the initial post-therapy study is probably insufficient to fully explain the essentially complete lack of uptake in the metastases and brain. It is postulated that, in addition to a possible competitive effect, the elevated glucose level caused a downregulation of the glucose receptors

of the wide applicability of this nuclear medicine clearance equation, it is a relatively fundamental equation from the point of view of the initial biodistribution of radiopharmaceuticals and image interpretation. In Part III, Quantitative Evaluation in Nuclear Medicine Studies, the use of the clearance equation will be evaluated more fully in all of the nuclear medicine studies in which it is applicable.

References

1. Klingensmith WC, Eshima D, Goddard J. Nuclear medicine procedure manual. 10th ed. Englewood: Wick Publishing; 2012.
2. Schelbert HR. PET: molecular imaging & its biological applications. New York: Springer; 2004. p. 403.

3. Vallabhajosula S. Pharmokinetics and modeling. In: Vallabhajosula S, editor. Molecular imaging. New York: Springer; 2009. p. 208–14.
4. Goris M. Compartmental systems. In: Goris M, editor. Nuclear medicine applications and their mathematical basis. Singapore: World Scientific; 2011. p. 197–205.
5. Koeppe RA. Data analysis and image processing. In: Wahl RL, editor. Principles and practice positron emission tomography. Philadelphia: Lippincott Williams & Wilkins; 2002. p. 65–99.
6. Wahl RL. Principles of cancer imaging with fluorodeoxyglucose. In: Wahkl RL, editor. Principles and practice positron emission tomography. Philadelphia: Lippincott Williams & Wilkins; 2002. p. 100–10.
7. Larsen NA, Perl W. Compartmental analysis. In: Larsen NA, Perl W, editors. Tracer kinetic methods in medical physiology. New York: Raven Press; 1979. p. 137–55.
8. Klingensmith WC. Tc-99m-MAG3 camera based measurement of renal clearance: should the result be normalized for body surface area? J Nucl Med Technol. 2013;41:279–82.
9. Fritzberg AR, Whitney WP, Kuni CC, Klingensmith WC. Biodistribution and renal excretion of Tc-99m-N, N′-bis-(mercaptoacetamido) ethylenediamine. Effect of renal tubular transport inhibitors. Int J Nucl Med Biol. 1982;9:79–82.
10. Alberts B, Johnson A, Lewis J, Raff M, Roberts K, Walter P. Intracellular vesicular traffic. In: Molecular biology of the cell. 5th ed. New York: Garland Science; 2008. p. 798.
11. Kamisako T, Kobayashi Y, Takeuchi K, et al. Recent advances in bilirubin metabolism research: the molecular mechanism of hepatocyte bilirubin transport and its clinical relevance. J Gastroenterol. 2000;35:659–64.
12. Czernin J, Satyamurthy N, Schiepers C. Molecular mechanisms of bone F-18-NaF deposition. J Nucl Med. 2010;51:1826–9.
13. Paik JY, Lee KH, Choe YS, et al. Augmented ^{18}F-FDG uptake in activated monocytes occurs during the priming process and involves tyrosine kinases and protein kinase C. J Nucl Med. 2004;45:124–8.

Mean Transit Time: The Central Volume Principle

5

Introduction

The so-called central volume principle can be understood by referring to the diagram in Fig. 5.1. The central volume principle describes the relationship among flow, F; volume, V; and mean transit time, $\bar{T}$, as a simple equation [1, 2],

$$F\left(\mathrm{mL}/\mathrm{s}\right)=\frac{V\left(\mathrm{mL}\right)}{\bar{T}\left(\mathrm{s}\right)} \tag{5.1}$$

Here volume is the volume of the single compartment; flow is the constant flow of fluid into, through, and out of the single compartment; and mean transit time is the average transit time of all subpathways through the volume weighted by the volume of each subpathway. The equation can be rearranged to define the mean transit time,

$$\bar{T}\left(s\right)=\frac{V\left(\mathrm{mL}\right)}{F\left(\mathrm{mL}/\mathrm{s}\right)} \tag{5.2}$$

It is obvious from Eqs. 5.1 to 5.2 that if we know any two of the three factors or parameters in the central volume principle equation, we can calculate the third parameter. The easiest parameter to measure in clinical images is volume, usually blood volume. Once a radiopharmaceutical that is essentially confined to the vascular space reaches equilibrium, its relative distribution will reflect blood volume. The hardest parameter to determine is flow, usually blood flow, and therefore, volume and mean transit time are usually determined first and flow is calculated or estimated secondarily.

In addition to playing an important role in a number of nuclear medicine studies as discussed below and in the clinical part of the book, Part III, Quantitative Evaluation in Nuclear Medicine Studies, the central volume principle plays a significant role in the derivation of the equation for evaluation of first circulation

W.C. Klingensmith III, *The Mathematics and Biology of the Biodistribution of Radiopharmaceuticals-A Clinical Perspective*,
DOI 10.1007/978-3-319-26704-3_5

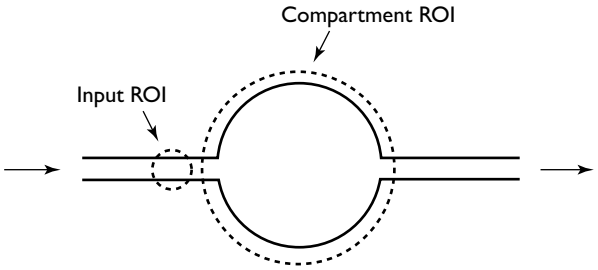

Fig. 5.1 Central volume principle. The drawing shows a simple single-compartment model. The *solid lines* depict a central compartment with a single input on the left and a single output on the right. The *broken circles* indicate regions of interest (*ROI*) for generating time-activity curves during the first pass of a bolus of activity through the model, i.e., no recirculation

time-activity curves, Chap. 6, Blood Flow: First Circulation Time-Activity Curves, and in the mathematical analysis of convolution and deconvolution, Chap. 7, Regional Transit Times: Convolution Analysis.

Conceptual Analysis of the Central Volume Principle

First, consider an instantaneous or impulse introduction of a bolus of radiopharmaceutical at the input to a compartment. Such an injection is sometimes referred to as a delta input or delta function and is depicted graphically in Fig. 5.2.

Now assume that there is plug flow through the compartment so that the transit times through all subpathways through the compartment are the same (Fig. 5.3a). There is no dispersion of the bolus as a function of time and distance traveled (times T, 2T, and 3T). However, in most flowing systems including biological systems, laminar flow predominates with the fastest flow in the center of the tube or vessel and the slowest flow at the margins. The cross-sectional velocity profile approximates a parabola and the bolus length elongates as a function of distance traveled (Fig. 5.3b).

Now consider the appearance of the time-activity curve from a ROI over a compartment generated from the passage of a plug bolus (Fig. 5.4). There appears to be one pathway with all of the activity entering the compartment at zero seconds and leaving it at 15 s. The mean or average transit time will be 15 s.

The mean or average transit time can be calculated by multiplying the amount of activity, 100 %, times the transit time of 15 s, and then dividing the result, 1,500 %-seconds, by the total amount of activity, 100 %, to give 15 s.

In Fig. 5.5 the amount of activity entering the compartment is unchanged and the activity again enters as an impulse bolus. However, now we have two pathways through the compartment. Each pathway contains one half of the total flow and, therefore, one half of the activity. In addition, the top pathway has one third less volume than before and, therefore, a shorter transit time by 5 s. Conversely, the bottom pathway has one third more volume and, therefore, a longer transit time by 5 s (Fig. 5.5). We can determine the mean transit time by calculating a weighted

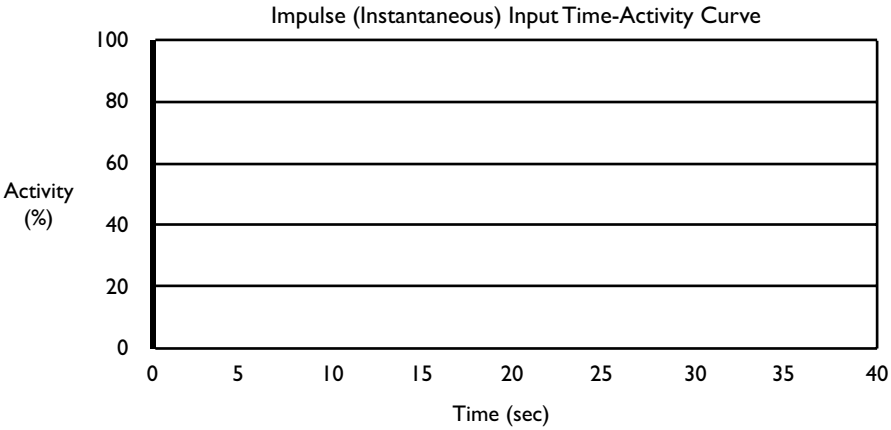

Fig. 5.2 Instantaneous or impulse injection. The curve is generated from the input ROI, not the compartment ROI (Fig. 5.1). The graph demonstrates an instantaneous or impulse input of activity into the compartment. This type of discrete input is also referred to as a delta function

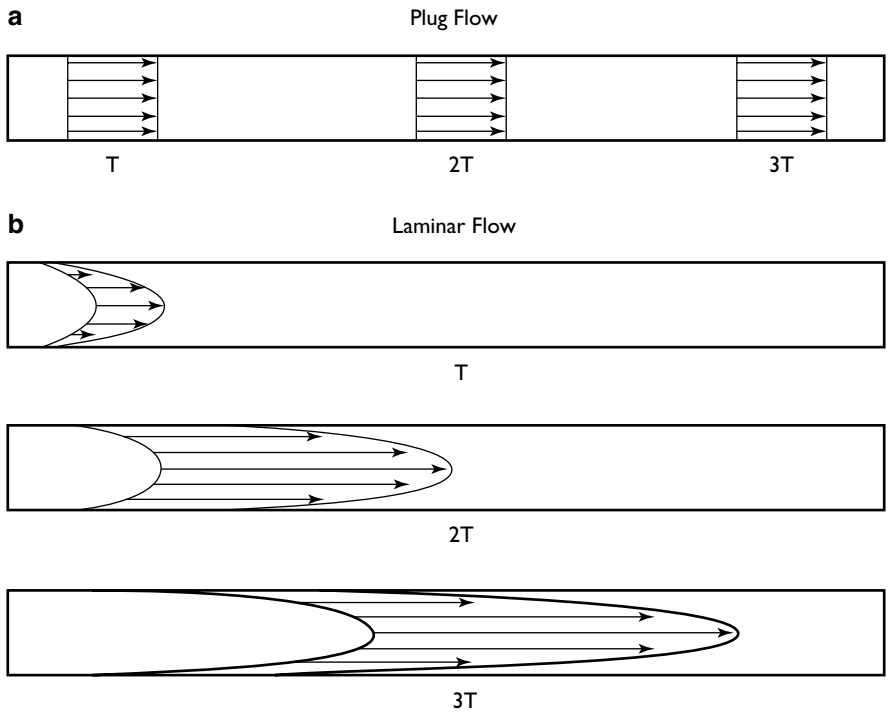

Fig. 5.3 Plug and laminar flow. Panel (**a**) demonstrates the behavior of plug flow at three sequential times (T, 2T, and 3T) after injection of tracer into a flowing system. The relatively discrete shape of the bolus of tracer does not change over time. Panel (**b**) demonstrates laminar flow, typical of biologic systems. Because flow is fastest in the center of a tubular system and falls to near zero at the margins, the bolus elongates as a function of distance traveled

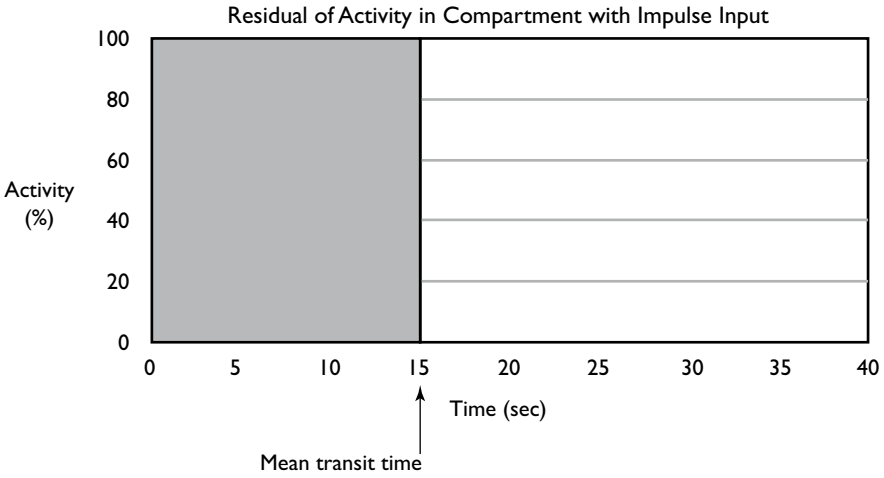

Fig. 5.4 Time-activity curve of plug flow through a compartment. The combination of an impulse introduction of tracer into a compartment and plug flow through the compartment results in a sudden onset of radioactivity in the time-activity curve at time zero, then constant activity, and finally a sudden drop in activity to zero at the time of the mean transit time, 15 s

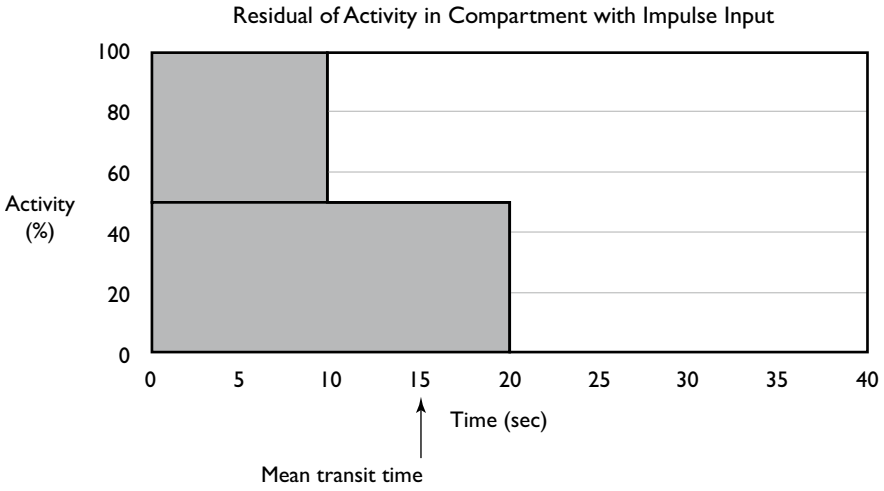

Fig. 5.5 Time-activity curve of plug flow through two pathways in a compartment. Each pathway contains one half of the total flow. The transit time in the *top* pathway is 5 s less than the mean transit time in Fig. 5.4 and the transit time in the *bottom* pathway is 5 s longer. Therefore, the average or mean transit time is unchanged at 15 s

average of the pathways through the compartment. In this case the calculation is 50 % times 10 s plus 50 % times 20 s divided by 100 % or again a mean transit time of 15 s. The overall mean transit time is unchanged as required by the fact that the total flow and volume are unchanged.

Mathematical Analysis of the Central Volume Principle

Now we will look at the general mathematical approach for calculating the mean transit time when there is an impulse input but no limit to the number of pathways, e.g., laminar flow (Fig. 5.6). The residual activity in the compartment is expressed as an equation in terms of activity as a function of time.

In general, in clinical studies, when a bolus of radiopharmaceutical enters and passes through a compartment, the time-activity curve from the compartment is the convolution of the shape of the input bolus and the fractional distribution of transit times through the compartment. However, in the special case when the entering bolus is an instantaneous impulse, the time-activity curve for the compartment will have the same shape as the frequency distribution of transit times (Figs. 5.6 and 5.7).

Then the mean transit time can be calculated by integrating the time-activity curve of the compartment, which has the same effect as weighting the prevalence of the different transit times, and dividing by the total activity, which is equivalent to the initial activity at time zero, A_0,

$$\bar{T}(\mathrm{s}) = \frac{\int_0^T A(t)\,\mathrm{d}t\,(\mu\mathrm{Ci\text{-}s})}{A_0\,(\mu\mathrm{Ci})} \tag{5.3}$$

or integrating the frequency distribution of transit times, which weights the prevalence or percentage of the different transit times, T_{Tran}, and dividing by the sum of the frequencies, or 100 % [1–4]. "T" is the end of the first circulation,

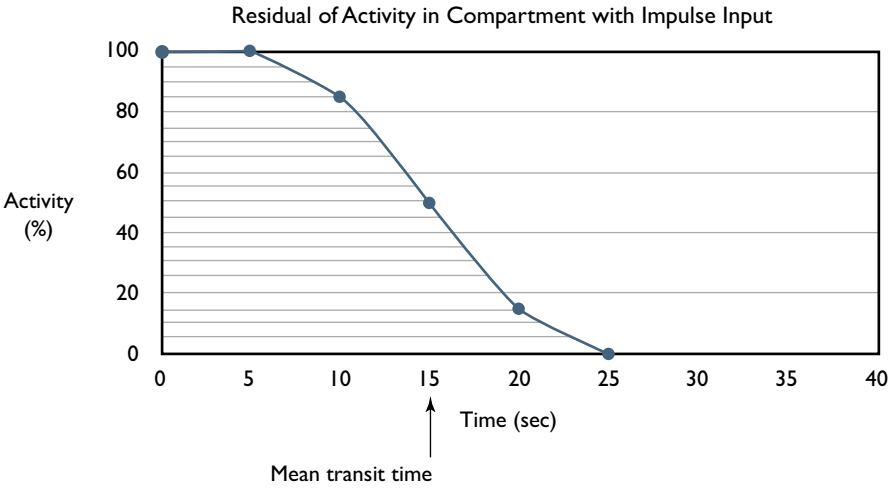

Fig. 5.6 Compartment time-activity curve with impulse input. Because the input is an impulse, all of the activity enters the compartment at zero time. At 5 s none of the activity has passed through the compartment, and at 10 s 20 % of the activity has passed through and out of the compartment. At 15 s an additional 40 % of activity has passed through the compartment and so forth

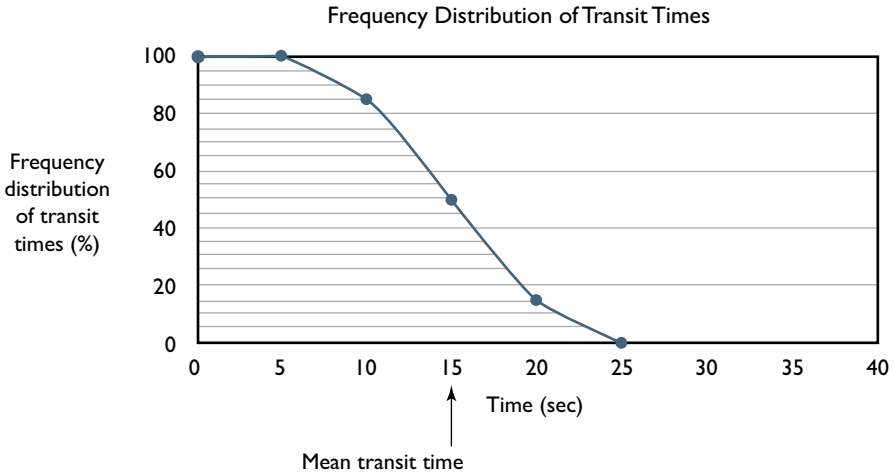

Fig. 5.7 Frequency distribution of transit times. This curve is identical to the one in Fig. 5.6 except for the units of the *Y*-axis. Here the units of the *Y*-axis is "frequency distribution of transit times" in percent rather than "activity" in μCi

$$\bar{T}(\mathrm{s}) = \frac{\int_0^T T_{\mathrm{Tran}}(t)\,\mathrm{d}t\,(\%\text{-}\mathrm{s})}{100(\%)} \tag{5.4}$$

Notice that the curves with units of either activity or percent of transit times effectively reflect the change in residual tracer within the compartment as a function time. Also, notice that the parameter and unit on the *Y*-axis, either percent or activity (μCi), appears in both the numerator and denominator and cancels.

Clinical Applications of the Central Volume Principle

A number of nuclear medicine studies involve the central volume principle, either in studies that are based on flowing fluid, such as blood or cerebrospinal fluid, or that are based on peristalsis (Tables 5.1 and 5.2). However, no nuclear medicine study utilizes the central volume principle in its pure form. The problem is that no nuclear medicine study has a simple compartment and an impulse injection at the entrance to the compartment. Table 5.3 lists the variants of the central volume principle that are found in nuclear medicine studies.

The Ventricular Shunt Study with Tc-99m-DTPA measures the washout half time of the shunt reservoir, which assumes that the tracer is uniformly distributed in the reservoir immediately following injection. The small volume of the reservoir and the turbulence caused by the injection make this assumption reasonable. Thus, the movement of the activity out of the compartment is a washout from the compartment and not a transit time through the compartment.

Table 5.1 Studies that involve the central volume principle, continuous flow, and measurement of a transit time

Study	Radiopharmaceutical	Transit time parameter	Upper limit of normal
Cisternography	In-111-DTPA	Subarachnoid space: lumbar to superior sagittal sinus	24 h
Ventricular Shunt Study	Tc-99m-DTPA	Shunt reservoir: half time of washout from reservoir	Varies with manufacturer
Cardiac Gated Blood Pool Study	Tc-99m-red blood cells	Pulmonary vascular space: right ventricle to left ventricle	6 s
Hepatobiliary Study	Tc-99m-trimethylbromo-IDA	Biliary tract: hepatocytes to extrahepatic bile ducts	10 min
Renal Glomerular Filtration Study	Tc-99m-DTPA	Tubular lumens: glomeruli to calyces	5 min
Renal Tubular Secretion Study	Tc-99m-MAG3	Tubular lumens: tubular cells to calyces	5 min

Table 5.2 Studies that involve the central volume principle and measurement of a transit time but with intermittent movement

Study	Radiopharmaceutical	Transit time parameter	Upper limit of normal
Esophageal Motility Study	Tc-99m-sulfur colloid in water	Esophagus: 90 % emptying	15 s
Gastric Emptying Study	Tc-99m-sulfur colloid labeled oatmeal	Gastric: half time of emptying	60 min

Table 5.3 Variants of the central volume principle in nuclear medicine studies

Form of central volume principle	Study example	Transit time parameter	Measurement compared to $\overline{T}$
Standard	None	Mean transit time	=
Compartment washout	Ventricular Shunt Study	Washout half time	1/2
Leading edge, impulse injection	Cisternography	Leading edge transit time	<
Leading edge, no impulse injection	Hepatobiliary Study	Leading edge transit time	<
Percent emptying, peristalsis	Gastric Emptying Study	Half time of emptying	< or >

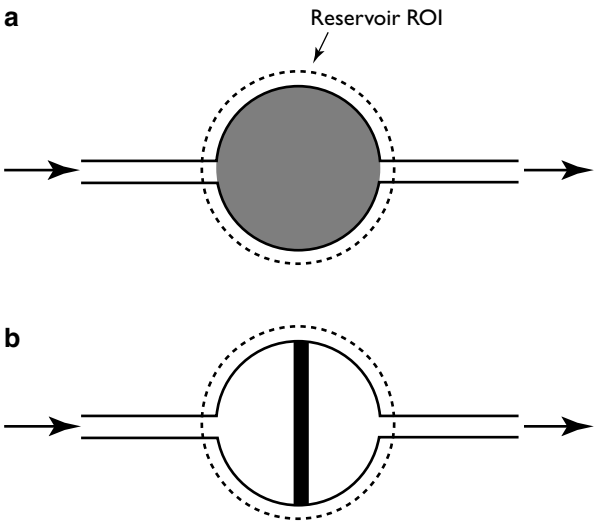

Fig. 5.8 Washout half time vs. mean transit time. In the case of the mean transit time through a compartment, the tracer is injected as an impulse at the input. In the case of the washout transit time, the tracer is initially evenly distributed throughout the compartment (**a**). If the tracer is conceptually concentrated in the mid plane of the compartment, the left to right average distribution is unchanged and it can be understood that the washout transit time will be half of the mean transit time (**b**)

Panel a of Fig. 5.8 shows the tracer (in gray) evenly distributed throughout the reservoir. Panel b shows the tracer after it has been conceptually moved in equal amounts from the left and right sides of the reservoir to the center plane. Thus, when the tracer is evenly distributed throughout the compartment initially, the effective volume that the tracer has to pass through is half the volume of the compartment. Since the washout half time equals one half of the mean transit time of the reservoir, the mean transit time could be easily calculated but rarely is because the adjustment can be made in the normal range.

Although the central volume principle requirement that the input to a compartment be instantaneous is rarely met, it is met in the Cisternography Study. Here the tracer, In-111-DTPA, is injected into the cerebrospinal fluid of the lumbar thecal sac. It then flows upward into the intracranial subarachnoid space and around the cerebral hemispheres and finally is absorbed by the arachnoid villa of the superior sagittal sinus. The problem with applying the standard central volume principle is that the cerebrospinal fluid compartment has a complicated shape and is never entirely within the field of view at a given time. Instead, the leading edge transit time is measured visually, no ROIs are used.

The evaluation of the leading edge transit time through the pulmonary vasculature in the Cardiac Gated Blood Pool Study with Tc-99m-RBCs is unique in that it is determined visually from the leading edge at the beginning and end of the compartment, i.e., from the leading edge appearance of the first circulation of tracer in

the right ventricle to the leading edge appearance of tracer in the left ventricle. The most common cause of an increased pulmonary leading edge transit time is left ventricular failure, which causes a decrease in cardiac output, i.e., flow, and pulmonary congestion, i.e., an increase in pulmonary vascular volume. Both changes cause an increase in the pulmonary vascular transit time.

In three studies, the Hepatobiliary Study, Renal Tubular Secretion Study, and Renal Glomerular Filtration Study, the leading edge transit time through parenchyma is measured visually (Table 5.1). In each study it is impractical to determine when the leading edge enters the parenchymal excretory pathway so the time of injection is used. This modification works because the transit time from site of injection to organ parenchyma is short, approximately 15 s, compared to the time it takes for the tracer to pass through the parenchyma and reach the proximal excretory collecting system of the respective organs, 10 min for the hepatobiliary system and 5 min for renal parenchyma. In the case of the two renal studies, the parenchymal transit time is also measured with ROIs and time-activity curves. The half time from the peak should occur by 10 min after the peak.

In the case of the Esophageal Transit Study and the Gastric Emptying Study, the initial input is relatively quick and at the proximal end of the compartment in question, similar to an impulse input. But the esophagus and stomach do not have fixed volumes and the movement is secondary to peristalsis, not constant flow. In addition, it is more convenient to measure a standardized normal percent of emptying at a standard time after tracer administration rather than to try to measure a mean transit time.

The central volume principle is at work to a varying degree in a number of other nuclear medicine studies, but in those studies evaluation of a transit time is not considered to be clinically useful.

The clinical uses of the central volume principle will be discussed in greater detail in Part III, Quantitative Evaluation in Nuclear Medicine Studies.

References

1. Goris M. Non-compartmental models. In: Goris M, editor. Nuclear medicine applications and their mathematical basis. Singapore: World Scientific; 2011. p. 233–4.
2. Lassen NA, Perl W. Volume/flow or mass/flux ratio (mean transit time): bolus injection. In: Lassen NA, Perl W, editors. Tracer kinetic methods in medical physiology. New York: Raven Press; 1979. p. 76–89.
3. Thomas GB, Finney RL. Moments and center of mass. In: Thomas GB, Finney RL, editors. Elements of calculus and analytic geometry. Reading: Addison-Wesley Publishing; 1989. p. 345.
4. Stewart J. Moments and centers of mass. In: Stewart J, editor. Calculus. 2nd ed. Pacific Grove: Brooks/Cole Publishing; 1991. p. 499.

Blood Flow: First Circulation Time-Activity Curves

6

Introduction

Theoretically, the best method for evaluating pure regional blood flow with a radiopharmaceutical is to use a radiopharmaceutical that is not cleared, e.g., Tc-99m-RBCs, inject it intravenously, and acquire rapid serial images of the radiopharmaceutical as it passes through the structure(s) of interest during the first circulation. For practical reasons, radiopharmaceuticals that are partially cleared during the first circulation are used in most cases. In addition, it is difficult to measure regional blood flow accurately in absolute terms so the measurement of regional blood flow is generally performed on paired organs so the measurement(s) can be made in relative terms. This approach usually provides a normal side for comparison as an added benefit.

Table 6.1 shows four nuclear medicine studies which routinely include imaging of paired structures during the first circulation. Tc-99m-DTPA in the Brain Death Study is not cleared from the vascular space of the brain as long as the blood-brain barrier is intact. The radiopharmaceuticals in other three studies are partially cleared during the first circulation, but the resulting images can still be evaluated for blood flow. In addition to visual evaluation of the images, regions of interest (ROIs) can be placed over the paired structures of interest to generate time-activity curves. Currently, this is performed only in the two renal studies. In this chapter, the information content of these paired time-activity curves and the mathematics for extracting this information are analyzed.

The mathematics that apply to the first circulation of a radiopharmaceutical also apply to the first circulation of other imaging indicators such as CT density contrast material and MR magnetic susceptibility material (Table 6.1) [1–6]. However, because of the higher spatial resolution of CT, a time-indicator curve from the input artery can also be generated, which in turn can be used to deconvolve the time-indicator curve of the ROI, calculate the mean transit time through the region of interest, and directly calculate the blood flow of the region of interest using the

W.C. Klingensmith III, *The Mathematics and Biology of the Biodistribution of Radiopharmaceuticals-A Clinical Perspective*,
DOI 10.1007/978-3-319-26704-3_6

Table 6.1 Radiologic studies that include imaging of paired structures during the first circulation

Procedure	Radiopharmaceutical/indicator	Extraction efficiency	Generate time-indicator curves
Renal Tubular Excretion Study	Tc-99m-MAG3	65 %	Yes
Renal Glomerular Filtration Study	Tc-99m-DTPA	Low	Yes
Bone Mineral Study	Tc-99m-MDP	Low	No
Brain Death Angiography Study	Tc-99m-DTPA	Very low	No
CT of the brain	I-127-iothalamate	Very low	Yes
MR of the brain	Gd-153-DTPA	Very low	Yes

central volume principle. Unfortunately, it is difficult to be sure that the input artery does in fact directly supply the entire blood flow into and through the ROI in question. The differences between evaluating blood flow with radiopharmaceuticals and CT density contrast are discussed in more detail at the end of this chapter (Convolution analysis is discussed in Chap. 7: Mean Transit Times: Convolution Analysis.).

Derivation of the Equation for Evaluation of Regional Blood Flow from First Circulation Time-Activity Curves

Regional blood flow can be noninvasively evaluated by injecting a relatively nondiffusible and noncleared radiopharmaceutical intravenously and recording its passage through paired peripheral structures such as the two cerebral hemispheres, two kidneys, or two lower extremities. The use of paired structures with the assumption that blood flow would normally be symmetrical simplifies the analysis by eliminating the need to correct for photon attenuation and by allowing blood flow to be evaluated in a relative fashion instead of in absolute terms.

The data is readily quantified by generating time-activity curves from paired regions of interest. It has been intuitively assumed that when the paired time-activity curves are symmetrical, the blood flow is likely to be normal and conversely; this assumption is usually, but not always, correct. It has also been assumed that relative blood flow can be calculated from the time-activity curves, but this has proved to be an oversimplification. Determination of the physiologic information content of first circulation paired time-activity curves is explored below [1, 2].

It should be noted that there are several nuclear medicine studies that are named perfusion studies but actually measure clearance: Lung Perfusion Study with Tc-99m-MAA, Brain Perfusion Study with Tc-99m-HMPAO/Tc-99m-ECD, Hepatic Artery Perfusion Study with Tc-99m-MAA, and Myocardial Perfusion Studies (multiple radiopharmaceuticals). In general, the results of these studies primarily reflect perfusion or blood flow, but not always. This discrepancy is discussed at greater length in Chap. 4: Evaluation of Clearance. It is also worth noting that strictly speaking the word perfusion implies the delivery of nutrients such as oxygen and glucose to tissues via the blood, whereas the studies in this chapter only evaluate blood flow with no implication relative to the delivery of nutrients.

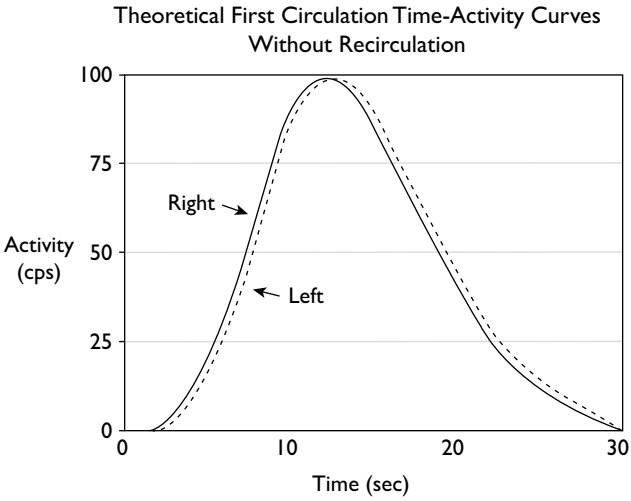

Fig. 6.1 Paired first circulation time-activity curves without clearance or recirculation. The bolus of tracer is elongated as it enters the ROIs because of laminar flow. The curve rises and falls to zero because of the absence of clearance and recirculation of the tracer (*cps* counts per second)

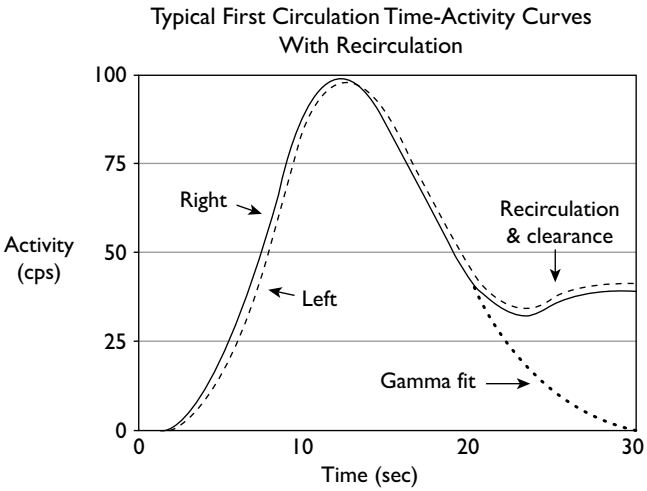

Fig. 6.2 Paired first circulation time-activity curves with clearance and recirculation. The time-activity curves never return to baseline because the leading edge of the first circulation reenters the ROIs before the tail end leaves and, in addition, some of the tracer may be cleared. However, a mathematical gamma fit has been performed to simulate a time-activity curve with no recirculation

Figure 6.1 shows the theoretical appearance of time-activity curves that would be generated from ROIs placed over paired structures following the intravenous injection of a nondiffusible and noncleared radiopharmaceutical during the first circulation without recirculation.

The time-activity curves that are actually obtained from the studies listed in Table 6.1 are different from those depicted in Fig. 6.1 because (1) some of the radiopharmaceuticals in question moves out of the vascular space, particularly Tc-99m-MAG3 in the kidneys, and (2) recirculating tracer reenters the ROIs before the end of the first circulation (Fig. 6.2). The end result is that the downslope of the time-activity curves never reaches zero.

However, it is theoretically possible to compensate for recirculation and clearance of the tracer by performing a "gamma fit" to the initial clinical time-activity curve (Fig. 6.2). See discussion below.

Mathematically, we start with the Stewart-Hamilton equation, which describes the relationship among the amount of an indicator that is injected intravenously, the cardiac output, and the integral of the concentration of an indicator, here a radiopharmaceutical, as a function of time at an arterial sampling site [7].

$$A = F_{CO} \times \int_0^T C(t)\,\mathrm{d}t \tag{6.1}$$

This equation states that if a given amount of radiopharmaceutical, A (μCi), is injected as a bolus into the proximal circulation and undergoes uniform mixing in a central chamber, then measurement of the concentration of radiopharmaceutical, $C(t)$ (μCi/mL), at some distal point during the first circulation. T and the concentration during recirculation are determined by extrapolation [4] will permit calculation of cardiac output, F_{CO} (mL/min).

It is important to note that the concentration and the mean transit time of indicator in the branches of the arterial system during the first circulation are related to volume and flow in such a way that the integral, $\int_0^T C(t)\,\mathrm{d}t$, is a constant regardless of the sampling site [1]. This fact is implicit in the Stewart-Hamilton equation since the terms, A and F_{CO}, are both constants for a given injection.

When an external detector is substituted for blood sampling, the Stewart-Hamilton equation becomes,

$$G \times A = F_{co} \times \int_0^T R(t)\,\mathrm{d}t / V_r \tag{6.2}$$

Here G is a conversion factor that converts the indicator, with units of disintegrations per second, to the reading of the external detector, $R(t)$, with units of counts per second, and V_r is the regional blood volume [5]. Since V_r is unknown and not easily determined, the integral with an external detector, $\int_0^T R(t)\,dt / V_r$, is significantly different from the integral with blood sampling, $\int_0^T C(t)\,\mathrm{d}t$. A modified form of Eq. 6.2 has been used to measure cardiac output with a radiotracer, external detection, and a single blood sample at equilibrium [8–10].

Equation 6.2 is now converted from an equation for cardiac output to an equation for regional blood flow by multiplying both sides by the fraction of the cardiac output which passes through the ROI.

$$G \times A \times F_r / F_{co} = F_r \times \int_0^T R(t)\,\mathrm{d}t / V_r \tag{6.3}$$

Here F_r is regional blood flow. Since the integral $\int_0^T R(t)\,dt / V_r$ is constant for all ROIs for a given injection, it can be seen that the fraction of the injected dose that passes through a ROI on the first circulation, $G \times A \times F_r / F_{co}$, varies directly with regional blood flow, F_r.

As the blood volume of the ROI, V_r, cannot be determined, it is desirable to eliminate this term using the relationship flow equals volume divided by the mean transit time (see Chap. 5: Mean Transit Time: Central Volume Principle).

$$G \times A \times F_r / F_{co} = 1/\bar{T}_r \times \int_0^T R(t)\,dt \tag{6.4}$$

Here "$\bar{T}_r$" is the mean transit time through the ROI. It is important to note that cancellation of the term V_r within the integral is equivalent to multiplying the constant, $\int_0^T R(t)\,dt / V_r$, times the blood volume of the ROI, V_r. Consequently, the resulting integral, $\int_0^T R(t)\,dt$, is linearly proportional to the blood volume of the ROI.

Equation 6.4, the equation for regional blood flow, contains three unknowns in addition to F_r and cannot be solved for a single ROI. For paired ROIs, regions one and two, the conversion factor, G; the injected dose, A; and the cardiac output, F_{co}, are the same for both ROIs and cancel giving,

$$\frac{F_{r1}}{F_{r2}} = \frac{1/\bar{T}_{r1} \times \int_0^{T_1} R_1(t)\,dt}{1/\bar{T}_{r2} \times \int_0^{T_2} R_2(t)\,dt} \tag{6.5}$$

Since the integral $\int_0^T R(t)\,dt$ reflects only regional blood volume, it can be seen from Eq. 6.5 that when the Stewart-Hamilton equation is modified for paired ROIs, it reduces to the form of relative flow equals relative volume divided by the relative mean transit time, or the central volume principle.

Figures 6.3 and 6.4 diagrammatically summarize the effects of branching and changes in regional volume, mean transit time, and flow on the physical shape of the bolus and the resulting time-activity curve for single pathways; cardiac output is constant.

Plug flow with the numbers representing tracer activity is depicted, but similar results would be expected for laminar flow. It can be seen that (1) the fraction of the injected dose which passes through a ROI varies with the fraction of cardiac output which passes through a ROI (Fig. 6.3); (2) when the volume of the sampling site is held constant (as with blood sampling and measurements per mL), changes in flow do not result in changes in the integral of the first circulation time-activity curve because of compensatory changes in the mean transit time (Fig. 6.3); and (3) when the volume of the sampling site is varied and the amount of indicator injected and

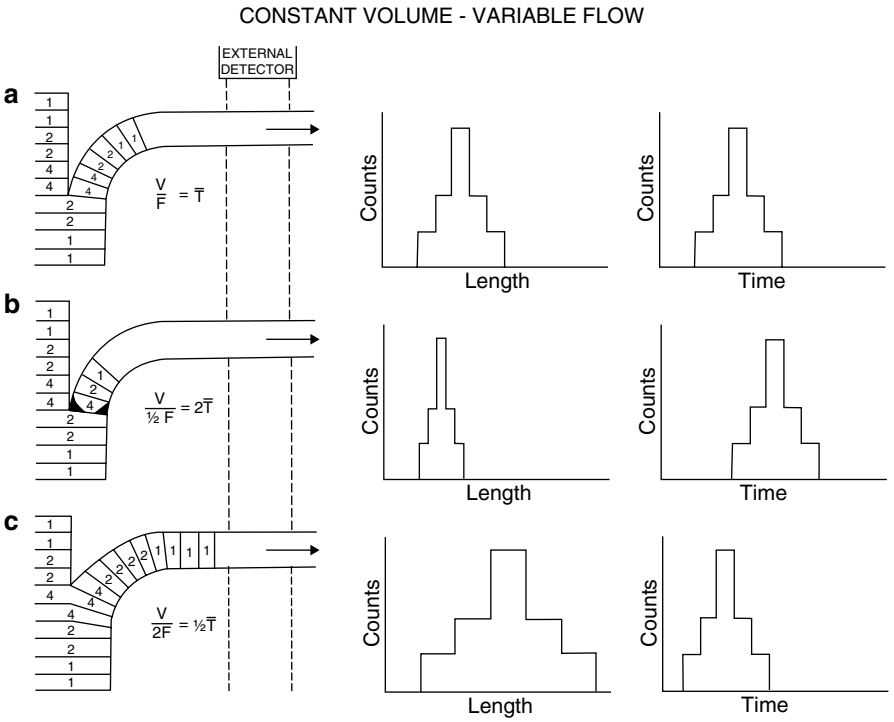

Fig. 6.3 The numbers in the vascular system on the left represent tracer activity (*1st column*). As flow is varied but volume is held constant in the side branch under study (**a**–**c**): (1) the amount of tracer passing through the side branch varies directly with flow (*2nd column*) and (2) when the volume of the sampling site is held constant (as with blood sampling and measurements per mL), changes in flow do not result in changes in the integral of the first circulation time-activity curve because of compensatory changes in the mean transit time (*3rd column*)

the cardiac output are held constant (e.g., multiple ROIs following one injection), the integral of the first circulation time-activity curve varies directly with the blood volume of the sampling site of ROI (Fig. 6.4). The equations beneath the side branches in Figs. 6.3 and 6.4 indicate that more than one combination of change in regional flow and volume can account for a change in mean transit time.

The equation for relative blood flow to paired ROIs, Eq. 6.5, can be solved if the mean transit times through the ROIs can be calculated. Unfortunately, the mean transit time through the ROIs cannot be determined from the time-activity curve from the ROI because the time-activity curve is a function of the physical shape of the bolus as it enters the ROI as well as the frequency distribution of transit times through the ROI [11]. This point is diagrammatically illustrated in Fig. 6.5.

Flow, volume, and the mean transit time are constant, but the shape of the time-activity curve varies with the physical shape of the bolus. The physical shape of the bolus depends mainly on the conditions of injection, laminar flow, and the distance from the injection site to the ROI.

The input of blood flow to the ROI is through one or more relatively small arteries making it difficult to determine the shape of the incoming radiotracer profile by

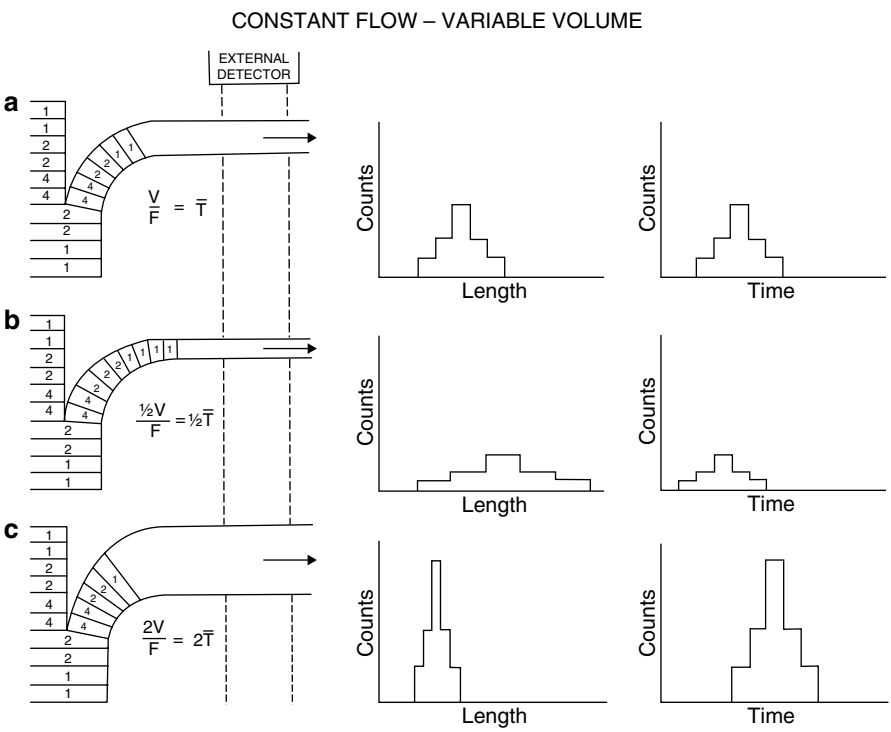

Fig. 6.4 As volume is varied but flow is held constant in the side branch under study (*1st column*), the integral of the first circulation time-activity curve varies directly with the blood volume of the sampling site of the ROI (*3rd column*)

imaging. If this difficult problem can be solved in the future, deconvolution analysis of the washout curve will yield the frequency distribution of transit times through the ROI and, thus, the mean transit time through the ROI. The mean transit time through the ROI could then be divided into the blood volume of the ROI to obtain the blood flow through the ROI specifically.

Although the relative mean transit time through paired ROIs cannot be measured, differences in the mean transit time from the point of bolus division in the aortic arch can be estimated by determining differences in the first moment time for each time-activity curve about the time of injection,

$$T_{\mathrm{m}} = \frac{\int_0^T t \times R(t)\,\mathrm{d}t}{\int_0^T R(t)\,\mathrm{d}t} \tag{6.6}$$

Here T_{m} is the first moment time about the time of injection, T is the end of the first circulation through the ROI, and t is instantaneous time. The first moment time represents the mean transit time from the point of injection to and through the ROI (more accurately, to some point within the ROI). Any difference between the first moment or

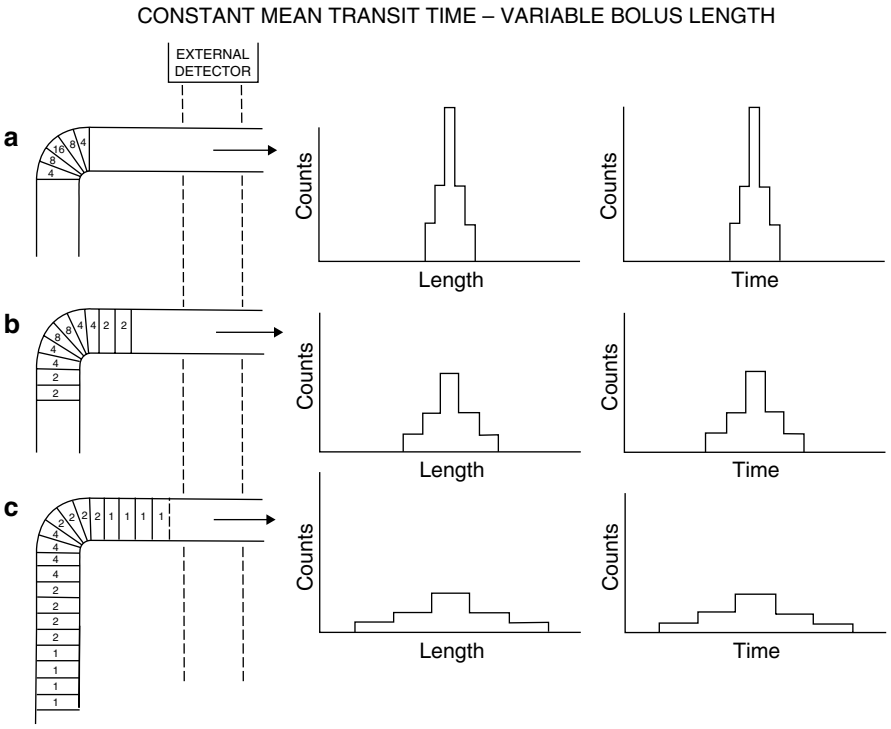

Fig. 6.5 Variable bolus shape. When the bolus shape is varied and all other parameters are kept constant (**a**–**c** in *1st column*), the time-activity curve varies directly with changes in bolus shape (*2nd column*). However, the area under the curve is constant (*3rd column*)

mean transit times from the point of injection to and through paired ROIs will reflect a difference in the mean transit times from the point of bolus division in the aortic arch to and through the paired ROIs because prior to that point there is only one bolus and one mean transit time. This concept is diagrammatically illustrated in Fig. 6.6.

Using the first circulation blood flow studies of the kidney as an example, regional renal blood flow can then be evaluated by measuring differences in the two physiologic parameters: (1) the mean transit time from the aorta to and through the ROIs and (2) regional blood volume. Regional blood volume is measured from the integral $\int_0^T R(t)\,dt$ as explained above. When a significant asymmetry exists in either of the two physiologic parameters, the abnormal time-activity curve of the pair is determined on the basis of other information in the nuclear medicine study or clinical data. Each time-activity curve of interest is then classified into one of the nine possible combinations of normal, increased, or decreased blood volume and normal, increased, or decreased mean transit time to and through the ROI (Fig. 6.7).

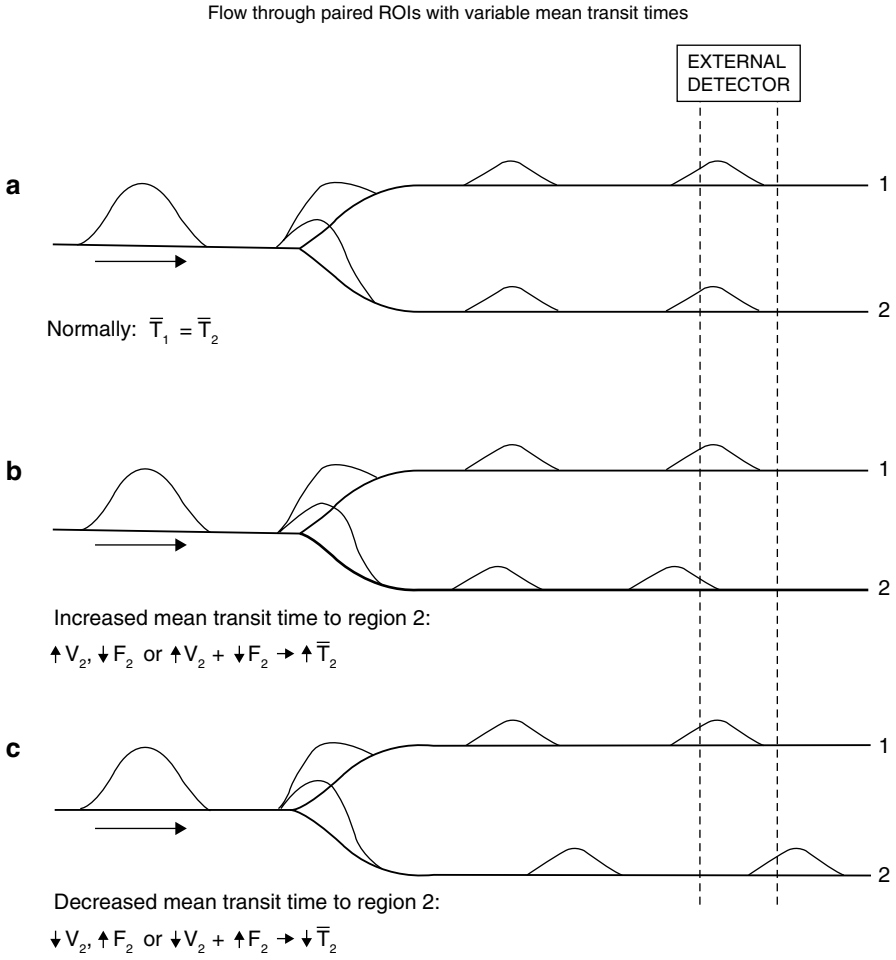

Fig. 6.6 If appropriate changes in flow and/or volume cause an increase in mean transit time in pathway two, the bolus will arrive later at the ROI (**a** v **b**). Conversely, with a decrease in mean transit time in pathway two, the bolus will arrive earlier at the ROI (**a** v **c**)

The findings are related to regional blood flow by the relationship flow equals volume divided by the mean transit time. However, the two physiologic parameters cannot be treated as a quotient because the meant transit time measurement is from the aorta to and through the ROI, not just through the ROI. Thus, the result is not always specific: a normal regional blood volume and an increased mean transit time to and through the ROI can be explained by either decreased flow through the ROI or an increased mean transit time from the aortic arch to the ROI (e.g., a long pathway secondary to collateral flow).

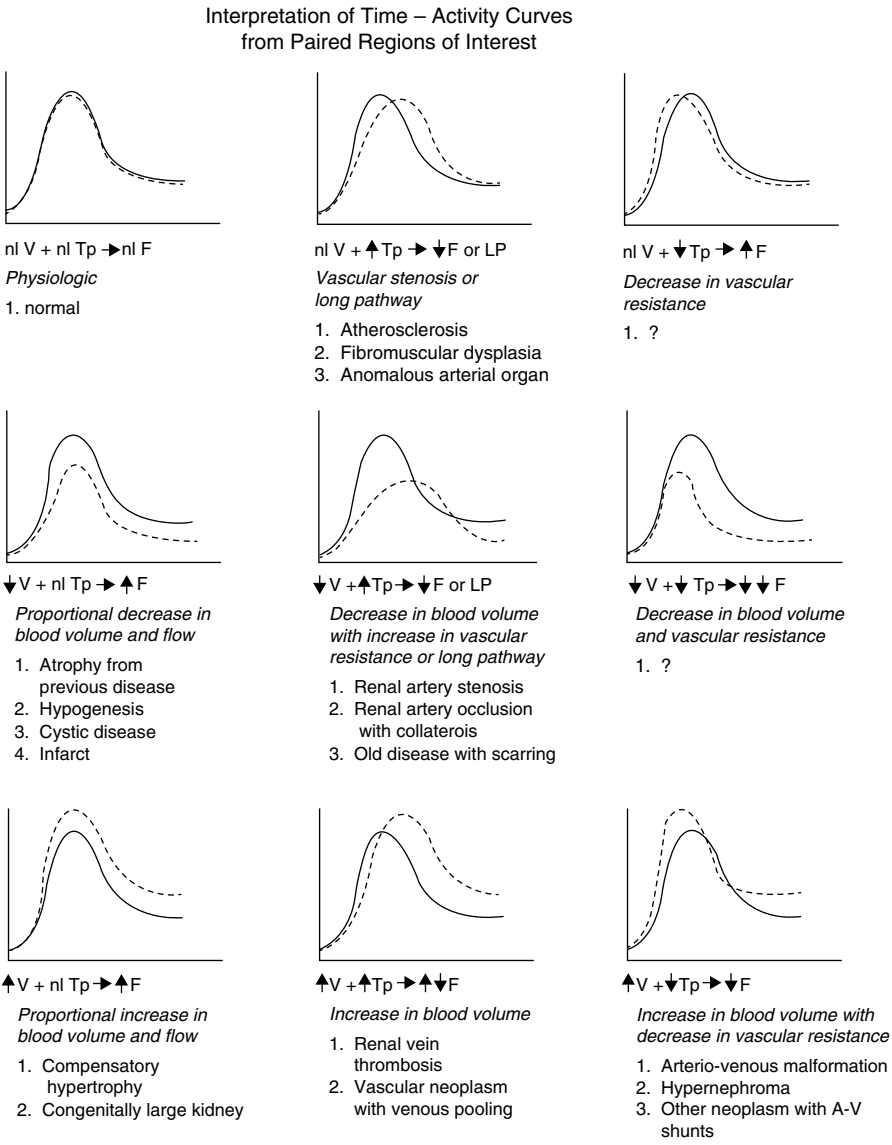

Fig. 6.7 Indices for regional blood volume and transit time to and through a ROI. Each parameter can be categorized as normal, increased, or decreased. This results in nine combinations of findings. Each of the nine different time-activity curve findings implies a pathophysiologic interpretation and a differential diagnosis (*F* flow; *V* volume; *Tp* peak time; *LP* long pathway; *broken line* is the abnormal curve)

Practical Considerations in Using the First Circulation Time-Activity Curves for Evaluation of Regional Blood Flow in Clinical Studies

When a radiopharmaceutical is introduced into the body intravenously in order to acquire images during the first circulation for evaluation of blood flow, an attempt is made to keep the radiotracer as compact as possible as it passes through the circulation. A relatively compact bolus of radiotracer will give a sharper rise and fall in the signal from the serial images that subsequently facilitates analysis. To this end, the injection is usually performed using the Oldendorf technique [12]. In this technique, a tourniquet or blood pressure cuff is placed on the arm and inflated to a pressure between venous and arterial pressure so that blood can enter the arm, but not leave resulting in engorgement of the distal veins.

The small volume of radiopharmaceutical is then injected into a vein, and the blood pressure cuff is quickly removed. The blood in the engorged peripheral venous system propels the radiopharmaceutical centrally to the heart from where it will be distributed systemically in proportion to the distribution of cardiac output. However, the radiopharmaceutical never arrives at the arterial site of interest in a compact form because of laminar flow (see Chap. 5: Mean Transit Time: Central Volume Principle). This phenomenon lengthens the bolus as a function of distance traveled. By the time the bolus reaches the capillary bed in the organ of interest, the bolus is quite long.

Laminar flow causes two problems. First, it lengthens the bolus so that it does not enter the distal ROI in a discrete fashion, and, second, before the elongated bolus has completely passed through the ROI during the first circulation, the leading edge of the recirculating bolus is already reentering the ROI. This phenomenon results in the time-activity curves shown in Fig. 6.2.

In order to calculate both the relative difference in the mean transit time from the aorta to and through the ROIs and the relative blood volume of the ROIs, it must be possible to integrate the time-activity curve during the entire first circulation of the radiopharmaceutical. To accomplish this in the face of recirculating radiopharmaceutical entering the ROIs before the entire first circulation bolus has left the ROIs, a process called a "gamma fit" is applied to the downslope of the time-activity curves (Fig. 6.2). The gamma fit function is a polynomial equation that is adjusted to match a time-activity curve from the arrival of tracer in the ROI to the point at which recirculation begins. The fitted curve is then extended to the baseline.

The evaluation process can be simplified by using indices of the two physiologic parameters in question: (1) the relative blood volume of the ROIs and (2) relative difference in the mean transit time from the aorta to and through the ROIs (Fig. 6.8). Three studies, one experimental and two clinical, have shown that the time of peak activity in the time-activity curve is a good index of the mean transit time from the aorta to and through the ROI, and that the activity level at equilibrium can be used as an index of the blood volume in the ROI [2, 13, 14]. These indices not only facilitate quantitative evaluation by not requiring the gamma fit process but allow visual evaluation as well.

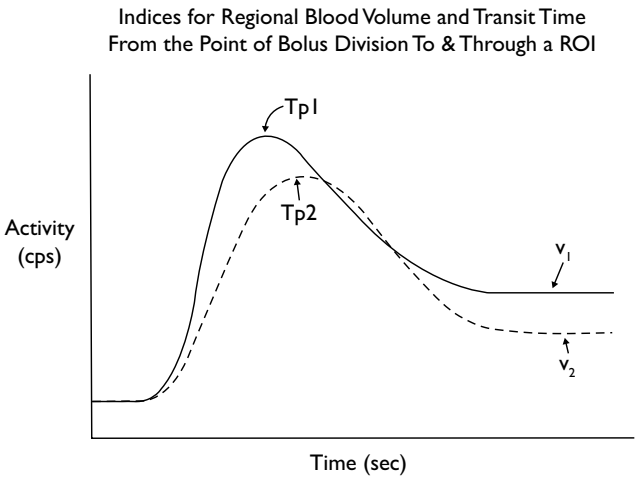

Fig. 6.8 On theoretical and experimental grounds, the amount of activity in a ROI at equilibrium varies with regional blood volume. And, on experimental grounds, the time of peak activity corresponds with the mean transit time from the point of bolus division to and through the ROI.

Clinical Experience with Analysis of the First Circulation Time-Activity Curves for Regional Blood Flow

The method of interpreting first circulation time-activity or time-indicator curves described above has been applied to cerebral blood flow in a variety of brain pathology [2, 14]. In one publication, 36 proven cases of brain pathology were collected from the literature with the requirement that each patient must have had a first circulation time-indicator study and that the curves were reproduced in the publication. In none of the cases were the curves interpreted using the physiologic method described above. In general, the first circulation time-indicator curves were merely characterized as abnormally asymmetrical [14].

Of the 36 cases, 11 were evaluated with radiotracer angiography and 25 were evaluated with dynamic CT. The proven etiologies were compared to the theoretical etiologies that had been published for the nine possible combinations of normal, increased, or decreased mean transit time to and through a ROI and regional blood volume [1]. Twenty six (72 %) of the cases fell into the predicted categories, three (8 %) fell into non-predicted categories, and seven (19 %) had etiologies that were not considered in the theoretical classification [14].

Modification of the Equation for Evaluation of Regional Blood Flow from First Circulation Time-Density Curves for Use with Computed Tomography

Software applications are available from the manufacturers of CT scanners that convert rapid serial images of the brain obtained during the first circulation of intravenous contrast material into parametric images that purport to show regional blood volume, mean transit time, and blood flow within each tomographic image [3–6]. The greater spatial resolution of CT images compared to gamma camera images allows placement of a region of interest over the anterior cerebral artery and generation of a time-density curve that can be treated as the input function to the region of interest of the portion of brain to be evaluated.

The mean transit time through the cerebral region of interest can be calculated by first deconvolving the cerebral time-density curve by the input time-density curve to obtain the frequency distribution of transit times or impulse residue function through the cerebral region of interest (see Chap. 7: Mean Transit Times: Convolution Analysis). Then the mean transit time through the cerebral region of interest can be calculated by dividing the integral of the impulse residue function by the value of the maximum height of the impulse residue function [3]. The contrast enhancement at equilibrium or the integral of the cerebral time-density curve can be used as a measurement of regional blood volume [2, 3]. At this point, the blood flow through the cerebral region of interest can be determined by dividing the regional cerebral blood volume by the mean transit time through the cerebral region of interest using the central volume principle [3].

This approach is critically dependent on the measured input curve being an accurate reflection of the true CT contrast density curve that enters the cerebral region of interest during the first circulation. However, some or all of the arterial input into the cerebral region of interest may come from arteries other than the anterior cerebral artery and have time-density curves that may differ from the time-density curve of the anterior cerebral artery. In addition, some arteries or veins may pass through the cerebral region of interest without connecting to capillary beds within the region of interest, in which case they would contribute to regional blood volume, but not to blood flow to the tissue within the region of interest.

References

1. Klingensmith WC. Physiologic interpretation of time-activity curves from cerebral flow studies: theoretical considerations. J Nucl Med Allied Sci. 1980;24:73–8.
2. Klingensmith WC, Lotter MG, Knowles G, et al. Physiologic interpretation of time-activity curves from cerebral flow studies: initial clinical evaluation. J Nucl Med Allied Sci. 1980;24:79–84.
3. Nabavi DG, Cenic A, Craen RA, et al. CT assessment of cerebral perfusion: experimental validation and initial clinical experience. Radiology. 1999;213:141–9.
4. Eastwood JD, Lev MH, Azhari T, et al. CT perfusion scanning with deconvolution analysis: pilot study in patients with acute middle cerebral artery stroke. Radiology. 2002;222:227–36.
5. Nabavi DG, Cenic A, Henderson S, et al. Perfusion mapping using computed tomography allows accurate prediction of cerebral infarction in experimental brain ischemia. Stroke. 2001;32:175–83.
6. Hoeffner EG, Case I, Jain R, et al. Cerebral perfusion CT: technique and clinical applications. Radiology. 2004;231:632–44.
7. Stewart GNJ. Researches on the circulation time and on the influences which effect it. IV. The output of the heart. J Physiol. 1897;22:159.
8. Moore JW, Kinsman JM, Hamilton WF, et al. Studies on the circulation II. Cardiac output determinations; comparison of the injection method with the direct fick procedure. Am J Physiol. 1929;89:331.
9. Donato L, Giuntini C, Lewis ML, et al. Quantitative radiocardiography. I. Theoretical considerations. Circulation. 1962;26:174.
10. MacIntyre WJ, Pritchard WH, Eckstein RW, et al. The determination of cardiac output by a continuous recording system utilizing iodinated I-131 human serum albumin. I. Animal studies. Circulation. 1951;4:552–6.
11. Pearce ML, McKeever WP, dow P, et al. The influence of injection site upon the form of dye-dilution curves. Circ Res. 1953;1:111–6.
12. Oldendorf WH, Kitano M, Shimizu S. Evaluation of a simple technique for abrupt intravenous injection of radioisotope. J Nucl Med. 1965;6:205–9.
13. Klingensmith WC. Regional blood flow with first circulation time-indicator curves: a simplified, physiologic method of interpretation. Radiology. 1983;149:281–6.
14. Klingensmith WC. Evaluation of a physiologic method of interpreting first circulation time-indicator curves. Invest Radiol. 1986;21:566–70.

Regional Transit Times: Convolution Analysis

7

Introduction

There are five nuclear medicine studies in which a series of time-dependent images depict the movement of the radiopharmaceutical through a structure (Table 7.1). If a region of interest (ROI) is placed over the structure of interest, the shape of the resulting time-activity curve is determined by a combination, or convolution, of the shape of the incoming bolus of radiopharmaceutical and the spectrum of transit times through the structure of interest. The structure of interest may be either the vascular bed of an organ or an excretory pathway through the parenchyma of an organ.

The first four studies in Table 7.1 include rapid serial images during the first circulation of a radiopharmaceutical through a vascular bed for the purpose of evaluating blood flow through paired regions of interest. Two of these studies include the routine generation of time-activity curves, the Renal Tubular Secretion Study with Tc-99m-MAG3 and the Renal Glomerular Excretion Study with Tc-99m-DTPA, and two studies do not, the Brain Death Study with Tc-99m-DTPA and the three-phase Bone Mineral Study with Tc-99m-MDP of the lower extremities. However, the same principles that are used to evaluate paired time-activity curves can be used to visually evaluate the paired structures in the rapid serial images acquired during the first circulation.

There are three studies in Table 7.1 that include rapid serial images during the movement of a radiopharmaceutical through an excretory system that excretes molecular waste from the blood. Two of these studies are of paired organs: the Renal Tubular Secretion Study with Tc-99m-MAG3 in which serial images depict the tracer moving from the tubular cells through the tubular lumens to the calyces and the Renal Glomerular Filtration Study with Tc-99m-DTPA in which serial images depict the tracer moving from the glomeruli through the tubular lumens to the calyces. One study is of an unpaired organ: the Hepatobiliary Study with Tc-99m-trimethylbromo-IDA in which serial images depict the tracer moving from the hepatocytes through the liver parenchyma into the extrahepatic biliary tract.

W.C. Klingensmith III, *The Mathematics and Biology of the Biodistribution of Radiopharmaceuticals-A Clinical Perspective*,
DOI 10.1007/978-3-319-26704-3_7

Table 7.1 Nuclear medicine studies that include serial images of tracer moving through the vascular or excretory pathway of an organ

Procedure	Radiopharmaceutical	Parameter	Paired structures	Time-activity curves
Renal tubular secretion study	Tc-99m-MAG3	Blood flow	Yes	Yes
		Parenchymal transit	Yes	Yes
Renal glomerular filtration study	Tc-99m-DTPA	Blood flow	Yes	Yes
		Parenchymal transit	Yes	Yes
Bone mineral study (three phase)	Tc-99m-MDP	Blood flow	Yes	No
Brain death angiography study	Tc-99m-DTPA	Blood flow	Yes	No
Hepatobiliary study	Tc-99m-trimethyl-bromo-IDA	Parenchymal transit	No	No

Time-activity curves are generated in the two renal studies, but not in the hepatobiliary study.

In all of these studies and for evaluation of both blood flow and excretion through parenchyma, the radiopharmaceutical bolus will be elongated as it approaches the organ of interest, even though it starts out as a discrete plug bolus at the site of intravenous injection (Fig. 7.1). The elongation of the bolus is caused by the physical process of laminar flow, which causes the length of the bolus to increase in proportion to the distance traveled through the vascular system.

Figure 7.2 demonstrates how variation in bolus shape affects the time-activity curve shape with all other factors held constant. However, in keeping with the Stewart-Hamilton equation, the area under the time-activity curve remains constant.

One difference between the application of convolution analysis to the study of vascular systems and excretory systems is that, while vascular systems involve just one set of transit times added sequentially to the incoming elongated bolus, excretory systems have an additional process, clearance via an extraction mechanism, that moves the radiopharmaceutical from the blood into the excretory pathways. This extra biologic process adds another variable, which may have a significant impact.

Convolution and its inverse, deconvolution, are mathematical concepts that will be explained in some detail below [1, 2]. Although the actual calculations are not performed in nuclear medicine studies, a conceptual knowledge of convolution and deconvolution is helpful in interpreting blood flow and excretory images [3]. Examples of the use of these concepts are given in the various chapters of Part III, Quantitative Evaluation in Nuclear Medicine Studies.

Conceptual Analysis of Convolution

Consider the simple diagram in Fig. 7.3. There is a central compartment with one way for fluid to flow in on the left and one way for fluid to flow out on the right. In addition, regions of interest (ROIs) are drawn at the location of fluid input and around the compartment as a whole.

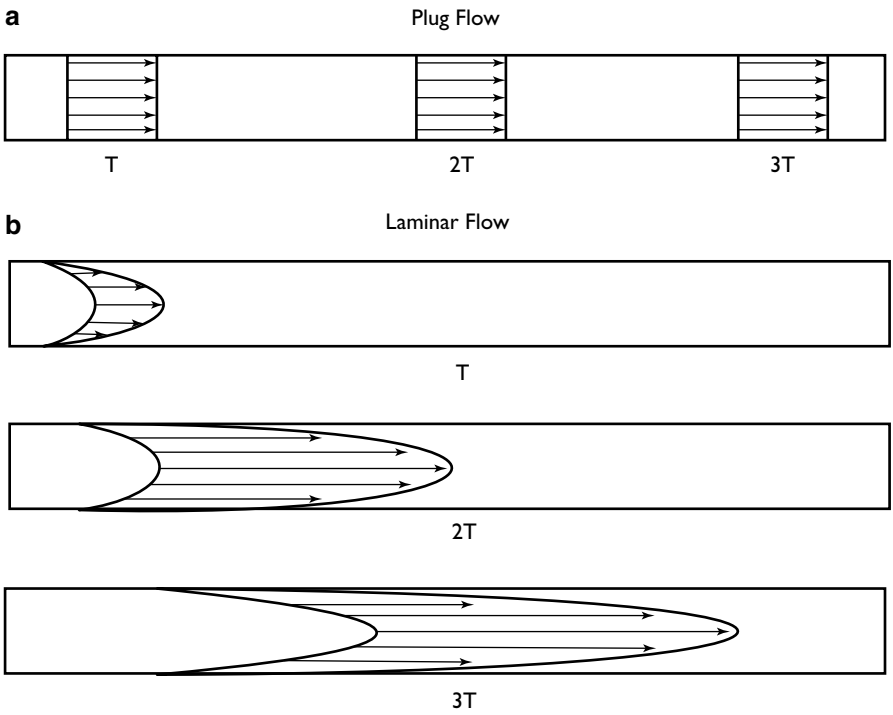

Fig. 7.1 Plug and laminar flow. Panel **a** demonstrates the behavior of plug flow at three sequential times (T, 2T, and 3T) after injection of tracer into a flowing system. The relatively discrete shape of the bolus of tracer does not change over time. Panel **b** demonstrates laminar flow, typical of biologic systems. Because flow is fastest in the center of a tubular system and falls to near zero at the margins, the bolus elongates as a function distance traveled (T, 2T, and 3T)

In the case of evaluating blood flow through the vascular system of an organ, the input structure on the left represents the arterial inflow into the organ, the compartment represents the vascular system within the organ, and the output structure on the right represents the venous flow out of the organ. In the case of an excretory system like the renal tubular secretion system or hepatobiliary system, the input structure represents the arterial supply to the parenchyma, the compartment represents the parenchyma, and the output structure represents the excretory structures that carry fluid from the parenchyma, i.e., calyces and more distal excretory structures in the case of the kidneys and extrahepatic biliary tract in the case of the liver and hepatobiliary system.

For both vascular and excretory systems, there are thousands of individual pathways through an organ. Not all of the vascular or excretory pathways will have the same transit time. The transit time may vary because the pathways have different: amounts of flow, lengths, or luminal diameters. In disease the variation in transit times through these pathways often increases greatly.

Figure 7.4 shows the distribution of transit times through the compartment in Fig. 7.3.

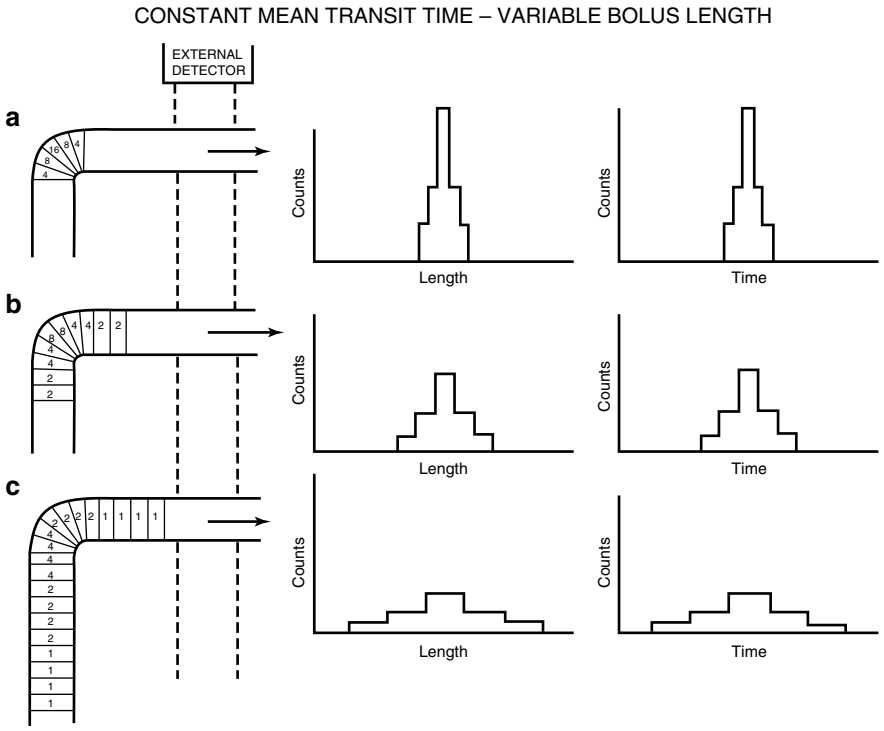

Fig. 7.2 Variable bolus shape. When the bolus shape is varied (**a**–**c**) and all other parameters are kept constant, the time-activity curve varies directly with changes in bolus shape (*1st* and *2nd columns*). However, the area under the curve is constant (*3rd column*)

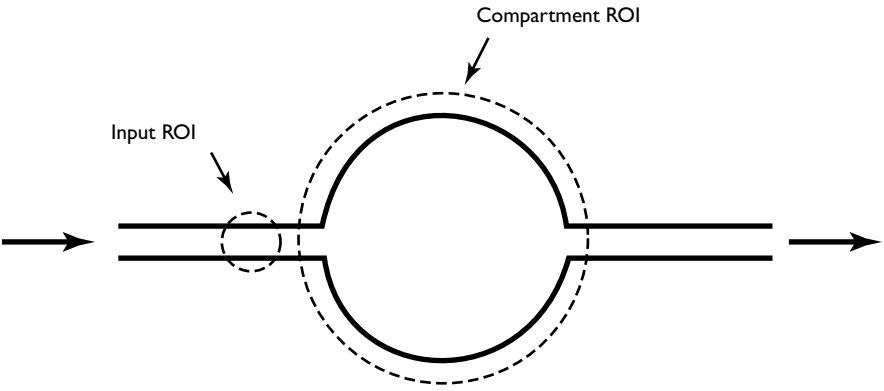

Fig. 7.3 Simple single compartmental model. The *solid lines* depict a single central compartment with a single input on the left and a single output on the right. The *broken circles* indicate regions of interest (ROIs) for generating time-activity curves during the passage of a bolus of tracer

Figure 7.5 depicts an instantaneous or impulse injection of tracer into the compartment. The time-activity curve is recorded from the ROI over the input site, not the compartment itself.

A true instantaneous injection is never encountered in the clinical setting. However, it is useful to initially look at a simple impulse injection before considering the more complex situation of an input bolus that is spread out over distance and time.

Figure 7.6 shows the percent of activity left in the compartment as a function of time assuming that the activity was introduced into the compartment as an impulse

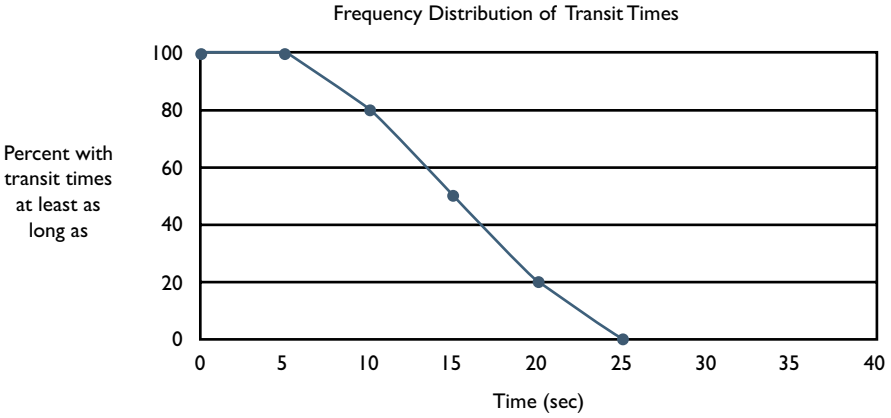

Fig. 7.4 Frequency distribution of transit times through a compartment. The graph shows that the shortest transit time through the ROI is 5 s and the longest is 25 s

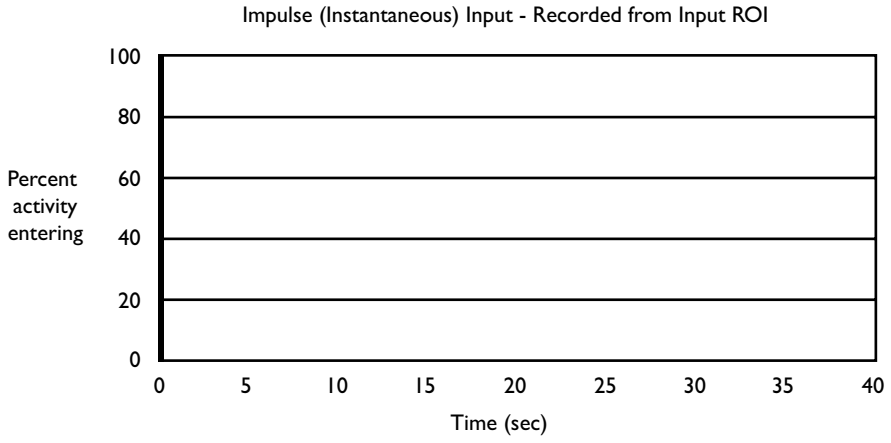

Fig. 7.5 Impulse introduction of tracer. The graph shows an impulse introduction of tracer into the compartment. The time-activity curve is from the ROI at the input to the compartment, not from the compartment itself

or instantaneous injection. Again, 100 % of the radiopharmaceutical enters the compartment initially at one point in time. Then at 5 s none of the radiopharmaceutical will have exited the compartment, at 10 s 20 % of the original amount will have exited, at 15 s 50 % will have exited, at 20 s 80 % will have exited, and by 25 s all of the tracer will have exited. The curve is unchanged from the curve of the distribution of transit times in Fig. 7.4 except for the units on the Y-axis because all of the radiopharmaceutical enters the compartment simultaneously and the transit times are determined by measuring the transit time of individual pathways and displaying them with the same starting time. This is the simplest form of the convolution. No deconvolution is needed.

Table 7.2 presents the same simple impulse input example, but in table form. First, notice that the red numbers in the first row and first column are times in seconds. Second, notice that the green numbers in the second row are the percent of tracer exiting the compartment at the indicated time. Thus, no tracer exits at 0 or 5 s, 20 % of the original amount exits at 10 s, 30 % of the original amount exits at 15 s, another 30 % of the original amount exits at 20 s, and the final 20 % exits at 25 s. Third, notice that the blue numbers in the second column indicate the amount of the incoming bolus that enters the compartment as a function of time. In this case the total amount of radiopharmaceutical is 100 and all of the radiopharmaceutical enters at time zero. The numbers within the outlined black rectangle indicate the amount of radiopharmaceutical remaining in the compartment as a function of time. At zero and 5 s 100 % remains in the compartment, at 10 s 80 % remains, at 15 s 50 % remains, etc. There is no activity in the other cells within the box because the entire input bolus enters the compartment at time zero. The bottom row of the entire table shows the sum of activity that remains in the compartment as a function

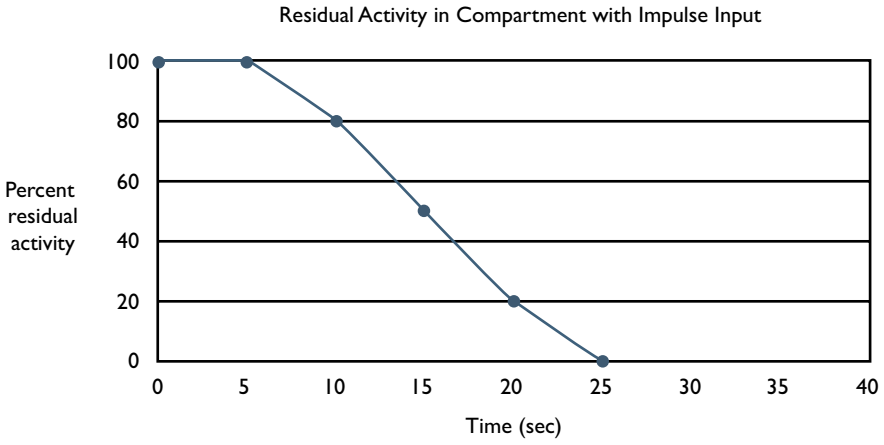

Fig. 7.6 Residual activity in a compartment vs. time. The graph shows residual activity in a compartment as a function of time following an impulse input. With an impulse injection, the curve will be identical to the frequency distribution of transit times (Fig. 7.4)

of time. The amounts are the same as the first row within the black rectangle because, again, no activity enters after time zero.

Now we consider the effect on the graphs and table if the input bolus is a typical non-impulse bolus. Fig. 7.7 shows the shape and activity as a function of time of an incoming bolus that has length because of laminar flow. We will discuss the curve

		Input										
	Sec		0	5	10	15	20	25	30	35	40	45	Sum
Percent exiting			0	0	20	30	30	20	0	0	0	0	
	0	100	100	100	80	50	20	0					350
	5	0											0
	10	0											0
	15	0											0
	20	0											0
Activity in ROI			100	100	80	50	20	0	0	0	0	0	350

Sum = Sum of counts from each cohort as it passes through ROI.

Table 7.2 Convolved activity in compartment with impulse input. Sum = Sum of counts from each cohort as it passes through ROI

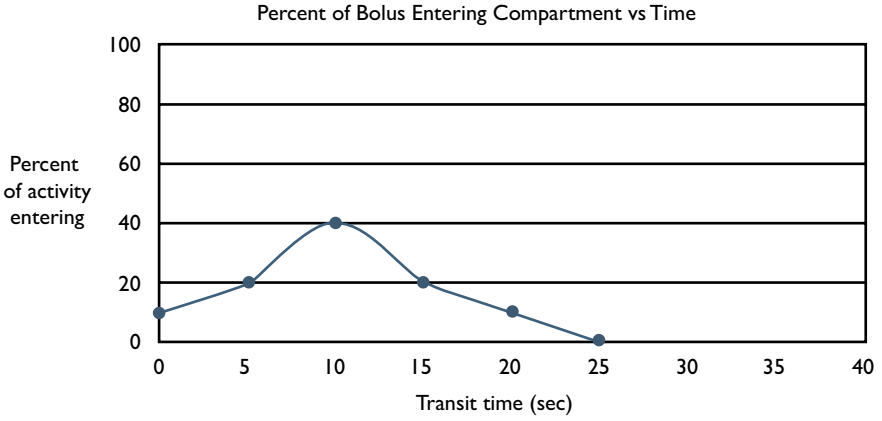

Fig. 7.7 Percent of bolus entering compartment vs. time. The graph shows the percent of a typical non-impulse bolus entering a compartment over time. The elongated bolus enters the compartment over 25 s. This curve is generated from the input ROI in Fig. 7.3

in discrete terms, but in actuality it would be continuous. Ten percent of the incoming bolus enters the compartment at 0 s, 20 % enters at 5 s, 40 % enters at time 10 s, etc. This means that at each of the time points that we are considering, 5 s intervals, a new cohort of activity will begin to pass through the compartment with the distribution of transit times shown in Fig. 7.4 and the residue versus time curve shown in Fig. 7.6. The time-activity curve in Fig. 7.7 is generated from the input ROI in Fig. 7.3.

Table 7.3 presents the information for compartment activity when the input is distributed over time as is typical in clinical studies. Compared to Table 7.2 the second column (blue numbers) now shows tracer entering the compartment over five successive points in time. In addition, within the black rectangle (corresponding to the compartment), the amount of residual activity for each entering cohort is shown as a function of time with the appropriate weighting for the amount entering and the appropriate time shift to reflect the time of entry into the compartment. The total amount of activity in the compartment at any one point in time is shown in the bottom row opposite the heading "Activity in ROI."

In general, for a given amount of radiopharmaceutical, the time-activity curve from the compartment ROI will be much broader and flatter with a non-impulse input compared to an impulse input (Fig. 7.8).

		Input										
Sec		0	5	10	15	20	25	30	35	40	45	Sum
Percent exiting		0	0	20	30	30	20	0	0	0	0	
0	10	10	10	8	5	2	0					35
5	20		20	20	16	10	4	0				70
10	40			40	40	32	20	8	0			140
15	20				20	20	16	10	4	0		70
20	10					10	10	8	5	2	0	35
Activity in ROI		10	30	68	81	74	50	26	9	2	0	350

Sum = Sum of counts from each cohort as it passes through ROI.
Activity is in arbitrary units.

Table 7.3 Convolved activity in compartment with non-impulse input. Sum = Sum of counts from each cohort as it passes through ROI. Activity is in arbitrary units

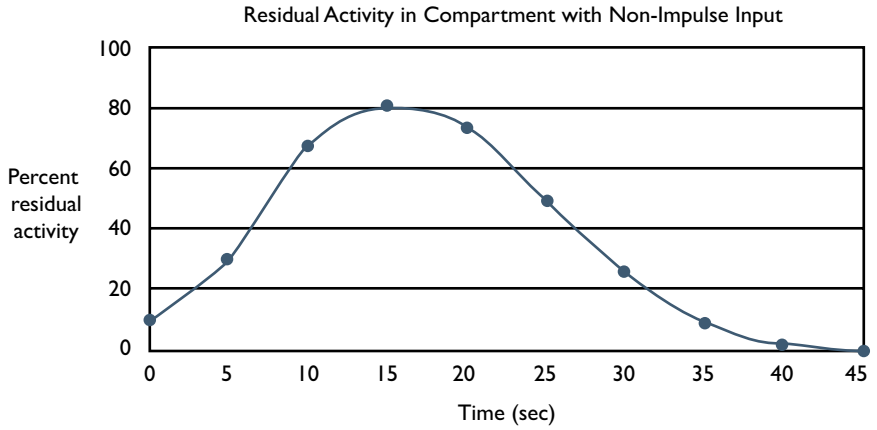

Fig. 7.8 Residual activity in a compartment with a non-impulse input. The residual activity curve with a non-impulse input is the convolution of the elongated input curve and the distribution of transit times through the compartment

Mathematical Analysis of Convolution

The same concepts of convolution presented above in terms of graphs and tables will now be presented mathematically. However, it is important to note that the following equations do not need to be solved, or even directly used, in order to apply the concepts of convolution to image interpretation.

The mathematical version of convolution is the time-activity curve (expressed as a function) for the non-impulse input curve, $f(i)$, convolved with the transit time distribution curve (expressed as a function) for the compartment, $f(g)$, to yield the observed time-activity curve (expressed as a function) of the passage of the radiopharmaceutical through the compartment, $f(a)$,

$$f(a) = f(g) \otimes f(i) \tag{7.1}$$

where '$\otimes$' is the convolution operator, which performs the same three operations demonstrated above in graphical and table form. The three operations are: (1) weighting the parenchymal response by the amount of radiopharmaceutical entering the parenchyma at a given time (multiplication), (2) shifting the resulting curve in time to correspond to the changing entry time (subtraction), and (3) summing the resulting time-activity curves to produce the final observed parenchymal time-activity curve or function (addition).

Equation 7.1 can be expanded in calculus form as the convolution integral,

$$A(t) = \int_0^T I(u)\ G(t-u)\,du \tag{7.2}$$

where on the left hand side $A(t)$ is the observed compartmental time-activity curve or function and on the right hand side: (1) the two functions within the integral, input and response, are multiplied together to give the appropriate cohort weighting, (2) the variable u produces the cohort time shift (T is the end of the first circulation), and (3) the integral summates the cohorts.

If it were possible to measure the input time-activity curve, $I(u)$, as the radiopharmaceutical bolus entered a vascular bed or excretory region, then the input curve could be used to deconvolve (the inverse of convolution) the time-activity curve generated from the structure under study, $A(t)$, which in turn would yield the transit time function for the vascular or excretory region of interest (Fig. 7.4). The transit time function can be used to calculate the mean transit time through the region of interest. The mean transit time is of great interest because, in conjunction with the regional blood volume of a structure, it can be used to calculate the flow through the structure using the central volume principle (see Chap. 5, Mean Transit Time: Central Volume Principle). Unfortunately, nuclear medicine studies, at least currently, do not have the spatial resolution to generate accurate input time-activity curves.

Clinical Applications of Convolution and Transit Times

We will use the Renal Tubular Secretion Study with Tc-99m-MAG3 as an example of how to evaluate the transit time of a radiopharmaceutical through an excretory organ in a clinical study. There are actually two transit times that are evaluated in the Renal Tubular Excretion Study: (1) blood flow to and through the kidneys and (2) passage of the tracer through the parenchyma. Here we will only discuss evaluation of the parenchymal transit time, which is quantitated both visually and with time-activity curves. Then, in Part III, Quantitative Evaluation of Nuclear Medicine Studies, we will examine the specific approach to the evaluation of transit times in all of the nuclear medicine studies that involve transit times, integrate the transit time findings with other physiologic parameters, and survey examples of diseases that cause abnormal transit times.

Figure. 7.9 shows a complete set of images from a normal Renal Tubular Secretion Study in the top half of the composite, and documentation of the placement of ROIs and resulting time-activity curves in the bottom half. We will focus on the components that relate to evaluating the transit time through the excretory pathways of the renal parenchyma. The pertinent images and time-activity curves are the so-called delayed images from 1 min to the end of the study at 30 min (Fig. 7.10) and the time-activity curves generated from the cortical ROIs (Fig. 7.11), respectfully.

The cortical ROIs are used instead of the whole-kidney ROIs so that the time-activity curves reflect just the renal parenchyma without contamination from activity in the collecting system, i.e., calyces, infundibula, and renal pelvis.

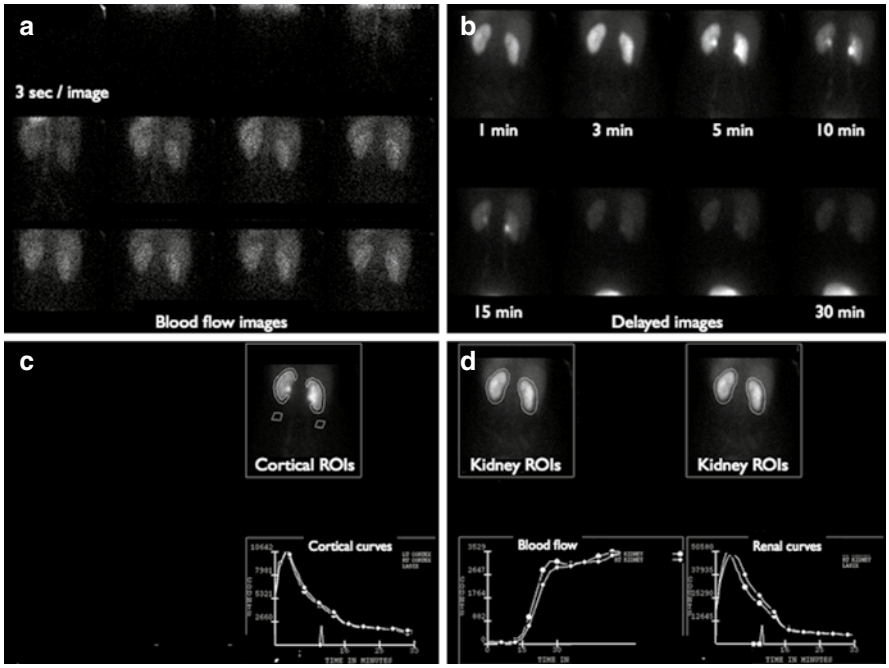

Fig. 7.9 Normal renal tubular secretion study with Tc-99m-MAG3. The *upper left* panel shows the blood flow images. The *upper right* images are the delayed images. The *lower two* panels show the placement of ROIs and the resultant time-activity curves

As explained above the evaluation of parenchymal transit cannot be done in the ideal way of using deconvolution to generate a curve of residue transit times because of the difficulty of measuring the input time-activity curve to the renal parenchymal. However, parenchymal transit times can be evaluated in a fairly robust fashion using visual evaluation of the images and analysis of the cortical time-activity curves.

The visual evaluation of the images relative to transit times begins by checking the first circulation blood flow images (Fig. 7.9a) to determine if there was any problem with the incoming time-activity curve, most commonly because of an extravasated injection. This is done by looking to see how many 3 s images show the aorta; it should be no more than four images or 12 s.

Then the delayed images (Fig. 7.10) are visually compared to a mental image of normal. The leading edge transit time through the renal parenchyma, i.e., the time that activity is first seen in the collecting system, should occur between 3 and 5 min, i.e., the upper collecting systems should appear in the 3 or 5 min image. A delay, beyond 5 min, indicates a prolonged parenchymal transit time and usually acute renal disease, e.g., acute tubular necrosis. The prolonged parenchymal transit time may be caused by parenchymal edema and narrowing of the tubular lumens. Chronic

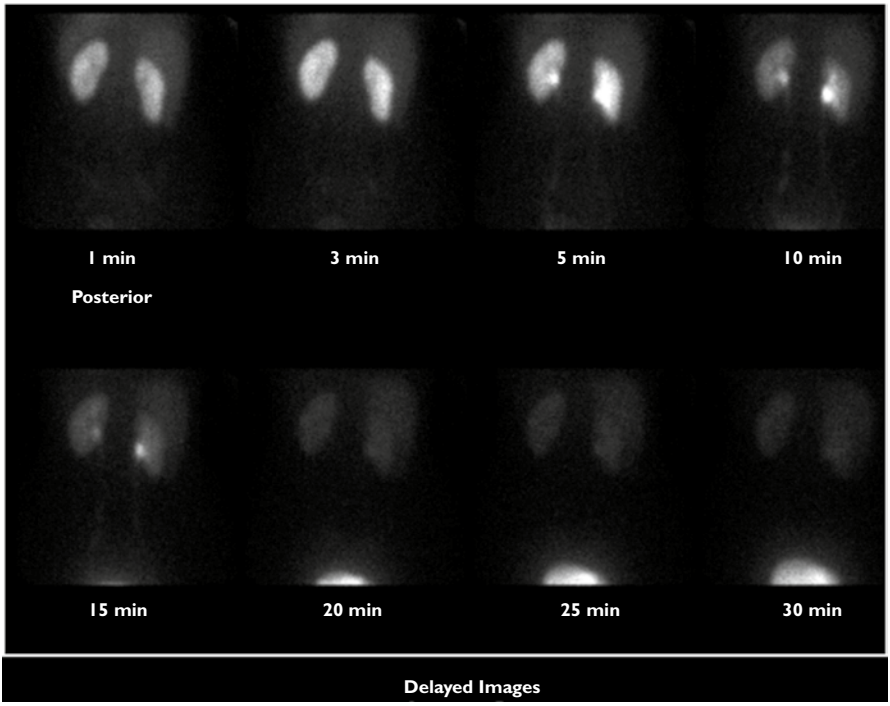

Fig. 7.10 Delayed images from Fig. 7.9. These images are used to determine the leading edge transit time trough the parenchyma. Normally, activity should be seen in the calyces by 5 min

renal disease without an acute component usually does not significantly prolong the parenchymal transit time, e.g., chronic glomerulonephritis.

The cortical time-activity curves provide a more quantitative measure of the leading edge transit time through the parenchyma (Fig. 7.11). The upper limits of normal is 4 min consistent with the criterion that activity should be seen in the collecting system no later than in the 5 min image.

Since the concentration of activity in the blood peaks soon after injection of the radiopharmaceutical and then continuously falls, the activity in the renal tubular lumen will also peak with the initial excreted activity and then gradually fall. Thus, after a time sufficient for the leading edge of activity in the tubular lumen to reach the calyces (leading edge transit time), there will be more activity leaving the parenchyma than entering it (Fig. 7.12).

In addition to the leading edge transit time, there is a second measurement that is useful in evaluating parenchymal transit time, the time following peak activity at which the cortical (parenchymal) time-activity curve reaches a value that is half of the peak value, that is, the half peak time. Normally, the half peak value

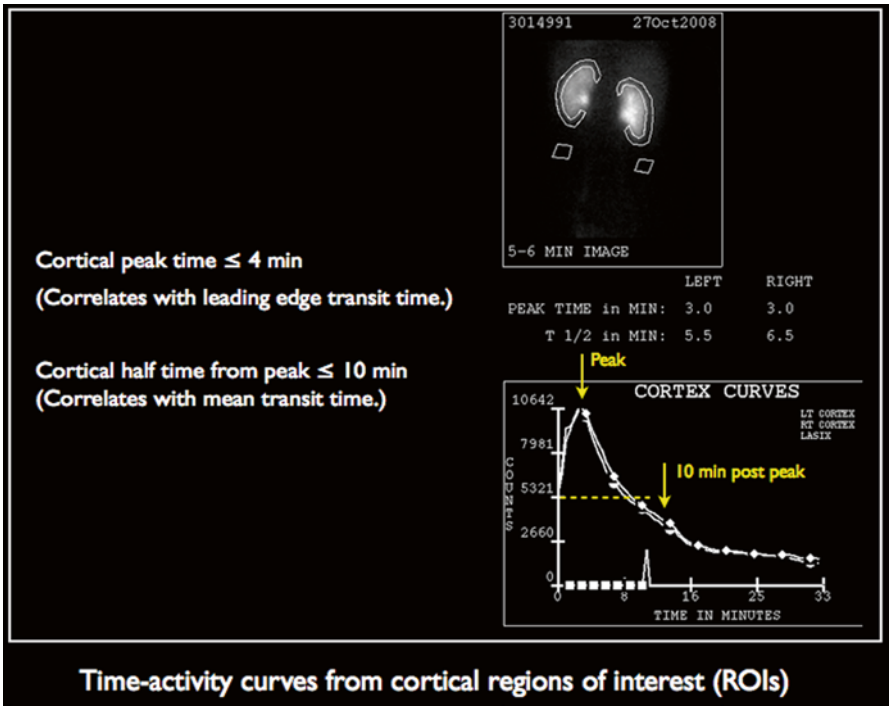

Fig. 7.11 Normal cortical time-activity curves. The peak time of the cortical time-activity curve corresponds to the leading edge transit time. In addition, the peak activity should drop at least in half by 10 min after the peak time

occurs by 10 min from the peak time (Fig. 7.11). This measurement is relatively sensitive to the mean parenchymal transit time. Any prolongation of the half peak time beyond 10 min is another indication of a prolonged parenchymal transit time and of an acute renal parenchymal process such as acute tubular necrosis.

It is not infrequent to have a normal leading transit time, i.e., excretion of activity into the collecting structures by 5 min, but a prolonged half peak time, i.e., half peak time of more than 10 min after the peak. This combination usually results from regional variation of disease and transit times in the kidney. If at least twenty percent of a kidney is normal, the parenchyma will excrete enough radiopharmaceutical with a normal transit time to give a normal leading edge transit time. However, because eighty percent of the kidney has a prolonged transit time, the overall half peak transit time will be prolonged. An example of a disease that typically causes this combination in transit time parameters is acute pyelonephritis. Visual evaluation of the images will show normal tracer washout in some of the renal parenchyma and delayed tracer transit in the rest of the parenchyma.

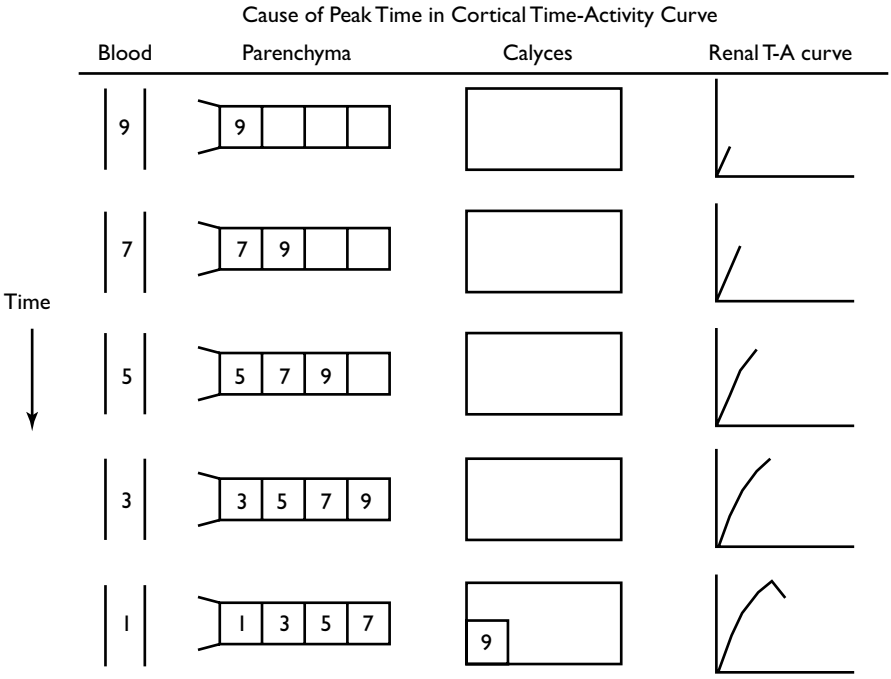

Fig. 7.12 Cause of peak time in cortical time-activity curve. This diagram shows the concentration of tracer in the blood falling after the initial introduction of tracer. This phenomenon causes the concentration of tracer entering the tubular lumen to fall over time as well. Thus, when activity first leaves the tubular lumen and enters the calyces, more activity will leave the parenchyma than enters and the cortical time-activity curve will peak

References

1. Lassen NA, Perl W. Convolution analysis. In: Lassen NA, Perl W, editors. Tracer kinetic methods in medical physiology. New York: Raven Press; 1979.
2. Goris M. Compartmental systems. In: Goris M, editor. Nuclear medicine applications and their mathematical basis. Singapore: World Scientific; 2011. p. 197–205.
3. Klingensmith WC. Physiologic interpretation of time-activity curves from cerebral flow studies: theoretical considerations. J Nucl Med Allied Sci. 1980;24:73–8.

Quantitation of Function: Relative Measurements

8

Introduction

Essentially all diagnostic nuclear medicine studies are made up of a series of images. Interpretation of most of these studies involves visual assessment of the biodistribution of a radiopharmaceutical as depicted in the images without any numeric quantification, e.g., Bone Imaging Study with Tc-99m-MDP. In fact, the eye-brain complex is moderately accurate in estimating the relative amounts of radiopharmaceutical within various structures in images. And visual inspection can identify and compensate for overlap of structures and artifacts better than quantitative results generated from regions of interest (ROIs).

However, in a significant number of diagnostic nuclear medicine procedures, it is useful to quantitate one or more functional parameters such as myocardial perfusion in the Myocardial Perfusion Study with Tc-99m-sestamibi. The quantitative measurement can be in either relative or absolute terms. When the quantitative measurement is in relative terms, either it compares the amount of activity in one area to the amount of activity in another area, often in the same image, or it compares the activity in the same structure in multiple images acquired at different points in time. Table 8.1 lists those studies that typically include quantitative measurements of function in relative terms.

In contrast, a quantitative measurement is in absolute terms when the amount of activity in an area or structure of interest within an image is compared to the amount of activity that was injected. The evaluation may end with the percent uptake in the structure in question, e.g., Thyroid Uptake Measurement with I-123, or the percent uptake may be converted to a physiologic parameter, e.g., renal clearance in terms of effective renal plasma flow (ERPF) in the Renal Tubular Secretion Study with Tc-99m-MAG3. Absolute measurements are discussed in Chap. 9, Quantitation of Function: Absolute Measurements.

Relative quantitative measurements require techniques or strategies that compensate or correct for (1) attenuation of photons that are emitted from the structure

W.C. Klingensmith III, *The Mathematics and Biology of the Biodistribution of Radiopharmaceuticals-A Clinical Perspective*,
DOI 10.1007/978-3-319-26704-3_8

Table 8.1 Nuclear medicine studies that involve the measurement of relative activity

Procedure	Radiopharmaceutical	Functional parameter	Image type	Attenuation correction	Background subtraction
Cardiovascular system					
Cardiac Gated Blood Pool Study	Tc-99m-red blood cells	Ejection fraction	Planar	No	Background ROI
Myocardial Perfusion Study	N-13-ammonia	Myocardial perfusion (clearance)	PET-CT	CT density map	Tomography
Myocardial Perfusion Study	Rb-82 as rubidium chloride	Myocardial perfusion (clearance)	PET-CT	CT density map	Tomography
Myocardial Perfusion Study	Tc-99m-sestamibi	Myocardial perfusion (clearance)	SPECT(-CT)	Comparison to normal range	Tomography
Myocardial Perfusion Study	Tl-201 as thallous chloride	Myocardial perfusion (clearance) Myocardial viability (equilibrium)	SPECT(-CT)	Comparison to normal range	Tomography
Myocardial Viability Study	F-18-FDG	Myocardial viability (clearance)	PET-CT	CT density map	Tomography
Central nervous system					
Ventricular Shunt Study	Tc-99m-DTPA	Washout time	Planar	No	No background activity
Gastrointestinal system					
Esophageal Motility Study	Tc-99m-sulfur colloid	Transit time	Planar	No (?)	No background activity
Gastric Emptying Study	Tc-99m-sulfur colloid	Transit time	Planar	Geometric mean of opposing images	No background activity
Hepatic Artery Perfusion Study	Tc-99m-MAA	Hepatic artery perfusion (clearance)	Planar	Geometric mean of opposing images	No background activity
Hepatobiliary Study	Tc-99m-trimethylbromo-IDA	Gallbladder ejection fraction	Planar	No	Background ROI
Genitourinary system					
Renal Glomerular Filtration Study	Tc-99m-DTPA	Half time of peak cortical activity	Planar	No	Background ROI
Renal Tubular Excretion Study	Tc-99m-MAG3	Half time of peak cortical activity	Planar	No	Background ROI
Renal Tubular Function Study	Tc-99m-DMSA	Clearance	Planar	No	Background ROI

of interest in the direction of the imaging machine or probe but are deflected or absorbed in the intervening tissue and (2) extraneous photons from radioactivity that is outside of the structure of interest but within the field of view of the imaging machine or probe. The issue of limited geometry of the field of view of the imaging machine is not a problem in relative measurements because the field of view is the same in all images. This is also true for factors such as infiltration of an intravenously injected radiopharmaceutical, which will decrease the delivery of tracer to all tissues because the decrease will be the same everywhere and cancel for relative measurements.

Quantitative Measurement of Relative Function: Overview

In Table 8.1 under "Attenuation correction," no explicit attenuation correction is performed in many planar studies in which multiple measurements are made in the same location over time. It is assumed that there is relatively little change in attenuation over time, and since one time point is compared to another, attenuation implicitly cancels. In the case of SPECT images, it is assumed that the tomographic reconstruction is sufficient to minimize the effect of attenuation so that activity in one location can be compared to another location at the same point in time.

In the case of PET-CT, there is relatively accurate attenuation correction inherent in the PET images because both the PET and CT images are tomographic and have essentially uniform spatial resolution across the field of view, and the CT images are density maps that correlate with the spatial distribution of attenuation so that they can be used to correct the PET images for photon attenuation.

The geometric mean method of relative attenuation correction is used for the Gastric Emptying Study and the Hepatic Artery Perfusion Study because the structures of interest vary in their distance to the anterior and posterior body surfaces in a given patient. The mathematic explanation for why the geometric mean corrects for relative attenuation when the activity varies in its distance to the anterior and posterior body surfaces is presented below.

In Table 8.1 under "Background subtraction," it can be seen that those studies that generate tomographic images or in which the radiopharmaceutical is confined to the structure of interest, e.g., Ventricular Shunt Study and Gastric Emptying Study, no background subtraction is needed. This leaves the Cardiac Gated Blood Pool Study with Tc-99m-RBCs, the Hepatobiliary Study with Tc-99m-trimethylbromo-IDA, and the three renal studies as studies that benefit from background subtraction. The formula for performing background subtraction is discussed below.

The issue of detection geometry varies among imaging modalities and studies, but since it is the same within a study for all images and since the measurements are all relative, the effect of detection geometry occurs in both the numerator and denominator and cancels. Therefore, no adjustment needs to be made to compensate for suboptimal detection geometries in relative quantification.

Quantitative Measurement of Relative Function: Attenuation Correction

Uniform Attenuation The equation for attenuation of a beam of photons passing through tissue is

$$A(\text{cps}) = A_0(\text{cps})e^{\mu x} \tag{8.1}$$

where A is the detected activity or intensity of photons in terms of counts per second, A_0 is the original activity in terms of counts per second, μ is the linear attenuation coefficient with units of 1/cm, x is the length of tissue that the photons pass through in centimeters, and e is the natural log. The parameter μ varies with the density of the tissue and the energy of the photons.

Figure 8.1 shows a diagram of a cross section of the abdomen at the level of the kidneys with a gamma camera positioned posteriorly. The broken lines indicate the tissue that photons that originate in the kidneys need to pass through on their way to the gamma camera. There will also be some attenuation of photons by renal tissue, self-absorption. In the three renal studies, the anatomy of the kidneys and the thickness and density of the tissue between the kidneys and gamma camera are assumed to be quite symmetrical. (*A* somewhat more refined approach is used when correcting renal counts in the Renal Tubular Secretion Study with Tc-99m-MAG3 in order to determine the absolute clearance as effective renal plasma flow (ERPF)) Thus, for relative measurements, e.g., left and right, the number of counts recorded from ROIs placed over the right and left kidneys can be compared by dividing one by the other:

$$\frac{A_{\text{L}}(\text{cps})}{A_{\text{R}}(\text{cps})} = \frac{A_{0\text{L}}e^{-\mu x}(\text{cps})}{A_{0\text{R}}e^{-\mu x}(\text{cps})} \tag{8.2}$$

The factors relating to attenuation, i.e., the density of the tissue and the length of the pathway through the tissue will be essentially the same on the two sides and cancel:

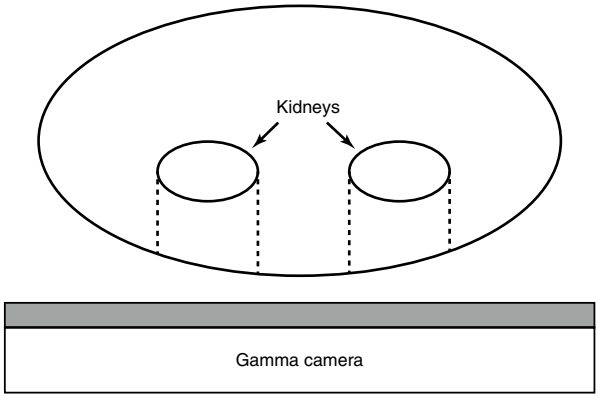

Fig. 8.1 Diagram of abdominal cross section through the kidneys. There is a single gamma camera (collimator in *gray*) posterior to the patient. The *broken lines* enclose tissue that will attenuate gamma rays that originate from renal activity. There will also be some attenuation of gamma rays by the renal tissue itself (self-absorption)

$$\frac{A_{\mathrm{L}}\,(\mathrm{cps})}{A_{\mathrm{R}}\,(\mathrm{cps})} = \frac{A_{0\mathrm{L}}\,(\mathrm{cps})}{A_{0\mathrm{R}}\,(\mathrm{cps})} \tag{8.3}$$

Thus, the ratio of counts in the ROIs over the left and right kidneys in the images will reflect the ratio of the actual amount of radiopharmaceutical in the left and right kidneys.

Use of the Geometric Mean In studies like the Gastric Emptying Study with Tc-99m-sulfur colloid-labeled oatmeal, multiple images are acquired over time as the radiopharmaceutical passes through the stomach. However, the successive components of the stomach, fundus, body, and antrum, are at different distances from the anterior and posterior skin surfaces (Fig. 8.2).

The arrows indicate the movement of radiopharmaceutical from the posterior fundus to the more anteriorly placed body and then to the anteriorly placed antrum. These three tomograms of the stomach would normally be in three different images from cephalad to caudad levels in the abdomen.

Thus, for the number of counts in different portions of the stomach to be comparable in either the anterior or posterior image alone, there needs to be a form of attenuation correction that takes into account the varying distance of the stomach components from the posterior and anterior skin surfaces. This is not possible without knowing the distance of the various stomach components to the skin. However, by acquiring simultaneous anterior and posterior images over time, identical ROIs

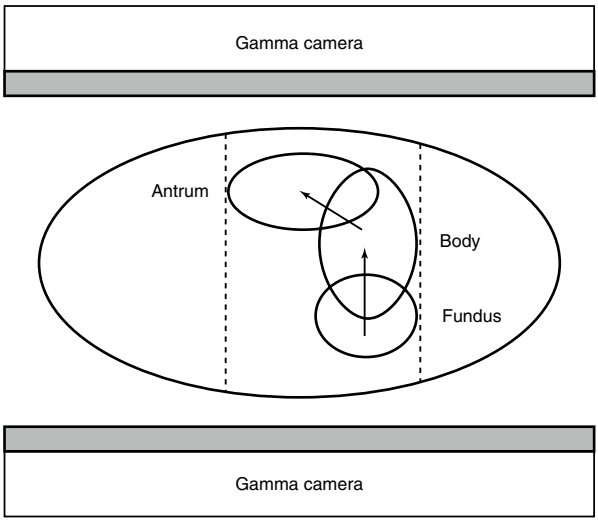

Fig. 8.2 Dual-headed gamma camera. Dual opposed gamma cameras are positioned anterior and posterior to the upper abdomen in a Gastric Emptying Study. Three images through the fundus, body, and antrum are superimposed to demonstrate that the position of a test meal varies in the anteroposterior direction as it passes through the stomach. Quantitating the data with the geometric mean approach compensates for this variable

can be placed over the stomach in both the anterior and posterior images, the counts can be measured at multiple time points, and then the geometric mean can be calculated for each time point.

The geometric mean, in general, is the *n*th root of the product of *n* numbers. In the case of anterior and posterior images, it is the second (square) root of the anterior and posterior ROI counts multiplied together. If the total distance from anterior skin to posterior skin is taken to be *d* and the distance from the anterior skin to the stomach lumen is *x* then the distance from the posterior skin to the stomach lumen will be $d-x$, giving,

$$A_{\mathrm{GM}}\left(\mathrm{cts}\right)=\left[A_0e^{-\mu x}\left(\mathrm{cts}\right)\ A_0e^{-\mu(d-x)}\left(\mathrm{cts}\right)\right]^{1/2} \tag{8.4}$$

where A_{GM} is the geometric mean of the activity in the stomach as determined from the anterior and posterior images, A_0 (cts) $e^{-\mu x}$ is the counts recorded from the anterior gastric region of interest, and A_0 (cts) $e^{-\mu(I-x)}$ is the counts recorded from the posterior region of interest. The right-hand side of Eq. 8.4 can be simplified,

$$\left[A_0\ e^{-\mu x}\left(\mathrm{cts}\right)\ A_0\ e^{-\mu(d-x)}\left(\mathrm{cts}\right)\right]^{1/2}=\left[A_0^2\ e^{-\mu d}\right]^{1/2}\left(\mathrm{cts}\right)=A_0e^{-\mu d/2}\left(\mathrm{cts}\right) \tag{8.5}$$

Notice that the distances from the anterior and posterior skin surfaces in the exponents add to *d* and, therefore, do not affect the result. Thus, the geometric mean is independent of the location of the activity in the anteroposterior dimension.

We can then make a relative comparison of the activity remaining in the stomach at any subsequent time compared to the initial activity in the stomach with additional simplification of the equation (the different times are indicated by subscripts "1" and "2"),

$$\frac{A_{\mathrm{GM2}}\left(\mathrm{cts}\right)}{A_{\mathrm{GM1}}\left(\mathrm{cts}\right)}=\frac{A_{02}e^{-\mu d/2}\left(\mathrm{cts}\right)}{A_{01}e^{-\mu d/2}\left(\mathrm{cts}\right)}=\frac{A_{02}\left(\mathrm{cts}\right)}{A_{01}\left(\mathrm{cts}\right)} \tag{8.6}$$

Normal criteria can then be established for the fraction or percent of the initial meal remaining in the stomach at one or more times after ingestion of the meal [1, 2]. As an example, a worksheet for calculating the time-activity curve for gastric emptying is included at the end of this chapter.

Comparison to a Normal Range Another method of dealing with attenuation is to perform no attenuation correction (planar images) or incomplete attenuation correction (SPECT) and to instead compare the quantitative data to a normal range that accounts for variable, but relatively reproducible, attenuation as a function of location. An example of this approach is the evaluation of myocardial perfusion with single-photon radiopharmaceuticals, e.g., Myocardial Perfusion Study with T-99m-sestamibi [3]. The apparent distribution of myocardial perfusion in the images of the left ventricle is a function of normal variation, e.g., decreased myocardium in the apex, and attenuation from differing amounts and densities of tissue between myocardium and the gamma camera. Attenuation also varies with gender, e.g., breast attenuation, so that breast size must be taken into account for females.

Quantitative Measurement of Relative Function: Background Correction

The issue of activity outside of the organ of interest contributing counts to the ROI placed over the organ of interest falls into three categories: (1) no activity outside of the organ of interest, (2) planar imaging with activity behind and in front of the organ of interest, and (3) tomography (SPECT or PET) (Table 8.1).

If the radiopharmaceutical is confined to the organ or structure of interest, e.g., Gastric Emptying Study with Tc-99m-sulfur colloid oatmeal, then there is essentially no activity in other structures and no need for background correction. Four studies in Table 8.1 fall into this category. However, if there is a significant amount of activity in the tissues around the organ of interest and planar imaging is used, then there will be unwanted counts in the ROI, e.g., Renal Tubular Secretion Study with Tc-99m-MAG3 (Fig. 8.3). Five studies in Table 8.1 are in this category.

Typically, correction for background counts is performed by placing a so-called "background" ROI, ~*B*, adjacent to the organ of interest, *K*, in a location that is expected to contain an amount of activity that is similar to the amount anterior and posterior to the organ of interest, region *B* (Fig. 8.4).

Then the average counts per pixel in the background ROI are subtracted from each of the pixels in the ROI over the organ in question.

$$K_{\mathrm{C}}(\mathrm{cts}) = \left[\left(K(\mathrm{cts}) + B(\mathrm{cts})\right) / P_{\mathrm{K}}(\mathrm{px}) - {\sim}B(\mathrm{cts}) / P_{{\sim}\mathrm{B}}(\mathrm{px})\right] P_{\mathrm{K}}(\mathrm{px}) \quad (8.7)$$

Here K_{C} is background corrected counts from a kidney ROI; $K+B$ is the number of counts in the kidney ROI, kidney + background; P_{K} is the number of pixels (px) in the kidney ROI; and $P_{\sim\mathrm{B}}$ is the number of pixels in the background ROI.

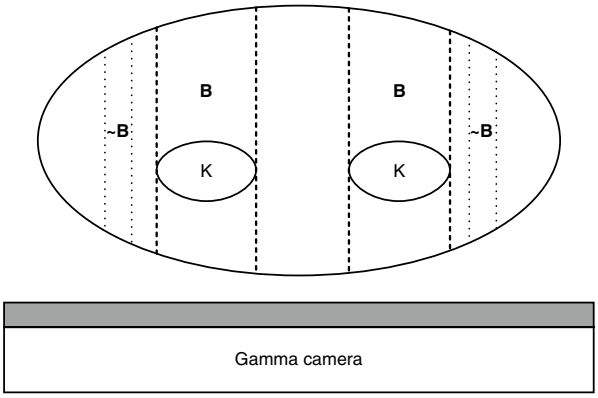

Fig. 8.3 Diagram of an abdominal cross section through the kidneys. There is a single gamma camera (collimator in *gray*) posterior to the patient. The *broken lines* enclose extrarenal tissue, *B*, that is included in the renal ROI and will contribute unwanted counts to the measurement of activity in the kidneys, *K*. An imprecise correction for background activity can be made by measuring the counts in a ROI, ~*B*, that is placed over tissue that contains approximately the same amount of activity as the background tissue anterior and posterior to the organ of interest

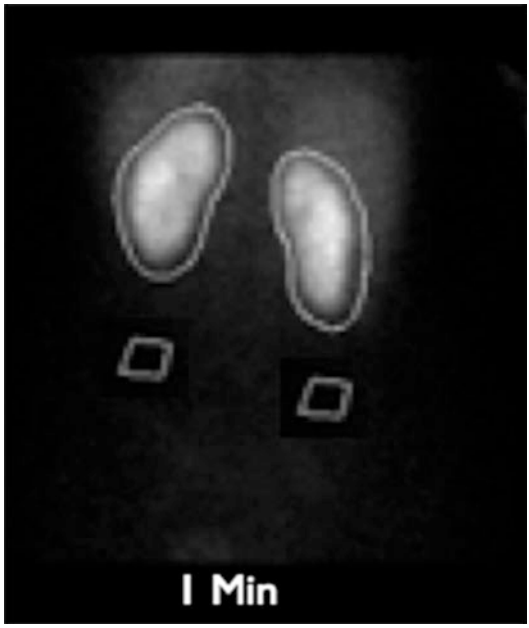

Fig. 8.4 Posterior planar 1 min image from a renal tubular secretion study. The image shows ROIs placed around the kidneys and just below the kidneys for use in background subtraction

In addition, there are another five studies in Table 8.1 in which there is activity outside of the organ of interest, but imaging is done tomographically with either SPECT-CT or PET-CT, which essentially eliminates the issue of activity outside of the organ of interest contributing counts to the ROI of the organ of interest. Over time as more and more nuclear medicine studies are performed with tomography, particularly PET-CT, fewer studies will need post image processing correction for background activity.

Quantitative Measurement of Relative Function: Relative Clearance of Two Kidneys

In the Renal Tubular Secretion Study (Tc-99m-MAG3) and Renal Glomerular Filtration Study (Tc-99m-DTPA), renal clearance is quantitated in both absolute and relative terms. For the relative quantitative measurement, the clearance of each kidney is compared to the total. First, the counts in the renal ROIs for each kidney are corrected for background activity as discussed above. Then, the percent of total renal clearance in each kidney can be calculated from the simple equation,

$$\mathrm{RK}_{\mathrm{Cl}}(\%) = \frac{\mathrm{RK}(\mathrm{cpm})}{\mathrm{RK}(\mathrm{cpm}) + \mathrm{LK}(\mathrm{cpm})} \times 100(\%) \tag{8.8}$$

where $\mathrm{RK}_{\mathrm{Cl}}$ (%) is the percent clearance of the right kidney and RK (cpm) and LK (cpm) are background corrected counts per minute for the right and left kidneys. The percent clearance of the left kidney is calculated in the same fashion.

Note that the clearance of each kidney is related to the total clearance of both kidneys in percent terms and that the clearance or uptake of tracer in the kidneys at a given time is not related to the amount of tracer administered and, therefore, is not in absolute terms and cannot be expressed in standard units of milliliters per minute (mL/min).

Gastric Emptying Worksheet

GASTRIC EMPTYING WORKSHEET

Nuclear Medicine Department

Institution_____

Name_____ ID_____ Age_____ Sex_____

Referring physician_____ Date_____

TECHNOLOGIST TO COMPLETE

Is the patient a diabetic? Yes___ No___

Has the patient had any gastrointestinal surgery? Yes___ No___

If so, describe _____

Does the patient take any medications to stimulate gastric emptying? Yes___ No___

If so, which _____

NOTE: Many nuclear medicine computers have software that performs one or more of the steps below automatically.

IMAGE ANALYSIS

STEP 1 Determine cpm/gastric ROI in all images and correct for radioactive decay:

Time to begin imaging	Time post ingestion	cpm/gastric ROI	Decay correction factor	Corrected cpm/ gastric ROI
_____	0 min ANT	_____	1.00	_____
	0 min POST	_____	1.00	_____
_____	15 min ANT	_____	1.03	_____
	15 min POST	_____	1.03	_____
_____	30 min ANT	_____	1.06	_____
	30 min POST	_____	1.06	_____
_____	45 min ANT	_____	1.09	_____
	45 min POST	_____	1.09	_____
_____	60 min ANT	_____	1.12	_____
	60 min POST	_____	1.12	_____

STEP 2 Correct for attenuation:

Time	ANT Corrected cpm/ gastric ROI		POST Corrected cpm/ gastric ROI		Product		Square root
0 min	_____	x	_____	=	_____	√	_____
15 min	_____	x	_____	=	_____	√	_____
30 min	_____	x	_____	=	_____	√	_____
45 min	_____	x	_____	=	_____	√	_____
60 min	_____	x	_____	=	_____	√	_____

STEP 3 Plot the square root results on the Gastric Emptying Study graph.

STEP 4 Compare the half time of gastric emptying to the normal range for age (same values for males & females) [1].

Age	Normal range	Reproducibility
20-40 yr	10-60 min	≤ 30 min
40-60 yr	10-40 min	≤ 20 min
60-80 yr	10-30 min	≤ 15 min

Technologist _____

References

1. Klingensmith WC, Rhea KL, Wainwright EA, et al. The gastric emptying study with oatmeal: normal range and reproducibility as a function of age and sex. J Nucl Med Technol. 2010;38:186–90.
2. Abell TL, Camilleri M, Donohoe K, et al. Consensus recommendations for gastric emptying scintigraphy:a joint report of the American Neurogastroenterology and Motility Society and the Society of Nuclear Medicine. Am J Gastroenterol. 2008;103:753–63; J Nucl Med Technol. 2008;36:44–54.
3. Widding A, Hesse B, Gadsboll N. Technetium-99m sestamibi and tetrofosmin myocardial single-photon emission tomography: can we use the same reference data base? Eur J Nucl Med. 1997;24:42–5.

Quantitation of Function: Absolute Measurements

9

Introduction

Essentially all diagnostic nuclear medicine studies are made up of a series of images. Interpretation of most of these studies involves visual assessment of the biodistribution of a radiopharmaceutical as depicted in the images without any numeric quantification. However, in a significant number of diagnostic nuclear medicine studies, it is useful to quantitate one or more functional parameters. These quantitative measurements can be in either relative or absolute terms.

Unlike measurements that are calculated in relative terms, i.e., as ratios between regions of interest (ROIs) in one or more images, measurements that are calculated in absolute terms are ratios between a region of interest in a single image and the total amount of radiopharmaceutical that is injected intravenously or occasionally swallowed. The measurement of activity in the structure of interest goes in the numerator and the measurement of the amount of administered radiopharmaceutical goes in the denominator. Thus, absolute measurements are absolute in the sense that they are directly related to the total amount of administered radiopharmaceutical, which is known in absolute terms.

Quantitative Measurement of Absolute Function: Overview

Table 9.1 lists the four nuclear medicine studies that include an absolute quantitative measurement along with the corresponding biologic parameter. When the quantitative measurement is in absolute terms, the initial calculation is the amount of radiopharmaceutical in the structure of interest compared to the total amount of radiopharmaceutical administered, i.e., the dose. The result may be expressed as simply percent uptake, e.g., Thyroid Uptake Measurement with I-123, or as percent

W.C. Klingensmith III, *The Mathematics and Biology of the Biodistribution of Radiopharmaceuticals-A Clinical Perspective*,
DOI 10.1007/978-3-319-26704-3_9

Table 9.1 Studies that measure absolute activity - biologic parameters

Procedure	Radiopharmaceutical	Initial calculation	Related biologic parameter	Biologic parameter quantitated	Extraction mechanism saturable
Endocrine system					
Thyroid Uptake Measurement	I-123	Percent thyroid uptake	Thyroid hormone synthesis (mole/min)	No	Yes
Genitourinary system					
Renal Glomerular Filtration Study	Tc-99m-DTPA	Percent renal uptake	Renal clearance by glomerular filtration (mL/min)	Yes	No
Renal Tubular Excretion Study	Tc-99m-MAG3	Percent renal uptake	Renal clearance by tubular excretion (mL/min)	Yes	No
Tumor imaging					
Tumor Glucose Metabolism Study	F-18-FDG	Percent uptake per voxel	Glucose metabolic rate (mole/min)	No	Yes

uptake which is secondarily converted to a biologic or physiologic parameter such as renal clearance, e.g., Renal Glomerular Filtration Study with Tc-99m-DTPA and Renal Tubular Secretion Study with Tc-99m-MAG3, or as percent uptake per voxel normalized for body weight to give a standard uptake value (SUV), e.g., Tumor Glucose Metabolism Study with FDG. Only the two renal clearance measurements are converted into physiologic terms (Table 9.1).

Both relative and absolute quantitative measurements require techniques or strategies that compensate or correct for (1) attenuation of photons that are emitted from the structure of interest in the direction of the imaging machine or probe but are deflected or absorbed in the intervening tissue and (2) extraneous photons from radioactivity that is outside of the structure of interest but within the field of view of the imaging machine or probe (Table 9.2). In addition, in absolute measurements either the administered dose, initially in millicuries, needs to be converted to counts per minutes or the measurement of activity in the structure of interest in the image, initially in counts per minute, must be converted to millicuries. There are also numerous factors, predominantly biologic, that can affect the degree of localization/uptake/clearance of the radiopharmaceutical in the structure of interest after a given amount of time after administration that are most important when quantitation is in absolute terms.

Table 9.2 Studies that measure absolute activity - technical parameters

Procedure	Radiopharmaceutical	Functional parameter	Image type	Attenuation correction	Background subtraction	Field of view
Endocrine system						
Thyroid Uptake Measurement	I-123	Thyroid uptake (clearance)	Probe	Neck phantom	Similar shaped structure without thyroid: thigh	Measure dose in phantom with probe
Genitourinary system						
Renal Glomerular Filtration Study	Tc-99m-DTPA	Glomerular filtration (clearance)	Planar	Estimated from height, weight, and age	Background ROI	Measure dose with gamma camera and collimator
Renal Tubular Excretion Study	Tc-99m-MAG3	Tubular excretion (clearance)	Planar	Estimated from height, weight, and age	Background ROI	Measure dose with gamma camera and collimator
Tumor imaging						
Tumor Glucose Metabolism Study	F-18-FDG	Glucose metabolism (clearance)	PET-CT	CT density map	Tomography	PET-CT scanner calibrated

Quantitative Measurement of Absolute Function: Thyroid Uptake Measurement

First, we will address determining the denominator of the thyroid uptake ratio. The Thyroid Uptake Measurement is the only nuclear medicine study in which a phantom is used to simulate the part of the body to be imaged or assessed, in this case the neck (Fig. 9.1).

The I-123 dose that the patient will swallow is placed in a hole in the phantom. The hole is positioned to mimic the position of the thyroid within the patient's neck. The photons emanating from the phantom are recorded with the same open face scintillation probe that is used to evaluate the patient's thyroid and with the same detection geometry. This measurement, after subtracting the negligible air background activity, converts the amount of activity in the I-123 capsule, in millicuries, into counts per minute that have undergone attenuation similar to what will happen in the patient's neck. In addition, the detection geometry of the probe and the phantom mimics the patient situation. The result is placed in the denominator of the thyroid uptake calculation.

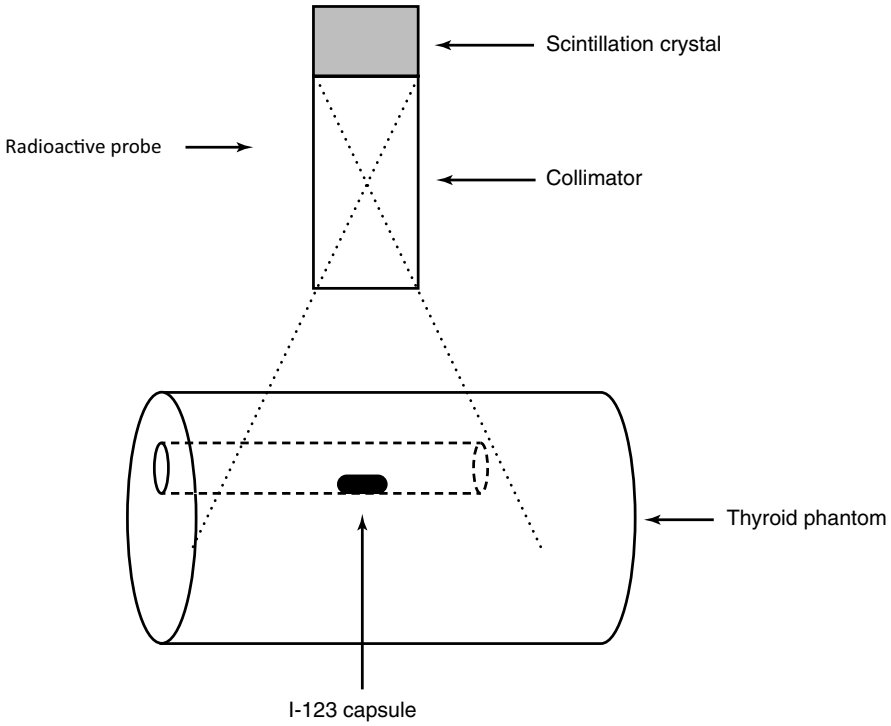

Fig. 9.1 Thyroid phantom with I-123 capsule. The lucite thyroid phantom simulates the size, shape, and density of the patient's neck. The I-123 capsule is placed in a hole that is positioned to simulate the position of the thyroid within the neck. The thyroid probe is positioned above the phantom at a distance that will be reproduced when measuring the activity in the patient's neck and thigh

Now, we will address determining the numerator of the thyroid uptake ratio. Two readings are made of the patient with the thyroid probe, one of the neck and one of the thigh, and both are acquired in the anterior projection with the same distance between the probe and the neck or thigh as was used to measure the I-123 capsule in the thyroid phantom. If the photons emanating from the patient's neck were being recorded as an image, a ROI could be placed adjacent to the thyroid for background correction. However, since no image is generated, only a number, another method must be used. By tradition a measurement of photons emanating from the thigh is used as an estimate of background activity since the thigh in most patients is roughly the thickness of the neck. The background corrected thyroid counts per minute, after accounting for the decay of I-123 between the phantom and patient measurements, are placed in the numerator. We now have

$$\text{Thyroid uptake}(\%) = \frac{\text{Thyroid}(\text{cpm}) - \text{Thigh}(\text{cpm})}{\text{Phantom}(\text{cpm}) - \text{Air}(\text{cpm})} \times 100\ \% \qquad (9.1)$$

An example of a worksheet for calculating the percent thyroid uptake is included at the end of this chapter.

Quantitative Measurement of Absolute Function: Renal Clearance Studies

In the following discussion, it is important to keep in mind that the word "clearance" can be used in two ways. First, clearance can refer to the standard physiologic definition of clearance, which is expressed as milliliters of blood completely cleared of a substance on a per minute basis (mL/min), i.e., a rate. Second, it can refer to the process of moving a substance or tracer from blood into an organ or tissue. In this context, the longer the time interval from intravenous injection to acquisition of an image, the greater will be the amount of tracer transferred (cleared) from blood into an organ or tissue, i.e., a rate times an amount of time. The units here are millicuries, usually expressed as millicuries per organ or tissue at a particular time (mCi/organ at a specified time). The mathematical relationship between the traditional equation for clearance and equation for an amount of tracer cleared in a given time is discussed in Chap. 4, Evaluation of Clearance. Also, the terms "uptake" and "localization" are often used to mean "clearance" in the second sense.

There are two renal studies in Table 9.1 that measure clearance in absolute terms: the Renal Tubular Secretion Study with Tc-99m-MAG3 and the Renal Glomerular Filtration with Tc-99m-DTPA. The same approach is used in both studies: (1) convert the dose to be administered, initially in millicuries, to counts per minute, (2) account for attenuation and background activity, and (3) maintain a consistent field of view. Once the percent uptake of the administered dose in the two kidneys at a certain point in time is determined, an additional step is required to convert the percent uptake to clearance in terms of milliliters per minute. Thus, the percent uptake is multiplied by an appropriate conversion factor with units of milliliter per minute

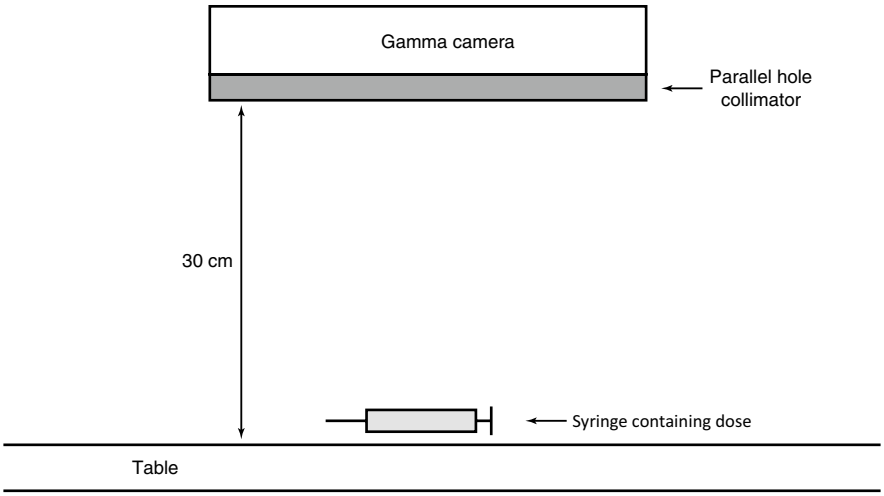

Fig. 9.2 Imaging the syringe containing the dose of Tc-99m-MAG3. Imaging the dose of Tc-99m-MAG3 in the syringe before it is administered to the patient converts the dose from activity measured in mCi to counts per minute. The 30 cm distance between the syringe and gamma camera prevents dead time in the electronic circuits of the gamma camera

divided by percent, mL/min-%, to give renal clearance as a function of either tubular secretion or glomerular filtration in units of mL/min. In the discussion below tubular secretion will be used as the example.

First, we will address determining the denominator of the renal uptake ratio by converting the radiopharmaceutical dose in millicuries into a measure of the dose in counts per minute using the same equipment and geometry that is used for imaging the patient. The syringe containing the dose "*D* (mCi)" is placed 30 cm from the front of a gamma camera fitted with the same low-energy high-resolution collimator that will be used to image the patient (Fig. 9.2).

Following injection of the dose into the patient, the residual tracer in the syringe, "*R* (cpm)," is measured in the same manner and subtracted from the initial whole dose measurement to obtain the net amount of tracer injected into the patient, "Inj (cts)."

$$\mathrm{Inj}(\mathrm{cpm}) = D(\mathrm{cpm}) - R(\mathrm{cpm}) \tag{9.2}$$

This result is placed in the denominator of the percent renal uptake equation.

Now, we will address determining the numerator of the renal uptake ratio. The goal is to measure renal clearance from blood into the kidneys by way of tubular secretion. However, the cleared tracer does not stay in the kidneys but passes through the renal parenchyma and exits the kidneys by flowing with the tubular filtrate into the calyces. At this point, the tracer moves passively with the urine through the collecting systems and ultimately accumulates in the bladder.

The renal study consists of a series of images over time that initially predominantly reflect blood flow into the kidneys, then clearance into the kidneys, and then

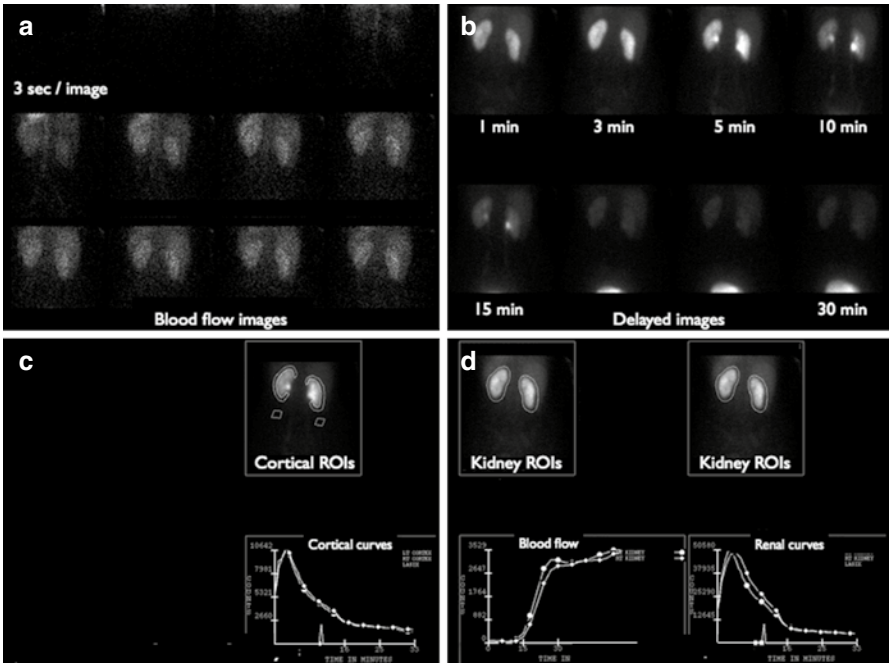

Fig. 9.3 Normal renal tubular secretion study with Tc-99m-MAG3. (**a**) Blood flow images, (**b**) delayed images, (**c**) cortical ROI quantification, and (**d**) renal ROI quantification

transit time through the renal parenchyma, and, finally, flow down the collecting system into the bladder. The image selected for the measurement of clearance is the one that predominantly shows clearance with relatively little activity in blood and no activity in the upper collecting system. This image is usually one acquired between 1 and 3 min after the injection of the radiopharmaceutical, most commonly the 1–2 min image. The activity in the kidneys is measured in terms of counts per minute by placing ROIs over the entire kidneys (Fig. 9.3).

Typically, correction for background counts is performed by placing a so-called "background" region of interest, ~*B*, adjacent to the organ of interest, *K*, in a location that is expected to contain an amount of activity that is similar to the amount anterior and posterior to the organ of interest, region ~*B* (Fig. 9.4).

Then the average counts per pixel in the background region of interest are subtracted from each of the pixels in the region of interest over the organ in question.

$$K_{\mathrm{C}}\left(\mathrm{cts}\right)=\left[\left(K\ \left(\mathrm{cts}\right)+B\ \left(\mathrm{cts}\right)\right)/P_{\mathrm{k}}\left(\mathrm{px}\right)-\sim B\left(\mathrm{cts}\right)/P_{\sim \mathrm{B}}\left(\mathrm{px}\right)\right]P_{\mathrm{K}}\left(\mathrm{px}\right) \quad (9.3)$$

Here K_{C} is background corrected counts from a kidney ROI; $K + B$ is the number of counts in the kidney ROI, kidney + background; P_{K} is the number of pixels (px) in the kidney ROI; and $P_{\sim \mathrm{B}}$ is the number of pixels in the background ROI.

We must also correct for attenuation. However, with planar imaging, we cannot directly measure the distance between the mid-portion of the kidneys and the

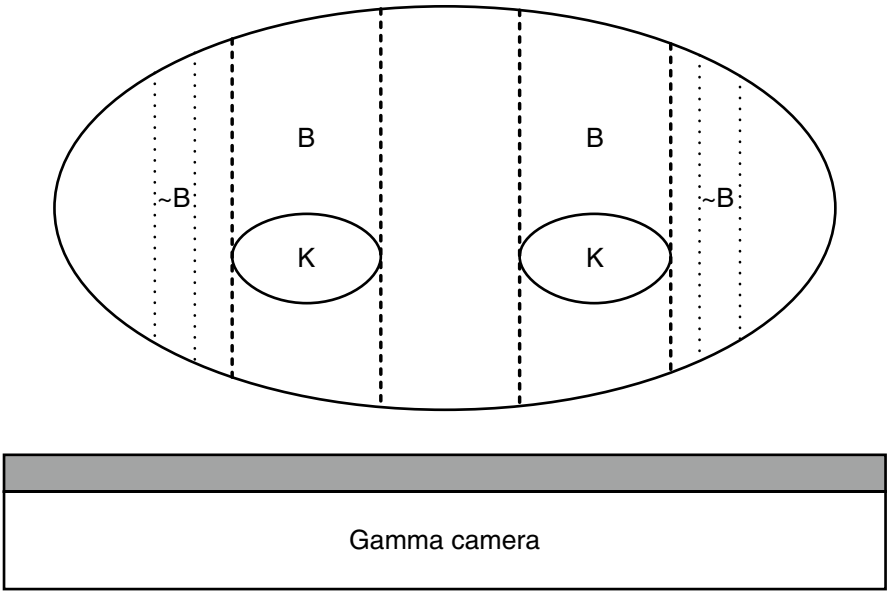

Fig. 9.4 Diagram of an abdominal cross section through the kidneys. There is a single gamma camera (*collimator in gray*) posterior to the patient. The broken lines enclose extrarenal tissue, *B*, that is included in the renal region of interest and will contribute unwanted counts to the measurement of activity in the kidneys, *K*. An imprecise correction for background activity can be made by measuring the counts in a region of interest, ~*B*, that is placed over tissue that contains approximately the same amount of activity as the background tissue anterior and posterior to the organ of interest

posterior surface of the skin. Empiric equations based on CT images of the abdomen have been developed that estimate the kidney to posterior skin distance for both the left and right kidneys based on the patient's age, weight, and height [1].

$$RK_{\mathrm{D}}\left(\mathrm{mm}\right)=\left[151.3\times W\ \left(\mathrm{kg}\right)\div H\ \left(\mathrm{cm}\right)\right]+0.22\ \ \mathrm{Age}\ \left(\mathrm{yr}\right)+0.77 \tag{9.4}$$

$$LK_{\mathrm{D}}\left(\mathrm{mm}\right)=\left[161.7\times W\ \left(\mathrm{kg}\right)\div H\ \left(\mathrm{cm}\right)\right]+0.27\ \ \mathrm{Age}\ \left(\mathrm{yr}\right)+0.70 \tag{9.5}$$

Here RK_D and LK_D are the mid-kidney to posterior skin depth of the right and left kidneys, respectively, while W and H stand for the patient's weight and height, respectively. Kidney depth is then inserted into the expression for determining attenuation of photons passing through a medium of given density $e^{-\mu x}$, where μ is the linear attenuation coefficient with units of 1/cm, x is the length of tissue that the photons pass through in centimeters (either RK_D or LK_D), and e is the natural log. The parameter μ varies with the density of the tissue and the energy of the photons.

We can now calculate the percent uptake for each kidney:

$$\mathrm{Kidney\ \ uptake}\left(\%\right)=\frac{K_{\mathrm{C}}\left(\mathrm{cpm}\right)\div e^{-\mu x}}{D\left(\mathrm{cpm}\right)}\times 100\ \ \% \tag{9.6}$$

Next the percent uptakes of the two kidneys are added together,

$$\text{Total kidney uptake}\ (\%) = \text{RK}_{\text{U}}(\%) + \text{LK}_{\text{U}}(\%) \tag{9.7}$$

Finally, the "Total kidney uptake" is multiplied by a conversion factor, J (mL/min–%), that converts the percent of injected dose cleared into the kidneys as demonstrated in the 1–2 min image to renal clearance in terms of the traditional effective renal plasma flow (ERPF) with units of milliliters per minute,

$$ERPF\,(\text{mL/min}) = \text{Total kidney uptake}\ (\%) \times J\ (\text{mL/min}-\%) \tag{9.8}$$

The ERPF result is compared to a normal range. No correction for body surface area (BSA) is needed as correction for body surface area is inherent in measuring renal clearance with an intravenously injected tracer [2] (see Chap. 10, Other Quantitative Techniques).

Quantitative Measurement of Absolute Function: Tumor Glucose Metabolism Study

The Tumor Glucose Metabolism Study with FDG is used to detect cancer throughout the body and to follow its response to therapy. Tumors are initially identified visually, but then the amount of FDG uptake or glucose clearance in one or more tumors is usually evaluated. Quantification of glucose metabolism is useful in determining whether a tumor is progressing or regressing in serial studies.

Cancers can occur essentially anywhere in the body. Frequently the boundaries of the tumor are not well defined and the tumors may have necrotic centers, which will not exhibit glucose metabolism. For these reasons, it is often not possible to draw a region of interest around a tumor or to exclude non-metabolically active portions of a tumor. The practical solution is to place a ROI around the structure that is felt to be cancer and evaluate its glucose metabolic activity based on the pixel within the ROI with the greatest amount of activity.

The most common method of quantitating glucose metabolism with FDG in images is to express the amount of FDG in each pixel of a PET image in terms of the standard uptake value (SUV). The SUV is defined as

$$\text{SUV} = \frac{\text{FDG in tissue}\ (\text{mCi/mL}) \times (\text{mL/gm})}{\text{Activity injected}\ (\text{mCi}) / \text{Body weight}\ (\text{gm})} \tag{9.9}$$

Note that the units in the numerator and denominator cancel so the SUV parameter is unitless. This outcome is dependent on the assumption expressed in the numerator that one milliliter of the patient's body volume will equal one milligram of weight, an assumption that frequently does not hold. Consider the variation in weight among a milliliter of expanded lung, muscle, and bone cortex. Also note that if the injected activity were uniformly distributed throughout the body by volume with no excretion, the SUV would be one everywhere in the body. However, the amount of uptake or clearance of FDG into tissues normally varies in a relatively

consistent fashion from one organ to another so that even in a normal subject the SUV varies from one organ to another [3, 4].

The equation for SUV appears simple and, in fact, the denominator is. The first factor in the denominator expands to give

$$\text{Activity injected}\ \left(\text{mCi}\right) = D_{\text{S}}\left(\text{mCi}\right) - D_{\text{R}}\left(\text{mCi}\right) \tag{9.10}$$

Here the initial total dose, D_{S}, and the residual activity in the syringe, D_{R}, are both measured in a dosimeter in units of millicuries, and, therefore, the net amount of radiopharmaceutical injected, activity injected, is also in units of mCi.

However, the numerator is more complex than it looks. The images, acquired at 1 h after injection, reflect clearance of FDG and, therefore, glucose into tissues. Thus, we can replace the numerator in Eq. 9.9 with the relative nuclear medicine equation for clearance (see Chap. 4, Evaluation of Clearance),

$$A\left(\text{mCi/gm}\right) = F\left(\text{mL/min-gm}\right) \times \text{EE} \times P_{\text{Nl}} / P_{\text{Act}} \times \int_0^T C\left(t\right)\ \text{d}t\ \left(\text{mCi-min/mL}\right) \tag{9.11}$$

Here A (mCi/gm) is the activity in a gram of tissue, F (mL/min-gm) is blood flow per gram of tissue, "EE" is extraction efficiency (no units), P_{Nl} / P_{Act} is the ratio of the usual or normal concentration of competing molecules or substances to the actual concentration (no units), and $\int_0^T C\left(t\right)\text{d}t\left(\text{mCi-min/mL}\right)$ is the total amount of tracer in the blood from injection to the end of image acquisition, T (min), that was available to be cleared. However, the PET scanner does not directly measure tissue activity in millicuries but in counts per minute. Therefore, two additional factors need to be added to Eq. 9.11, a sensitivity factor, S (cpm/mCi), that reflects the sensitivity of the PET scanner in counts per minute to actual tissue activity in millicuries and a recovery factor, R (mCi/cpm), that converts the counts per minute recorded by the PET scanner back to millicuries. The inherent measurement of the scanner is in counts per minute, so R must be determined by moving a known radioactive source through the field of view of the PET scanner while recording the counts per minute that scanner measures. The fully expanded equation for SUV is

$$\text{SUV} = \frac{R\left(\text{mCi/cpm}\right) \times S\left(\text{cpm/mCi}\right) \times F\left(\text{mL/min-gm}\right) \times \text{EE} \times P_{\text{Nl}} / P_{\text{Act}} \times \int_0^T C\left(t\right)\text{d}t\left(\text{mCi-min/mL}\right)}{\left[D\left(\text{mCi}\right) - R\left(\text{mCi}\right)\right] / \text{Body weight(gm)}} \tag{9.12}$$

Inaccuracies in the SUV calculation can be introduced through any of the variables in Eq. 9.12 but are much more likely to occur because of an error in one of the factors in the numerator [5–7]. These potential errors are discussed in detail in Chap. 20, Tumor Imaging.

Renal Tubular Clearance (% Uptake) Worksheet

RENAL TUBULAR CLEARANCE (% UPTAKE) WORKSHEET

Nuclear Medicine Department

Institution _____

Patient name_____ ID_____ Date_____

Referring physician_____ Weight_____(kg) Height_____(cm) Age____(yr)

NOTE: Many nuclear medicine computers have software that performs one or more of the steps below automatically.

STEP 1 Calculate the net injected dose from the syringe images:

pre injection (cpm)-post injection (cpm) = net injected dose (cpm)

_____(cpm)-_____(cpm) = _____(cpm)

STEP 2 Calculate the renal depth of both kidneys using the method of Taylor:

[151.3 x weight (kg) ÷ height (cm)] + 0.22 age (yr) + 0.77 = right kidney depth (mm)

[151.3 x _____(kg) ÷ _____(cm)] + 0.22 x _____(yr) + 0.77 = _____(mm)

[161.7 x weight (kg) ÷ height (cm)] + 0.27 age (yr) + 0.7 = left kidney depth (mm)

[161.72 x _____(kg) ÷ _____(cm)] + 0.27 x _____ (yr) + 0.7 = _____(mm)

STEP 3 Calculate the percent uptake of the injected dose in each kidney at 2 to 3 minutes using the equation:

$$\frac{[A-B] \times P \times 100\%}{[e \exp -\mu Y] \times D} = U\ (\%)$$

Where: U = percent uptake (%)
A = counts per pixel right or left kidney (cpm/px)
B = counts per pixel corresponding background (cpm/px)
P = pixels in kidney region of interest (px)
e = natural log = 2.718 (no units)
μ = attenuation coefficient for Tc-99m = 0.0153 (1/mm)
Y = kidney depth (mm)
D = net counts for syringe containing dose (cpm)
exp = exponent

Right kidney:

$$\frac{[\_\_\_\_\_(cpm/px) - \_\_\_\_\_(cpm/px)] \times \_\_\_\_\_(px) \times 100\%}{[2.718 \exp -0.153\ (1/mm) \times \_\_\_\_\_(mm)] \times \_\_\_\_(cpm)} = \_\_\_\_\_\%\ \text{uptake}$$

Left kidney:

$$\frac{[\_\_\_\_\_(cpm/px) - \_\_\_\_\_(cpm/px)] \times \_\_\_\_\_(px) \times 100\%}{[2.718 \exp - 0.153\ (1/mm) \times \_\_\_\_\_(mm)] \times \_\_\_\_(cpm)} = \_\_\_\_\_\%\ \text{uptake}$$

STEP 4 Add the percent uptakes of the two kidneys together to obtain the global percent uptake (a measure of renal clearance):

right (% uptake) + left (% uptake) = global (% uptake)

_____(% uptake) + _____(% uptake) = _____(% uptake)

STEP 5 Multiply the total kidney percent uptake by a system appropriate factor to convert to ERPF.

Technologist_____

Thyroid Uptake Worksheet

THYROID UPTAKE WORKSHEET
Nuclear Medicine Department
Institution_____

Name_____ ID_____ Age_____ Sex_____

Referring physician_____ Date_____

Zero Hour (time_____)

	counts per minute
Dose in phantom (standard)	
Background	-
Net (standard)	

6 Hour Uptake (time_____)

	counts per minute
Neck	
Thigh (background)	-
Net	

	counts per minute
Standard at zero time	
Decay correction factor	x
Corrected standard	

6 hour uptake = (net neck cpm / corrected standard cpm) x 100% = _____%

24 Hour Uptake (time_____)

	counts per minute
Neck	
Thigh (background)	-
Net	

	counts per minute
Standard at zero time	
Decay correction factor	x
Corrected standard	

24 hour uptake = (net neck cpm / corrected standard cpm) x 100% = _____%

• Normal Range: 6 hours = _____%; 24 hours = _____% •

Technologist_____

References

1. Taylor A. Formulas to estimate renal depth in adults. J Nucl Med. 1994;35:2054–5.
2. Klingensmith WC. Tc-99m-MAG3 camera based measurement of renal clearance: should the result be normalized for body surface area? J Nucl Med Technol. 2013;41:279–82.
3. Paquet N, Albert A, Foidart J, et al. Within-patient variability of F-18-FDG: standardized uptake values in normal tissues. J Nucl Med. 2004;45:784–8.
4. Wang Y, Chiu E, Rosenberg J, et al. Standardized uptake value atlas: characterization of physiological 2-deoxy-2-F-18-fluoro-D-glucose uptake in normal tissues. Mol Imaging Biol. 2007;9:83–90.
5. Boellaard R. Standards for PET image acquisition and quantitative data analysis. J Nucl Med. 2009;50:11S–20.
6. Vriens D, Visser EP, de Geus-Oei LF, et al. Methodological considerations in quantification of oncological FDG PET studies. Eur J Nucl Med. 2010;37:1408–25.
7. Keyes JW. SUV: standard uptake value or silly useless value? J Nucl Med. 1995;36:1836–9.

Other Quantitative Techniques

10

Introduction

This chapter examines four quantitative techniques that do not fit easily into the preceding chapters (Table 10.1). One is a quantitative technique with general applicability, and the other three are nuclear medicine studies with unusual quantitative techniques. The body surface area normalization technique is a general method to determine whether an equation that measures a biologic function in absolute terms should be normalized for body surface area (BSA). The Cystogram - Direct Study with Tc-99m-DTPA is performed primarily to detect vesicoureteral reflux during either bladder filling or voiding. However, the study can also be used to measure the post-void residual volume of urine in the bladder. The GLOFIL® study uses an intravenous injection of I-125-iothalamate, a molecule that is cleared from the blood by glomerular filtration, to measure renal clearance in absolute terms. The study involves blood and urine sampling but no imaging. And Cisternogram with In-111-DTPA is performed mainly to evaluate the flow of cerebrospinal fluid (CSF) from the lumbar subarachnoid space to the superior sagittal sinus. However, in patients with suspected CSF rhinorrhea, the study can be modified to help detect and locate the site of a leak and to roughly quantitate the amount of leak.

Body Surface Area Normalization

General

There are several quantitative measurements of the clearance of substances from the blood in laboratory medicine as well as in nuclear medicine that require normalization for body surface area before a single normal range can be used for all patients regardless of size. At the same time, there are other quantitative measurements in which normalization for BSA is inherent in the method and secondary

W.C. Klingensmith III, *The Mathematics and Biology of the Biodistribution of Radiopharmaceuticals-A Clinical Perspective*,
DOI 10.1007/978-3-319-26704-3_10

Table 10.1 Other nuclear medicine studies involving quantitative techniques

Procedure	Radiopharmaceutical	Functional parameter
General		
Body surface area normalization	N/A	Body surface area normalization
Central nervous system		
Cisternography	In-111-DTPA	CSF rhinorrhea
Genitourinary system		
Cystogram – Direct	Tc-99m-DTPA	Post-void residual urine volume
GLOFIL® Study	I-125-iothalamate	Glomerular filtration (clearance)

normalization for BSA is not required. In at least one nuclear medicine study, the Renal Tubular Secretion Study with Tc-99m-MAG3, there has been disagreement in the literature relative to whether the result should be normalized for BSA [1]. The body surface area normalization procedure is a mathematical technique that directly determines whether an equation should be normalized for BSA.

In order to calculate a clearance rate of any substance from the blood, two pieces of information are needed: (1) the amount of test substance transferred from blood into the organ in question during a given period of time and (2) the amount of test substance in the blood or plasma that was available for clearance during the same period of time. The measurement of test substance may be in terms of the concentration of the test substance in the blood, e.g., plasma creatinine on a milligram per milliliter basis, or on the basis of the total dose of radiopharmaceutical that is injected intravenously at the start of the study in millicuries. The amount of cleared test substance goes in the numerator and the amount of available test substance in blood over the relevant time period goes in the denominator. In the case of a clearance measurement with a radiopharmaceutical that is injected in its entirety at the beginning of the study, there is a conversion factor in the numerator with units of "mL".

In general, the technique for determining whether normalization for BSA is needed involves: (1) expanding the numerator and denominator of the clearance equation in question, (2) substituting the term "BSA" for each factor that varies with patient size and "1" for each factor that does not vary with patient size, and (3) simplifying the transformed equation. If the result is "BSA," the measurement varies with BSA and needs to be multiplied by "1.73 m^2/BSA_P" where "BSA_P" is the patient's BSA. If the result is "1," the measurement does not vary with BSA and does not need to be normalized for BSA. And, if the result is "1/BSA," the measurement varies inversely with BSA and needs to be multiplied by "$BSA_P/1.73\ m^2$."

The studies listed in Table 10.2 all include a measurement of clearance in absolute terms. Notice that the list includes the creatinine clearance test, a non nuclear medicine study, and the GLOFIL® test, which does not involve imaging and is not discussed elsewhere in this book. All of these studies measure the clearance rate from blood into an organ or a lesion (in the case of the glucose tumor metabolism with F-18-FDG) and will be analyzed for the need to perform secondary normalization for BSA.

Table 10.2 Studies with absolute quantification and the mechanism for BSA normalization

Procedure	Radiopharmaceutical	Functional parameter	Comment	Blood sampling	Normalization for BSA
Endocrine system					
Thyroid uptake measurement	I-123	Thyroid uptake (clearance)	Organ based	No	Inherent (via blood volume)
Genitourinary system					
Creatinine clearance test (non nuclear medicine study)	Creatinine	Glomerular filtration (clearance)	Organ based	Yes	Secondary (via BSA)
Renal Glomerular Filtration Study	Tc-99m-DTPA	Glomerular filtration (clearance)	Organ based	No	Inherent (via blood volume)
Renal Tubular Excretion Study	Tc-99m-MAG3	Tubular excretion (clearance)	Organ based	No	Inherent (via blood volume)
GLOFIL®	I-125-iothalamate	Glomerular filtration (clearance)	Organ based	Yes	Secondary (via BSA)
Tumor imaging					
Tumor Glucose Metabolism Study	F-18-FDG	Glucose metabolism (clearance)	Gram based	No	Inherent (via body weight)

Table 10.3 Parameters affecting renal clearance of creatinine

Patient size	Kidney size	Renal blood flow	Plasma volume	EE	Creatinine production	Creatinine plsm conc	Creatinine excreted	BSA correction
Average	–	–	–	–	–	–	–	Yes
Small	↓	↓	↓	–	↓	–	↓	Yes
Large	↑	↑	↑	–	↑	–	↑	Yes
						Denominator	Numerator	

– average or unchanged, ↓ decreased; ↑ increased, *EE* extraction efficiency, *plsm conc* plasma concentration

Creatinine Clearance Test

We start with the non nuclear medicine creatinine clearance test. Table 10.3 evaluates the relationship between patient size and the creatinine clearance rate in a conceptual, non-mathematical manner [1]. Three patient sizes are listed: average, small, and large. Notice that the physiologic parameters, kidney size, renal blood flow, blood volume, and creatinine production, all vary with patient size or BSA. On the other hand, the extraction efficiency for glomerular filtration does not vary with

patient size. And, because creatinine production and blood volume both vary directly with patient size, the blood creatinine concentration does not vary with patient size. However, the amount of creatinine excreted will vary directly with patient size because renal blood flow varies directly with patient size and, therefore, the creatinine clearance result will require normalization for BSA. The terms "denominator" and "numerator" at the bottom of Table 10.3 indicate that the parameters "Creatinine plsm conc" and "Creatinine excreted" go in the denominator and numerator of the renal clearance equation, respectively.

Now we will look at the same question, i.e., whether normalization for patient size is needed in the creatinine clearance measurement, from a mathematical point of view. The relevant equation for renal creatinine clearance, Cl (mL/min), before any secondary normalization for BSA, is,

$$\mathrm{Cl}\left(\mathrm{mL/min}\right) = \frac{U\left(\mathrm{mg/min}\right)}{P\left(\mathrm{mg/mL}\right)} \tag{10.1}$$

Here U is the amount of creatinine in a 24 h urine collection on a per minute basis and P is the plasma concentration of creatinine in milligrams per milliliter. The initial step of multiplying the concentration of creatinine in the 24 h urine collection times the urine volume has been omitted.

When the creatinine clearance equation is normalized for BSA, the ratio, 1.73 m^2/BSA_P, is added where 1.73 m^2 is the BSA of a normal-sized person and BSA_P is the BSA of the patient with units of meters squared understood,

$$\mathrm{Cl}\left(\mathrm{mL/min}\right) = \frac{U\left(\mathrm{mg/min}\right)}{B\left(\mathrm{mg/mL}\right)} \times \frac{1.73\ \mathrm{m}^2}{\mathrm{BSA_P}} \tag{10.2}$$

Equation 10.2 indicates that the renal clearance result with the creatinine clearance method is explicitly normalized for BSA.

At this point we return to Eq. 10.1 and expand the numerator and denominator. First, we expand the numerator that represents the amount of test substance cleared in a certain amount of time into the physiologic factors that determine the amount of test substance that is cleared. These factors, as discussed in detail in Chap. 4, Evaluation of Clearance, are blood flow to the kidneys, F (mL/min-kidneys); the extraction efficiency for the test substance in question, which will depend primarily on the extraction mechanism, EE (no units); and the concentration of the test substance in plasma as a function of time during the uptake period: $\int_0^T P(\mathrm{t})\,\mathrm{d}t\left(\mathrm{mCi-min/mL}\right)$. Here T is the time at the end of the urine collection, 24 h. The final equation for creatinine uptake in the numerator is,

$$U\left(\mathrm{mg/min}\right) = F\left(\mathrm{mL/min}\right) \times \mathrm{EE} \times \int_0^T P\left(t\right)\mathrm{d}t\left(\mathrm{mg-min/mL}\right) / T\left(\mathrm{min}\right) \tag{10.3}$$

Substituting the right-hand side of Eq. 10.3 into Eq. 10.1 and expanding the factor P in both the numerator and denominator gives,

$$\mathrm{Cl}(\mathrm{mL/min}) = \frac{F(\mathrm{mL/min}) \times \mathrm{EE} \times \int_0^T [\mathrm{TPCr/TPV}](t)\,\mathrm{d}t(\mathrm{min}) / T(\mathrm{mg-min/mL})}{\mathrm{TPCr}(\mathrm{mg}) / \mathrm{TPV}(\mathrm{mL})} \tag{10.4}$$

where TPCr is total plasma creatinine and TPV is total plasma volume.

Now we can substitute either BSA or 1 for each physiologic factor depending on whether the factor varies with patient size. This gives,

$$\mathrm{Cl}(\mathrm{mL/min}) \sim \frac{\mathrm{BSA} \times 1 \times [\mathrm{BSA/BSA}] \times 1/1}{\mathrm{BSA/BSA}} \tag{10.5}$$

which reduces to,

$$\mathrm{Cl}(\mathrm{mL/min}) \sim \mathrm{BSA} \tag{10.6}$$

indicating that renal clearance, as measured by the creatinine clearance method, varies with patient size, and therefore, the result requires normalization for BSA. Note that when the normalization factor shown in Eq. 10.2 is added to Eq. 10.6, the BSA in Eqs. 10.2 and 10.6 cancel so that the creatinine clearance result no longer varies with BSA, i.e., it has been normalized for BSA. Also, note that in the equations in this chapter, the symbol '~' is used to mean "varies with."

Organ-Based Clearance Studies with Radiopharmaceutical Imaging

Now we apply a similar analysis to those nuclear medicine studies that involve administration of a radiopharmaceutical followed by imaging that depicts the clearance of radiopharmaceutical from blood into an organ in absolute terms [1]. These studies are the Renal Tubular Secretion Study with Tc-99m-MAG3, the Renal Glomerular Filtration Study with Tc-99m-DTPA, and the Thyroid Uptake Study with I-123. Both the conceptual and mathematical analyses are the same for all three studies. These three studies are organ based.

Table 10.4 evaluates the relationship between patient size and the organ clearance rate in a conceptual, non-mathematical manner for radiopharmaceutical methods [2]. Again, three patient sizes are listed, average, small, and large, and again, the physiologic parameters organ size, organ blood flow, and blood volume all vary with patient size or BSA. Because tracer dose can be assumed to be the same for all patient sizes and blood volume varies directly with patient size, the blood tracer

Table 10.4 Parameters affecting clearance of radiopharmaceuticals into organs

Patient size	Organ size	Organ blood flow	Plasma volume	EE	Tracer dose	Tracer plsm conc	Tracer uptake	BSA correction
Average	–	–	–	–	–	–	–	No
Small	↓	↓	↓	–	–	↑	–	No
Large	↑	↑	↑	–	–	↓	–	No
					Denominator		Numerator	

– average or unchanged, ↓ decreased, ↑ increased, *EE* extraction efficiency, *plsm conc* plasma concentration

concentration will vary inversely with patient size. The extraction efficiency for all three studies will not vary with patient size. The end result is that the amount of tracer cleared will not vary with patient size because, while the organ blood flow varies directly with patient size, the tracer concentration in the blood varies inversely with patient size. Thus, the result does not require correction for BSA. The terms "denominator" and "numerator" at the bottom of Table 10.4 indicate that the parameters "tracer dose" and "tracer uptake" go in the denominator and numerator of the renal clearance equation, respectively.

Now we will look at the same question, i.e., whether correction for patient size is needed in organ-based tracer clearance measurements, from a mathematical point of view. The relevant equation for organ clearance, Cl (mL/min), is,

$$\mathrm{Cl}\left(\mathrm{mL/min}\right) = \frac{F\left(\mathrm{mL/min}\right) \times \mathrm{EE} \times \int_0^T \left[D/\mathrm{TPV}\right](t)\,\mathrm{d}t \;\left(\mathrm{min-cpm/mL}\right)}{D\left(\mathrm{cpm}\right)} \tag{10.7}$$

where F is blood flow, EE is extraction efficiency, D is total plasma tracer, TPV is total plasma volume, and T is time from injection to the end of acquisition of the clearance image. The conversion factor in the numerator with units of mL/min has been left out. The conversion factor converts percent uptake on the right-hand side of the equation to clearance on the left and is a constant.

Now we substitute either BSA or 1 for each physiologic factor depending on whether the factor varies with patient size,

$$\mathrm{Cl}\left(\mathrm{mL/min}\right) \sim \frac{\mathrm{BSA} \times 1 \times \left[1/\mathrm{BSA}\right] \times 1}{1} \tag{10.8}$$

Table 10.5 Parameters affecting clearance of glucose into tumor as standard uptake value (SUV)

Patient size	Tumor size per gram	Tumor blood flow per gram	Blood volume	EE	Tracer dose per gram	Tracer bld conc	Tumor uptake per gram	BSA correction
Average	–	–	–	–	–	–	–	No
Small	–	–	↓	–	↑	↑	↑	No
Large	–	–	↑	–	↓	↓	↓	No
					Denominator		Numerator	

– average or unchanged, ↓ decreased, ↑ increased, *EE* extraction efficiency, *bld conc* blood concentration

which reduces to,

$$\mathrm{Cl}\left(\mathrm{mL/min}\right) \sim 1 \tag{10.9}$$

indicating that the result does not need to be normalized for BSA.

Gram of Tissue-Based Studies with Radiopharmaceutical Imaging

Now we apply the same analysis to clearance of FDG into tumor in the Tumor Glucose Metabolism Study [2–4]. The equation for the SUV is,

$$\mathrm{SUV} = \frac{\mathrm{FDG\,in\,tissue}\left(\mathrm{mCi/mL}\right)\left(\mathrm{mL/gm}\right)}{\mathrm{Dose}\left(\mathrm{mCi}\right)/\mathrm{Body\,weight}\left(\mathrm{gm}\right)} \tag{10.10}$$

Here, unlike the three organ-based clearance studies above, the tumor uptake (clearance) is on a per volume basis and the tracer dose is on a per gram basis. Note that in the numerator it is assumed that a gram corresponds to a milliliter although this is not always the case.

Table 10.5 evaluates the relationship between patient size and the tumor clearance in a conceptual, non-mathematical manner. Again, three patient sizes are listed: average, small, and large. Notice that, unlike the physiologic parameters in Tables 10.3 and 10.4, the parameters tumor size per gram and tumor blood flow per gram do not vary with patient size or BSA. The extraction efficiency will not vary with patient size. Because the tracer dose can be assumed to be the same for all patient sizes and blood volume varies directly with patient size, the blood tracer concentration will vary inversely with patient size. In addition, the tracer dose per gram and tumor uptake per gram vary inversely with patient size. Because the tracer

dose per gram is in the denominator and the tumor uptake per gram is in the numerator, the inverse effect of size cancels and the SUV will not vary with patient size. Thus, the result does not require normalization for BSA.

Now we will look at the same question, i.e., whether normalization for patient size is needed in the measurement of the SUV in the Tumor Glucose Metabolism Study, from a mathematical point of view. The relevant equation for SUV (unitless) after expansion is,

$$\mathrm{SUV} = \frac{F\left(\mathrm{mL/min-gm}\right)\times \mathrm{EE}\times P_{\mathrm{Nl}}/P_{\mathrm{Act}}\times\int_0^T\left[D/\mathrm{TBV}\right](t)\,\mathrm{d}t\ \left(\mathrm{mCi-min/mL}\right)}{D\left(\mathrm{mCi}\right)/\mathrm{Body\,weight}\left(\mathrm{gm}\right)} \tag{10.11}$$

where $P_{\mathrm{Nl}}/P_{\mathrm{Act}}$ is the ratio of the normal concentration of glucose in the blood to the actual concentration of glucose in the blood. The ratio of normal to injected glucose is included here because the extraction mechanism for glucose transport into the cell is saturable. The other variables are defined above.

Now we can substitute either BSA or a 1 for each physiologic factor depending on whether the factor varies with patient size,

$$\mathrm{SUV} \sim \frac{1\times 1\times 1\times\left[1/\mathrm{BSA}\right]\times 1}{1/\mathrm{BSA}} \tag{10.12}$$

which reduces to,

$$\mathrm{SUV} \sim 1 \tag{10.13}$$

indicating that the result does not need to be normalized for BSA. Effectively, the *Body weight* factor normalizes the equation for body size. Otherwise, the result would have to be normalized by 1/BSA.

GLOFIL® Study

The GLOFIL® study is a non-imaging study that is performed with an intravenous injection of I-125-iothalamate. The ligand, iothalamate, is a CT contrast material [5]. I-125-iothalamate is cleared in the kidneys by glomerular filtration. Beginning 45 min after injection of the radiopharmaceutical, the patient empties his/her bladder and blood sample #1 is obtained. Forty-five minutes later, the patient again empties his/her bladder as urine sample #1 and blood sample #2 is obtained. After another 45 min, the patient again empties his/her bladder as urine sample #2 and blood sample #3 is obtained (Fig. 10.1).

The radioactivity in the urine and blood samples is measured on a per milliliter basis and the two plasma values on either side of the two urine collections are averaged. If the blood level of tracer decreased in a linear fashion, the clearance rate of tracer obtained by dividing the tracer in the each urine collection by the mean of the beginning and ending blood concentration of tracer would be accurate. However, since the decrease in blood tracer over time is exponential, the result will underestimate the clearance rate by a small amount (Fig. 10.1).

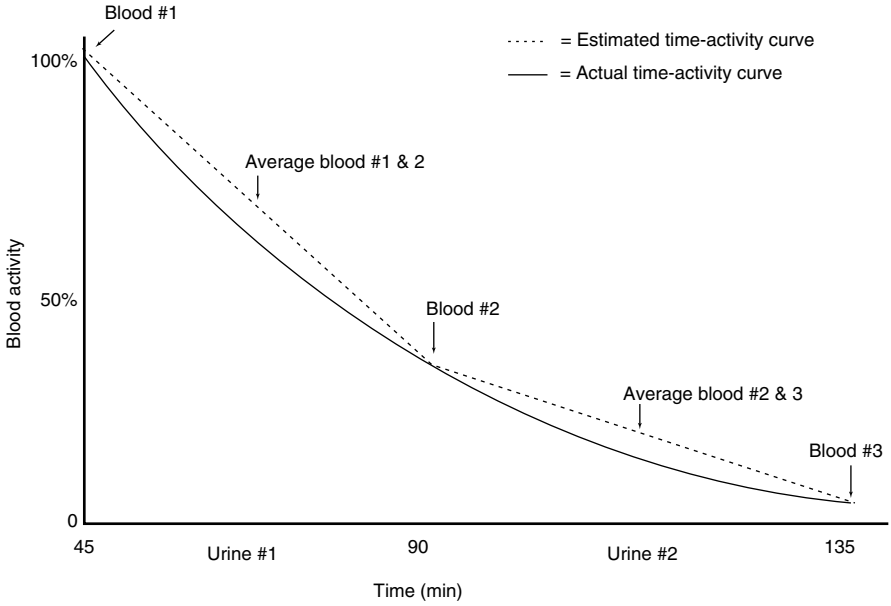

Fig. 10.1 Graph of "blood activity" vs. "time." Note that time on the *X*-axis starts at 45 min. There are three blood collections at 45, 90, and 135 min and two urine collections at 90 and 135 min. The first and second blood collections and the second and third blood collections are averaged to match the urine collections

Table 10.6 Parameters affecting renal clearance with GLOFIL® method

Patient size	Renal size	Renal blood flow	Blood volume	EE	Tracer dose	Tracer bld conc	Tracer excreted	BSA correction
Average	–	–	–	–	–	–	–	Yes
Small	↓	↓	↓	–	–	↑	–	Yes
Large	↑	↑	↑	–	–	↓	–	Yes
						Denominator	Numerator	

– average or unchanged, ↓ decreased, ↑ increased, *EE* extraction efficiency, *bld conc* blood concentration

Table 10.6 analyzes the effect of patient size on various physiologic and tracer parameters. Again, three patient sizes are listed: average, small, and large. Notice that the physiologic parameters renal size, renal blood flow, and blood volume all vary with patient size or BSA, while the extraction efficiency will not vary with patient size. Because tracer dose can be assumed to be the same for all patient sizes but blood volume varies directly with patient size, the blood tracer concentration will vary inversely with patient size. At the same time, the amount of tracer cleared and excreted will not vary with patient size because the direct effect of patient size on renal blood flow is offset by the inverse effect of patient size on blood tracer concentration. Since the amount of tracer excreted in the urine is measured and goes

in the numerator and the concentration of tracer in the blood is measured and goes in the denominator, the glomerular filtration clearance rate will need to be normalized for patient size, i.e., BSA.

Now we will look at the same question, i.e., whether correction for patient size is needed in the GLOFIL® measurement of renal clearance, from a mathematical point of view. The equation for renal clearance by glomerular filtration prior to any normalization for BSA and using the symbols from the Product Insert is,

$$C\left(\text{mL}/\text{min}\right)=\frac{U\left(\text{cpm}/\text{mL}\right)\times V\left(\text{mL}/\text{min}\right)}{P\left(\text{mean cpm}/\text{mL}\right)} \tag{10.14}$$

where C is renal clearance rate by glomerular filtration in milliliters per minute, U is urine radioactivity in counts per minute per milliliter, V is urine flow rate in milliliters per minute, and P is mean plasma radioactivity in counts per minute per milliliter.

We then expand Eq. 10.14 and revert to the symbols used throughout this book to give,

$$\text{Cl}\left(\text{mL}/\text{min}\right)=\frac{F\left(\text{mL}/\text{min}\right)\times \text{EE}\times \int_{45}^{135}\left[D/\text{TBV}\right]\text{d}t\left(\text{min}\right)/T\left(\text{min}-\text{cpm}/\text{mL}\right)}{D\left(\text{cpm}\right)/\text{TBV}\left(\text{mL}\right)} \tag{10.15}$$

where "45" and "135" are the times (in minutes) of the start and end of the study relative to the time of injection of the radiopharmaceutical.

Now we can substitute either BSA or 1 for each physiologic factor depending on whether the factor varies with patient size, to give,

$$\text{Cl}\left(\text{mL}/\text{min}\right)\sim \frac{\text{BSA}\times 1\times\left[1/\text{BSA}\right]\times 1/1}{1/\text{BSA}} \tag{10.16}$$

which reduces to,

$$\text{Cl}\left(\text{mL}/\text{min}\right)\sim \text{BSA} \tag{10.17}$$

indicating that the result must be normalized for BSA. The final GLOFIL® equation is,

$$C\left(\text{mL}/\text{min}\right)=\frac{U\left(\text{cpm}/\text{mL}\right)V\left(\text{mL}/\text{min}\right)}{P\left(\text{mean cpm}/\text{mL}\right)}\times\frac{1.73\ \text{m}^2}{\text{BSA}} \tag{10.18}$$

In summary, with proper manipulation an equation that measures a physiologic or molecular biologic parameter can be made to indicate whether it must be normalized for BSA or not.

Cystogram - Direct

The Direct Cystogram with Tc-99m-DTPA is performed primarily in children to detect vesicoureteral reflux. However, the images and voided urine volume can be used to noninvasively determine the post-void residual volume of urine in the bladder [6]. Figure 10.2 shows a cross-sectional diagram of a patient at the level of the bladder pre void and post void with some post-void residual urine in the bladder.

ROIs are placed around the bladder in the two diagrams (broken lines) and the counts per minute are measured. The volume of voided urine is also measured. Then the formula for determining the post-void residual urine volume is,

$$\mathrm{RBV}(\mathrm{mL}) = \frac{\mathrm{RBA}(\mathrm{cpm}) \times \mathrm{VU}(\mathrm{mL})}{\mathrm{FBA}(\mathrm{cpm}) - \mathrm{RBA}(\mathrm{cpm})} \tag{10.19}$$

where RBV is residual bladder volume in milliliters, RBA is residual bladder activity in counts per minute, VU is voided urine in milliliters, and FBA is full bladder activity in counts per minute.

Equation 10.19 can be rearranged to prove that RBV (mL) represents the residual bladder volume,

$$\frac{\mathrm{RBV}(\mathrm{mL})}{\mathrm{RBA}(\mathrm{cpm})} = \frac{\mathrm{VU}(\mathrm{mL})}{\mathrm{FBA}(\mathrm{cpm}) - \mathrm{RBA}(\mathrm{cpm})} = \frac{\mathrm{VU}(\mathrm{mL})}{\mathrm{VUA}(\mathrm{cpm})} \tag{10.20}$$

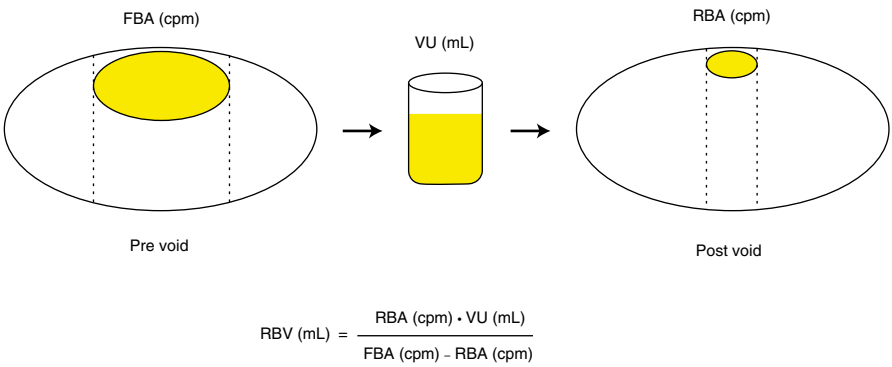

Fig. 10.2 Diagrams of the same pelvic cross section through the bladder pre and post void. The broken lines depict ROIs over the bladder. The equation for calculating the residual bladder volume is shown

Equation 10.20 demonstrates that the ratio of residual bladder volume, RBV (mL), to residual bladder activity, RBA (cpm), on the left side of the equation equals the ratio of voided urine volume, VU (mL), to voided urine activity, VUA (cpm), on the right side of the equation. Therefore, urine activity in counts per minute directly reflects urine volume in milliliters once a change in bladder activity is calibrated to a known change in urine volume [6]. VUA is voided urine activity, but it is unmeasured because the photon attenuation in a beaker would not match the photon attenuation of urine in the bladder.

Cisternography with Nasal Pledgets

When the Cisternography with In-111-DTPA study is done for the purpose of diagnosing CSF rhinorrhea and identifying its location, nasal pledgets of a standard size are placed in the anterior and posterior portions of both nasal cavities 2 h after the intrathecal injection of In-111-DTPA and removed 4 h later [7]. In addition, blood samples are drawn at the same times. The pledget and plasma specimens are counted in a gamma well counter, and the results are expressed as the ratio of the amounts of activity in the pledgets, i.e., nasal cavities, relative to the amount of activity in plasma,

$$\mathrm{NPR} = \frac{P_{\mathrm{Act}}\left(\mathrm{cpm}/0.5\,\mathrm{mL}\right)}{B_{\mathrm{Act}}\left(\mathrm{cpm}/0.5\,\mathrm{mL}\right)} \tag{10.21}$$

Here, NPR is the nasal pledget to plasma ratio, P_{Act} is pledget activity in counts per minute per 0.5 mL (the volume of fluid that a pledget is expected to absorb), and B_{Act} is activity in counts per minute per 0.5 ml of plasma [7].

This measurement represents a quasi-absolute measurement. The amount of activity in the pledgets (reflecting the degree of leakage of labeled CSF from the subarachnoid space through a break in the dura and skull base into the nasal cavities) goes in the numerator, and the amount of activity in the plasma (serving as a proxy for the amount of In-111-DTPA that was administered intrathecally) goes in the denominator. There is no need to correct for background activity or attenuation.

However, there is a significant weakness in the approach of the cisternogram to measuring the amount of In-111-DTPA that leaks into the nasal cavity. In-111-DTPA primarily reaches the blood as CSF is absorbed into the superior sagittal sinus by the arachnoid villa. But, it takes nearly 24 h for the tracer to pass from the lumbar region of the subarachnoid space to the convexity of the brain. Yet the nasal pledgets are removed from the nasal cavity at 6 h after injection of the tracer. The In-111-DTPA that is in the blood at the time of the 2 and 6 h blood samples probably leaks across the subarachnoid membrane and dura at the lumbar injection site and then passes with lymph flow into the vascular space. Other pathways are also possible.

The clinical application of to Cisternography is discussed more fully in Chap. 13: Central Nervous System.

References

1. Klingensmith WC. Tc-99m-MAG3 camera based measurement of renal clearance: should the result be normalized for body surface area? J Nucl Med Technol. 2013;41:279–82.
2. Boellaard R. Standards for PET image acquisition and quantitative data analysis. J Nucl Med. 2009;50:11S–20.
3. Vriens D, Visser EP, de Geus-Oei LF, et al. Methodological considerations in quantification of oncological FDG PET studies. Eur J Nucl Med. 2010;37:1408–25.
4. Keyes JW. SUV: standard uptake value or silly useless value? J Nucl Med. 1995;36:1836–9.
5. Maher FT, Nolan NG, Elveback LR. Comparisons of simultaneous clearances of I-125 labeled sodium iothalamate (Glofil) and of Inulin. Mayo Clin Proc. 1971;46:690–1.
6. Strauss BS, Blaufox MD. Estimation of residual urine and urine flow rates without urethral catheterization. J Nucl Med. 1970;11:81–4.
7. McKusick KA, Malmud LS, Kordela PA, et al. Radionuclide cisternography: normal values for nasal secretion of intrathecally injected In-111-DTPA. J Nucl Med. 1973;14:933–4.

Part III

Quantitative Evaluation in Nuclear Medicine Studies

Overview of Part III, Quantitative Evaluation in Nuclear Medicine Studies

11

The previous section, Part II, Mathematics of the Biodistribution of Radiopharmaceuticals, reviewed the mathematics that describes the biologic processes that determine the biodistribution of a radiopharmaceutical once it has been administered to a patient. Now in Part III, Quantitative Evaluation in Nuclear Medicine Studies, we will examine how an understanding of the mathematics of the biodistribution of radiopharmaceuticals facilitates (1) the design of optimal study protocols, (2) image interpretation, and (3) quantitation of important functional parameters. Each commonly performed nuclear medicine study is examined with an emphasis on how useful biologic information can be extracted and quantitated. Included for each nuclear medicine study is a brief discussion of the essential aspects of the radiopharmaceutical and relevant biology that are fundamental to the extraction mechanism.

This section proceeds systematically through the diagnostic nuclear medicine studies that are listed in the Nuclear Medicine Procedure Manual 2012–2014 except for several studies that are infrequently performed (see Appendix A: Diagnostic Nuclear Medicine Studies Covered in this Book and Table 11.1) [1]. None of the excluded studies include any unique mathematical technique.

Each organ system plus infection and tumor has its own chapter, and the chapters are presented in alphabetical order. The nuclear medicine studies included within each chapter are also arranged in alphabetical order. Many nuclear medicine studies are included that do not involve quantification of a functional parameter, but they are included for comparison and completeness and because the biodistribution of the radiopharmaceutical in these studies nevertheless follows the mathematics discussed in Part II, Mathematics of the Biodistribution of Radiopharmaceuticals. Eighteen of the 39 nuclear medicine studies that are discussed include some form of explicit quantification and the other 21 do not.

The discussion of each nuclear medicine study is divided into a set of subsections: Overview; Radiopharmaceutical Characteristics; Extraction Mechanism; Extraction Efficiency; Extraction Mechanism, Saturable or Non-saturable;

W.C. Klingensmith III, *The Mathematics and Biology of the Biodistribution of Radiopharmaceuticals-A Clinical Perspective*,
DOI 10.1007/978-3-319-26704-3_11

Table 11.1 Nuclear medicine studies not included in Part III

Study	Category	Reason
Thyroid Imaging Study (Tc-99m-pertechnetate)	Endocrine system	Infrequently performed; replaced by Thyroid Imaging Study (I-123)
Gastroesophageal Reflux Study (Tc-99m-sulfur colloid)	Gastrointestinal system	Infrequently performed
Helicobacter pylori Breath Test (C-14-urea)	Gastrointestinal system	Often not performed in a nuclear medicine lab
LeVeen Shunt Study (Tc-99m-sulfur colloid)	Gastrointestinal system	Infrequently performed
Bone Marrow Study (Tc-99m-sulfur colloid)	Hematologic system	Infrequently performed
Gallium Study (Ga-67-citrate)	Infection imaging	Infrequently performed; inaccurate
Pulmonary Aspiration Study (Tc-99m-sulfur colloid)	Pulmonary system	Infrequently performed
B-Cell Lymphoma Imaging Study (I-131-tositumomab)	Tumor imaging	Infrequently performed; inconvenient
Prostate Cancer Study (In-111-capromab)	Tumor imaging	Infrequently performed; inaccurate

Interventions; Imaging; Protocol Design; Protocol Summary Diagram; and Quantitative Measurement(s).

The "Overview" subsection very briefly describes the biologic process(es) that the study images. The "Radiopharmaceutical Characteristics" subsection describes the basic characteristics of each radiopharmaceutical such as its chemical structure and molecular weight. An optimal radiopharmaceutical is critically important to achieving the goal of a high target to background activity ratio.

> With a good radiopharmaceutical, you can see the lesion with a poor imaging system.
> With a poor radiopharmaceutical, you won't see the lesion even with a good imaging system.
>
> Manny Subramanian, 1976
> Upstate Medical Center, Syracuse, NY

Of course, ideally all components of a study should be optimized: the radiopharmaceutical, the imaging equipment, the protocol, patient preparation, quantitative analysis, and the overall interpretation. Appendix B: Radiopharmaceuticals and their Use in Clinical Studies lists all of the radiopharmaceuticals that are discussed in this book and all of the nuclear medicine studies that are performed with each individual radiopharmaceutical.

The "Extraction Mechanism" subsection is of great importance and attempts to summarize the current knowledge of the biologic mechanism that extracts each radiopharmaceutical from the flowing blood. Table 11.2 lists a single example of each of the various extraction mechanisms in approximate order of decreasing extraction efficiency. The table demonstrates a rough inverse correlation between extraction efficiency and time from administration of the radiopharmaceutical to

Table 11.2 Extraction mechanisms for clearing radiopharmaceuticals from blood

Example study	Radiopharmaceutical	Specific mechanism	Extraction efficiency	Saturable	Time to start clearance image
Pulmonary Perfusion Study	Tc-99m-macroaggregated albumin	Microembolization	100 %	No	15 s
Renal Tubular Secretion Study	Tc-99m-MAG3	Anion excretion pathway	65 %	No	1 min
Renal Glomerular Filtration Study	Tc-99m-DTPA	Passive filtration based on size	20 %	No	1 min
Myocardial perfusion	N-13-ammonia	Lipophilicity	High	No	3 min
Liver-Spleen Study	Tc-99m-sulfur colloid	Phagocytosis by sinusoidal macrophages	High	No	5 min
Hepatobiliary Study	Tc-99m-trimethylbromo-IDA	Organic ion transport system	Moderate-high	Yes	5 min
Tumor Glucose Metabolism Study	F-18-fluorodeoxyglucose	GLUT glucose transporters	Moderate	Essentially	60 min
Bone Mineral Study	F-18 as sodium fluoride	Exchange of F^- for OH^- in hydroxyapatite	Moderate	No	60 min
Bone Mineral Study	Tc-99m-MDP/HMDP	Adherence of PO_4 tracers to surface of bone	Low-moderate	No	2 h
White Blood Cell Migration Study	Tc-99m-white blood cells	Migration secondary to chemotaxis	Low	No	2 h
Somatostatin Receptor Study	In-111-pentetriotide	Cell membrane signal receptor	Low	Yes	4 h
Thyroid Imaging Study	I-123 as sodium iodide	Na^+ / I^- symporter (NIS) protein	Low	Yes	6 h
B-cell Lymphoma Imaging Study	In-111-ibritumomab tiuxetan [Zevalin]	Cell membrane CD20 epitope	Very low	Yes	2–24 h

acquisition of clearance images. Other factors that are not listed are also important in determining the optimal time for imaging clearance, e.g., blood flow and excretion of the radiopharmaceutical from the structure in question. In the normal situation, blood flow times extraction efficiency equals clearance rate. Appendix C: Tables of Clearance Mechanisms contains a set of tables that lists the nuclear medicine studies that utilize each of the various clearance mechanisms. And Appendix D: Distribution of Cardiac Output in the Body at Rest lists the percent of cardiac output, blood flow per organ, and blood flow per 100 g of organ for the major organs of the body.

A few nuclear medicine studies involve extraction of the radiopharmaceutical from a flowing substance other than blood, e.g., lymph in the case of the Lymphoscintigraphy Study with filtered Tc-99-sulfur colloid; and in several nuclear medicine studies, there is no extraction of the radiopharmaceutical from the compartment into which the radiopharmaceutical is introduced, e.g., Cardiac Gated Blood Pool Study with Tc-99m-red blood cells. A significant amount of nuclear medicine research is devoted to identifying extraction mechanisms that, once imaged with an optimal radiopharmaceutical, will provide important clinical information. Initial insights often come from advances in molecular biology.

Many of the simplest extraction mechanisms have already been utilized as the basis of current standard nuclear medicine studies, e.g., microembolization, glomerular filtration, and phagocytosis (Table 11.2). There are probably very few similar, mainly physiologic, mechanisms yet to be exploited. On the other hand, it is likely that only a small percentage of potentially useful extraction mechanisms related to the cell membrane have been identified or explored. Proteins imbedded in cell membranes that could possibly serve as an extraction mechanism fall into at least three categories: (1) membrane transport proteins, (2) receptors for signal molecules, and (3) epitopes that are antigenic.

The need for transport proteins within cell membranes arises from the fact that the lipid bilayer of the cell membrane is relatively impermeable to all but small lipophilic molecules (Fig. 11.1) [2]. Transmembrane transport proteins fall into three general categories: (1) channel proteins, (2) passive transporters (or facilitated diffusion), and (3) active transporters (Fig. 11.2) [3].

Channels passively transport inorganic ions down a concentration gradient. Different channels exist for ions of varying size and charge. The interaction of a molecule with a channel is relatively weak. Passive transporters bind a specific molecule or class of molecules. The binding process causes a conformational change in the transporter that moves the molecule across the cell membrane, again down a concentration gradient.

Active transporters move molecules across the cell membrane against a gradient and, therefore, require the input of energy. The energy may come from ATP hydrolysis or an ion gradient (Figs. 11.2 and 11.3) [3, 4]. In the case of active transport driven by ATP hydrolysis, the conformational change of the transporter protein is driven by energy from the release of a phosphate group from ATP. In the case of active transport driven by an ion gradient, the other solute may move in the same

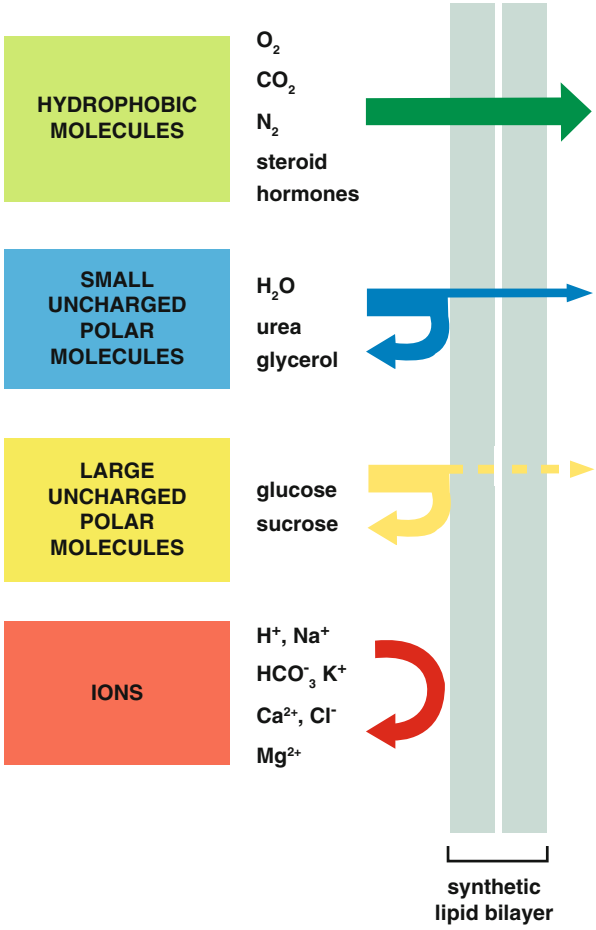

Fig. 11.1 Relative permeability of a cell-like lipid bilayer. The smaller the molecule and, more importantly, the less strongly it associates with water, the more rapidly the molecule diffuses across the lipid bilayer (© Garland Science 2008)

direction as the primary solute, a symporter, or in the opposite direction, an antiporter (Fig. 11.3). The extraction mechanism of thyroid epithelial cells for I-123 in the Thyroid Imaging Study is an example of a symporter; I-123 and Na^+ move across the cell membrane together.

Receptors on cell surfaces for signaling molecules provide another type of extraction mechanism. The signaling molecule binds to receptors on the cell surface with high specificity. The signaling molecule remains on the cell surface but changes the conformation of the receptor protein on the inside of the cell, which triggers a cascade of molecular events that culminates in various changes in the cell's metabolism. The signaling molecule can be converted into a radiopharmaceutical that will localize to cells in proportion to the degree of expression of the signaling receptors in question. The radioisotope label must be attached to the signaling molecule some distance from the binding domain on the signaling molecule. An example of this extraction mechanism in a nuclear medicine study is the Somatostatin Receptor Study with In-111-Octreotide.

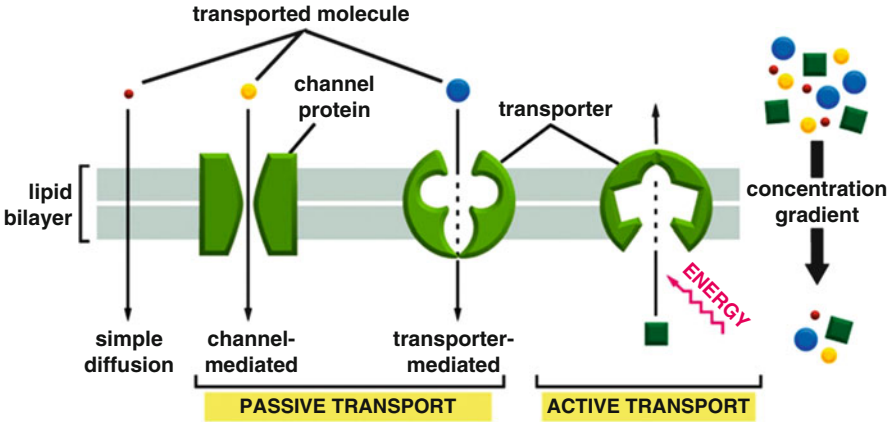

Fig. 11.2 Comparison of active and passive transport. Passive transport down an electrochemical gradient occurs spontaneously, either by simple diffusion through the lipid bilayer or by facilitated diffusion through channels and passive transporters. By contrast, active transport requires input of metabolic energy (© Garland Science 2008)

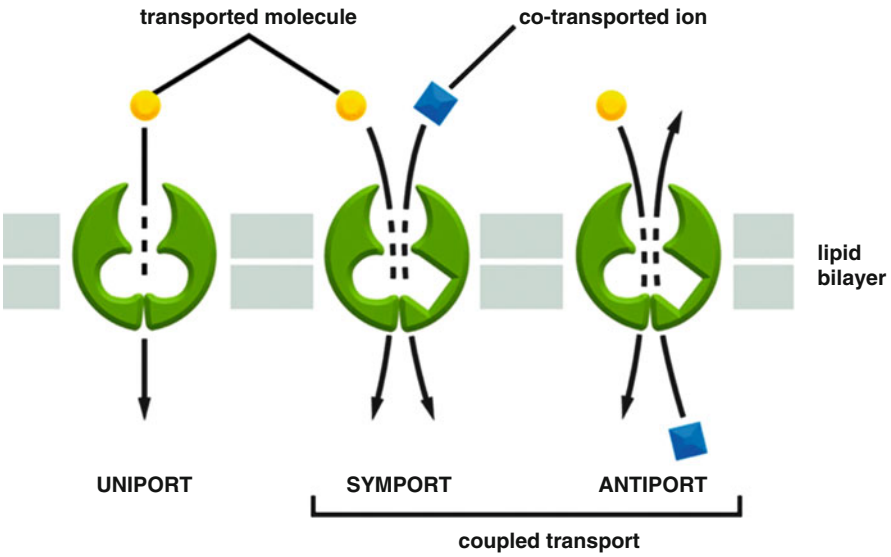

Fig. 11.3 Three types of active transporter-mediated movement. This diagram shows transporters functioning as uniporters, symporters, and antiporters. In each type of transport, the energy is supplied by an electrochemical gradient (© Garland Science 2008)

The extraction mechanism with the highest specificity is the binding of an antibody to an antigen or epitope. An antibody can distinguish between two proteins that differ by only one amino acid or between optical isomers of the same molecule [5]. Cells express many proteins on their surface which can serve as relatively

characteristic markers for cells of interest such as prostate cancer or B-cell lymphoma. However, because of their large size, antibodies are slow to leave the vascular space and enter the interstitium, and foreign antibodies can induce patient antibodies that inactivate the administered antibodies. Some progress has been made in reducing antibody size without affecting binding specificity and humanizing antibodies to eliminate the induction of patient antibodies, but the problems are still significant. Primarily for these reasons, there are no successful antibodies for imaging and only one successful antibody for therapy. In-111-ibritumomab tiuxetan [Zevalin] is effective therapy for B-cell lymphoma even though it does not always achieve a high target to background ratio because lymphomas are very radiosensitive [6].

An interesting extraction mechanism is the labeling of white blood cells that then follow cytokine and chemokine gradients to areas of infection by the process of diapedesis. However, the localization or clearance process is slow, which increases the radiation dose to the patient and delays obtaining diagnostic information. In addition, the patient's blood has to be sent to a laboratory for cell labeling and then the labeled cells are reinjected, which runs the risk of laboratory error. Tc-99m-HMPAO-white blood cells are still occasionally used for imaging infection but have been largely replaced by F-18-fluorodeoxyglucose.

The "Extraction Efficiency" subsection indicates the percent of potentially available radiopharmaceutical that is normally cleared. Sometimes this percent is well known, e.g., 20 % for glomerular filtration, but often it can only be estimated from the length of time following injection that it takes to achieve a target to background ratio that is sufficient for imaging. For example, the extraction efficiency must be high in the Liver-Spleen Study with Tc-99m-sulfur colloid because imaging can begin within 5 min, and it must be low in the Prostate Cancer Study with In-111-capromab [ProstaScint®] because imaging must be delayed until approximately 3 days after injection of the radiopharmaceutical. These estimates ignore the role of blood flow.

The "Extraction Mechanism, Saturable or Non-saturable" subsection simply indicates whether the extraction mechanism can be saturated or not. The microembolization extraction mechanism in the Pulmonary Perfusion Study with Tc-99m-MAA cannot be saturated, but the sodium/iodide symporter extraction mechanism in the Thyroid Imaging Study with I-123 can be saturated, e.g., free iodide associated with CT iodinated contrast material.

The "Interventions" subsection indicates whether any interventions, e.g., medications or exercise, are used in a study. An example is pharmacologic or exercise stress in the various myocardial perfusion studies. The "Imaging" subsection indicates what imaging equipment is used, e.g., simple scintillation probe, gamma camera, or PET-CT machine. The "Protocol Design" subsection briefly describes the rationale of the study protocol and the "Protocol Summary Diagram" depicts the timing of radiopharmaceutical administration, image acquisition, and any interventions. It also includes labels that indicate what physiologic or molecular biologic process is reflected in the images. The definitions of the symbols used in the "Protocol Summary Diagrams" are listed in Fig. 11.4.

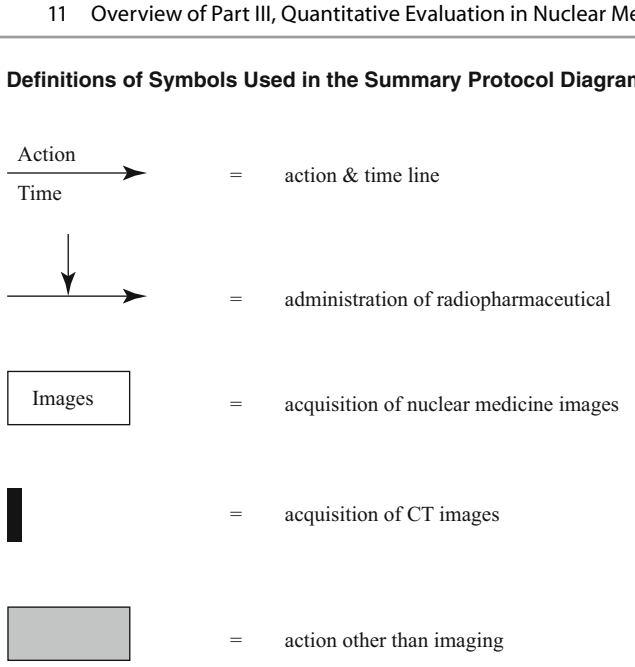

Fig. 11.4 Definitions of symbols used in the protocol summary diagrams

The "Quantitative Measurement" subsection examines in detail any quantitative measurement that is a routine part of the study. This includes the type of measurement as discussed in Part II, Mathematics of the Biodistribution of Radiopharmaceuticals, the normal range, the pathologic meaning of the measurement, and selected clinical examples.

There are many variables involved in any nuclear medicine study and, therefore, many different, but satisfactory, ways to perform, interpret, and quantify nuclear medicine studies. The approach presented here is felt to be representative.

The nuclear medicine therapeutic procedures are not included because essentially every therapeutic procedure has a corresponding diagnostic study with an identical radiopharmaceutical biodistribution.

References

1. Klingensmith WC, Eshima D, Goddard J. Nuclear medicine procedure manual 2012–14. 10th ed. Englewood: Wick Publishing; 2012.
2. Membrane transport of small molecules and the electrical properties of the cell. In: Albert B, Johnson A, Lewis J, Raff M, Roberts K, Walter P, editors. Molecular biology of the cell. 5th ed. New York: Garland Science; 2008. p. 652.
3. Membrane transport of small molecules and the electrical properties of the cell. In: Albert B, Johnson A, Lewis J, Raff M, Roberts K, Walter P, editors. Molecular biology of the cell. 5th ed. New York: Garland Science; 2008. p. 654.

4. Membrane transport of small molecules and the electrical properties of the cell. In: Albert B, Johnson A, Lewis J, Raff M, Roberts K, Walter P, editors. Molecular biology of the cell. 5th ed. New York: Garland Science; 2008. p. 656.
5. The adaptive immune system. In: Albert B, Johnson A, Lewis J, Raff M, Roberts K, Walter P, editors. Molecular biology of the cell. 5th ed. New York: Garland Science; 2008. p. 1540.
6. Goldsmith SJ. Radioimmunotherapy of lymphoma: Bexxar and Zevalin. Semin Nucl Med. 2010;40:122–35.

Cardiovascular System

12

Cardiac Gated Blood Pool Study: Rest (Tc-99m-Red Blood Cells)

Overview The resting Cardiac Gated Blood Pool Study provides information about pulmonary blood flow during the first circulation of the radiopharmaceutical, and then, after equilibration of the radiopharmaceutical, it provides information about cardiac chamber volumes, including ejection fraction, as a function of the cardiac cycle.

Radiopharmaceutical characteristics The Tc-99m-red blood cell is one of the largest radiopharmaceuticals with a diameter of approximately 8 μm, a thickness of approximately 2 μm, and a central thickness of approximately 1 μm (Fig. 12.1) [1].

Extraction mechanism None. The Tc-99m-red blood cells are confined to the vascular space. The diameter of a capillary is similar to that of a red blood cell so that the red blood cells pass through the capillaries in a single file.

Extraction efficiency 0 %.

Extraction mechanism, saturable or non-saturable N/A.

Interventions None.

Imaging Gamma camera planar imaging is most commonly used. Some institutions use gamma camera SPECT or SPECT-CT.

Protocol design The vascular space is labeled by injecting Tc-99m-red blood cells intravenously. The protocol consists of two parts, acquisition of sequential 1 s images for 30 s during the first circulation beginning at the time of injection and acquisition of delayed gated images of the heart in the anterior, left anterior oblique, and left lateral projections. It takes an average of 20 s for a red blood cell to complete one cycle through the vascular system, so, in conjunction with laminar flow and mixing in the cardiac chambers, equilibrium is achieved quickly.

Acquisition of the images of the left ventricle at various phases throughout the cardiac cycle requires a special technique. Normally planar images are acquired from 1 to 5 min in order to record enough counts to have reasonable statistics in the image. However, a cardiac cycle lasts only about 1 s and optimal temporal

W.C. Klingensmith III, *The Mathematics and Biology of the Biodistribution of Radiopharmaceuticals-A Clinical Perspective*,
DOI 10.1007/978-3-319-26704-3_12

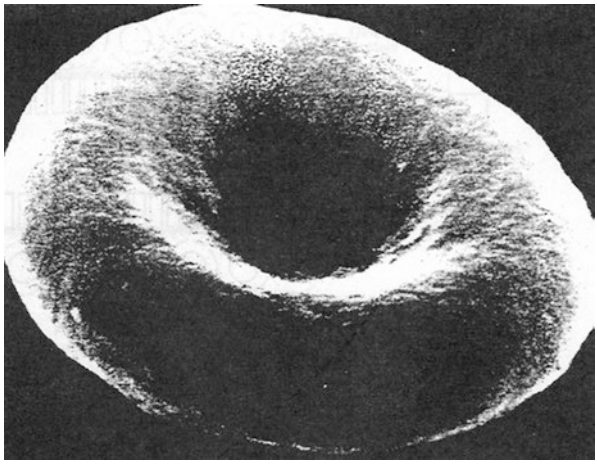

Fig. 12.1 Scanning electron micrograph of human red blood cell (From Freedman [1])

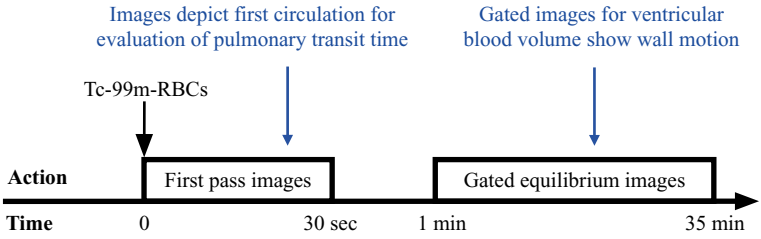

Fig. 12.2 Protocol summary diagram

resolution during the cardiac cycle requires approximately 16 images. Thus, it is impossible to record enough counts for statistical reliability in each of 16 images during one cardiac cycle.

This problem is solved by attaching electrocardiograph (EKG) leads to the patient and sending the EKG signal to a computer that records the incoming counts from the gamma camera. The computer assigns incoming counts to the 16 images depending on the elapsed time since the last Q wave. After approximately 600 s or 10 min, there is an appropriate number of counts in each of the 16 images (Fig. 12.2).

Quantitative measurement (visual): Pulmonary transit time The pulmonary transit time is evaluated by a simple index, the time it takes for the leading edge of the first circulation bolus to pass from the right ventricle to the left ventricle. Specifically, it is the difference in time from the first appearance of the bolus in the right ventricle to the first appearance of the bolus in the left ventricle. The conceptual equation is,

$$\bar{T}\left(\text{sec}\right) = \frac{V\left(\text{mL}\right)}{F\left(\text{mL}/\text{sec}\right)} \approx T_{\text{LE}}\left(\text{sec}\right) \tag{12.1}$$

Here the central volume principle equation (see Chap. 5, Mean Transit Time: Central Volume Principle) has been solved for mean transit time instead of flow. $\bar{T}$ represents the mean transit time of blood flow through the pulmonary arterial circulation, V represents pulmonary blood volume, and F represents pulmonary blood flow. However, since the pulmonary blood volume and blood flow cannot be easily determined, the mean transit time cannot be calculated. Instead, the leading edge transit time, T_{LE}, is used as an index of the mean transit time. Because of laminar flow, the leading edge transit time will always be shorter than the mean transit time.

Pulmonary transit time: normal values The leading edge pulmonary transit time should not exceed 6 s. Greater values indicate an increased pulmonary blood volume and/or a decreased pulmonary blood flow. The most common cause of a prolonged leading edge pulmonary transit time is left ventricular failure, which causes both an increase in pulmonary blood volume and a decrease in pulmonary blood flow secondary to a decrease in cardiac output.

Quantitative measurement: left ventricular ejection fraction The left ventricular ejection fraction, a key measure of cardiac function, is an example of relative quantification in nuclear medicine images in that it is unrelated to the amount of radiopharmaceutical that was administered (see Chap. 8, Quantitation of Function: Relative Measurements).

Since there is little change in photon attenuation between the end diastolic and end systolic images of the left ventricle, and since the left ventricular ejection fraction is a relative measurement, there is no need to know the absolute amount of activity in the left ventricle and attenuation correction is unnecessary.

However, since there is significant activity in the tissues around the left ventricle, background correction is needed. Figure 12.3 shows a planar image of the heart from the LAO projection (adjusted to optimize the separation between the left and right ventricles) with a region of interest (ROI) over the left ventricle and a background ROI over the lower left lung. The background ROI must not overlap the left ventricle, even at end diastole. The equation for background correction of an ROI is given in Chap. 8 as Eq. 8.3 and is not reproduced here.

The equation for left ventricular ejection fraction, after the end diastolic and end systolic ROIs are corrected for background activity, is simply

$$\mathrm{EF_{LV}}(\%) = \frac{\mathrm{LV_{ED}}(cts) - LV_{ES}(cts)}{\mathrm{LV_{ED}}(cts)} \times 100(\%) \tag{12.2}$$

Here, "$\mathrm{EF_{LV}}$ (%)" is the left ventricular ejection fraction in percent, "$\mathrm{LV_{ED}}$ (cts)" is the background corrected counts in the left ventricle at end diastole, and "$\mathrm{LV_{ES}}$ (cts)" is the background corrected counts in the left ventricle at end systole.

The same approach can be used to evaluate the right ventricular ejection fraction. With planar imaging, there is some unavoidable overlap of the ventricle and corresponding atrium, which is not corrected for. However, the Cardiac Gated Blood Pool Study may be performed with SPECT or SPECT-CT [6]. SPECT eliminates the need for background correction, and SPECT-CT also corrects for photon

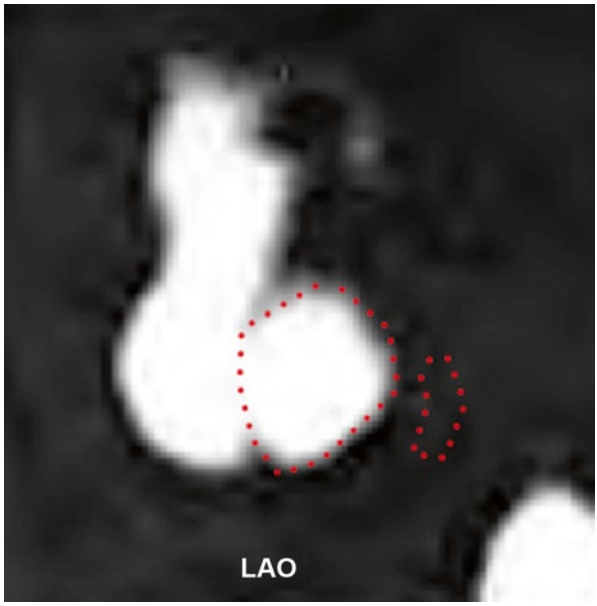

Fig. 12.3 Left anterior oblique (LAO) cardiac gated blood pool image of the heart. ROIs have been placed over the left ventricle for left ventricular volume counts and lower left lung for background counts (Corbett et al. [5])

attenuation, but there is relatively little increase in accuracy of the ejection fraction measurement [2]. The same concepts and equation are used to calculate the gallbladder ejection fraction in the Hepatobiliary Study (see Chap. 15, Gastrointestinal System).

Left ventricular ejection fraction: normal values See Table 12.1 [3, 4]. Values are given where values could be identified in the literature separately for males and females. At the same time, there are many published studies confirming a strong correlation between measurement of the left ventricular ejection fraction in various nuclear medicine studies and measurement of the left ventricular ejection fraction by CT or MRI. Females have a smaller left ventricle than males and a slightly higher ejection fraction. This results in a lower cardiac reserve.

Lymphoscintigraphy (Filtered Tc-99m-Sulfur Colloid)

Overview The Lymphoscintigraphy Study demonstrates the flow of lymph from the site of injection into the interstitial space through the draining lymphatics to the sentinel lymph node(s).

Radiopharmaceutical characteristics The commercially available Tc-99m-sulfur colloid that is injected intravenously contains colloidal particles that are too large to easily pass through the interstitial spaces. Therefore, the commercial Tc-99m-sulfur colloid is filtered prior to injection for lymphoscintigraphy. The filtration process reduces the maximum colloidal particle size from 5.0 to 0.22 μm [6].

Table 12.1 Normal values for quantitative parameters

Parameter	Working Normal range	Actual Normal range	References
Cardiac gated blood pool study			
Leading edge pulmonary transit time	≤6 s	–	–
Ejection fraction (rest) – male	50–75 %	48–72 %	[3, 4]
Ejection fraction (rest) – female	–	–	–
Myocardial perfusion study – N-13-ammonia			
Ejection fraction (rest) – male and female	50–75 %	49–73 %	[10]
Myocardial perfusion study – Rb-82-rubidium			
Ejection fraction (rest) – male	–	–	–
Ejection fraction (rest) – female	40–70 %	40–68 %	[14]
Ejection fraction (stress) – male	–	–	–
Ejection fraction (stress) – female	50–75 %	50–74 %	[14]
Myocardial perfusion study – Tc-99 m-sestamibi			
Ejection fraction (<45 years, rest) – male	45–65 %	45–65 %	[20]
Ejection fraction (<45 years, rest) – female	40–75 %	41–73 %	[20]
Ejection fraction (45–65 years, rest) – male	45–70 %	47–71 %	[20]
Ejection fraction (45–65 years, rest) – female	45–80 %	47–81 %	[20]
Ejection fraction (>65 years, rest) – male	45–75 %	46–74 %	[20]
Ejection fraction (>65 years, rest) – female	55–85 %	56–86 %	[20]
Myocardial perfusion and viability – Tl-201			
Ejection fraction – male	45–75 %	45–73 %	[18]
Ejection fraction – female	50–85 %	51–83 %	[18]
Myocardial viability – F-18-FDG			
Ejection fraction – male	–	–	–
Ejection fraction – female	–	–	–

Extraction mechanism Filtered Tc-99m-sulfur colloid is cleared from the flowing lymph by the mechanism of phagocytosis by macrophages that line the sinusoids of lymph nodes (Fig. 12.4). (See Chap. 4, Evaluation of Clearance for a conceptual and mathematical discussion of clearance). Macrophages are relatively large cells measuring 20–30 μm in diameter, much larger than the 7 μm diameter of a capillary [6, 7]. When a circulating macrophage enters a capillary, it temporarily obstructs the capillary while it squeezes through the capillary to reach the venule. Since there is no blood flow through the capillary while the macrophage is blocking the lumen, no colloidal particles can flow past macrophages.

However, sinusoids, which are found in the liver, spleen, and bone marrow in the vascular system, and in the lymph nodes in the lymph system, are much larger than capillaries with a diameter of 30–40 μm [6]. The macrophages adhere to the sides of the sinusoid, and the blood carrying the colloidal particles flows along the sides of the macrophages. This allows the colloidal particles to bind to the surface of the macrophages and to be phagocytized.

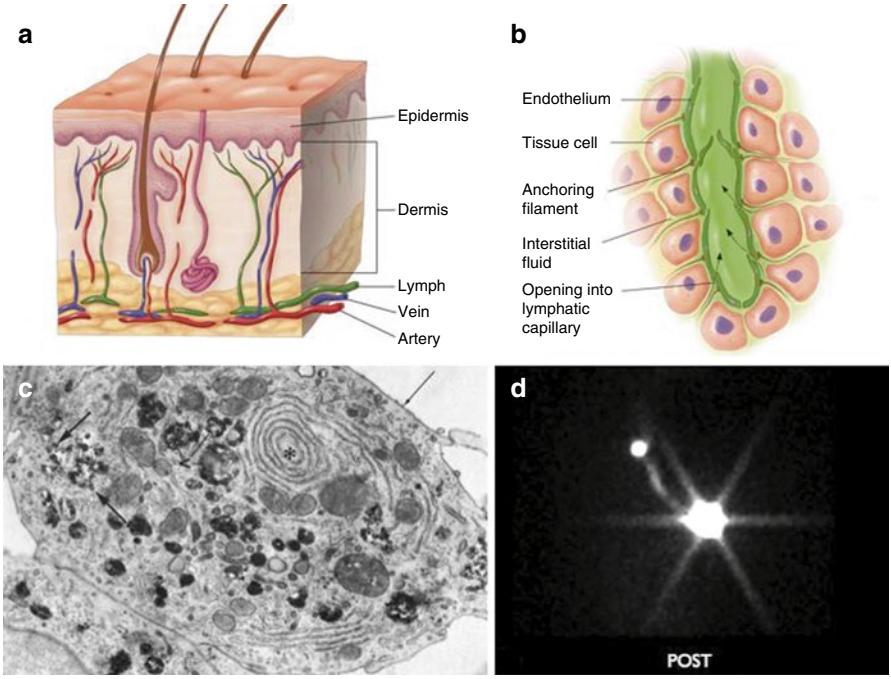

Fig. 12.4 Biology of lymphoscintigraphy. (**a**, **b**) Diagrams of skin and terminal lymph vessel. Injection of sulfur colloid should be in the superficial dermis to maximize movement of colloid from the interstitium into lymphatic vessels. (**c**) Electron micrograph of a macrophage in a lymph node shows multiple vacuoles containing phagocytized carbon particles (From Nopajaroonsri and Simon [7], Fig 7, p 25). (**d**) Patient with melanoma upper left back. Tracer injection site is in the middle of an image with star-shaped artifacts. Lymph vessel is seen passing to focal uptake in a left axillary sentinel lymph node

Extraction efficiency The extraction efficiency of lymph nodes for colloid in general, including filtered Tc-99m-sulfur colloid, is high. From clinical experience, very little radiopharmaceutical passes through a sentinel lymph node to reach a second-tier lymph node during the typical duration of a lymphoscintigraphy study.
Extraction mechanism, saturable or non-saturable Non-saturable.
Interventions None.
Imaging Gamma camera planar imaging with a high-resolution, low-energy collimator is most commonly used. Some institutions use gamma camera SPECT or SPECT-CT, particularly in the case of complex anatomy, e.g., neck lymphoscintigraphy.
Protocol design The filtered Tc-99m-sulfur colloid is injected intradermally with a 30 gauge needle so as to produce a visible wheal. The location and duration of imaging depends on the purpose of the study. The delayed images are timed to show clearance of the tracer from lymph vessels into mononuclear phagocytes or macrophages (Fig. 12.5).
Quantitative measurement None.

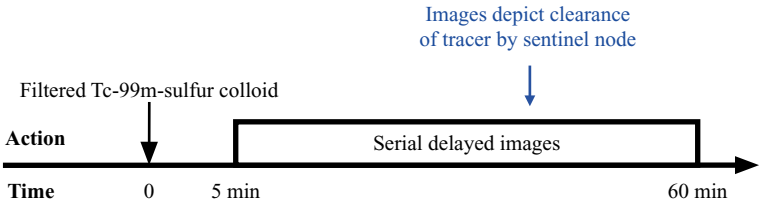

Fig. 12.5 Protocol summary diagram

Myocardial Perfusion Study (N-13-Ammonia)

Overview The Myocardial Perfusion Study with N-13-ammonia is used to evaluate the distribution of blood flow and perfusion to the myocardium at rest and stress [8]. In addition, the images are routinely gated to show regional wall motion and to allow calculation of the left ventricular ejection fraction.

Despite the fact that the title of the study says "myocardial perfusion," the images actually reflect myocardial clearance. This is true of all of the nuclear medicine studies that have the word "perfusion" in the title. Relative clearance will reflect relative perfusion or blood flow as long as the extraction efficiency is uniform throughout the range of coronary blood flow that is being imaged, but this is not always the case. For example, the extraction efficiency is higher in myocardium at low flow rates than at high flow rates (Fig. 12.6) [8].

Radiopharmaceutical characteristics Ammonia is a relatively small molecule with a molecular weight of 17.04. It exists in the blood predominantly in the form of the ammonium ion, NH_4^+.

Extraction mechanism Ammonia passes readily into the myocardial cells, mostly by passive diffusion of lipid-soluble ammonia across the cell membrane [8]. Inside the cell, ammonia converts to the ammonium ion, and then glutamine synthetase catalyzes the incorporation of ammonia into glutamic acid to form glutamine (Fig. 12.7). Because there is a large intracellular pool of glutamine and its turnover is slow, washout of N-13-labeled glutamine is slow [8].

Extraction efficiency The exact extraction efficiency is unknown but empirically appears to be high. The extraction efficiency of all myocardial perfusion radiopharmaceuticals falls off at higher coronary flow rates, i.e., the degree of localization of tracer in the myocardium is not a linear function of the blood flow. This phenomenon supports the fact that the images reflect clearance (Fig. 12.6) [8]. In addition, this means that the decreased blood flow to ischemic areas will be underestimated.

Extraction mechanism, saturable or non-saturable Non-saturable.

Interventions Image acquisition is done twice, once at rest and once following pharmacologic stress that significantly dilates normal coronary arteries. This maneuver reveals areas of coronary ischemia at stress that are not apparent at rest.

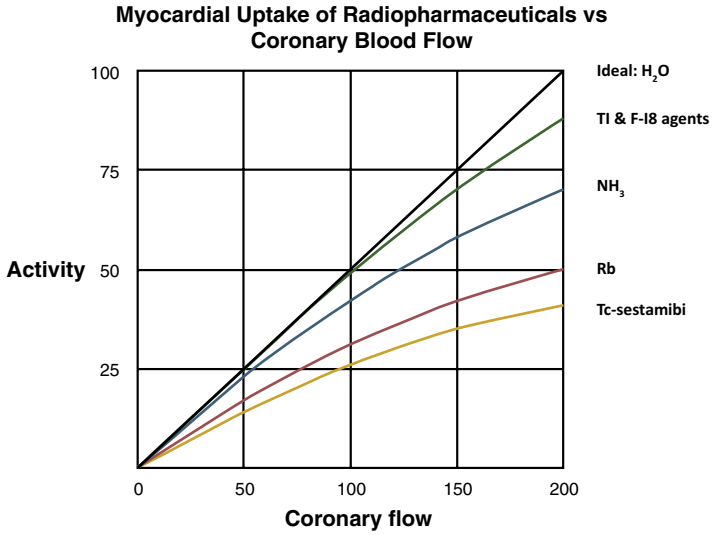

Fig. 12.6 Myocardial uptake (clearance) of radiopharmaceuticals vs coronary blood flow. None of the radiopharmaceuticals that are used for measuring myocardial blood flow or perfusion are entirely accurate because they actually measure clearance and the extraction efficiency decreases as blood flow increases (From Schelbert [8], p. 403)

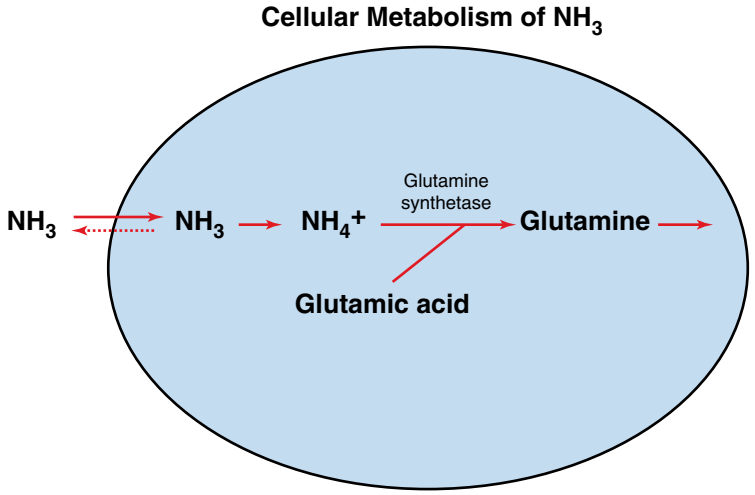

Fig. 12.7 Cellular metabolism of NH_3. N-13-ammonia diffuses freely through the capillary and cellular walls and then combines with glutamic acid to form glutamine, which traps the N-13 within the cell

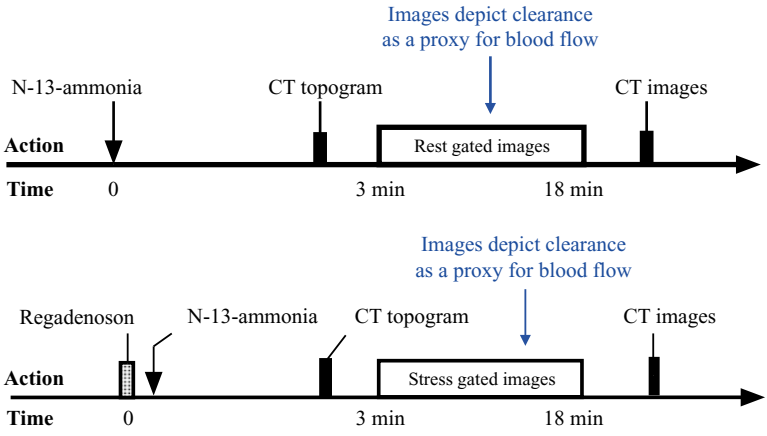

Fig. 12.8 Protocol summary diagram

Imaging N-13 is a positron emitter so imaging is done with a PET-CT scanner. Because PET-CT images are tomographic, there is no need for background correction, and, since the CT images provide density maps for attenuation correction, no additional attenuation correction is required.

Protocol design Because of the short 10 min half-life of N-13, the stress acquisition can be begun as soon as 30 min after the rest acquisition with very little residual activity from the rest injection present in the stress images. The image acquisition process is gated for subsequent evaluation of left ventricular wall motion and ejection fraction (Fig. 12.8).

Quantitative measurement: myocardial perfusion (clearance) The myocardial activity is measured throughout the left ventricle based on the transaxial tomograms. The three-dimensional results are then displayed on a relative basis in a two-dimensional "bull's-eye". In the case of PET-CT, there is no need to secondarily correct for background activity or attenuation. The activity distribution in the left ventricle of an individual patient is compared to normal ranges on a gender-specific basis (Fig. 12.9) [9]. This is an example of quantitation of function on a relative basis (see Chap. 8, Quantitation of Function: Relative Measurement).

Left ventricular ejection fraction: normal values No separate normal ranges for males and females were identified in the literature. The listed reference consisted of six males and six females (Table 12.1) [10]. Females, in general, have a smaller left ventricle than males and a slightly higher ejection fraction.

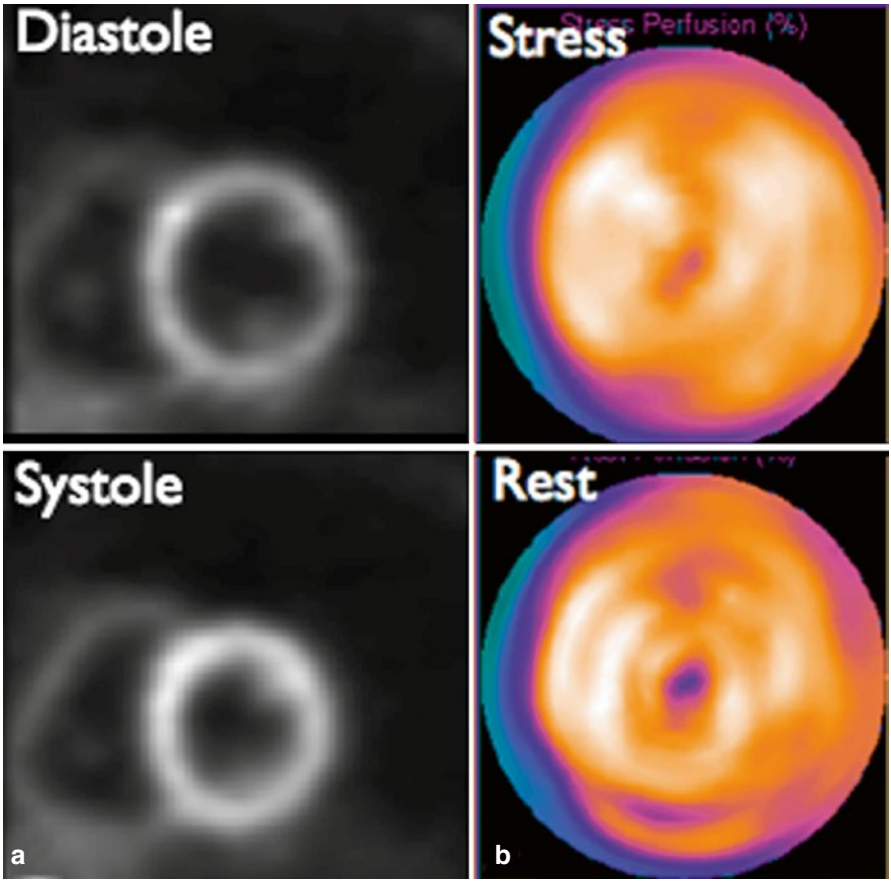

Fig. 12.9 Normal transaxial tomograms and bull's-eye displays from a gated N-13-ammonia myocardial perfusion study. (**a**) Transaxial myocardial perfusion images from the mid-left ventricle at systole and diastole. Note that two left and one right papillary muscles are visible and that when the ventricles contract with systole, the walls thicken. (**b**) The counts in the left ventricle are displayed in "bull's-eye" mode on a pseudo-color scale with the apical counts at the center and the basilar counts at the periphery of the disk

Myocardial Perfusion Study (Rb-82-Rubidium Chloride)

Overview The Myocardial Perfusion Study with Rb-82-rubidium is used to evaluate the distribution of blood flow and perfusion to the myocardium at rest and stress [11, 12]. In addition, the images are routinely gated to show regional wall motion and to allow calculation of the left ventricular ejection fraction [13].

However, despite the fact that the title of the study says "myocardial perfusion," the images actually reflect myocardial clearance. This is true of all of the nuclear medicine studies that have the word "perfusion" in the title. Relative clearance will reflect relative perfusion or blood flow as long as the extraction efficiency is

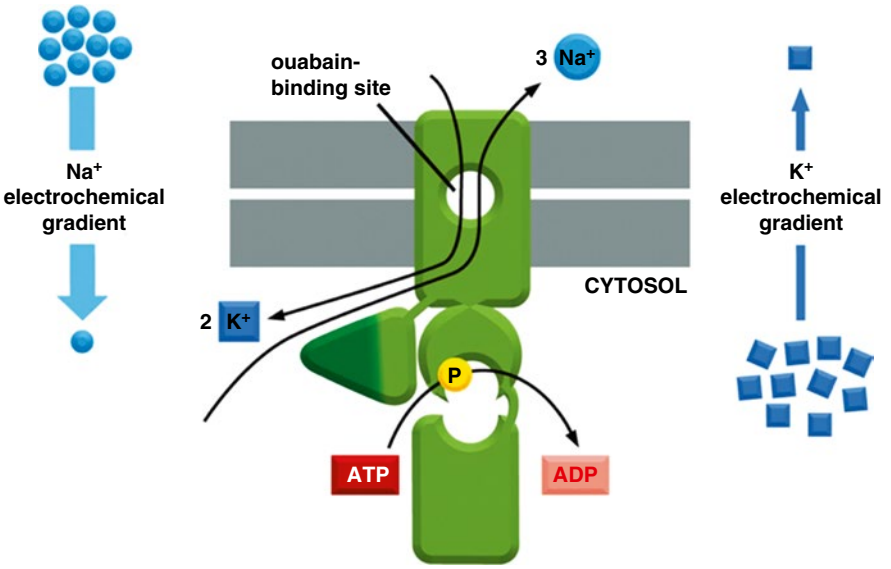

Fig. 12.10 The Na^+-K^+ pump. This transporter actively pumps Na^+ out and K^+ into the cell against their electrochemical gradients. For every molecule of ATP hydrolyzed inside the cell, three Na^+ are pumped out and two K^+ are pumped in (©Garland Science 2008)

uniform throughout the volume that is being imaged, but often it is not. For example, the extraction efficiency is higher in myocardium at low flow rates than at high flow rates (Fig. 12.6) [8].

Radiopharmaceutical characteristics Rubidium is a simple ion with a molecular weight of 85.47. It exists in the blood predominantly in the form of Rb^+.

Extraction mechanism Rubidium-82 is a physiologic analog of potassium and is actively transported into cells via the sodium-potassium pump. The concentration of potassium in the cell is 10–30 times higher than outside the cell. Small amounts of rubidium-82 constantly leak out of the cell and then are pumped back in until an equilibrium is reached (Fig. 12.10).

Extraction efficiency The exact extraction efficiency is unknown but empirically appears to be high. The extraction efficiency of all myocardial perfusion radiopharmaceuticals falls off at higher coronary flow rates, i.e., the degree of localization of tracer in myocardium is not a linear function of blood flow [8]. This phenomenon supports the fact that the images reflect clearance (Fig. 12.6). In addition, this means that the decreased blood flow to ischemic areas will be underestimated.

Extraction mechanism, saturable or non-saturable Non-saturable.

Interventions Image acquisition is done twice, once at rest and once following pharmacologic stress that significantly dilates normal coronary arteries. This maneuver reveals areas of coronary ischemia at stress that are not apparent at rest.

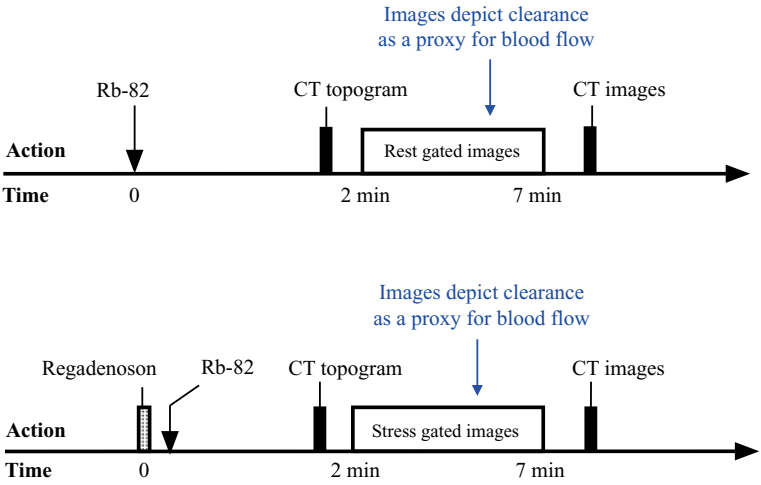

Fig. 12.11 Protocol summary diagram

Imaging Rb-82 is a positron emitter so imaging is done with a PET-CT scanner. Because PET-CT images are tomographic, there is no need for background correction, and, since the CT images provide density maps for attenuation correction, no additional attenuation correction is required.

Protocol design Because of the short 75 s half-life of Rb-82, the stress acquisition can be started just 30 min after the rest acquisition with very little residual activity from the rest injection present in the stress images. The image acquisition process is gated for subsequent evaluation of left ventricular wall motion and ejection fraction (Fig. 12.11).

Quantitative measurement: myocardial perfusion (clearance) The myocardial activity is measured throughout the left ventricle based on the transaxial tomograms. The three-dimensional results are then displayed on a relative basis in a two-dimensional "bull's-eye". In the case of PET-CT, there is no need to secondarily correct for background activity or attenuation. The activity distribution in the left ventricle of an individual patient is compared to gender-specific normal range (Fig. 12.9b).

Left ventricular ejection fraction: normal values No normal ranges for males were identified. Females have a smaller left ventricle than males and a slightly higher ejection fraction (Table 12.1) [14].

Myocardial Perfusion Study (Tc-99m-Sestamibi)

Overview The Myocardial Perfusion Study with Tc-99m-sestamibi is used to evaluate the distribution of blood flow and perfusion to the myocardium at rest and stress [15]. In addition, the images are routinely gated to show regional wall motion and to allow calculation of the left ventricular ejection fraction.

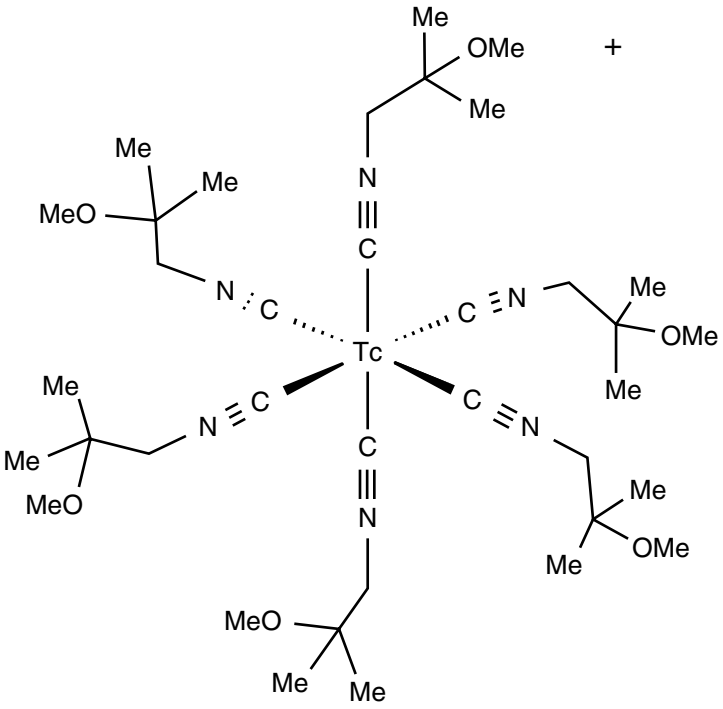

Fig. 12.12 Chemical structure of Tc-99m-sestamibi. "Me" stands for methyl group, CH_3. The radioisotope label, Tc-99m, is at the center

However, despite the fact that the title of the study says "myocardial perfusion," the images actually reflect myocardial clearance. This is true of all of the nuclear medicine studies that have the word "perfusion" in the title. Relative clearance will reflect relative perfusion or blood flow as long as the extraction efficiency is uniform throughout the volume that is being imaged, but often it is not. For example, the extraction efficiency is higher in myocardium at low flow rates than at high flow rates (Fig. 12.4).

Radiopharmaceutical characteristics Tc-99m-sestamibi has a molecular weight of 777.69. Its molecular structure is shown in Fig. 12.12.

Extraction mechanism Tc-99m-sestamibi (methoxyisobutylisonitrile) is a lipophilic cationic complex that passively diffuses across the myocardial membrane and binds to proteins within the mitochondria [16]. The myocardial washout is slow with a half-time of 7 h.

Extraction efficiency The exact extraction efficiency is moderate at 38 % [16]. The extraction efficiency of all myocardial perfusion radiopharmaceuticals falls off at higher coronary flow rates, i.e., the degree of localization of tracer in myocardium is not a linear function of blood flow [8]. This phenomenon supports the fact that the myocardial images of the biodistribution of Tc-99m-sestamibi reflect clearance rather than blood flow or perfusion (Fig. 12.6). In addition, this means that the decreased blood flow to ischemic areas will be underestimated.

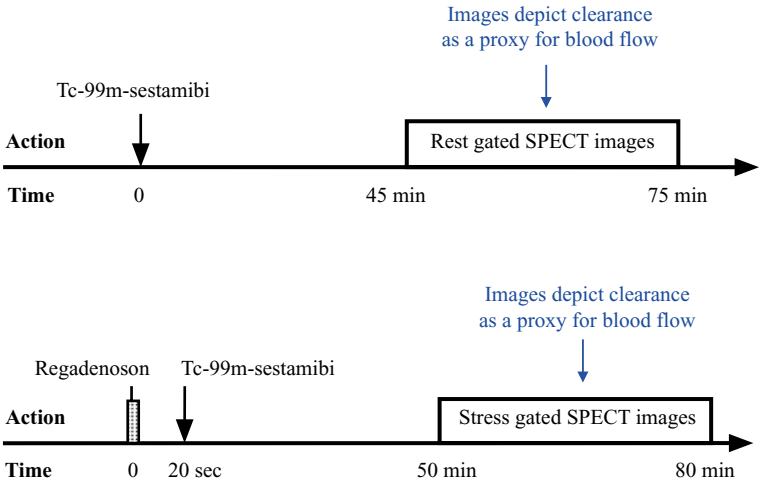

Fig. 12.13 Protocol summary diagram

Extraction mechanism: saturable or non-saturable Non-saturable.
Interventions Image acquisition is done twice, once at rest and once following pharmacologic stress that significantly dilates normal coronary arterioles and causes up to a 500 % increase in coronary blood flow [17]. This maneuver reveals areas of coronary ischemia at stress that are not apparent at rest.
Imaging Tc-99m-sestamibi is a single-photon emitter so imaging is done with a SPECT gamma camera. Because SPECT images are tomographic, there is no need for background correction. If imaging is done with SPECT-CT, the CT density maps allow a moderate degree of attenuation correction.
Protocol design Because of the relatively long half-life of Tc-99m-sestamibi, a 1-day rest and stress study requires that the second study is done with an administration of twice as much radiopharmaceutical as the first study so that the activity remaining from the first injection will be overwhelmed by the activity injected for the second acquisition. Usually, the rest study is done first and the stress study is done second. The image acquisition process is gated for subsequent evaluation of left ventricular wall motion and ejection fraction (Fig. 12.13).
Quantitative measurement: myocardial perfusion (clearance) The myocardial activity is measured throughout the left ventricle based on the transaxial tomograms. The three-dimensional results are then displayed on a relative basis in a two-dimensional "bull's-eye". In the case of SPECT-CT, there is no need to secondarily correct for background activity or attenuation. The activity distribution in the left ventricle of an individual patient is compared to normal ranges on a gender-specific basis (Fig. 12.9).
Left ventricular ejection fraction: normal values Females have a smaller left ventricle than males and a slightly higher ejection fraction (Table 12.1) [18–20]. In addition, the left ventricular ejection fraction increases with age for both males and females.

Myocardial Perfusion and Viability Study (Tl-201-Thallous Chloride)

Overview The Myocardial Perfusion and Viability Study with Tl-201-thallous chloride is used to evaluate the distribution of perfusion in the myocardium at stress and viability at rest [21]. In addition, the images are gated to show regional wall motion and to allow calculation of the left ventricular ejection fraction.

However, despite the fact that the title of the study includes "myocardial perfusion," the initial images actually reflect myocardial clearance. This is true of all of the nuclear medicine studies that have the word "perfusion" in the title. Relative clearance will reflect relative perfusion or blood flow as long as the extraction efficiency is uniform throughout the volume that is being imaged, but often it is not. For example, the extraction efficiency is higher in myocardium at low flow rates than at high flow rates, and the difference varies from one myocardial radiopharmaceutical to another (Fig. 12.6) [8].

Radiopharmaceutical characteristics Tl-201-thallous has a molecular weight of 204.37. It exists in the blood predominantly in the form of Tl^+.

Extraction mechanism The thallous ion behaves like K^+ because they both have a single positive charge and similar ionic radii [9]. Thus, Tl^+ is actively transported across the cell membrane by the Na-K pump (Fig. 12.10).

Extraction efficiency The exact extraction efficiency is moderate. The extraction efficiency of all myocardial perfusion radiopharmaceuticals falls off at higher coronary flow rates, i.e., the degree of localization of tracer in myocardium is not a linear function of blood flow. This phenomenon supports the fact that the myocardial images of the biodistribution of Tl-201-thallium reflect clearance rather than blood flow or perfusion (Fig. 12.6). This phenomenon supports the fact that the images reflect clearance (Fig. 12.6). In addition, this means that the decreased blood flow to ischemic areas will be underestimated.

Extraction mechanism, saturable or non-saturable Non-saturable.

Interventions Image acquisition is done twice, once at stress, either exercise or pharmacologic, and once approximately 3 h later at rest, so-called delayed images, for myocardial viability.

Imaging Tl-201 is a single-photon emitter so imaging is performed with a SPECT gamma camera. Because SPECT images are tomographic, there is no need for background correction. If imaging is done with SPECT-CT, the CT density maps allow a moderate degree of attenuation correction.

Protocol design The initial stress images demonstrate areas of ischemia at stress as well as areas that would also be ischemic at rest. However, the delayed images depict the distribution of viable myocardium even though it may be ischemic at rest. All viable myocardial cells have intact cell membranes and intact Na-K pumps so they will have normal potassium intracellular spaces. Thus, even cells that are ischemic at rest, but viable, will show thallium in the delayed images. This is the definition of hibernating myocardium. Without images of perfusion of myocardium at rest, it is not possible to differentiate hibernating myocardium (ischemic at rest, but viable) from stress ischemia (ischemic at stress, but normal perfusion at rest).

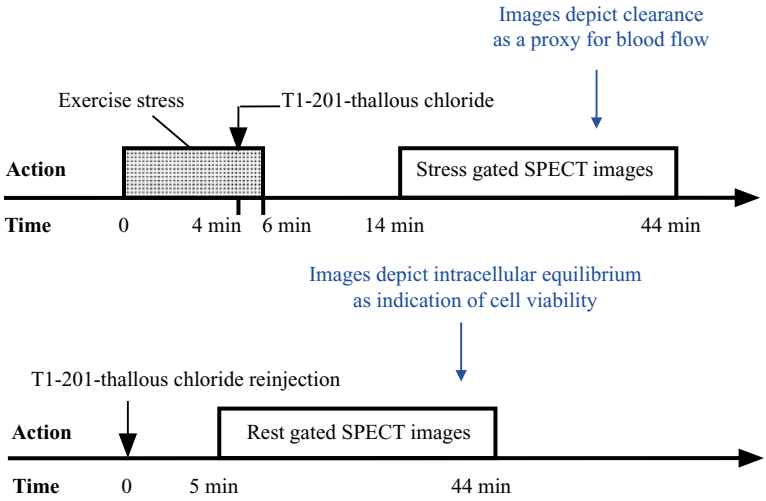

Fig. 12.14 Protocol summary diagram

The image acquisition process is gated for subsequent evaluation of left ventricular wall motion and ejection fraction (Fig. 12.14).

Quantitative measurement: myocardial perfusion (clearance) The myocardial activity is measured throughout the left ventricle based on the transaxial tomograms. The three-dimensional results are then displayed on a relative basis in a two-dimensional "bull's-eye" (Fig. 12.5b). In the case of SPECT-CT, there is no need to secondarily correct for background activity or attenuation. The activity distribution in the left ventricle of an individual patient is compared to normal ranges on a gender-specific basis [21–24].

Left ventricular ejection fraction: normal values Females have a smaller left ventricle than males and a slightly higher ejection fraction (Table 12.1) [3, 18].

Myocardial Viability Study (F-18-Fluorodeoxyglucose)

Overview Normal myocardium generates energy by metabolizing either free fatty acids or glucose. The myocardium utilizes free fatty acids unless there is circulating insulin present, as in the case of a recent meal containing significant carbohydrates. In addition, ischemic, but viable, myocardium uses mainly glucose because it switches from aerobic to anaerobic metabolism. Infarcted myocardium takes up neither glucose nor free fatty acids. Thus, the F-18-Fluorodeoxyglucose (FDG) Myocardial Viability Study, performed in the fed state, will detect myocardium that is ischemic at rest, but still viable (hibernating myocardium), and differentiates hibernating myocardium from infarct [25, 26].

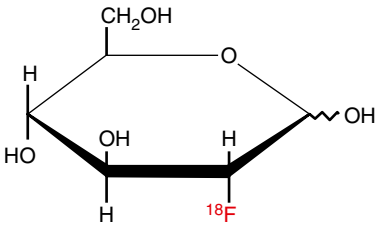

Fig. 12.15 F-18-fluorodeoxyglucose (FDG). The hydroxyl group on the second carbon of glucose has been replaced by a positron-emitting fluorine-18 atom to form the radiopharmaceutical FDG

Radiopharmaceutical characteristics FDG has a molecular weight of 193.17, and the chemical structure is shown in Fig. 12.15. It exists in the blood predominantly in the form of soluble FDG.

Extraction mechanism FDG is transported across cell membranes by transmembrane glucose transporters (Fig. 12.16). There are two main classes: glucose transporters (GLUTs) and sodium-dependent glucose transporters (SGLTs). FDG binds mostly to GLUTs, which are not found in the renal tubular cells. This difference explains the lack of reabsorption of FDG from the tubular lumen. There are 11 subtypes of GLUT transporters. The primary one in cardiac muscle is the GLUT4 transporter, whose expression is regulated by the level of insulin in the blood (Fig. 12.17) [26, 27].

Once inside the cell, FDG is phosphorylated by the hexokinase enzyme (Fig. 12.18). The addition of a phosphate group to FDG prevents the radiopharmaceutical from diffusing out of the cell. At the same time, the absence of a hydroxyl group at the second-carbon position prevents phosphorylated FDG from binding to the next enzyme in the glycolytic pathway. This fact prevents FDG from being metabolized and, in turn, prevents the radiolabel, F-18, from diffusing back out of the cell into the blood.

While differences in the metabolic behavior of FDG compared to native glucose make it an imperfect tracer of glucose, the differences actually improve FDG from an imaging point of view. If F-18 diffused back out of the cells, the contrast between cells that clear FDG and background including blood would be decreased. In addition, if FDG were reabsorbed by the kidneys, there would be a greater amount of FDG in the blood and again the contrast between cells that clear FDG and background would be decreased.

Extraction efficiency The exact extraction efficiency varies from organ to organ, and in some organs, i.e., heart, it depends greatly on whether there is insulin in the blood or not. In addition, as stated above, hypoxia, usually due to ischemia, increases the uptake of glucose and FDG in the myocardium.

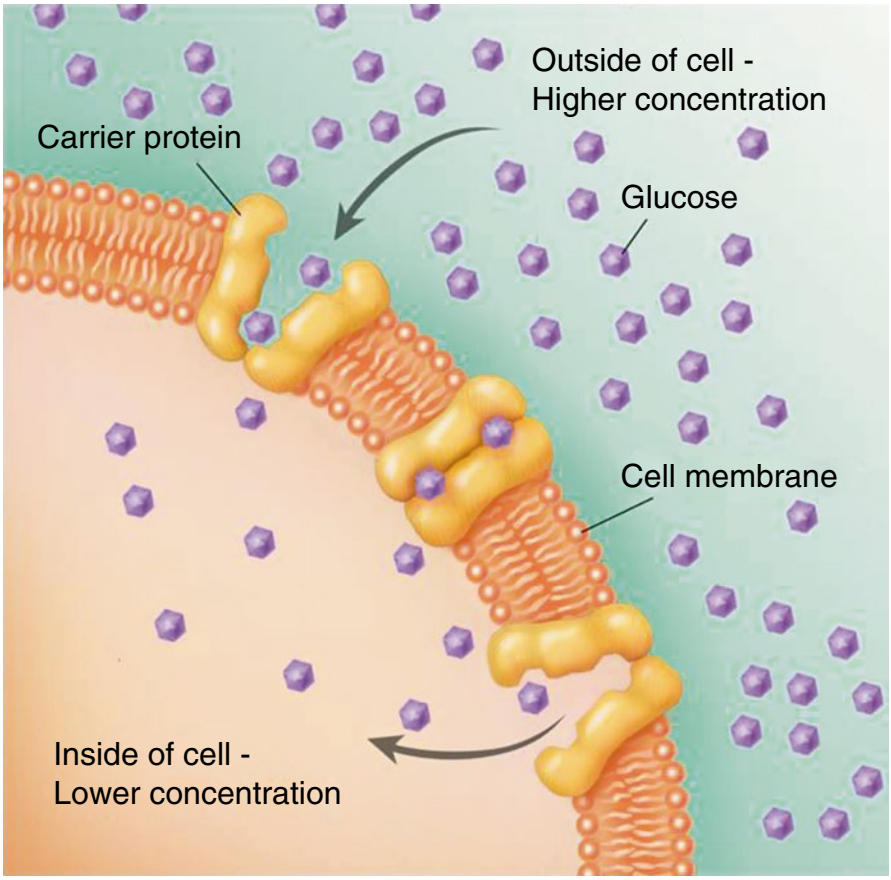

Fig. 12.16 Transport of glucose across the cell membrane by GLUT. GLUT transporters are an example of passive facilitative transport which is driven by the concentration gradient of glucose. The gradient is maintained by the intracellular phosphorylation of glucose. When glucose binds to the GLUT transporter, it induces a change in configuration of the transporter which transports the glucose across the cell membrane and causes the release of the glucose molecule in the intracellular space

Extraction mechanism saturable or non-saturable Saturable. Hyperglycemia increases competition for glucose receptors and decreases clearance of FDG. In addition, hyperglycemia can cause a downregulation of the GLUT receptors, e.g., GLUT4, so that not only is there an increase in nonradioactive glucose molecules for binding to the GLUT receptors, but there are fewer receptors (Fig. 12.17).

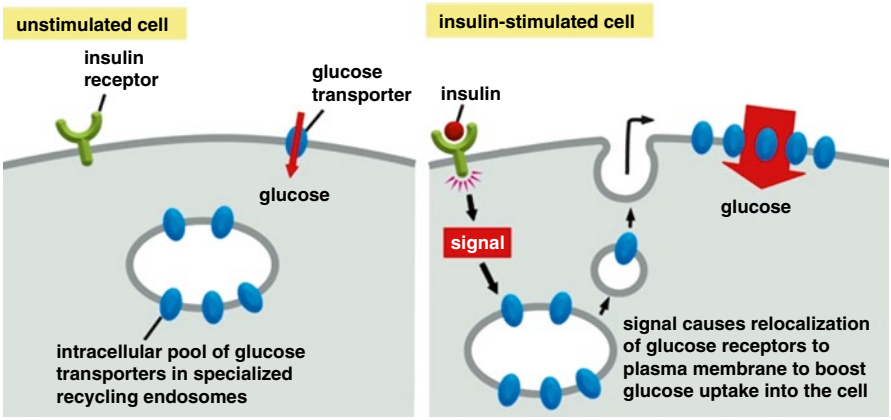

Fig. 12.17 Insulin regulation of cell membrane expression of GLUT4. GLUT4 is one of a family of passive facilitative glucose transporters. It is expressed in the cell membrane in response to the blood level of insulin. For the Myocardial Viability Study with FDG, the patient must be prepared with a high-carbohydrate meal to ensure that there will be circulating insulin at the time of FDG injection (©Garland Science 2008)

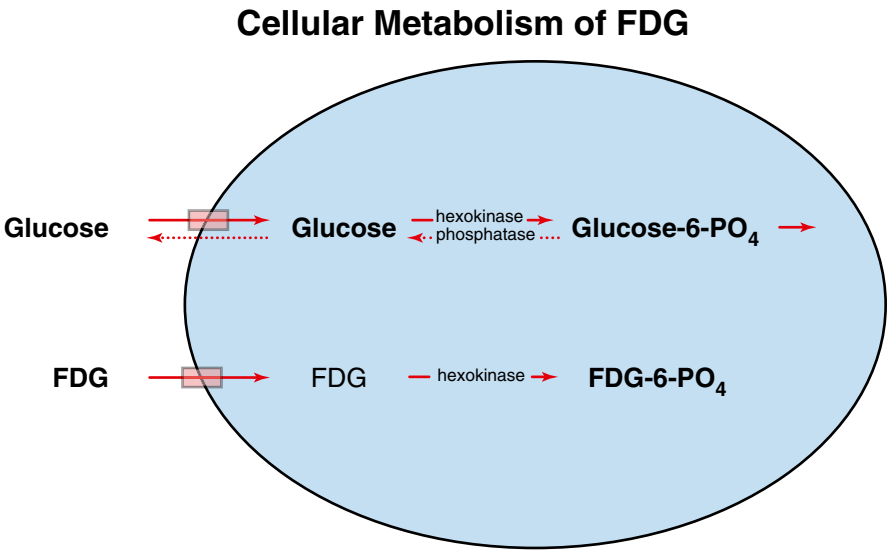

Fig. 12.18 Cellular uptake of glucose vs FDG. Most transmembrane glucose transport proteins bind to glucose and FDG equally. In addition, the hexokinase enzyme binds to and phosphorylates glucose and FDG equally well. However, the next enzyme in the glycolytic pathway binds phosphorylated glucose, but not phosphorylated FDG

Interventions The patient is instructed to eat a high-carbohydrate meal 2 h before injection of the radiopharmaceutical to ensure that there is some insulin in the blood. The postprandial carbohydrate meal increases the blood glucose level, which, in

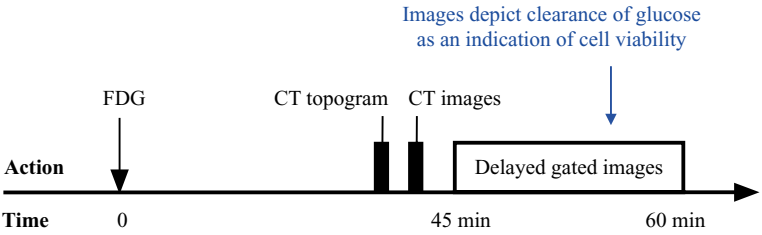

Fig. 12.19 Protocol summary diagram

turn, increases the blood insulin level. Increased blood insulin increases the GLUT4 expression and clearance rate in myocardial cells significantly.

Imaging F-18 is a positron emitter so imaging is done with a PET-CT scanner. Because the PET images are tomographic, there is no need for background correction. And because the CT images provide high-resolution density maps, the images are corrected for attenuation.

Protocol design The high-carbohydrate meal 2 h prior to injection of the FDG is critical. Without insulin in the blood, there may be no uptake or clearance of FDG by the myocardium or even patchy uptake which can be confusing.

The image acquisition process is gated for subsequent evaluation of the left ventricular wall motion and ejection fraction (Fig. 12.19).

Quantitative measurement: myocardial viability The myocardial activity is measured throughout the left ventricle based on the transaxial tomograms. The three-dimensional results are then displayed on a relative basis in a two-dimensional "bull's-eye". In the case of PET-CT, there is no need to secondarily correct for background activity or attenuation. The activity distribution in the left ventricle of an individual patient is compared to normal ranges on a gender-specific basis.

Left ventricular ejection fraction: normal values Normal values for the left ventricular ejection fraction could not be identified, but are probably similar to those listed for Tc-99m-sestamibi at rest. Females have a smaller left ventricle than males and a slightly higher ejection fraction (Table 12.1).

References

Cardiac Gated Blood Pool Study (Tc-99m-Red Blood Cells)

1. Freedman JC. Cell membranes. In: Sperelakis N, editor. Cell physiology sourcebook: essentials of membrane biophysics. 4th ed. London: Academic Press; 2012. p. 49.
2. Massardo T, Jaimovich R, Lavados H, et al. Comparison of radionuclide ventriculography using SPECT and planar techniques in different cardiac conditions. Eur J Nucl Med Mol Imaging. 2007;34:1735–46.
3. Berman DS, Maddahi J, Garcia EV, et al. Assessment of left and right ventricular function with multiple gated equilibrium cardiac blood pool scintigraphy. In: Berman DS, Mason DT, editors. Clinical nuclear cardiology. New York: Grune & Stratton; 1981. p. 247.
4. Jackson SA, Nickerson R, Martin RH, et al. Factors of variability in the radionuclide evaluation of global and regional left ventricular ejection fraction. J Nucl Med Technol. 1991;19:77–80.
5. Corbett JR, Akinboboye OO, Bacharach SL, et al. ASNC imaging guidelines for nuclear cardiology procedures. J Nucl Cardiol. 2008.

Lymphoscintigraphy (Filtered Tc-99m-Sulfur Colloid)

6. Goldfarb LR, Alazraki NP, Eshima D, et al. Lymphoscintigraphic identification of sentinel lymph nodes: clinical evaluation of 0.22 μm filtration of Tc-99m sulfur colloid. Radiology. 1998;208:505–9.
7. Nopajaroonsri C, Simon GT. Phagocytosis of colloidal carbon in a lymph node. Am J Pathol. 1971;65:25–42.

Myocardial Perfusion Study (N-13-Ammonia)

8. Schelbert HR. Positron emission tomography of the heart: methodology, findings in the normal and disease heart, and clinical applications. In: Phelps ME, editor. PET: molecular imaging and its clinical applications. New York: Springer; 2004. p. 402–3.
9. Eisner RL, Tamas MJ, Coninger K, et al. Normal SPECT thallium-201 bull's-eye display: gender differences. J Nucl Med. 1988;29:1901–9.
10. Hickey KT, Sciacca R, Sabahat B, et al. Assessment of cardiac wall motion and ejection fraction with gated PET using N-13 ammonia. Clin Nucl Med. 2004;29:243–8.

Myocardial Perfusion Study (Rb-82-Rubidium Chloride)

11. Santana CA, Folk RD, Garcia EV, et al. Quantitative Rb-82 PET-CT: development and validation of myocardial perfusion database. J Nucl Med. 2007;48:1122–8.
12. Fakhri GE, Kardan A, Sitek A, et al. Reproducibility and accuracy of quantitative myocardial blood flow assessment with Rb-82 PET: comparison with N-13-ammonia PET. J Nucl Med. 2009;50:1062–71.
13. Chander A, Brenner M, Lautamaki R, et al. Comparison of measures of left ventricular function from electrocardiographically gated Rb-82 PET with contrast-enhanced CT ventriculography: a hybrid PET-CT analysis. J Nucl Med. 2008;49:1643–50.
14. Bravo PE, Chien D, Javadi M, et al. Reference ranges for LVEF and LV volumes from electrocardiographically gated Rb-82 cardiac PET-CT using commercially available software. J Nucl Med. 2010;51:898–905.

Myocardial Perfusion Study (Tc-99m-Sestamibi)

15. Zanco P, Zampiero A, Favero A, et al. Myocardial technetium-99m sestamibi single-photon emission tomography as a prognostic tool in coronary artery disease: multivariate analysis in a long-term prospective study. Eur J Nucl Med. 1995;22:1023–8.
16. Gopal BS. Tc-99m-labeled radiopharmaceuticals. In: Gopal BS, editor. Fundamentals of nuclear pharmacy. New York: Springer; 2010. p. 124.
17. Duncker DJ, Bache RJ. Regulation of coronary blood flow during exercise. Physiol Rev. 2008;88:1009–86.
18. Ababneh AA, Sciacca RR, Kim B, et al. Normal limits for left ventricular ejection fraction and volumes estimated with gated myocardial perfusion imaging in patients with normal exercise test results: influence of tracer, gender, and acquisition camera. J Nucl Cardiol. 2000;7:661–8.
19. Rozanski A, Nicholes K, Yao SS, et al. Development and application of normal limits for left ventricular ejection fraction and volume measurements from Tc-99m-sestamibi myocardial perfusion gated SPECT. J Nucl Med. 2000;41:1445–50.
20. De Bondt P, Van de Wiele C, De Sutter J, et al. Age- and gender-specific differences in left ventricular cardiac function and volumes determined by gated SPET. Eur J Nucl Med. 2001;28:620–4.

Myocardial Viability Study (Tl-201-Thallous Chloride)

21. Schafers M, Matheja P, Hasfeld M, et al. The clinical impact of thallium-201 reinjection for the detection of myocardial hibernation. Eur J Nucl Med. 1996;23:407–13.
22. Eisner RL, Tamas MJ, Coninger K, et al. Normal SPECT thallium-201 bull's-eye display: gender differences. J Nucl Med. 1988;29:1901–9.
23. Garcia EV, DePuey G, Sonnemaker RE, et al. Quantification of the reversibility of stress-induce thallium-201 myocardial perfusion defects: a multicenter trial using bull's-eye polar maps and standard normal limits. J Nucl Med. 1990;31:1761–5.
24. Yamagishi H, Shirai N, Yoshiyama M, Teragaki M, et al. Incremental value of left ventricular ejection fraction for detection of multivessel coronary artery disease in exercise Tl-201 gated myocardial perfusion imaging. J Nucl Med. 2002;43:131–9.

Myocardial Viability Study (F-18-Fluorodeoxyglucose)

25. Schelbert HR. F-18-deoxyglucose and the assessment of myocardial viability. Semin Nucl Med. 2002;32:60–9.
26. Abraham A, Nichol G, Williams KA, et al. F-18-FDG PET imaging of myocardial viability in an experienced center with access to F-18-FDG and integration with clinical management teams: the Ottawa-FIVE substudy of the PARR 2 trial. J Nucl Med. 2010;51:567–74.
27. Wood IS, Trayhurn P. Glucose transporters (GLUT and SGLT): expanded families of sugar transport proteins. Br J Nutr. 2003;89:3–9.

Central Nervous System

13

Brain Death Angiography Study (Tc-99m-DTPA)

Overview The images of the Radionuclide Brain Death Angiography Study depict the regional distribution of blood flow to and the vascular volume in the brain and surrounding structures including the superior sagittal sinus [1].

Radiopharmaceutical characteristics The radiopharmaceutical Tc-99m-DTPA is a combination of the ligand diethylenetriaminepentaacetic acid (pentetic acid), a metal chelator, and Tc-99m, a metal. Its chemical structure is shown in Fig. 13.1. The radiopharmaceutical has a molecular weight of 482.31.

Extraction mechanism None in the brain. In general, Tc-99m-DTPA readily passes through the capillary endothelium and equilibrates in the extracellular space. However, in the brain it remains in the vascular space except where the blood-brain barrier has been damaged.

Extraction efficiency Normally zero.

Extraction mechanism saturable or non-saturable Not applicable.

Interventions None.

Imaging Gamma camera planar imaging with a high-resolution low-energy collimator is the most commonly used.

Protocol design The protocol consists of two parts: acquisition of sequential two second images of the brain in the anterior projection for 30 s during the first circulation beginning at the time of injection and acquisition of delayed images of the brain in the anterior projection (Fig. 13.2).

Quantitative measurements None.

W.C. Klingensmith III, *The Mathematics and Biology of the Biodistribution of Radiopharmaceuticals-A Clinical Perspective*,
DOI 10.1007/978-3-319-26704-3_13

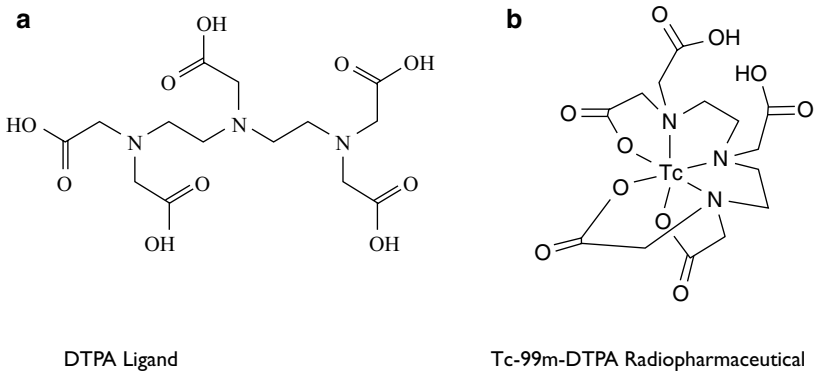

Fig. 13.1 Chemical diagrams of Tc-99m-DTPA. (**a**) Diethylenetriaminepentaacetic acid (*DTPA*) ligand without the radioisotope Tc-99m. (**b**) Tc-99m-DTPA after the metal chelator, DTPA, has chelated the metal, Tc-99m

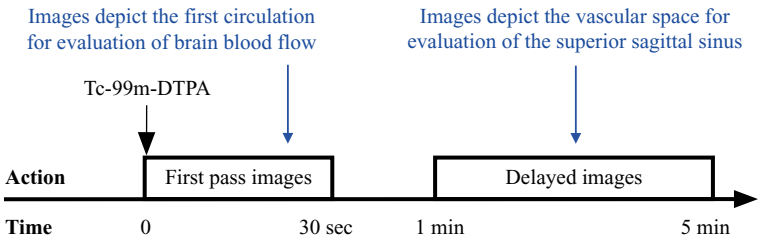

Fig. 13.2 Protocol summary diagram

Brain Glucose Metabolism Study (F-18-Fluorodeoxyglucose)

Overview The images of the Brain Glucose Metabolism Study with F-18-fluorodeoxyglucose (FDG) depict the distribution of glucose metabolism in the brain in a tomographic fashion. The sole energy source of the brain is glucose, and the gray matter uses three to four times as much glucose as the white matter on a per volume basis [2].

Radiopharmaceutical characteristics FDG is an analog of glucose and exists in blood predominantly in the form of soluble FDG. It has a molecular weight of 193.17, and its chemical structure is shown in Fig. 13.3.

Extraction mechanism FDG is transported across cell membranes by glucose transporters (GLUTs), which are passive facilitative transporters. Several GLUTs are found in the brain including GLUT1 and GLUT4 (Fig. 13.4) [3].

Once inside the cell, FDG is phosphorylated by the hexokinase enzyme. The addition of a phosphate group to FDG prevents the radiopharmaceutical from diffusing out of the cell. At the same time, the absence of a hydroxyl group at the second carbon position prevents phosphorylated FDG from binding to the next enzyme in the glycolytic pathway. This fact prevents FDG from being metabolized and, in turn, prevents the radiolabel, F-18, from diffusing back out of the cell into the blood (Fig. 13.5).

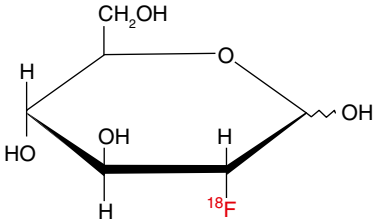

Fig. 13.3 F-18-Fluorodeoxyglucose (FDG). The hydroxyl group on the second carbon of glucose has been replaced by a positron emitting fluorine-18 atom to form the radiopharmaceutical FDG

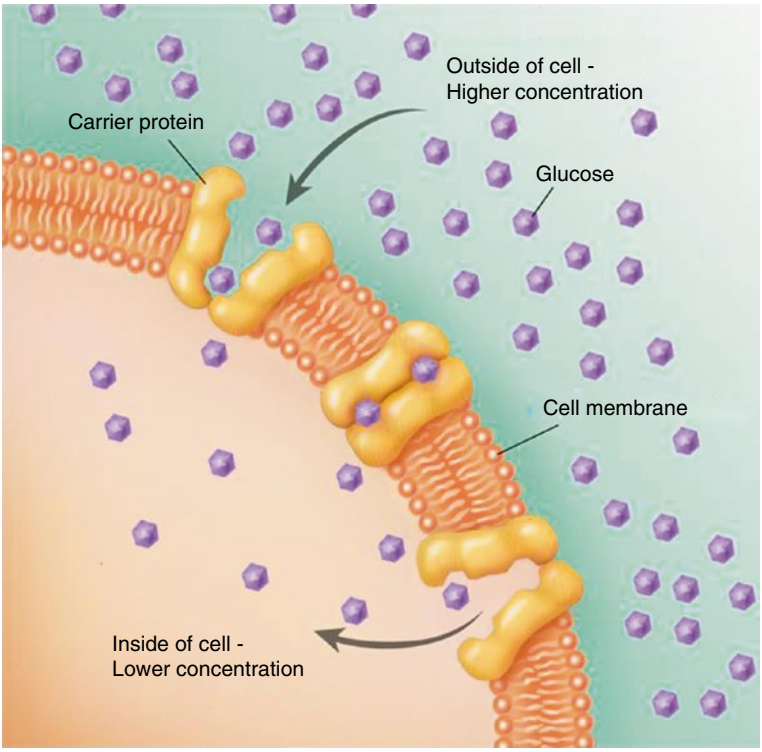

Fig. 13.4 Transport of glucose across the cell membrane by GLUT1. GLUT transporters are an example of passive facilitative transport which is driven by the concentration gradient of glucose. The gradient is maintained by the intracellular phosphorylation of glucose. When glucose binds to the GLUT transporter, it induces a change in configuration of the transporter which in turn causes the release of the glucose molecule in the intracellular space

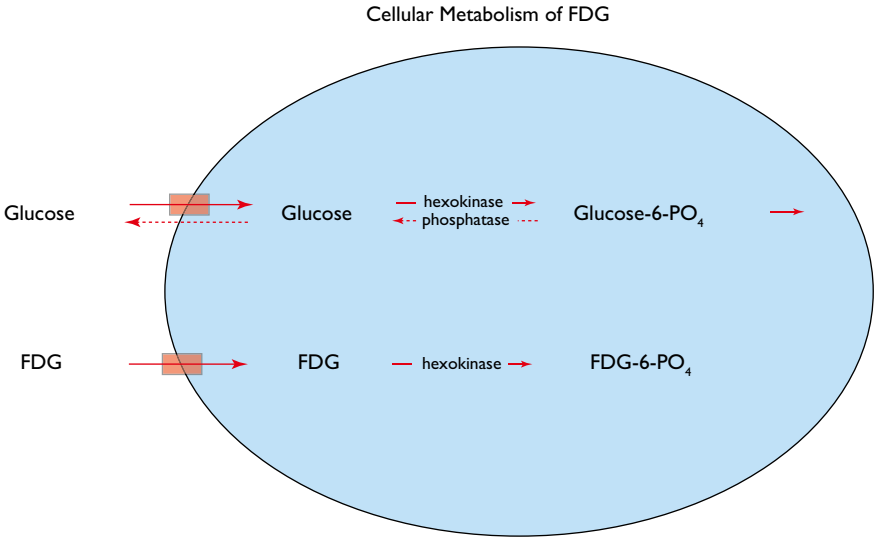

Fig. 13.5 Cellular uptake of glucose vs. FDG. Most transmembrane glucose transport proteins bind to glucose and FDG equally. In addition, the hexokinase enzyme binds to and phosphorylates glucose and FDG equally well. However, the next enzyme in the glycolytic pathway binds phosphorylated glucose, but not phosphorylated FDG

While differences in the metabolic behavior of FDG compared to native glucose make it an imperfect tracer of glucose, the differences actually improve FDG from an imaging point of view. If F-18 diffused back out of cells, the contrast between cells that clear FDG and background including blood would be decreased. In addition, if FDG were reabsorbed by the kidneys, there would be a greater amount of FDG in the blood and again the contrast between cells that clear FDG and background would be decreased.

Extraction efficiency The exact extraction efficiency of FDG in the brain is unknown but is probably higher in gray matter than in white matter [4].

Extraction mechanism saturable or non-saturable Saturable. Hyperglycemia increases competition for glucose receptors and decreases clearance of FDG. In addition, hyperglycemia can cause a downregulation of the GLUT receptors so that not only is there an increase in nonradioactive glucose to compete with FDG for GLUT receptors but there are fewer receptors (Fig. 13.6) [5].

Interventions None.

Imaging F-18 is a positron emitter so imaging is done with a PET-CT scanner. Because the PET images are tomographic, there is no need for background correction. And because the CT images provide high-resolution density maps, the PET images can be corrected for attenuation.

Protocol design High-resolution 15 min PET images are obtained beginning at 45 min after administration of the FDG. These glucose metabolism tomograms are compared to the high-resolution CT images of brain anatomy (Fig. 13.7).

Quantitative measurements None.

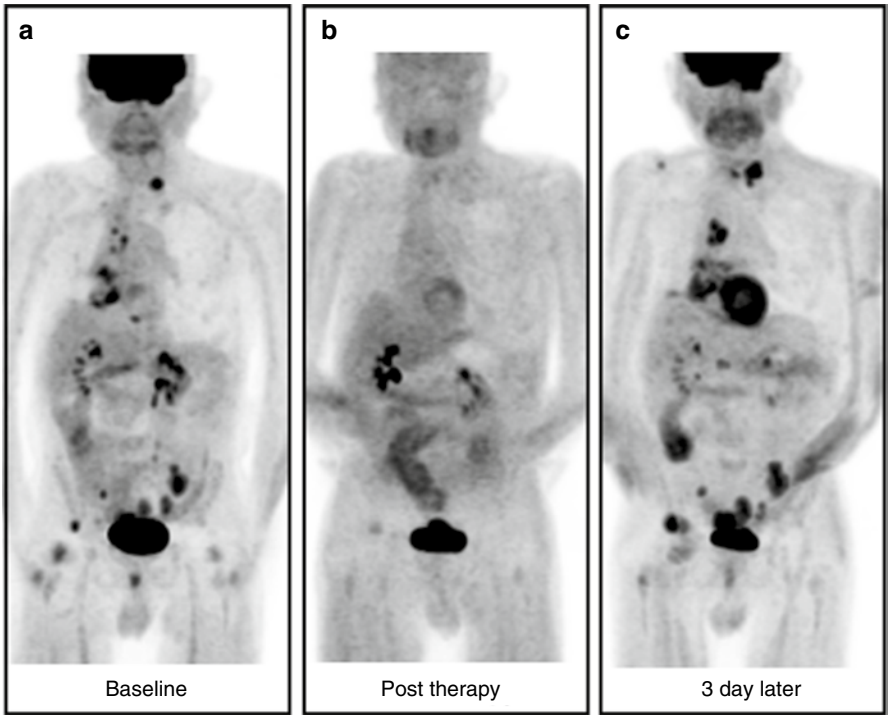

Fig. 13.6 A 76-year-old male with lung cancer. Anterior MIP (maximum intensity projection) images from sequential FDG PET-CT studies. (**a**) The baseline study shows widespread metastases. The blood glucose was 105 mg/dL. (**b**) Post-therapy (11 weeks later), the metastases appear to have resolved. Of note, there is very little FDG uptake in the brain. The patient was not known to be a diabetic, but the blood glucose was 260 mg/dL. (**c**) The patient was sent to his physician for treatment of newly diagnosed diabetes and the FDG study was repeated 3 days later. At the time of the repeat study, his blood glucose was 76 mg/dL. In comparison to the baseline study, the repeat study demonstrates progressive metastatic disease and normal brain uptake. The elevated blood glucose level at the time of the initial post-therapy study is probably insufficient to fully explain the essentially complete lack of uptake in the metastases and brain. It is postulated that, in addition to a possible competitive effect, the elevated glucose level caused a downregulation of the glucose receptors in tumor and the brain

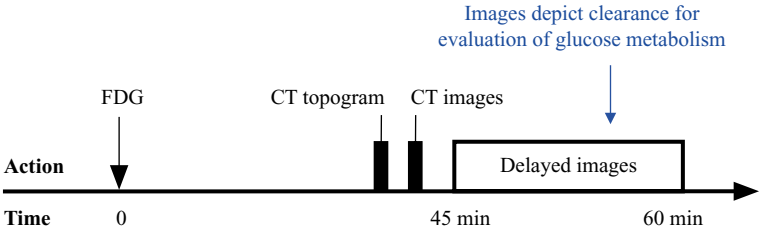

Fig. 13.7 Protocol summary diagram

Brain Perfusion Study (Tc-99m-HMPAO)

Overview The SPECT images of the Brain Perfusion Study depict the distribution of blood flow and perfusion to the various structures of the brain [6].

However, despite the fact that the title of the study says "brain perfusion," the images actually reflect brain clearance, i.e., primarily blood flow times extraction efficiency. This is true of all nuclear medicine studies that have the word "perfusion" in the title. Relative clearance will reflect relative perfusion or blood flow only as long as the extraction efficiency is uniform throughout the volume that is being imaged, but often it is not.

Radiopharmaceutical characteristics Tc-99m-HMPAO (hexamethylpropyleneamineoxime) is a lipophilic molecular complex with a molecular weight of 383.32. Its chemical structure is shown in Fig. 13.8.

Extraction mechanism Because of its lipophilic nature, Tc-99m-HMPAO diffuses readily across the endothelial capillaries of the brain, through the blood-brain barrier, and across the cell membranes of neurons (Fig. 13.9). Once in the intracellular space, most of Tc-99m-HMPAO becomes hydrophilic and is unable to diffuse back out of the cell. A small amount binds to intracellular components [8]. At high flow rates, Tc-99m-HMPAO underestimates cerebral blood flow [6].

Extraction efficiency The exact extraction efficiency in the brain is unknown but appears to be moderate [6].

Extraction mechanism saturable or non-saturable Non-saturable.

Interventions None.

Imaging Gamma camera SPECT imaging with a high-resolution low-energy collimator and SPECT computer software is the most commonly used.

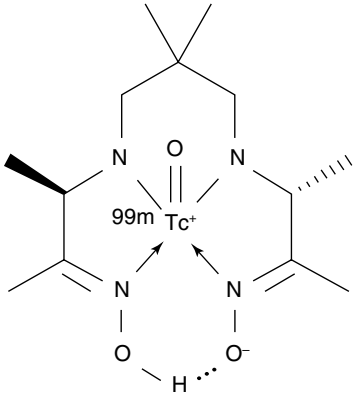

Tc-99m-HMPAO (exametazime)

Fig. 13.8 Tc-99m-HMPAO (Tc-99m-exametazime)

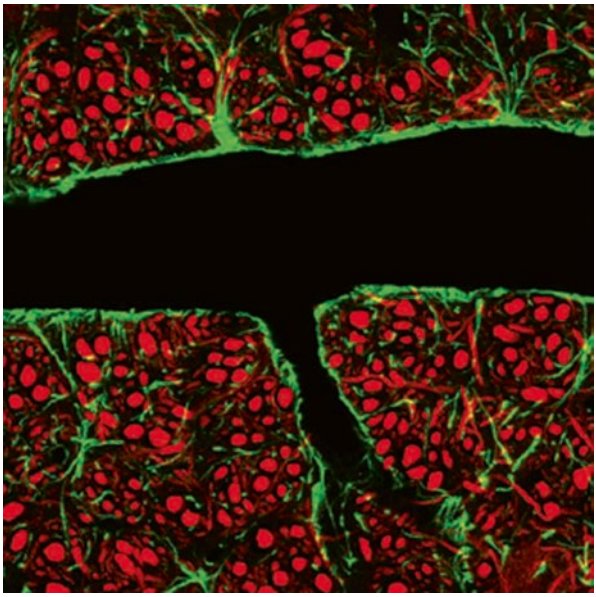

Fig. 13.9 Blood-brain barrier. The *red* structures represent neurons. The *green* structures are astrocytes that form the blood-brain barrier along the margins of vessel (Emily [7]; original in *Science Translational Medicine*)

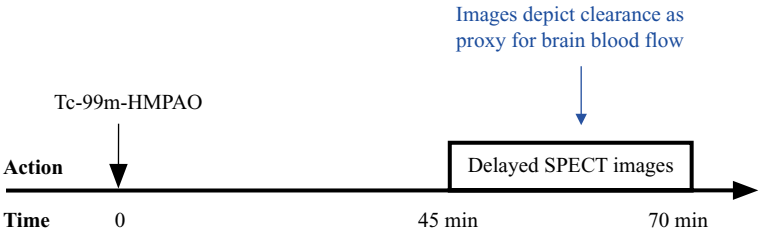

Fig. 13.10 Protocol summary diagram

Protocol design Forty-five minutes after injection of the radiopharmaceutical, SPECT images are acquired of the brain (Fig. 13.10).
Quantitative measurements None.

Cisternography (In-111-DTPA)

Overview Cisternography images depict the flow of cerebrospinal fluid along normal and abnormal pathways following injection of the tracer into the lumbar intrathecal space.
Radiopharmaceutical characteristics In-111-DTPA is a combination of the ligand diethylenetriaminepentaacetic acid (pentetic acid), a metal chelator, and In-111, a metal. It has a molecular weight of 508.22 D, and its chemical structure is shown in Fig. 13.11.

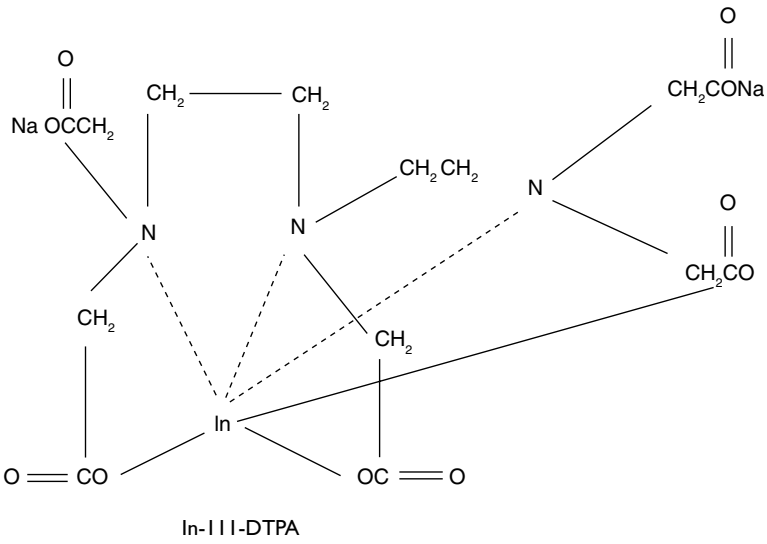

Fig. 13.11 Chemical structure of In-111-DTPA. Diethylenetriaminepentaacetic acid (DTPA) ligand with the radioisotope In-111

Extraction mechanism Until the In-111-DTPA reaches the superior sagittal sinus over the brain, there is no extraction or clearance of the tracer. Once the In-111-DTPA reaches the subarachnoid space over the convexity of the brain, it is reabsorbed along with cerebrospinal fluid (CSF) through the arachnoid villa and into the venous blood of the superior sagittal sinus. Following reabsorption, the tracer is carried away in the venous blood and excreted from the body by glomerular filtration in the kidneys. The exact mechanism by which CSF is reabsorbed by the arachnoid villa is unknown but may involve flow through a one-way valve in the cells of the arachnoid matter [9].

Since In-111-DTPA does not accumulate in the superior sagittal sinus, the images of the head do not directly reflect the reabsorption process, and no extraction mechanism is imaged. During the study, the tracer moves simply with the bulk flow of CSF, and the images demonstrate the pathway and speed of the movement of the tracer through the subarachnoid space from the lumbar region to the top of the brain (Fig. 13.12).

Extraction efficiency The extraction efficiency of In-111-DTPA at the arachnoid villa of the superior sagittal sinus is essentially 100 %.

Extraction mechanism saturable or non-saturable Non-saturable.

Interventions None.

Imaging Imaging is performed with a gamma camera fitted with a medium-energy parallel-hole collimator.

Protocol design The movement of In-111-DTPA in the CSF after intrathecal injection at the lumbar spine level is imaged over a 24 h period. Delayed images are acquired as needed (Figs. 13.12 and 13.13).

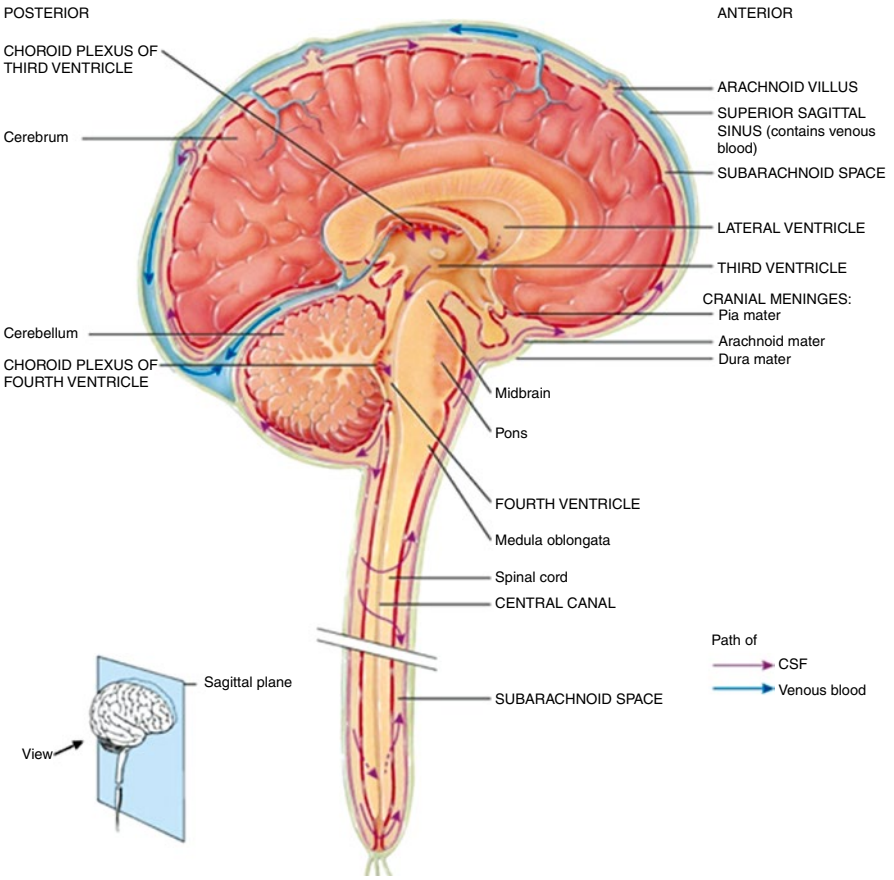

Fig. 13.12 Sagittal section of brain and spinal cord showing origin, pathway of flow, and site of reabsorption of CSF [10]

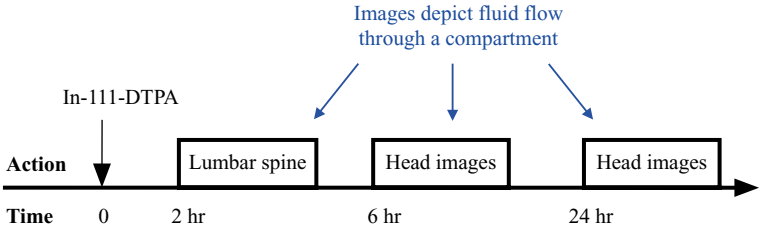

Fig. 13.13 Protocol summary diagram

Quantitative measurement The images essentially reflect the central volume principle (see Chap. 5, Mean Transit Time: Central Volume Principle).

$$\bar{T}\left(\text{sec}\right) = \frac{V\left(\text{mL}\right)}{F\left(\text{mL}/\text{sec}\right)} \sim T_{\text{LE}}\left(\text{sec}\right) \tag{13.1}$$

Here the "central volume principle" equation has been solved for mean transit time instead of flow. $\bar{T}$ represents the mean transit time of blood flow through the subarachnoid space, V represents the volume of the subarachnoid space, F represents the production and flow of CSF, and the symbol "~" stands for "varies as." However, since the subarachnoid space volume and CSF flow cannot be determined, the mean transit time cannot be calculated. Instead, the leading edge transit time, T_{LE}, is assessed visually by noting when the leading edge of the tracer reaches the region of the superior sagittal sinus. Of note, the pathway may change with disease, i.e., reabsorption may occur in the lateral ventricles in addition to or instead of the superior sagittal sinus. The upper limits of normal for the leading edge transit time of the bolus to reach the superior sagittal sinus is 24 hours.

When the cisternogram is performed for the purpose of identifying the source of CSF rhinorrhea, there is also a nonvisual quantitative measurement. Nasal pledgets of a standard size are placed into the anterior and posterior portions of both nasal cavities 2 h after the intrathecal injection of In-111-DTPA and removed 4 h later. In addition, blood samples are drawn at the same two times. The pledget and plasma specimens are counted in a gamma well counter, and the results are expressed as a ratio of the amounts of activity in the pledgets, i.e., nasal cavities, relative to the amount of activity in the plasma.

This measurement represents a quasi-absolute nuclear medicine measurement with plasma activity serving as a proxy for the amount of In-111-DTPA administered intrathecally and pledget activity reflecting the amount of labeled CSF that has leaked into the nasal cavities (see Chap. 10, Other Quantitative Techniques). Any increased activity in the pledgets comes from leakage of CSF containing a relatively high amount of activity from the subarachnoid space at the base of the brain through a break in the dura and skull base to reach the nasal cavity.

Quantitative measurement: Normal range The normal range for the pledget to plasma ratio is 1.3 or less [11].

Striatal Dopamine Transporter Study (I-123-Ioflupane [DaTscan®])

Overview The Striatal Dopamine Transporter Study with I-123-ioflupane depicts the prevalence and biodistribution of dopamine transporter receptors at the synaptic junction of the presynaptic neuron in the striatum (putamen and head of the caudate nucleus) [12, 13]. When stimulated by an action potential, i.e., electrical charge, presynaptic storage vesicles filled with dopamine fuse with the presynaptic plasma membrane and release the dopamine into the synaptic cleft. The dopamine molecules transmit a signal by binding to dopamine receptors on the postsynaptic plasma

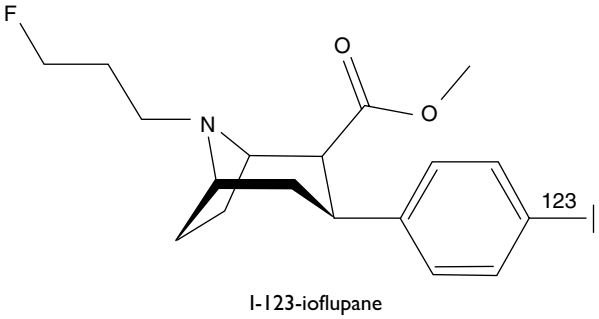

Fig. 13.14 Chemical structure I-123-ioflupane (DaTscan®)

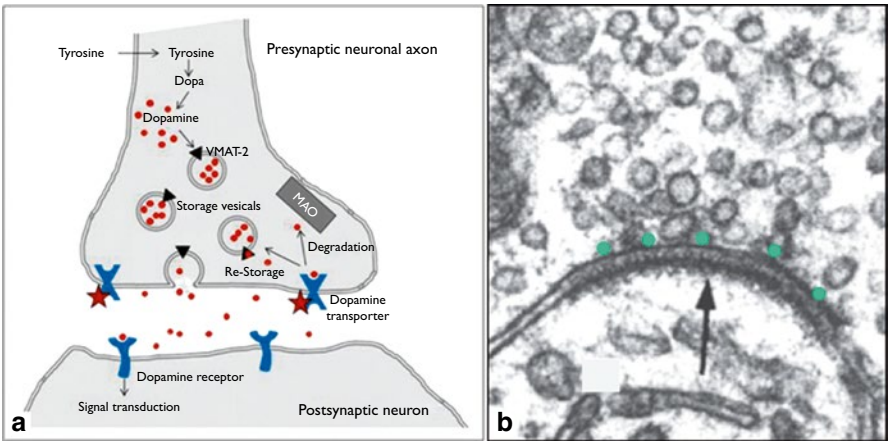

Fig. 13.15 Neuronal synapse. (**a**) *Red dots* represent dopamine which I-123-ioflupane traces. When an action potential reaches the nerve terminal, dopamine is released, passes across the synapse, and binds to dopamine receptors which initiates a postsynaptic signal. Then free dopamine binds to dopamine transporter receptors on the presynaptic side to be repackaged into vesicles and reused [15]. The *red stars* indicate where I-123-ioflupane binds to the dopamine transporter receptors. (**b**) Electron micrograph shows synaptic junction (*arrow*) with presynaptic axon above (distinguished by numerous vesicles containing neurotransmitters like dopamine) and the postsynaptic axon below with only a few vesicles. The *green dots* represent dopamine transporter proteins in the presynaptic plasma membrane [16]

membrane. The free dopamine molecules bind to dopamine transporters on the presynaptic plasma membrane and are internalized into storage vesicles for reuse [14].

Radiopharmaceutical characteristics I-123-ioflupane is derived from cocaine and is a Schedule II controlled substance under the Controlled Substance Act in the USA. Its molecular weight is 289.38 and its chemical structure is shown in Fig. 13.14.

Extraction mechanism I-123-ioflupane binds to the dopamine transporter on the presynaptic side of the synaptic junction (Fig. 13.15).

Extraction efficiency Unknown.

Extraction mechanism saturable or non-saturable Saturable. The drugs of abuse, cocaine and amphetamine, are the ones most likely to decrease the uptake of I-123-ioflupane significantly. These two drugs should be discontinued for 4–5

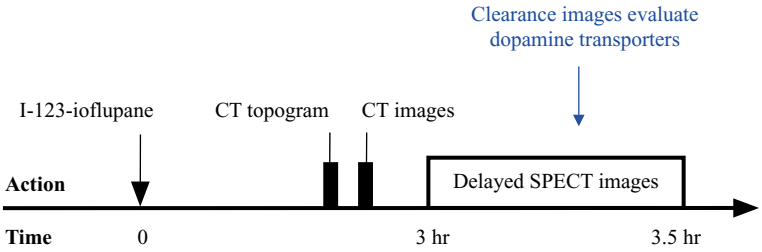

Fig. 13.16 Protocol summary diagram

plasma clearance half-lives before performing an I-123-ioflupane study [14]. A number of other drug classes and drugs bind to the dopamine transporter with high affinity and may interfere with the Striatal Dopamine Transporter Study [14].
Interventions None.
Imaging SPECT-CT imaging with a low-energy high-resolution gamma camera collimator and SPECT computer software is the most commonly used.
Protocol design SPECT-CT images of the brain are acquired at 3 h after intravenous administration of the radiopharmaceutical (Fig. 13.16).
Quantitative measurement None in general.

Ventricular Shunt Study (Tc-99m-DTPA)

Overview The Ventricular Shunt Study evaluates the patency of shunts by direct injection of the radiopharmaceutical into the shunt apparatus.
Radiopharmaceutical characteristics Tc-99m-DTPA is a combination of the ligand pentetic acid or diethylenetriaminepentaacetic acid, a metal chelator, and Tc-99m, a metal. Its molecular weight is 482.31 and the chemical structure shown in Fig. 13.1.
Extraction mechanism None. The Tc-99m-DTPA is in confined spaces, shunt tubing, and pleural, peritoneal, or vascular spaces.
Extraction efficiency Zero.
Extraction mechanism saturable or non-saturable Not applicable.
Interventions None.
Imaging Gamma camera planar imaging with a low-energy high-resolution collimator is the most commonly used.
Protocol design Imaging field: Head and shunt pathway; may include neck and chest or neck, chest, and abdomen. Anterior images are usually sufficient. Delayed images may be necessary if activity has not reached the pleura, peritoneum, or vascular space by the end of routine imaging (Fig. 13.17).
Quantitative measurement The Tc-99m-DTPA is not injected into the input port to the reservoir chamber but directly into the reservoir (Fig. 13.18).

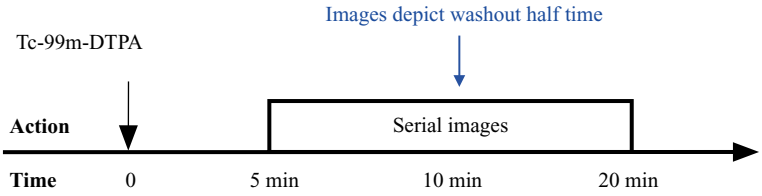

Fig. 13.17 Protocol summary diagram

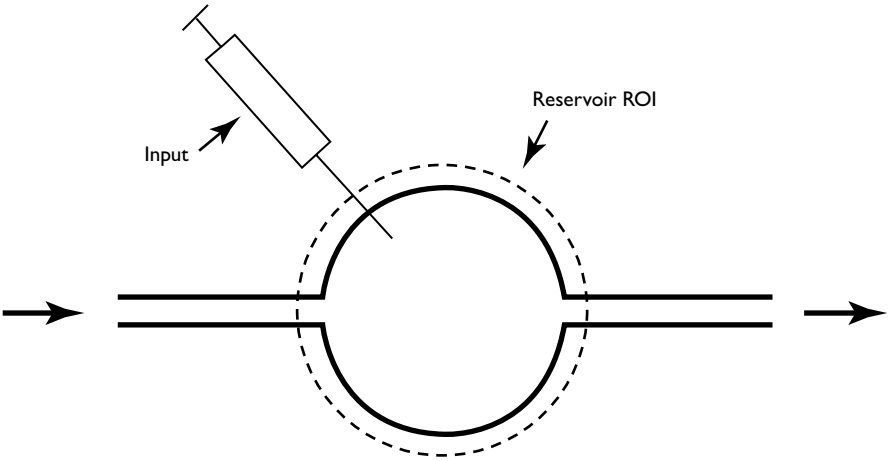

Fig. 13.18 Single compartment model. The *solid lines* depict a single compartment in the middle, a single input on the left, and a single output on the right. The *broken circle* indicates a region of interest (ROI) for generating a time-activity curve during the first pass of a bolus of activity through the model

Since the reservoir is a small volume and the injection will cause some turbulence in the reservoir, the tracer can be considered to be evenly distributed within the reservoir almost instantaneously. Then the time-activity curve from a ROI over the reservoir will show the residual tracer in the reservoir as a function of time, and the halftime of washout can be calculated.

This measurement is different from the mean transit time through a compartment in which the tracer is injected at the point of inflow, rather than throughout the compartment. The halftime of washout of tracer from a given volume when the tracer is initially uniformly distributed throughout the chamber will be half of the wash time when the tracer is injected at the entry to the chamber, that is, it will be half of the mean transit time (see Chap. 5, Mean Transit Time: Central Volume Principle).

Quantitative measurement: Normal range The residual halftime will vary with the make of reservoir because volume of the reservoir varies among manufacturers. These values have been calculated [17–19].

References

Brain Death Angiography Study (Tc-99m-DTPA)

1. Zuckier LS, Kolano J. Radionuclide studies in the determination of brain death: criteria, concepts, and controversies. Semin Nucl Med. 2008;38:262–73.

Brain Glucose Metabolism Study (F-18-Fluorodoxyglucose)

2. Herholz K, Heiss WD. Positron emission tomography in clinical neurology. Mol Imaging Biol. 2004;6:239–69.
3. Wood IS, Trayhurn P. Glucose transporters (GLUT and SGLT): expanded families of sugar transport proteins. Br J Nutr. 2003;89:3–9.
4. Silverman DHS, Melega WP. Molecular imaging of biological processes with PET: evaluating biologic bases of cerebral function. In: Phelps ME, editor. PET: molecular imaging and its biological applications. New York: Springer; 2004. p. 512.
5. Ishizu K, Nishizawa S, Yonekura Y, et al. Effects of hyperglycemia on FDG uptake in human brain and glioma. J Nucl Med. 1994;35:1104–9.

Brain Perfusion Study (Tc-99m-HMPAO)

6. Payne JK, Trivedi MH, Devous MD. Comparison of technetium-99m-HMPAO and xenon-133 measurements of regional cerebral blood flow by SPECT. J Nucl Med. 1996;37:1735–40.
7. Emily U. Can sound open the brain for therapies? Science. 2015;347:1187.
8. Suess E, Huck S, Reither H, et al. Uptake mechanism of technetium-99m-d, l-HMPAO in cell cultures of the dissociated postnatal rat cerebellum. J Nucl Med. 1992;33:108–14.

Cisternography (In-111-DTPA)

9. Sakka L, Coll G, Chazal J. Anatomy and physiology of cerebrospinal fluid. Eur Ann Otorhinolaryngol Head Neck Dis. 2011;128:309–16.
10. Cohen BJ. Memmler's the human body in health & disease. Wolters Kluwer Health; 2011.
11. McKusick KA, Malmud LS, Kordela PA, et al. Radionuclide cisternography: normal values for nasal secretion of intrathecally injected in-111-DTPA. J Nucl Med. 1973;14:933–4.

Striatal Dopamine Transporter Study (I-123-Ioflupane)

12. Djang DSW, Jansen MJR, Bhenen N, et al. SNM practice guideline for dopamine transporter imaging with I-123-ioflupane SPECT 1.0. J Nucl Med. 2012;53:154–63.
13. Membrane transport of small molecules and the electrical properties of the cell. In: Albert B, Johnson A, Lewis J, Raff M, Roberts K, Walter P, editors. Molecular biology of the cell. 5th ed. New York: Garland Science; 2008. p 808.

14. Booij J, Kemp P. Dopamine transporter imaging with I-123-FP-CIT SPECT: potential effects of drugs. Eur J Nucl Med. 2008;35:424–38.
15. Djang DSW, Jansen MJR, Bhenen N, et al. SNM practice guideline for dopamine transporter imaging with I-123-ioflupane SPECT 1.0. J Nucl Med. 2012;53:154–63.
16. Mescher AL. Junqueira's Basic histology text & atlas. New York: McGraw Hill Lange; 2013. p. 166.

Ventricular Shunt Study (Tc-99m-DTPA)

17. Harbert J, Haddad D, McCullough D. Quantitation of cerebrospinal fluid shunt flow. J Nucl Med. 1974;112:379–87.
18. Chervu S, Chervu LR, Vallabhajosyula B, et al. Quantitative evaluation of cerebrospinal fluid shunt flow. J Nucl Med. 1984;25:91–5.
19. Harbert JC, McCullough DC. Radionuclide tests of cerebral fluid shunt patency. J Nucl Med. 1984;25:112–4.

Endocrine System

14

Neuroectodermal/Norepinephrine Study (I-123-MIBG)

Overview The images of the Neuroectodermal/Norepinephrine Study primarily depict tumors that arise from the embryologic neural crest.

Radiopharmaceutical characteristics Metaiodobenzylguanidine (I-123-MIBG) is an analog of norepinephrine and is taken up by the adrenergic nervous system of tissues that are derived from the neural crest [1]. Its chemical structure is shown in Fig. 14.1. It has a molecular weight of 193.17.

Extraction mechanism I-123-MIBG is actively transported into pheochromocytoma cells and neuroblastoma cells. Once inside of pheochromocytoma cells, most of the tracer is actively transported into secretory granules. On the other hand, once inside neuroblastoma cells, most of the tracer remains in the cytoplasm (Fig. 14.2) [1].

Extraction efficiency The exact extraction efficiency is unknown. However, it is probably relatively low because a suitable lesion to background ratio is not achieved until 24 h after injection.

Extraction mechanism, saturable or non-saturable Saturable. Several classes of substances can compete with I-123-MIBG clearance: tricyclic antidepressants, antihypertensives, sympathetic amines, and cocaine [1].

Interventions None.

Protocol design A gamma camera with a high-resolution low-energy collimator and a computer with SPECT software are used to acquire planar and SPECT images at 24 h, and planar images at 48 h (Fig. 14.3). SPECT-CT can be used instead of SPECT.

Quantitative measurement None.

W.C. Klingensmith III, *The Mathematics and Biology of the Biodistribution of Radiopharmaceuticals-A Clinical Perspective*,
DOI 10.1007/978-3-319-26704-3_14

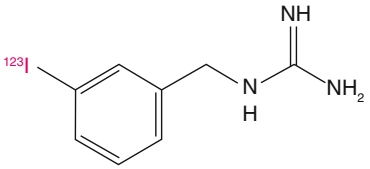

Fig. 14.1 Chemical structure of I-123-MIBG (metaiodobenzylguanidine)

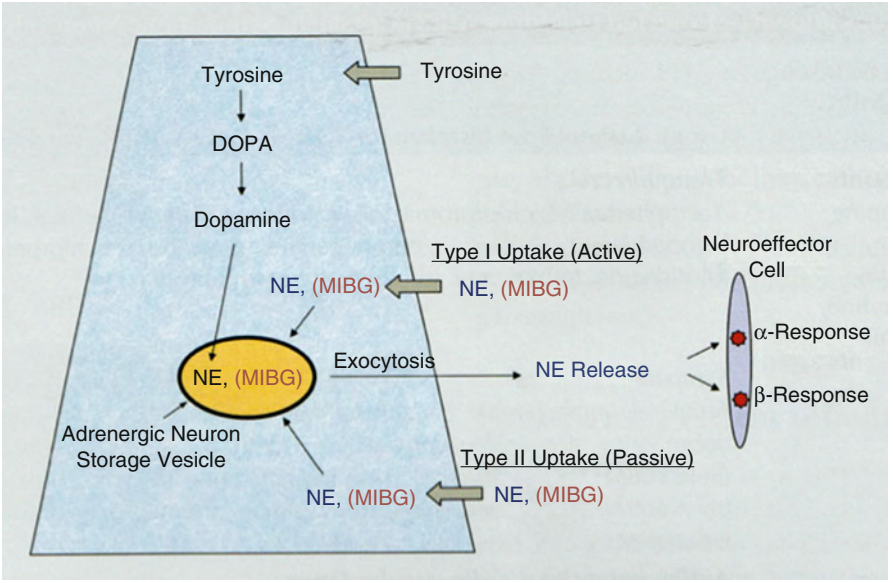

Fig. 14.2 Uptake (clearance) of I-123-MIBG by adrenal medullary cells. I-123-MIBG is mainly taken up into adrenal medullary cells by active transport, but there is also a passive transport pathway (Kowalsky *Radiopharmaceuticals in Nuclear Pharmacy*, p. 601)

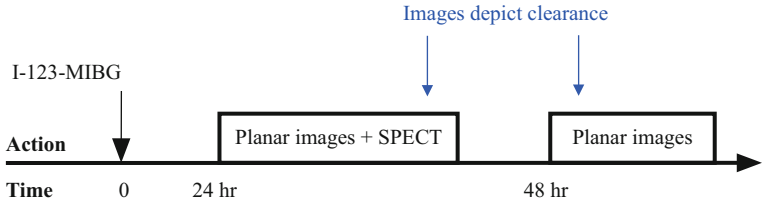

Fig. 14.3 Protocol summary diagram

Parathyroid Study (I-123 and Tc-99m-Sestamibi)

Overview The Parathyroid Study is performed with two radiopharmaceuticals, I-123 and Tc-99m-sestamibi. I-123 localizes only in the thyroid, while Tc-99m-sestamibi localizes in parathyroid adenomas and the adjacent thyroid. The I-123

images of the thyroid are subtracted from the Tc-99m-sestamibi images of thyroid and parathyroid adenoma, resulting in an image containing only the parathyroid adenoma. I-123 and imaging of the thyroid with I-123 are discussed in the next section.

Radiopharmaceutical characteristics The molecular structure of Tc-99m-sestamibi is shown in Fig. 14.4. Tc-99m-sestamibi has a molecular weight of 777.69.

Extraction mechanism Tc-99m-sestamibi (methoxyisobutylisonitrile) is a lipophilic cationic complex that passively diffuses across cell membranes and binds to proteins within the mitochondria. Tc-99m-sestamibi is taken up in parathyroid adenomas probably because there is an increased number of mitochondria in the hyperactive parathyroid cells [2].

Extraction efficiency The exact extraction efficiency of Tc-99m-sestamibi is unknown, but it takes only 15 min to achieve a satisfactory target to background ratio suggesting that the extraction efficiency for Tc-99m-sestamibi is higher than the extraction efficiency for I-123.

Extraction mechanism, saturable or non-saturable Non-saturable.

Interventions None.

Protocol design Imaging is done with a gamma camera fitted with a pinhole collimator and a SPECT-CT machine. All images are obtained with simultaneous

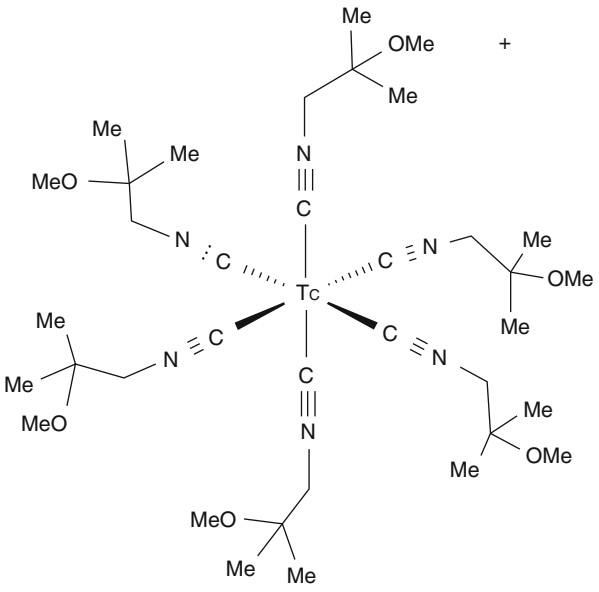

Fig. 14.4 Chemical structure of Tc-99m-sestamibi

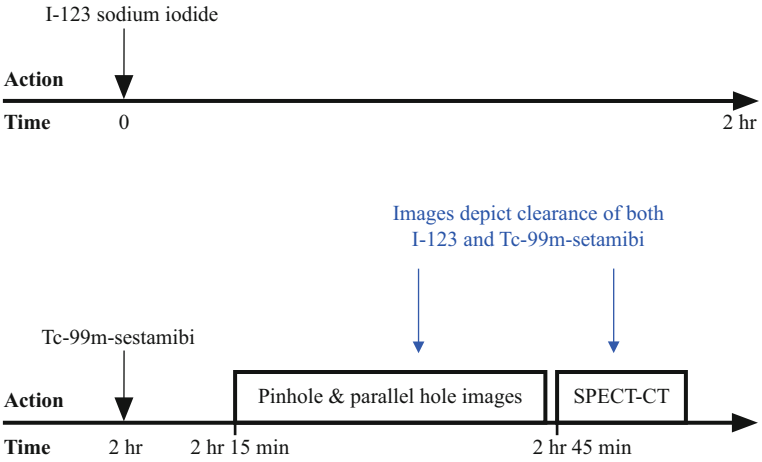

Fig. 14.5 Protocol summary diagram

acquisition of both I-123 and Tc-99m-sestamibi. First, anterior and anterior oblique pinhole images are obtained of the neck, then an anterior parallel hole image is acquired of the neck and upper chest for possible ectopic parathyroid adenomas, and finally SPECT-CT images are obtained of the neck and upper chest (Fig. 14.5).
Quantitative measurement None.

Thyroid Imaging and Uptake Study (I-123)

Overview The Thyroid Imaging and Uptake Study with radioiodine demonstrates the distribution of functioning thyroid tissue, including ectopic tissue, since thyroid tissue is the only tissue that concentrates large amounts of iodine. The uptake (clearance) measures the metabolic activity of the thyroid gland as reflected by the clearance of iodide from the blood into thyroid epithelial cells.
Radiopharmaceutical characteristics I-123 is an anion (I^-) with an atomic weight of 126.90.
Extraction mechanism Circulating iodide is bound to serum proteins, especially albumin. Iodide is cleared from the blood into thyroid epithelial cells as the first step in the synthesis of thyroid hormones.

Iodide clearance is a result of an active transport mechanism mediated by the Na^+/I^- symporter (NIS) protein, which is found in the basolateral membrane of thyroid follicular cells (Figs. 14.5, and 14.6). As a result of this active transport, the iodide concentration inside follicular cells of thyroid tissue is 20–50 times higher than in the plasma. The transport of iodide across the cell membrane is driven by the electrochemical gradient of sodium [3]. Once inside the follicular cells, the

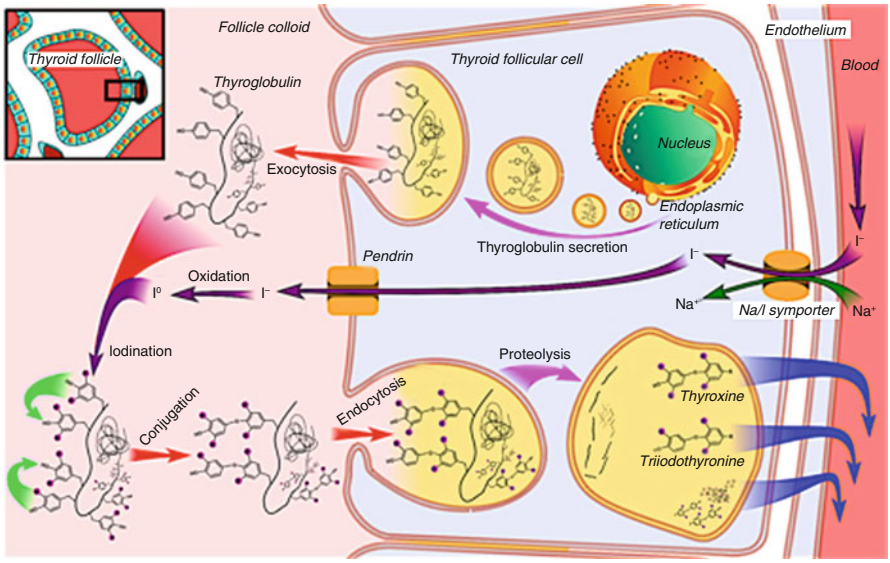

Fig. 14.6 Thyroid hormone synthesis. Of interest, thyroxine is synthesized in the colloid, not in the thyroid epithelial cell (Sodium-iodide symporter Wikipedia)

iodide diffuses to the apical membrane, where it is metabolically oxidized through the action of thyroid peroxidase to iodonium (I^0) which in turn iodinates tyrosine residues on the thyroglobulin proteins in the follicular colloid. Thus, NIS is essential for the synthesis of thyroid hormones (T_3 and T_4).

Extraction efficiency The normal extraction efficiency of I-123 is unknown, but it takes several hours to achieve an optimal target to background ratio.

The extraction efficiency is significantly decreased by the antithyroid medications propylthiouracil (PTU) and methimazole. These medications decrease the net thyroid uptake or clearance of iodide by inhibiting the enzyme thyroperoxidase, which normally oxidizes the anion iodide (I^-) to iodine (I^0) as part of thyroid hormone synthesis. While inhibition of thyroperoxidase does not affect the initial uptake or clearance of iodide NIS, it does significantly decrease the retention of iodide.

The uptake and clearance of iodide is greatly affected by the thyroid-stimulating hormone (TSH). TSH is synthesized in the anterior pituitary and released into the blood. In the thyroid, the TSH binds to the TSH receptor on the cell membrane of the thyroid epithelial cell and initiates an intracellular chain of actions that modulates thyroidal gene expression and iodide uptake [4].

Extraction mechanism, saturable or non-saturable Saturable. The most common source of competing anionic iodide is CT intravenous contrast. Other much less common sources of iodide are amiodarone and kelp.

Interventions None.

Protocol design Initially, the I-123 capsules are placed in a lucite neck phantom. A scintillation probe is used to measure the amount of activity in the phantom (see Chap. 9: Quantitation of Function: Absolute Measurements). The phantom simulates the photon attenuation that will subsequently occur in the patient's neck. The I-123 capsules are then removed from the phantom and administered to the patient. Six hours later, the scintillation probe is used to measure the activity in the thyroid within the patient's neck and in a thigh. The thigh measurement simulates the background activity in the patient's neck. Anterior and anterior oblique images are then acquired of the thyroid with a gamma camera fitted with a pinhole collimator (Fig. 14.7).

Quantitative measurement – Thyroid uptake (clearance) The measurement of thyroid clearance or uptake of iodide is an example of absolute quantification (see Chap. 9: Quantitation of Function: Absolute Measurements). The amount of radioactivity in the I-123 capsules is determined in a dosimeter. Then the capsules are placed in the neck phantom. The phantom simulates the attenuation that occurs between the thyroid gland and the anterior surface of the neck, and the background activity in the neck is simulated by the amount of radioactivity in the soft tissues of the lower thigh. There is no background radioactivity in the phantom.

A scintillation probe is positioned perpendicular to the phantom with the positioning bar directly over the capsule within the phantom. The scintillation crystal will be at a standard distance from the phantom, usually 25 cm [4]. The capsules are immediately administered to the patient. At 6 h, the probe is positioned anterior to the patient's neck with the positioning bar perpendicular to the neck and with the bar centered halfway between the thyroid cartilage and the suprasternal notch. The goal is to have the probe positioned relative to the thyroid with the same geometry that was used to position the probe relative to the capsule in the phantom.

Then, the probe is positioned over the thigh for the 6 h "background" measurement. It is assumed that the diameter and density of the thigh is roughly the same as

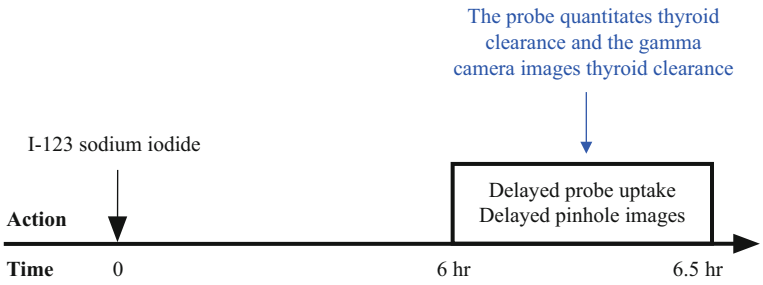

Fig. 14.7 Protocol summary diagram

the neck. The positioning bar should be perpendicular to the thigh with the bar centered just above the knee. The patient should void before counting over the thigh, and the bladder must be clearly outside of the field of view (see Thyroid Uptake worksheet below).

In general, the thyroid measurement can be done only at 6 h. The availability of an accurate thyroid-stimulating hormone blood test and the current practice of administering enough I-131 to make patients with hyperthyroidism from Graves disease hypothyroid makes measurement of thyroid turnover of iodide unnecessary. In addition, in patients with Graves disease, this approach also allows thyroid imaging with I-123, measurement of thyroid uptake with I-123, and treatment of the Graves disease with I-131 all in 1 day.

Quantitative measurement – Normal range There is no recent determination of the normal range of I-123 uptake (clearance) by the thyroid at 6 h. The lack of current data is unfortunate since factors such as the amount of iodine in the diet affect uptake measurements and dietary iodine may change over time. Various determinations of the normal range from the past are given in the references below [5–9].

Thyroid Metastases Study (I-123 and I-131)

Overview The Thyroid Metastases Study, with either I-123 or I-131 radioiodine, demonstrates the distribution of functioning thyroid tissue, both residual normal tissue in the thyroid bed and functioning metastases throughout the body.

Radiopharmaceutical characteristics I-123 is an anion (I^-) with an atomic weight of 122.90. I-131 is an anion (I^-) with an atomic weight of 130.90.

Extraction mechanism See discussion and figure above for Thyroid Imaging and Uptake Study.

Extraction efficiency See discussion and figure above for Thyroid Imaging and Uptake Study.

Extraction mechanism, saturable or non-saturable See discussion and figure above for Thyroid Imaging and Uptake Study.

Interventions None.

Protocol design The patient drinks water to clear any radioactive iodine from the esophagus. Images are acquired with a gamma camera fitted with either a low-energy high-resolution collimator for I-123 or a high-energy collimator for I-131. At 24 h after administration of I-123 and 7–10 days after administration of I-131, anterior and posterior images are acquired from the top of the head to the lower thighs using a whole body technique. Then a high-count anterior image of the neck is acquired with pinhole collimator (Fig. 14.8).

Quantitative measurement In general, none. A few institutions perform occasional I-131whole body dosimetry studies [10–12].

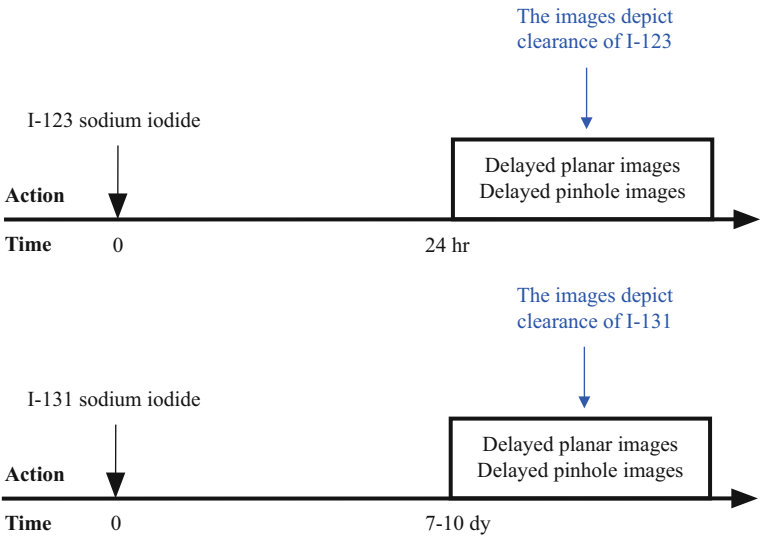

Fig. 14.8 Protocol summary diagram

Thyroid Uptake Worksheet

Nuclear Medicine Department

Institution_____

Name_____ ID_____ Age_____ Sex_____

Referring physician_____ Date_____

Zero Hour (time_____)

	counts per minute
Dose in phantom (standard)	
Background (air)	-
Net (standard)	

6 Hour Uptake (time_____)

	counts per minute
Neck	
Thigh (background)	-
Net	

	counts per minute
Standard at zero time	
Decay correction factor	x
Corrected standard	

6 hour uptake = (net neck cpm / corrected standard cpm) × 100% = _____%

• Normal Range: 6 hours = _____ to _____% •

Technologist_____

References

Neuroectodermal/Norepinephrine Study (I-123-MIBG)

1. Avram AM, Fig LM, Gross MD. Adrenal gland scintigraphy. Semin Nucl Med. 2006;36: 212–27.

Parathyroid Imaging (I-123, Tc-99m-sestamibi)

2. Mullan BP. Nuclear medicine imaging of the parathyroid. Otolaryngol Clin North Am. 2004; 37:909–39.

Thyroid Imaging & Uptake Study (I-123)

3. Hall JE. Synthesis and secretion of thyroid metabolic hormones. In: Guyton AC, Hall JE, editors. Textbook of medical physiology. 12th ed. Philadelphia: Saunders El Sevier; 2011. p. 908.
4. Mariusz WS, Valerie F, et al. Thyroid-stimulating hormone and thyroid-stimulating hormone receptor structure-function relationships. Phys Rev. 2002;82:473–502.
5. Oddie TH, Myhill J, Pirnique FG, et al. Effect of age and sex on the radioiodine uptake in euthyroid subjects. J Clin Endocrinol Metab. 1968;28:776–82.
6. Robertson JS, Nolan MG, Wahner HW, et al. Thyroid radioiodine uptakes and scans in euthyroid patients. Mayo Clin Proc. 1975;50:79–84.
7. Hooper PL, Turner JR, Conway MJ, et al. Thyroid uptake of I-123 in a normal population. Arch Intern Med. 1980;140:757–8.
8. Anderson BG, Powsner RA. Stability of values for thyroid radioiodine uptake. J Nucl Med. 1996;37:805–6.
9. Normal thyroid uptake values in Denver, Colorado: 6 hours = 7–20%, 24 hours = 14–30%. University of Colorado Medical School, Unpublished data, 1981.

Thyroid Metastases Study (I-123 & I-131)

10. Verburg FA, Hanscheid H, Biko J, et al. Dosimetry guided high activity I-131 therapy in patients with advanced differentiated thyroid carcinoma: Initial experience. Eur J Nucl Med. 2010;37:896–903.
11. Hindorf C, Glatting G, Chiesa C, et al. EANM Dosimetry Committee guidelines for bone marrow and whole body dosimetry. Eur J Nucl Med. 2010;37:1238–50.
12. Dorn R, Kopp J, Vogt H, et al. Dosimetry guided radioactive iodine treatment in patients with metastatic differentiated thyroid cancer. Largest safe dose using a risk adapted approach. J Nucl Med. 2003;44:451–6.

Gastrointestinal System

15

Esophageal Transit Study (Tc-99m-Sulfur Colloid in Water)

Overview The images of the Esophageal Motility Study demonstrate the movement of a bolus of swallowed material through the esophagus and into the stomach in a physiologic and quantitative fashion [1, 2].

Radiopharmaceutical characteristics The radiopharmaceutical consists of Tc-99m-sulfur colloid mixed in water. The size of the colloidal particles covers a wide range from 0.03 to 10 μm. Most particles are in the 0.4–0.8 μm range [3].

Extraction mechanism None. The Tc-99m-sulfur colloid remains in the esophagogastric lumen.

Extraction efficiency Zero percent.

Extraction mechanism saturable or non-saturable Not applicable.

Interventions None.

Imaging Imaging is performed with a dual-head gamma camera with low-energy high-resolution parallel-hole collimators.

Protocol design The patient lies in the supine position, imaging is performed with a dual-head gamma camera, and images are acquired in the anterior and posterior projections. The patient is instructed to swallow a 15 mL aliquot of the radiopharmaceutical in a single bolus and to follow this with dry swallows (no liquid) every 15 s for up to 10 min. Anterior and posterior digital images are acquired beginning when the patient swallows the radiopharmaceutical. The images are acquired for 1 s each for the first 15 s and then for 15 s each for up to 10 min (Fig. 15.1) [1, 2].

Quantitative measurement Evaluation of esophageal transit time is an example of a relative quantitative measurement (see Chap. 8, Quantitation of Function: Relative Measurements). The esophageal transit time is a relative measurement because multiple data points are generated over time from the same region of inter-

W.C. Klingensmith III, *The Mathematics and Biology of the Biodistribution of Radiopharmaceuticals-A Clinical Perspective*,
DOI 10.1007/978-3-319-26704-3_15

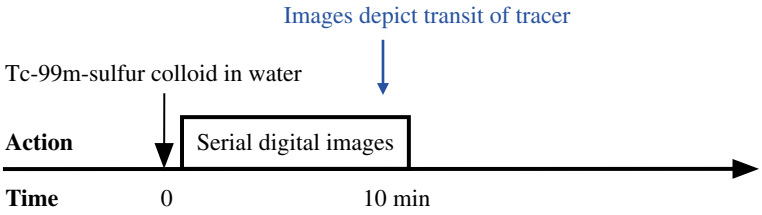

Fig. 15.1 Protocol summary diagram

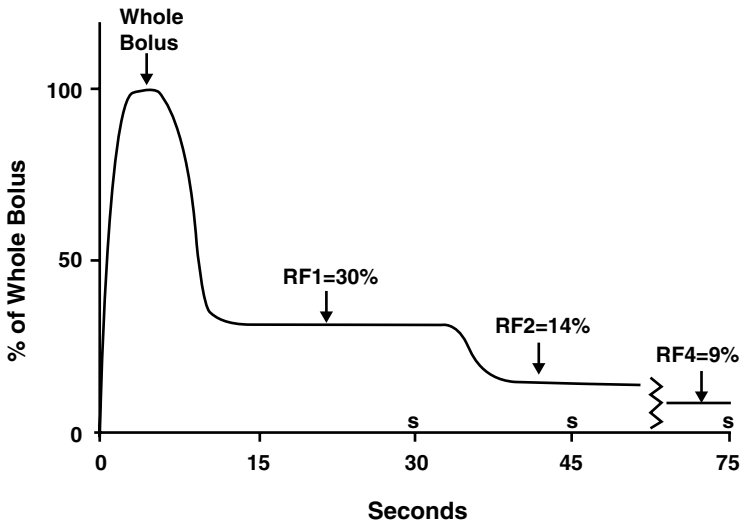

Fig. 15.2 Time-activity curve from esophageal transit study. The peak time, "whole bolus," represents the total amount of radiopharmaceutical that was administered. "RF" is the residual fraction of tracer in the esophagus after each swallow [1]

est (ROI). The measurements are not related to the amount administered radiopharmaceutical. No background subtraction is needed because the activity is limited to the organ of interest, the esophagus.

A ROI is drawn over the esophagus excluding the stomach in the anterior and posterior images. The geometric mean of the activity in the anterior and posterior images at each time point is calculated. The geometric mean process compensates for attenuation in a relative fashion (see Chap. 8, Quantitation of Function: Relative Measurements). The data can be displayed in multiple ways, but an esophageal emptying curve depicting the residual tracer in the esophagus similar to the gastric emptying curve is most convenient (Fig. 15.2).

The esophageal time-activity curve can be analyzed in various ways, but it is usually evaluated by calculating the meant transit time [2–5]. The upper limits for the mean transit time of esophageal emptying is 10 s [5].

Gastric Emptying Study (Tc-99m-Sulfur Colloid in Instant Oatmeal)

Overview The images of the Gastric Emptying Study demonstrate the movement of an ingested bolus of a labeled meal through the stomach into the small intestine. Various physiologic parameters may be quantified, but the most important parameter is the rate of emptying of the test meal. A wide variety of meals and protocols have been published and are in clinical use [6–10]. Here, we will focus on the relatively simple meal of instant oatmeal labeled with Tc-99m-sulfur colloid [10, 11].

Radiopharmaceutical characteristics Technetium-99m is firmly bound to sulfur colloid, which in turn binds to the contents of one packet of instant oatmeal. The Tc-99m-sulfur colloid should be added to the oatmeal before it is reconstituted with hot water to achieve optimal binding of the tracer to the instant oatmeal [7]. The reconstituted oatmeal is considered a semisolid meal. Compared to a solid meal a semisolid meal has the advantage that it can be ingested more quickly and produce a more defined start time.

Extraction mechanism None. The labeled oatmeal remains in the gastrointestinal lumen.

The radiopharmaceutical bolus moves through the stomach by peristalsis, which is under both neural and hormonal control. The neural control system has both an extrinsic component, the vagus nerve, and an intrinsic component consisting of several neural plexi within the gastric wall (Fig. 15.3) [12].

Extraction efficiency Zero percent.

Extraction mechanism saturable or non-saturable Not applicable.

Interventions In general, none [13].

Imaging Imaging is performed with a dual-head gamma camera with low-energy parallel-hole collimators.

Protocol design The patient is instructed to eat the oatmeal meal in less than 5 min. Then anterior and posterior images of the upper abdomen are acquired immediately and every 15 min for 1 h with the patient standing (Fig. 15.4). Delayed images are acquired if necessary.

Quantitative measurement The primary information from the Gastric Emptying Study is a quantitative measurement of the transit time of a labeled semisolid meal through the stomach.

The gastric emptying time is a relative measurement because the data is generated over time from the same anterior and posterior ROIs (see Chap. 8, Quantitation of Function: Relative Measurements). No background subtraction is needed because the activity is limited to the organ of interest, the stomach.

The geometric mean of the activity in the anterior and posterior images at each time point is calculated. The geometric mean process compensates for attenuation in a relative fashion. The data can be analyzed in multiple ways, but most commonly the half time of emptying is used [14]. The mean transit time could also be used and, in most cases, would give similar, but not identical, results.

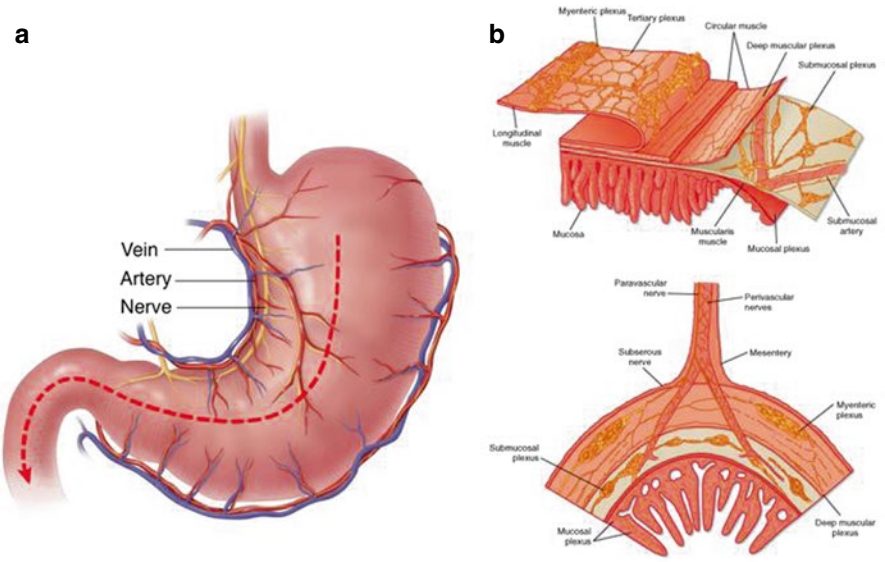

Fig. 15.3 (**a**, **b**) Anatomy and intrinsic myenteric plexi of the stomach. Gastric meals move through the stomach under hormonal and neural control. The neural system has both extrinsic (vagus nerve) and intrinsic (myenteric neural system) components [12]

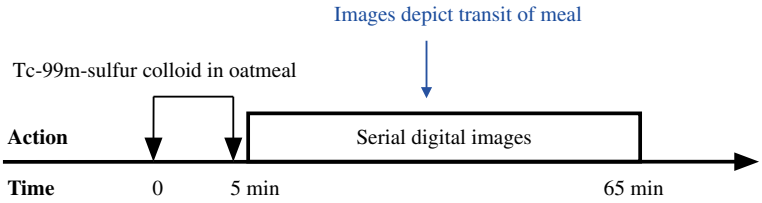

Fig. 15.4 Protocol summary diagram

The upper limits of normal for the half time of emptying of one packet of instant oatmeal vary with age (Table 15.1) [11]. The reproducibility of the gastric emptying study with an oatmeal meal also varies with age (Table 15.1).

Gastrointestinal Bleeding Study (Tc-99m-Red Blood Cells)

Overview The images of the Gastrointestinal Bleeding Study detect the extravasation of radiolabeled red blood cells from the vascular space into the gastrointestinal lumen. The subsequent movement of the extravasated red blood cells within the gastrointestinal lumen secondary to peristalsis allows localization of the site of bleed along the gastrointestinal tract [15, 16].

Table 15.1 Proposed and (actual) normal limits for gastric emptying times and reproducibility

	Normal range (min)		Reproducibility (min)	
Sex and age	LAO	A-P	LAO	A-P
Males and females				
20–40 years				
Proposed	10–60	10–60	≤30	≤30
Mean ± 2 sd	(0–62)	(0–67)	(0–34)	(0–39)
Range	(20–60)	(13–56)	(4–27)	(8–35)
40–60 years				
Proposed	10–40	10–40	≤20	≤20
Mean ± 2 sd	(0–52)	(0–50)	(0–22)	(0–19)
Range	(9–44)	(12–42)	(1–18)	(0–18)
60–80 years				
Proposed	10–30	10–30	≤15	≤15
Mean ± 2 sd	(0–30)	(0–28)	(0–22)	(0–15)
Range	(9–26)	(15–26)	(2–18)	(0–13)

Radiopharmaceutical characteristics The Tc-99m-red blood cell is one of the largest radiopharmaceuticals with a diameter of approximately 8 μm, a thickness of approximately 2 μm, and a central thickness of approximately 1 μm [17].
Extraction mechanism None. The Tc-99m-red blood cells are confined to the vascular space except when there is a gastrointestinal bleed, in which case the compartment that the Tc-99m-red blood cells occupy is effectively enlarged.
Extraction efficiency Not applicable.
Extraction mechanism saturable or non-saturable Not applicable.
Imaging Imaging is performed with a gamma camera and a low-energy high-resolution parallel-hole collimator [18].
Interventions None.
Protocol design Beginning at the time of injection of the radiopharmaceutical serial 1 min images are obtained. Every 30 min, the previous set of 30 images is reviewed in cine mode by the nuclear medicine physician while the next 30 min collection is started. This process is continued until: (1) a bleeding site is identified and localized, (2) the patient refuses further imaging, (3) the gamma camera is needed for another study, (4) the patient is needed elsewhere for another study, or (5) the nuclear medicine physician terminates the imaging session. Imaging can be restarted the following day. One injection of radiopharmaceutical allows imaging for up to 36 h (Fig. 15.5).
Quantitative measurement None.

Hepatic Artery Perfusion Study (Tc-99m-Macroaggregated Albumin)

Overview The images of the Hepatic Artery Perfusion Study depict the distribution of perfusion, actually clearance, via an hepatic artery catheter. The catheter is usually placed so that the injected tracer distributes to only one lobe of the liver.

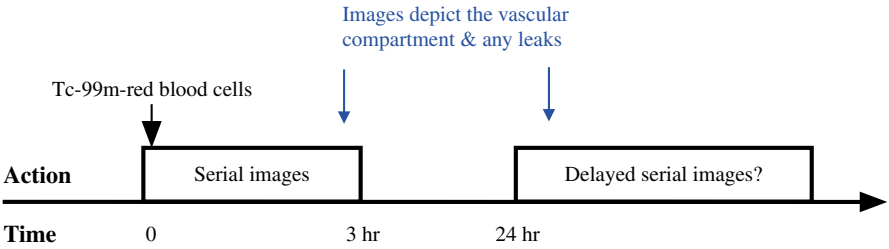

Fig. 15.5 Protocol summary diagram

However, if the catheter is not optimally placed, the tracer may go to both lobes and some tracer may go to the stomach or other extrahepatic locations.

In addition, if there are anatomic arteriovenous shunts within the liver, some Tc-99m-MAA will pass through the liver and embolize in the lung capillaries. The percent of Tc-99m-MAA that passes through the liver and lodges in the lungs can be quantified [19]. If excessive amounts of radiopharmaceutical reach the lungs, the amount of injected dose is reduced or the procedure is canceled.

Radiopharmaceutical characteristics Ninety percent of Tc-99m-macroaggregated particles range in size from 10 to 80 μm with a mean particle size of 30 μm. No particles exceed 150 μm [20].

Extraction mechanism Following intracatheter injection, the particles will embolize into arterioles of the first capillary bed they encounter.

However, the particles will pass through anatomic arteriovenous shunts. Thus, this radiopharmaceutical distributes according to clearance and is removed from flowing blood by microembolization into capillary beds. Even though there is very high blood flow through intrahepatic anatomic arteriovenous shunts, there will be very little localization or clearance of Tc-99m-macroaggregated in these structures. This fact demonstrates the inaccuracy of calling this study a perfusion study. This is another example of the use of clearance as a proxy for blood flow.

In the liver, the clearance of Tc-99m-macroaggregated will reflect blood flow except where there are intrahepatic arteriovenous shunts. Generally, the presence of the tracer in the lungs indicates the presence of intrahepatic arteriovenous shunts.

Extraction efficiency Essentially 100 % for arterioles and capillary beds.

Extraction mechanism saturable or non-saturable Not saturable.

Interventions None.

Imaging Imaging is initially performed with a gamma camera with a low-energy high-resolution parallel-hole collimator followed by imaging with a SPECT-CT machine [21].

Protocol design Following injection of the Tc-99m-macroaggregated albumin, anterior and posterior images of the lungs and upper abdomen are acquired. Then SPECT-CT images are obtained of the upper abdomen (Fig. 15.6).

Quantitative measurement The images are used to calculate the percent of Tc-99m-macroaggregated albumin that passed through the liver and embolized into the pulmonary capillary beds. This percentage is used to adjust the dose of

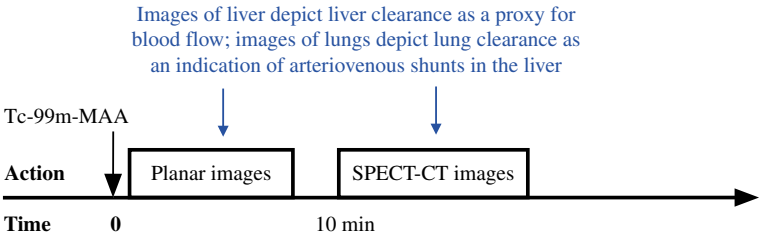

Fig. 15.6 Protocol summary diagram

Table 15.2 Dose reduction for intrahepatic shunting

Intrahepatic shunting (%)	Reduction percent
<10	No reduction
10–15	20 % reduction
15–20	40 % reduction
>20	No treatment

Y-90-spheres that can be injected for treatment of cancer in the liver [22]. Because of the possibility of radiation damage to the lungs, a moderate amount of shunting of Tc-99m-macroaggregated albumin to the lungs requires a moderate reduction in the dose of the Y-90-spheres and a large amount of shunting requires cancellation of the therapy (Table 15.2) [22].

The intrahepatic arteriovenous shunt determination represents a relative quantitative measurement in that one ROI of a part of the body is compared to another at the same point in time, but not to the amount of activity injected (see Chap. 8, Quantitation of Activity: Relative Measurements). Because the radiopharmaceutical is injected into the hepatic catheter, the activity is essentially limited to the liver and lungs, so no background correction is needed.

The geometric mean of the counts in the lungs and liver is calculated to account for attenuation in a relative fashion. ROIs are placed over these organs in the anterior and posterior images, the opposing counts are multiplied together, and then the square root is obtained. However, the geometric mean approach to compensating for attenuation is exact only when the density of tissue in all of the ROIs is the same, which is not the case for the lungs and the liver. For practical reasons, this limitation is ignored.

The applicable equation is,

$$\mathrm{IHAVS}(\%) = \frac{\left[L_{\mathrm{Ant}}(\mathrm{cpm}) \times L_{\mathrm{Post}}(\mathrm{cpm})\right]^{1/2}}{\left[\left[L_{\mathrm{Ant}}(\mathrm{cpm}) + H_{\mathrm{Ant}}(\mathrm{cpm})\right] \times \left[L_{\mathrm{Post}}(\mathrm{cpm}) + H_{\mathrm{Post}}(\mathrm{cpm})\right]\right]^{1/2}} \times 100(\%) \tag{15.1}$$

where "IHAVS" is intrahepatic arteriovenous shunt as a percent, L is both the lungs and H is the liver in counts per minute, and "Ant" and "Post" are the anterior and posterior projections.

Table 15.2 lists the algorithm for reducing the dose of Y-90-spheres (SIRTeX) for varying degrees of intrahepatic arteriovenous shunting [22].

Hepatic Hemangioma Study (Tc-99m-Red Blood Cells)

Overview The images of the Hepatic Hemangioma Study depict the amount of blood flow (early images) and vascular space (delayed images) within hepatic lesions. Hemangiomas are characterized by their relatively decreased blood flow and increased vascular volume compared to hepatic parenchyma and most other hepatic lesions [23].
Radiopharmaceutical characteristics The Tc-99m-red blood cell is one of the largest radiopharmaceuticals with a diameter of approximately 8 μm, a thickness of approximately 2 μm, and a central thickness of approximately 1 μm [17].
Extraction mechanism None. The Tc-99m-red blood cells are confined to the vascular space except when there is a gastrointestinal bleed, in which case the compartment that the Tc-99m-red blood cells occupy is effectively enlarged.
Extraction efficiency Zero percent.
Extraction mechanism saturable or non-saturable Not applicable.
Imaging Imaging is performed with a gamma camera with a low-energy high-resolution parallel-hole collimator.
Interventions None.
Imaging Images are acquired with a dual-headed SPECT gamma camera or SPECT-CT.
Protocol design Immediately following injection of the radiopharmaceutical, serial planar images of the liver are acquired for 90 s to evaluate blood flow to the lesion in question. Then static planar images of the liver are acquired in the anterior, posterior, right lateral, and left lateral projections. Finally, SPECT-CT images of the upper abdomen are acquired (Fig. 15.7).
Quantitative measurement None.

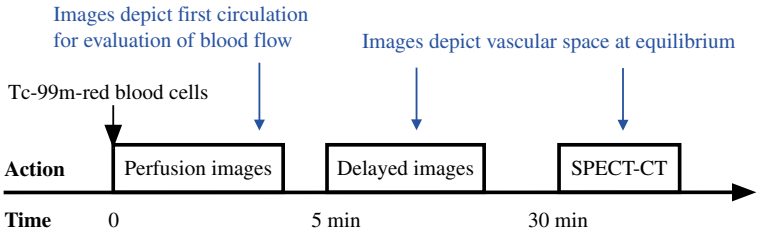

Fig. 15.7 Protocol summary diagram

Hepatobiliary Study (Tc-99m-Trimethylbromo-IDA)

Overview The images of the Hepatobiliary Study successively demonstrates hepatocyte clearance, hepatic parenchymal transit, and biliary excretion as the radiopharmaceutical moves from the injection site into the hepatobiliary system, through the intrahepatic bile ducts, and into the extrahepatic biliary system. In addition, the gallbladder ejection fraction is measured [24, 25].

Radiopharmaceutical characteristics The chemical structure of Tc-99m-trimethylbromo-IDA is shown in Fig. 15.8. It has a molecular weight of 408.18.

Extraction mechanism Following intravenous injection, Tc-99m-trimethylbromo-IDA reaches the sinusoids of the liver via the hepatic artery and portal vein where it is transported (cleared) into the hepatocytes via a system that excretes a class of relatively small organic anions. The mechanism of transporting the radiopharmaceutical across the sinusoidal membrane of the hepatocyte is not completely known, but may be passive diffusion along a radiopharmaceutical gradient [26, 27]. Once the radiopharmaceutical reaches the canalicular membrane of the hepatocyte, the tracer is actively transported by the multidrug resistance-associated protein (MRP2) from the hepatocyte into the bile canaliculus (Fig. 15.9) [28]. Thus, Tc-99m-trimethylbromo-IDA is one of a class of molecules that is excreted by the hepatobiliary excretory system.

Extraction efficiency Moderate-high, imaging begins at 15 min.

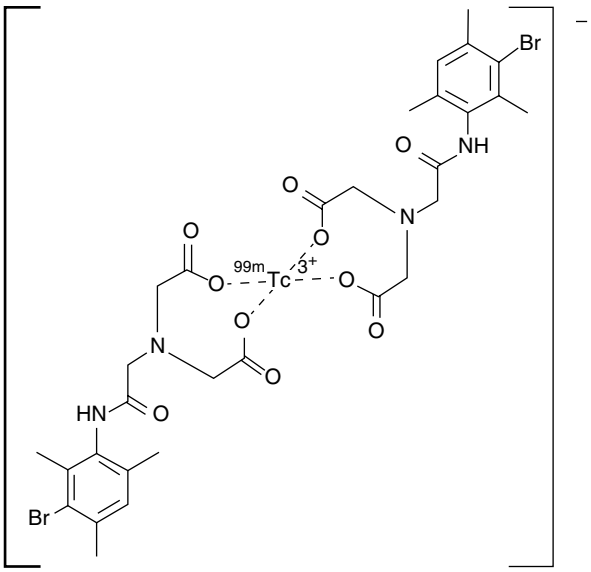

Fig. 15.8 Chemical structure of Tc-99m-trimethylbromo-IDA

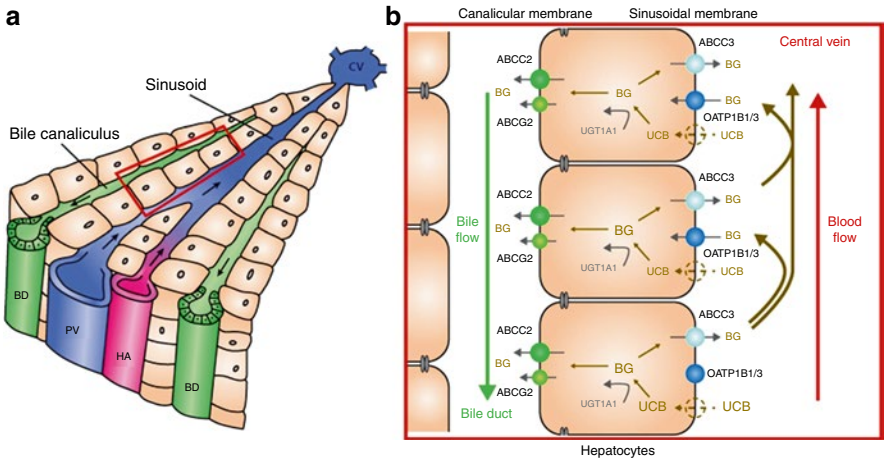

Fig. 15.9 Cellular biology of excretion of Tc-99m-trimethylbromo-IDA through the bilirubin excretion pathway. (**a**) Liver lobule: *BD* bile duct, *PV* portal vein, *HA* hepatic artery, *CV* central vein. (**b**) Unconjugated bilirubin (*UCB*) enters hepatocytes via passive diffusion and/or transporters. Tc-99m-trimethylbromo-IDA follows the same excretory pathway as bilirubin, but is not conjugated (van de Steeg et al. [27], fig 6)

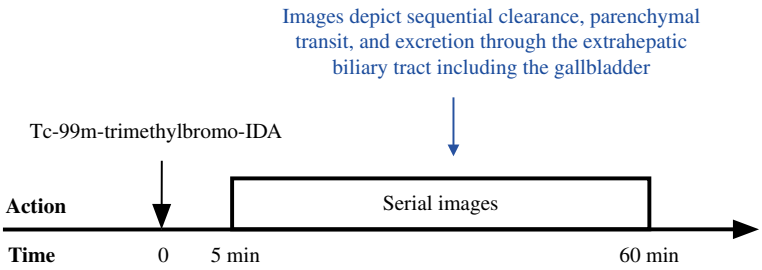

Fig. 15.10 Protocol summary diagram

Extraction mechanism saturable or non-saturable Saturable. Bilirubin is a competing molecule.

Interventions Kinevac, an analog of cholecystokinin, is frequently used to evaluate contraction of the gallbladder, and morphine can be used to cause closure of the sphincter of Oddi in order to enhance visualization of the gallbladder [29, 30].

Imaging Imaging is performed with a dual-headed gamma camera with a low-energy high-resolution parallel-hole collimator.

Protocol design Images are acquired in the anterior and right lateral projections beginning 5 min after injection through 60 min (Fig. 15.10) [24, 25].

Quantitative measurement (visual): Parenchymal transit time Radiopharmaceutical should appear in the extrahepatic biliary tract (usually the left or right hepatic ducts, but sometimes the gallbladder) by 15 min from injection of the radiopharmaceutical [24, 25].

Quantitative measurement: Gallbladder ejection fraction Assuming that the gallbladder is reasonably well visualized at the end of routine imaging at 60 min, the gallbladder ejection fraction can be measured in response to a 30 min infusion of Kinevac (analog of cholecystokinin) [30–33]. The 60 min anterior image from the routine image set is used as the pre-Kinevac baseline image of the gallbladder. After the 30 min infusion of Kinevac, another anterior image is obtained.

Since there is little change in photon attenuation between the end-diastolic and end-systolic images of the left gallbladder, and since the gallbladder ejection fraction is a relative measurement, there is no need to know the absolute amount of activity in the gallbladder, and attenuation correction can be ignored.

However, since there is significant activity in the tissues around the gallbladder, background correction is needed. The background ROI is placed medial to the gallbladder and must not overlap the gallbladder. The equation for background correction of an ROI is given in Eqs. 8.8 and 8.7 of Chap. 8, Quantitation of Function: Relative Measurement.

The equation for the gallbladder ejection fraction, after the pre- and post-Kinevac gallbladder ROIs are corrected for background activity, is simply

$$GB_{EF}(\%) = \frac{GB_{Pre}(\text{cpm}) - GB_{Post}(\text{cpm})}{GB_{Pre}(\text{cpm})} \times 100(\%) \tag{15.2}$$

Here, "GB_{EF} (%)" is the gallbladder ejection fraction in percent, "GB_{Pre} (cpm)" is the background-corrected counts per minute in the pre-Kinevac gallbladder, and "GB_{Post} (cpm)" is the background-corrected counts per minute in the post-Kinevac gallbladder.

Gallbladder ejection fraction: Normal range The lower limits of normal for gallbladder ejection fraction following a 30 min infusion of Kinevac is 30 % [31].

Liver-Spleen Study

Overview The images of the Liver/Spleen Study demonstrate the distribution of the intravascular mononuclear phagocyte (macrophage) system. The intravascular members of this cell system line the sinusoids of the liver (Kupffer cells), spleen, and bone marrow.

Radiopharmaceutical characteristics Tc-99m-sulfur colloid consists of the colloidal particles covering a wide range in size from 0.1 to 2 μm. Most particles are in the 0.4–0.8 μm range [34, 35].

Extraction mechanism Tc-99m-sulfur colloid and similar particles are removed from the circulation by macrophages via phagocytosis (Fig. 15.11) [36, 37].

Macrophages are large white blood cells which temporarily occlude capillary lumens until they are able to deform, pass through the capillary, and reenter the flowing blood in the venule. Thus, in most capillary beds, macrophages cannot phagocytose particles from blood flowing past them. However, in sinusoids the

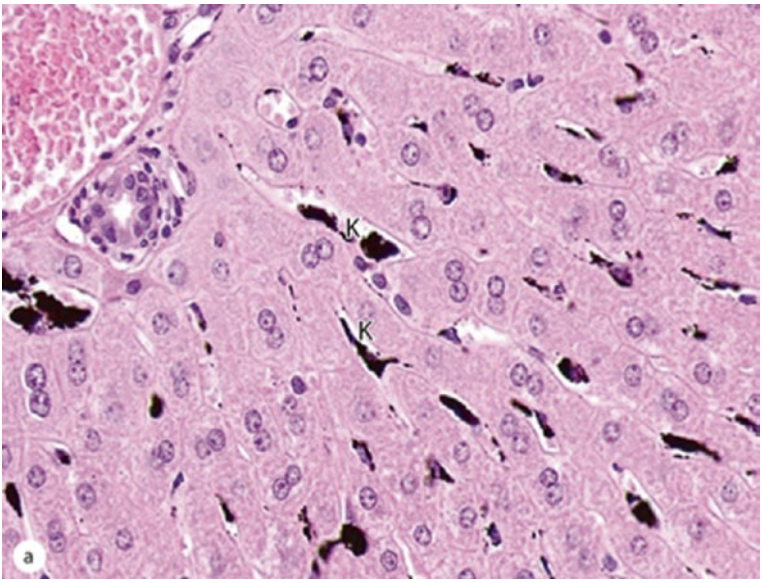

Fig. 15.11 Histologic image of rat liver following intravenous injection of particulate India ink. The Kupffer cells (macrophages) in the sinusoids (K) contain large amounts of particulate India ink. Notice that the Kupffer cells line the margins of the sinusoids and do not obstruct flow. Any circulating particles flow past the Kupffer cells and make contact with the pseudopods extending from the plasma membrane initiating phagocytosis (Junqueira's *Basic Histology: Text and Atlas*. Lange & McGraw Hill Mescher AL, 2013, p 336, fig 16-15)

lumen is larger than in ordinary capillaries, and macrophages can assume a marginal position without obstructing flow. Here colloidal particles brush up along the macrophages and are phagocytized.

Phagocytosis is a triggered process. The colloidal particles bind to the macrophages and initiate the process of invagination, the creation of a phagosome around the colloid, and the internalization of the phagosome by the macrophage.

Extraction efficiency High. At 5 min after intravenous injection of the Tc-99m-sulfur colloid, essentially all of the radiopharmaceutical has been cleared from the blood and imaging can begin. Normally, 80–85 % of the dose localizes in the liver, 5–10 % in the spleen, and the rest in the bone marrow [38].

Extraction mechanism saturable or non-saturable Non-saturable.

Interventions None.

Imaging Imaging is performed with a dual-headed gamma camera with a low-energy high-resolution parallel-hole collimator.

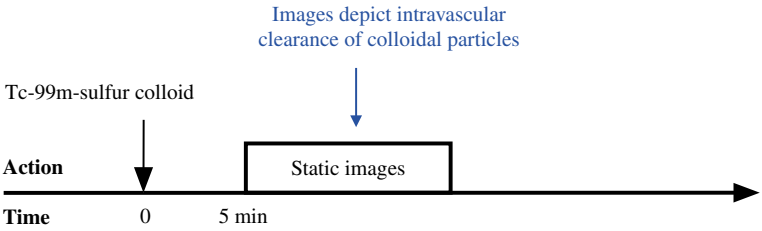

Fig. 15.12 Protocol summary diagram

Protocol design Anterior and posterior images are obtained of the upper abdomen in the anterior and posterior projections and in both lateral projections (Fig. 15.12).
Quantitative measurement None.

Meckel's Diverticulum Study (Tc-99m-Pertechnetate)

Overview The images of the Meckel's Diverticulum Study depict the uptake of pertechnetate within the abdomen. Pertechnetate is secreted by the mucosa of the stomach as well as by any ectopic gastric mucosa. Because pertechnetate exhibits only weak protein binding, it is also filtered by the kidneys.
Radiopharmaceutical characteristics The chemical structure of Tc-99m-pertechnetate is shown in Fig. 15.13. It has a molecular weight of 162.91.
Extraction mechanism Autoradographic evidence suggests that in the stomach, Tc-99m-pertechnetate is primarily secreted by the mucous producing epithelial cells [36, 37].
Extraction efficiency Moderate.
Extraction mechanism saturable or non-saturable Intravenous administration of perchlorate can compete with Tc-99m-pertechnetate, but this is rarely a clinical problem [36, 37].
Interventions There is some evidence that cimetidine can enhance the secretion of Tc-99m-pertechnetate [39, 40].
Imaging Images are acquired with a dual-head gamma camera fitted with a low-energy, high-resolution, parallel-hole collimator.
Protocol design Serial anterior and posterior static images are obtained for 1 h following injection of the Tc-99m-pertechnetate (Fig. 15.14).
Quantitative measurement None.

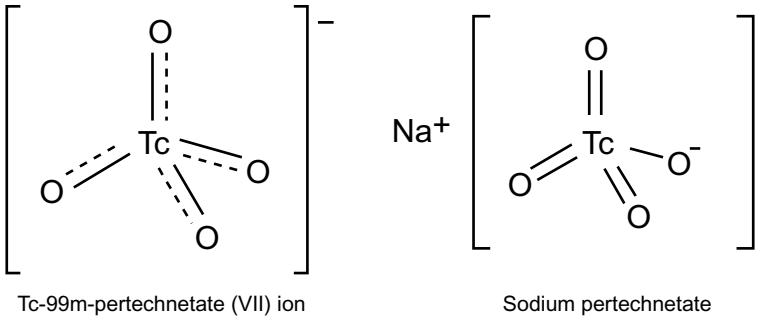

Fig. 15.13 Chemical structure of sodium pertechnetate

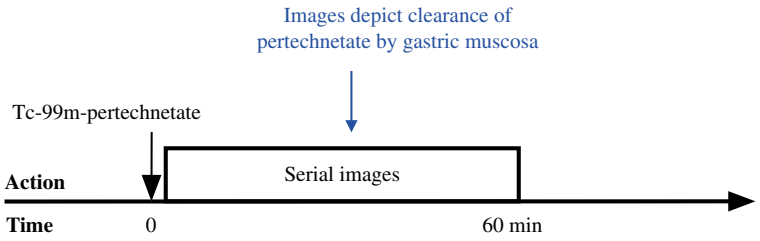

Fig. 15.14 Protocol summary diagram

References

Esophageal Transit Study (Tc-99m-Sulfur Colloid in Water)

1. Klein HA. Esophageal transit scintigraphy. Semin Nucl Med. 1995;25:306–17.
2. Mariani G, Boni G, Barreca M, et al. Radionuclide gastroesophageal motor studies. J Nucl Med. 2004;45:1004–28.
3. Eshima D, Eshima L, Gotti NM, et al. Technetium-99m-sulfur colloid for lymphoscintigraphy: effects of preparation parameters. J Nucl Med. 1996;37:1575–8.
4. Tatsch K, Voderholzer WA, Weiss MJ, et al. Reappraisal of quantitative esophageal scintigraphy by optimizing results with ROC analyses. J Nucl Med. 1996;37:1799–805.
5. Jorgensen F, Hesse B, Tromholt N, et al. Esophageal scintigraphy: reproducibility and normal ranges. J Nucl Med. 1992;33:2106–9.

Gastric Emptying Study (Tc-99m-Sulfur Colloid Labeled Oatmeal)

6. Fitzpatrick ML, Alderson AM. Solid food label for measurement of gastric emptying [Letter]. Br J Radiol. 1979;52:920–1.
7. Maloy TA, Herrera M, Zimmer M, et al. Optimal radiolabeling methods for Tc-99m-sulfur colloid oatmeal products for gastric emptying. J Nucl Med. 2011;52:498.
8. Abell TL, Camilleri M, Donohoe K, et al. Consensus recommendations for gastric emptying scintigraphy: a joint report of the American Neurogastroenterology and Motility Society and

the Society of Nuclear Medicine. Am J Gastroenterol. 2008;103:753–63 & J Nucl Med Technol. 2008;36:44–54.
9. Gryback P, Hermansson G, Lyrenas E, et al. Nationwide standardization and evaluation of scintigraphic gastric emptying: reference values and comparisons between subgroups in a multicenter trial. Eur J Nucl Med. 2000;27:647–55.
10. Klingensmith WC, Lawrence SP. The gastric emptying study: protocol design considerations. J Nucl Med Technol. 2008;36:195–9.
11. Klingensmith WC, Rhea KL, Wainwright EA, et al. The gastric emptying study with oatmeal: normal range and reproducibility as a function of age and sex. J Nucl Med Technol. 2010;38:186–90.
12. Koeppen BM, Stranton BA. Berne and Levy physiology. 6th ed. Mosby/Elsevier: Philadelphia; 2008, fig. 26–8, p. 494.
13. Urbain JLC, Vantrappen G, Janssens J, et al. Intravenous erythromycin dramatically accelerates gastric emptying in gastroparesis diabeticorum and normals and abolishes the emptying discrimination between solids and liquids. J Nucl Med. 1990;31:1490–3.
14. Ziessman HA, Atkins FB, Vemulakonda US, et al. Lag phase quantification for solid gastric emptying studies. J Nucl Med. 1996;37:1639–43.

Gastrointestinal Bleeding Study (Tc-99m-red Blood Cells)

15. Winzelberg GG, McKusick KA, Froelich JW, et al. Detection of gastrointestinal bleeding with Tc-99m-labeled red blood cells. Semin Nucl Med. 1982;12:139–46.
16. Zuckier LS. Acute gastrointestinal bleeding. Semin Nucl Med. 2003;33:297–311.
17. Freedman JC. Cell membranes. In: Sperelakis N, editor. Cell physiology sourcebook: essentials of membrane biophysics. 4th ed. London: Academic; 2012. p. 49.
18. Yama N, Ezoe E, Kimura Y, et al. Localization of intestinal bleeding using a fusion of Tc-99m-labeled RBC SPECT and x-ray CT. Clin Nucl Med. 2005;30:488–9.

Hepatic Artery Perfusion Study (Tc-99m-Macroaggregated Albumin)

19. Giammarile F, Bodei L, Chiesa C, et al. EANM procedure guideline for the treatment of liver cancer and liver metastases with intra-arterial radioactive compounds. Eur J Nucl Med. 2011;38:1393–406.
20. Hunt AP, Frier M, Johnson RA, et al. Preparation of Tc-99m-macroaggregated albumin from recombinant human albumin for lung perfusion imaging. Eur J Pharm Biopharm. 2006;62:26–31.
21. Hamami ME, Poeppel TD, Muller S, et al. SPECT-CT with Tc-99m-MAA in radioembolization with Y-90 microspheres in patients with hepatocellular cancer. J Nucl Med. 2009;50:688–92.
22. SIR-Spheres microspheres (Yittrium-90 Microspheres) Package insert. Wilmington: Sirtex Medical Inc.

Hepatic Hemangioma Study (Tc-99m-Red Blood Cells)

23. Schillaci O, Danieli R, Manni C, et al. Technetium-99m-labelled red blood cell imaging in the diagnosis of hepatic haemangiomas: the role of SPECT/CT with a hybrid camera. Eur J Nucl Med Mol Imaging. 2004;31:1011–5.

Hepatobiliary Study (Tc-99m-Trimethylbromo-IDA)

24. Klingensmith WC. Hepatobiliary imaging: normal appearance and normal variations. In: Gottschalk A, Hoffer PA, Berger HJ, Potchen EJ, editors. Diagnostic nuclear medicine. Baltimore: Williams and Wilkins; 1988.
25. Klingensmith WC, Spitzer VM, Fritzberg AR. The normal fasting and postprandial Tc-99m-diisopropyl-IDA hepatobiliary study. Radiol. 1981;141:771–6.
26. Kamisako T, Kobayashi Y, Takeuchi K, et al. Recent advances in bilirubin metabolism research: the molecular mechanism of hepatocyte bilirubin transport and its clinical relevance. J Gastroenterol. 2000;35:659–64.
27. van de Steeg E, Stranecky V, Hartmannova H, et al. Complete OAT1B1 and OATP1B3 deficiency causes human Rotor syndrome by interrupting conjugated bilirubin reuptake into the liver. J Clin Invest. 2012;122:519–28.
28. Jedlitschky G, Keier I, Hummel-Eisenbeiss J, et al. ATP-dependent transport of bilirubin glucronides by the multidrug resistance protein MRP1 and its heptocyte canalicular isoform MRP2. Biochem J. 1997;327:305–10.
29. Chen CC, Holder LE, Maunoury C, et al. Morphine augmentation increases gallbladder visualization in patients pretreated with cholecystokinin. J Nucl Med. 1997;38:644–7.
30. Ziessman HA, Fahey FH, Hixson DJ. Calculation of a gallbladder ejection fraction: advantage of continuous sincalide infusion over the three-minute infusion method. J Nucl Med. 1992;33:537–41.
31. Ziessman HA, Muenz L, Agarwal AK, et al. Normal values for sincalide cholescintigraphy: comparison of two methods. Radiol. 2001;221:404–10.
32. Xynos E, Pechlivanides G, Zoras OJ, et al. Reproducibility of gallbladder emptying scintigraphic studies. J Nucl Med. 1994;35:835–9.
33. Pons V, Sopena R, Hoyos M, et al. Quantitative cholescintigraphy: selection of random dose for CCK-33 and reproducibility of abnormal results. J Nucl Med. 2003;44:446–50.

Liver-Spleen Study (Tc-99m-Sulfur Colloid)

34. Klingensmith WC, Spitzer VM, Fritzberg AR, et al. Normal appearance and reproducibility of liver-spleen studies with Tc-99m-sulfur colloid and Tc-99m-microalbumin colloid. J Nucl Med. 1983;24:8–13.
35. Karesh S. Radiopharmaceuticals in nuclear medicine: consultants in nuclear medicine. www.nucmedtutorials.com/dwradiopharm/rad9.html.
36. Intracellular vesicular traffic. In: Alberts B, Johnson A, Lewis J, et al., editors. The molecular biology of the cell, 5th ed. New York, NY: Garland Science; 2008. p. 787–98.
37. Saha GB. Diagnostic uses of radiopharmaceuticals in nuclear medicine. In: Saha GB, editor. Fundamentals of nuclear pharmacy. 6th ed. New York: Springer; 2010.
38. Hindie E, Coals-Linhart N. Microautoradiographic study of technetium-99m colloid uptake by the rat liver. J Nucl Med. 1988;29:1118–21.

Meckel's Diverticulum Study (Tc-99m-Pertechnetate)

39. Williams JG. Pertechnetate and the stomach: a continuing controversy. J Nucl Med. 1983;24:633–6.
40. Emamian SA, Shalaby-Rana E, Majd M. The spectrum of heterotopic gastric mucosa in children detected by Tc-99m pertechnetate scintigraphy. Clin Nucl Med. 2001;26:529–35.

Genitourinary System

16

Cystogram–Direct (Tc-99m-Pertechnetate)

Overview The images of the retrograde or Cystogram–Direct are used for the diagnosis and follow-up of vesicoureteral reflux. In general, the study is more sensitive than radiographic methods because of the high contrast between instilled radioactivity in the bladder and the lack of radioactivity outside of the bladder.

Radiopharmaceutical characteristics Tc-99m-pertechnetate, Tc-99m-sulfur colloid, and Tc-99m-DTPA have all been used [1]. Tc-99m-pertechnetate is the least expensive. Its molecular structure is shown in Fig. 16.1. It has a molecular weight of 162.91.

Extraction mechanism None. The radiopharmaceutical equilibrates in a cavity, the bladder, and any patent connections to the bladder such as the ureters.

Extraction efficiency Zero percent.

Extraction mechanism, saturable or non-saturable Not applicable.

Interventions None.

Imaging Images are acquired with a dual-head gamma camera fitted with a low-energy, high-resolution, parallel-hole collimator.

Protocol design A Foley catheter is placed and the radiopharmaceutical is administered via the injection port of the catheter. Serial 10 s images are acquired during both filling and emptying for cine display (Fig. 16.2).

Quantitative measurement: Post-void residual The post-void residual volume of the bladder can be determined although this is not routine. A combination of the counts in the bladder ROI at the end of filling and after voiding in conjunction with measurement of the volume of voided urine allows calculation of the residual volume with the following equation,

$$\mathrm{RBV}(\mathrm{mL}) = \frac{\mathrm{RBA}(\mathrm{cpm}) \times \mathrm{VU}(\mathrm{mL})}{\mathrm{FBA}(\mathrm{cpm}) - \mathrm{RBA}(\mathrm{cpm})} \tag{16.1}$$

W.C. Klingensmith III, *The Mathematics and Biology of the Biodistribution of Radiopharmaceuticals-A Clinical Perspective*,
DOI 10.1007/978-3-319-26704-3_16

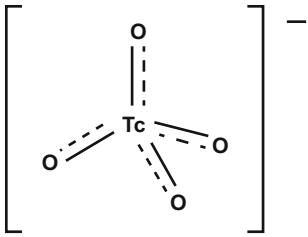

Fig. 16.1 Chemical structure of Tc-99m-pertechnetate (Tc-99m-pertechnetate (VII) ion.)

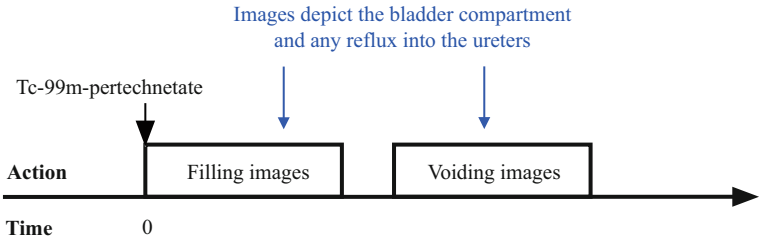

Fig. 16.2 Protocol summary diagram

where "RBV" is residual bladder volume in milliliters, "RBA" is residual bladder activity in counts per minute, "VU" is voided urine volume in milliliters, and "FBA" is full bladder activity in counts per minute. This equation is discussed in more detail in Chap. 10, Other Quantitative Techniques.

Renal Glomerular Filtration Study (Tc-99m-DTPA)

Overview The Renal Glomerular Filtration Study images Tc-99m-DTPA as it passes through the renal vascular system, renal glomeruli, renal tubular lumens, and collecting system. This series of images allows the sequential evaluation of renal blood flow, renal clearance by glomerular filtration, renal parenchymal transit time, and passage of urine through the renal collecting system.

Radiopharmaceutical characteristics Tc-99m-DTPA is a combination of the ligand diethylenetriaminepentaacetic acid (pentetic acid), a metal chelator, and Tc-99m, a metal. Its chemical structure is shown in Fig. 16.3. The molecular weight of the radiopharmaceutical is 482.31.

Extraction mechanism Tc-99m-DTPA is passively extracted (cleared) from the blood by renal glomerular filtration (Figs. 16.4, 16.5, and 16.6). Tc-99m-DTPA circulates in the plasma compartment of blood without significant protein binding. Tc-99m-DTPA is small compared to the pore size of the glomeruli (Table 16.1). For instance, inulin is approximately ten times larger than Tc-99m-DTPA, but inulin is easily filtered through the glomerulus [3].

Extraction efficiency The extraction efficiency for Tc-99m-DTPA is 20 %.

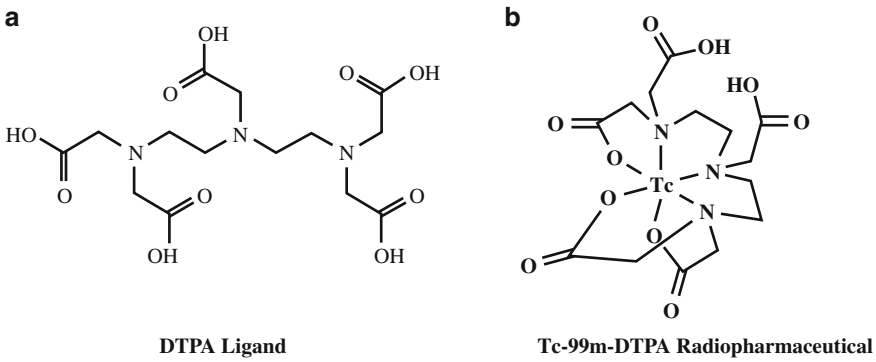

Fig. 16.3 Tc-99m-DTPA. (**a**) Diethylenetriaminepentaacetic acid (*DTPA*) ligand without the radioisotope Tc-99m. (**b**) Tc-99m-DTPA after the metal chelator, DTPA, has chelated the metal, Tc-99m

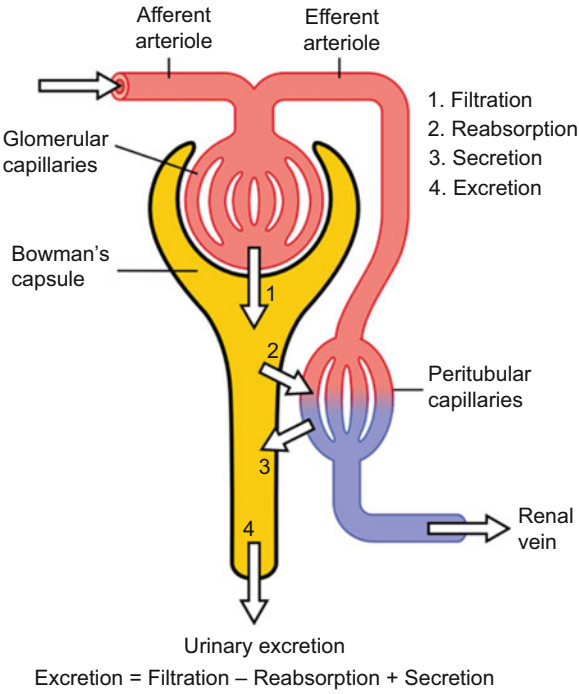

Fig. 16.4 Diagram of a nephron unit. Tc-99m-DTPA is cleared in the kidneys by glomerular filtration only (mechanism 1). Tc-99m-MAG3 is cleared primarily by tubular secretion (mechanism 3) (Hall [2])

Extraction mechanism, saturable or non-saturable The extraction mechanism is non-saturable. There is no specific receptor involved in the clearance of Tc-99m-DTPA by the renal glomerulus.

Interventions A diuretic such as Lasix is usually given at some time during the study.

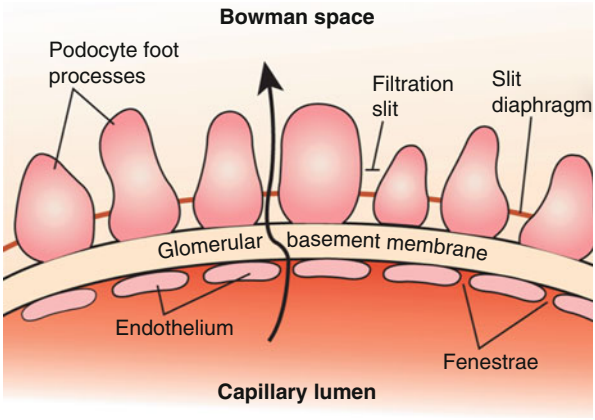

Fig. 16.5 Diagram of filtration apparatus of the renal glomerulus. Glomerular filtration involves the ultrafiltration of plasma. In the glomerulus, the capillary lining has gaps, fenestrae, between the endocytes. On the other side of the basement membrane, an array of podocyte foot processes support the basement membrane but have numerous filtration slits. This arrangement allows large amounts of fluid and small molecules to be filtered out of the vascular space and into Bowman space [4]

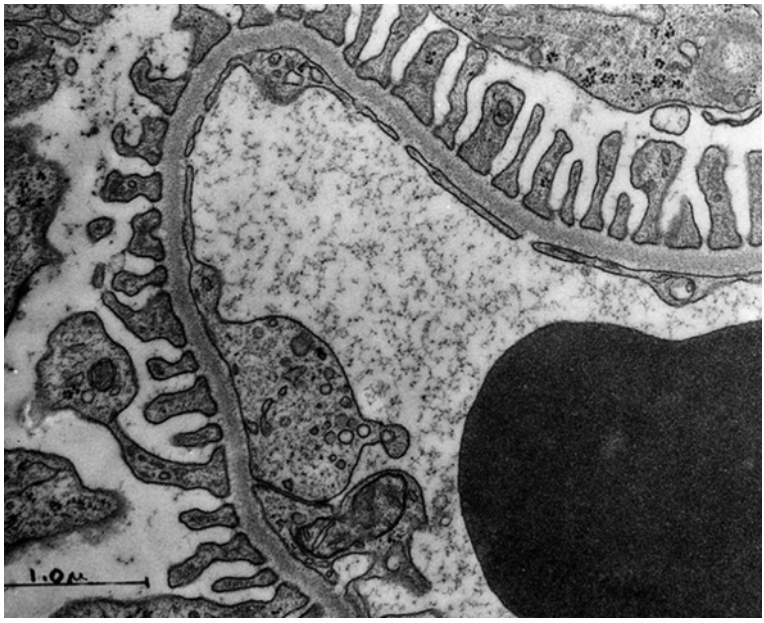

Fig. 16.6 Electron micrograph of a portion of the renal glomerulus. This image demonstrates the actual anatomy of the structures shown in the diagram above

Imaging Images are acquired with a dual-head gamma camera fitted with a low-energy, high-resolution, parallel-hole collimator.

Table 16.1 Restrictions to glomerular filtration of molecules

Substance	Molecular weight	Molecular radius (nm)	Filtrate/plasma
Water	18	0.10	1.00
Glucose	180	0.36	1.00
Inulin	5000	1.4	1.00
Myoglobin	17,000	2.0	0.75
Hemoglobin	68,000	3.3	0.01
Albumin	66,000	3.6	0.001

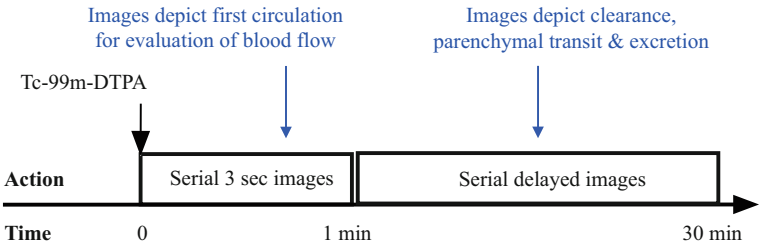

Fig. 16.7 Protocol summary diagram

Protocol design Serial images are acquired for 30 min beginning at the time of intravenous injection of the Tc-99m-DTPA. During the first 1 min, sequential 3 s images are acquired for the evaluation of blood flow to the kidneys during the first circulation of the tracer (see Chap. 6, Blood Flow: First Circulation Time-Activity Curves). Then delayed images are acquired periodically through the rest of the study for the evaluation of renal clearance by glomerular filtration, transit through the renal parenchyma, and passage of the tracer through the collecting system, i.e., from the renal calyces to the bladder (see Chaps. 4, Evaluation of Clearance and 7, Mean Transit Time: Convolution Analysis) (Fig. 16.7).

Lasix is commonly given at 10 min after injection of the Tc-99m-DTPA. This timing allows evaluation of renal function without the effect of Lasix in the images acquired before 10 min and then evaluation of the effect of Lasix in the images acquired after 10 min. (The diuretic effect of Lasix begins about 2 min after injection of the diuretic.)

Quantitative measurement Because Tc-99m-MAG3 has a significantly higher extraction efficiency than Tc-99m-DTPA, the Renal Tubular Secretion Study with Tc-99m-MAG3 has essentially replaced the Renal Glomerular Filtration Study with Tc-99m-DTPA. Since the quantitative analysis for the two studies is the same except for the normal ranges for clearance, the discussion of quantitative analysis will be given only for the Renal Tubular Secretion Study in the section that follows.

Renal Tubular Secretion Study (Tc-99m-MAG3)

Overview The Renal Tubular Secretion Study images Tc-99m-MAG3 as it passes through the vascular system, renal tubular cells, tubular lumens, and collecting system [5]. This series of images allows the sequential visual and quantitative evaluation of renal blood flow, clearance by tubular excretion, parenchymal transit time, and passage of urine through the renal collecting system.

Radiopharmaceutical characteristics Tc-99m-MAG3 is a disodium salt; its chemical structure is shown in Fig. 16.8. The molecular weight of the Tc-99m-MAG3 is 341.10.

Extraction mechanism Although Tc-99m-MAG3 is a relatively small molecule, it is highly bound to albumin and, therefore, functionally too large to be filtered by the glomeruli (Table 16.1). Instead, it is cleared by the renal organic anion transporter 1 (OAT1) mechanism in the proximal tubule of the kidney (Fig. 16.9) [6, 7]. OAT1 is an active transport mechanism located in the basolateral membrane of the tubular cells, facing the efferent artery. Movement of Tc-99m-MAG3 from the tubular cell across the brush border membrane into the tubular lumen is felt to be by facilitated transport. OAT1 excretes a wide variety of organic anions.

Extraction efficiency The extraction efficiency of Tc-99m-MAG3 is approximately 65 % [7, 9].

Extraction mechanism, saturable or non-saturable Although some compounds including probenecid significantly compete with Tc-99m-MAG3 under experimental conditions, saturation is not observed clinically [10].

Interventions A diuretic such as Lasix is usually given at some time during the study. In addition, ACE inhibitors can be given when the study is performed for the detection of renal artery stenosis as a cause of hypertension [11].

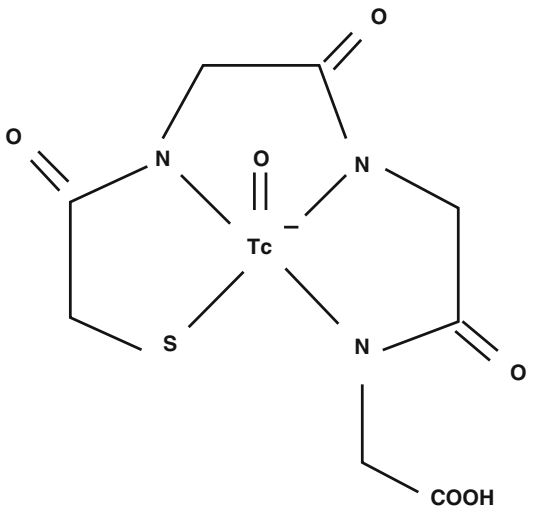

Fig. 16.8 Chemical structure of Tc-99m-MAG3

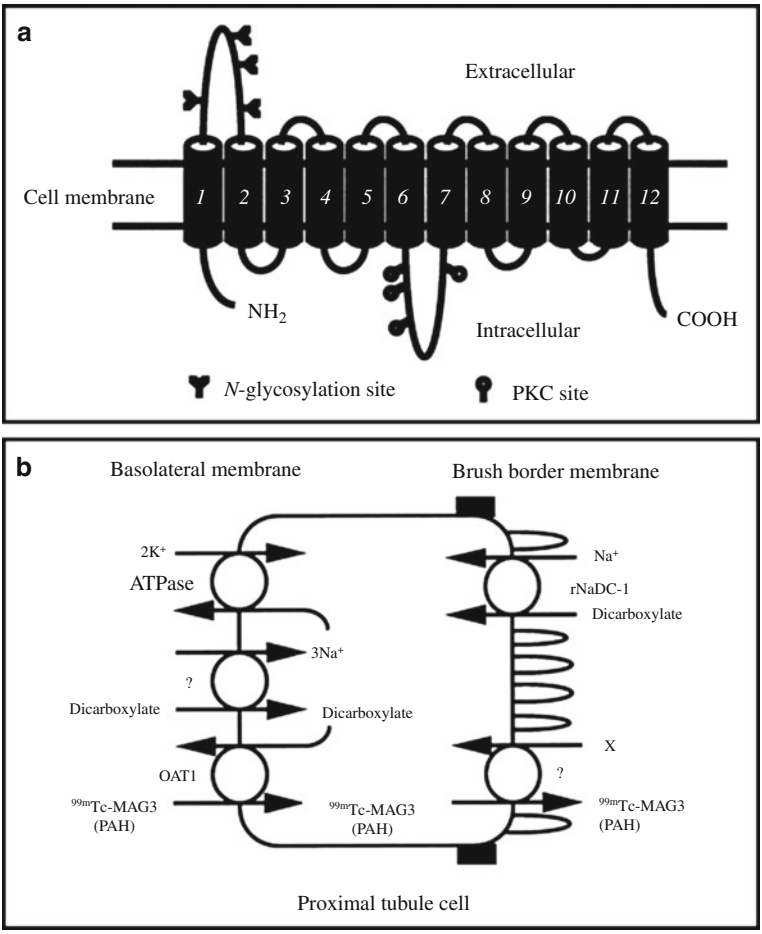

Fig. 16.9 Diagrams of a proposed mechanism for transport of Tc-99m-MAG3 across tubular cells. (**a**) Shows a possible structure for the organic anion transporter (OAT1) protein in the basolateral membrane. (**b**) Shows a possible complex series of events needed to secrete Tc-99m-MAG3 into the tubular lumen (the brush border membrane faces the tubular lumen) (Shikano et al. [8])

Imaging Images are acquired with a dual-head gamma camera fitted with a low-energy, high-resolution, parallel-hole collimator.

Protocol design Serial images are obtained for 30 min beginning at the time of intravenous injection of the Tc-99m-MAG3. Sequential 3 s images are obtained during the first 1 min for the evaluation of blood flow to the kidneys during the first circulation of the tracer (see Chap. 6, Blood Flow: First Circulation Time-Activity Curves). Then delayed images are obtained periodically through the rest of the study for the evaluation of renal clearance by tubular secretion, transit through the renal parenchyma, and passage of the tracer through the collecting system, i.e., from the renal calyces to the bladder (see Chaps. 6, Evaluation of Clearance and 7, Regional Transit Time: Convolution Analysis).

Lasix® (furosemide) is commonly given at 10 min after injection of the Tc-99m-MAG3. This timing allows the evaluation of renal function without the effect of Lasix in the images acquired before 10 min and then the evaluation of the effect of Lasix in the images obtained after 10 min (the diuretic effect of Lasix about 2 min after injection) (Fig. 16.10).

Quantitative measurements – Multiple An example of a normal renal study with Tc-99m-MAG3 is shown in Fig. 16.11.

The images of the Tc-99m-MAG3 renal study demonstrate and allow assessment of four functional parameters: (1) blood flow, (2) clearance, (3) parenchymal transit, and (4) excretion, i.e., tracer movement through the collecting systems from calyces to bladder. The Renal Tubular Secretion Study with Tc-99m-MAG3 demonstrates more biologic functions with corresponding mathematical descriptions than any other nuclear medicine study. The anatomic correlates of these four functional parameters are depicted diagrammatically in Fig. 16.12.

Table 16.2 summarizes the role that the mathematics described in Part II, Mathematics of the Biodistribution of Radiopharmaceuticals, plays in the evaluation of each of the four biologic parameters. The mathematical role varies from none for the "excretion" parameter, to two quantitative measurements for both "clearance" and "parenchymal transit time" parameters. Blood flow extends from the site of injection to the renal tubular cells. Clearance occurs at the interface of the efferent renal artery and the tubular cell. Parenchymal transit occurs from the tubular cell to the calyx. And excretion occurs from the calyx to the bladder. Except for the first few blood flow images during which the leading edge of the bolus is passing from the injection site to the kidneys, the images reflect more than one physiologic process at a time. However, as discussed below, images can be selected that predominantly show each of the four functional parameters.

In addition to routine visual evaluation of the images, time-activity curves are generated from two pairs of ROIs: (1) ROIs placed around the kidneys and upper collecting systems (calyces, infundibula, and renal pelves) and (2) ROIs placed over the renal cortical parenchyma, but excluding the calyces. In addition, ROIs are placed below the kidneys to estimate background activity (Fig. 16.11).

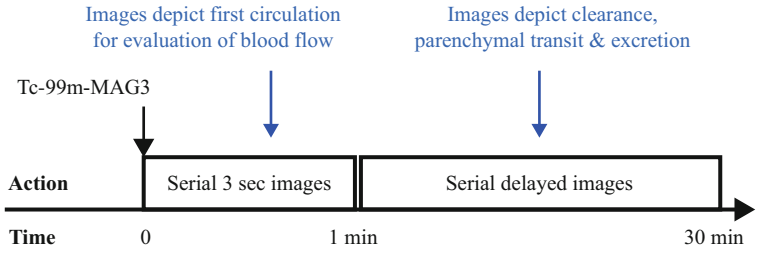

Fig. 16.10 Protocol summary diagram

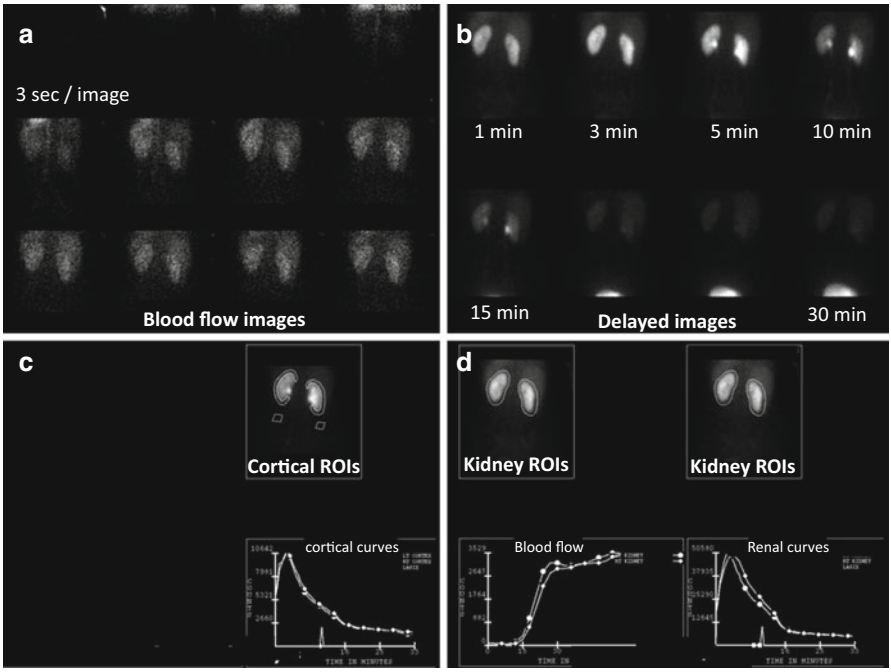

Fig. 16.11 Normal renal tubular secretion study with Tc-99m-MAG3. (**a**) 3 s sequential images during the first circulation depict renal blood flow. (**b**) Delayed images depict renal function from 1 min to the end of the study at 30 min. (**c**, **d**) Documentation of placement of ROIs and the resulting time-activity curves

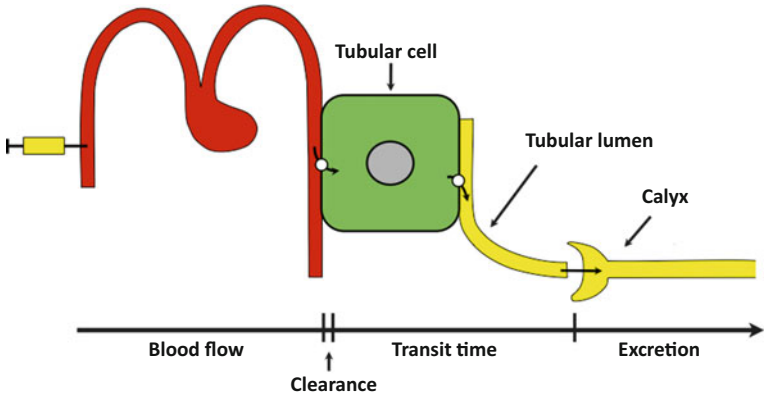

Fig. 16.12 Anatomic representation of physiologic steps from injection site to collecting system. Diagram shows the sequential passage of Tc-99m-MAG3 through four physiologic processes: (1) blood flow, (2) clearance, (3) parenchymal transit, and (4) excretory structures. The small white circles on the tubular cell indicate that membrane receptors are involved in these steps

Table 16.2 Renal Tubular Secretion Study: parameters and their assessment

Parameter	Quantitation in absolute terms	Quantitation in relative terms	Quantitative index	Visual assessment of images and/or T-A curves	Described mathematically
Blood flow	No	No	No	Yes	Yes (Chap. 6)
Clearance	Yes	Yes	No	Yes	Yes (Chap. 4)
Parenchymal transit time	No	No	Yes [3]	Yes	Yes (Chap. 7)
Excretion	No	No	No	Yes	No

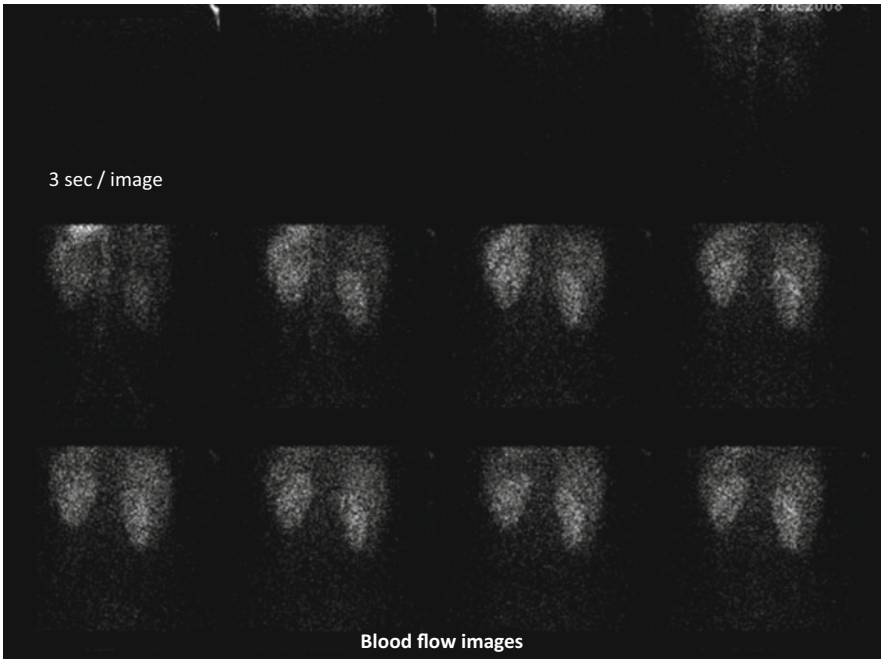

Fig. 16.13 Renal blood flow images. Serial 3 s posterior images demonstrate tracer first in the lung bases, then in the abdominal aorta, both kidneys, and the liver and spleen

The time-activity curves from the kidney and cortical ROIs are corrected for background activity (Fig. 16.11). However, except for the one parameter in which quantification of renal clearance is calculated in absolute terms, no attenuation correction is made for the other parameters because the two kidneys or portions thereof are compared to each other and are assumed to have similar photon attenuation.

The first step in the evaluation of the Tc-99m-MAG3 renal study is to visually evaluate the quality of the bolus of radiopharmaceutical (Fig. 16.13). A good bolus

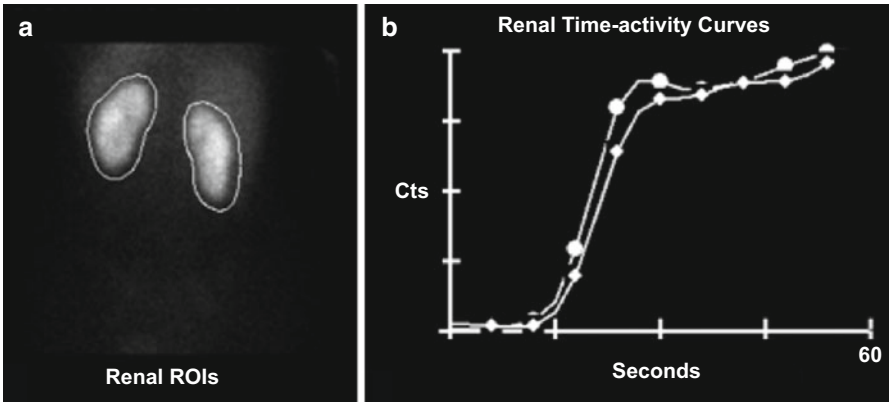

Fig. 16.14 Renal ROIs and time-activity curves. (**a**) ROIs placed around kidneys in 1 min image. (**b**) Time-activity curves plateau, rather than fall, because of the relatively high extraction efficiency (65 %) of the tubular cells for Tc-99m-MAG3

will appear and disappear from the abdominal aorta in approximately 10 s or in three to four consecutive 3 s images. Also, by visual assessment, the activity in the kidneys during the first circulation images should be symmetrical and exceed the concentration of activity in other structures of the abdomen. Normally, each kidney receives 10 % of cardiac output (see Appendix D).

Blood flow: Renal blood flow can be satisfactorily evaluated by visual analysis of the serial 3 s images acquired during the first 60 s and by visual analysis of the renal time-activity curves generated from the serial 1 s images acquired during the first 60 s (see Chap. 6, Blood Flow: First Circulation Time-Activity Curves). Although blood flow to the kidneys can be evaluated in relative terms by various quantitative analyses of the kidney time-activity curves, it is felt that these analyses do not add significant additional information beyond visual analysis of the curves [9]. In addition, the Tc-99m-MAG3 first circulation time-activity curves do not fall as much from their peaks as they would if the radiopharmaceutical were not cleared from the blood because approximately 65 % of Tc-99m-MAG3 is cleared and retained in the parenchyma during each circulation, i.e., a 65 % extraction efficiency. In fact, the time-activity curve does not peak at all, but plateaus (Fig. 16.14).

Clearance: Renal clearance of Tc-99-MAG3 from the blood into the renal parenchyma is evaluated visually, and quantitatively in both relative and absolute terms (Table 16.2). Clearance by any of these three methods is best evaluated in an image taken at a time when the kidneys have had some time to clear tracer from the blood, but before the tracer has had time to move through the parenchyma and start entering the collecting system. Most commonly this is the image acquired from 1 to 2 min (Fig. 16.15).

Visual assessment of clearance in normal kidneys shows symmetrical activity, greater activity than any other structures in the 1 min image, and greater activity than in the kidneys during the 60 s blood flow images. Initially, activity in the

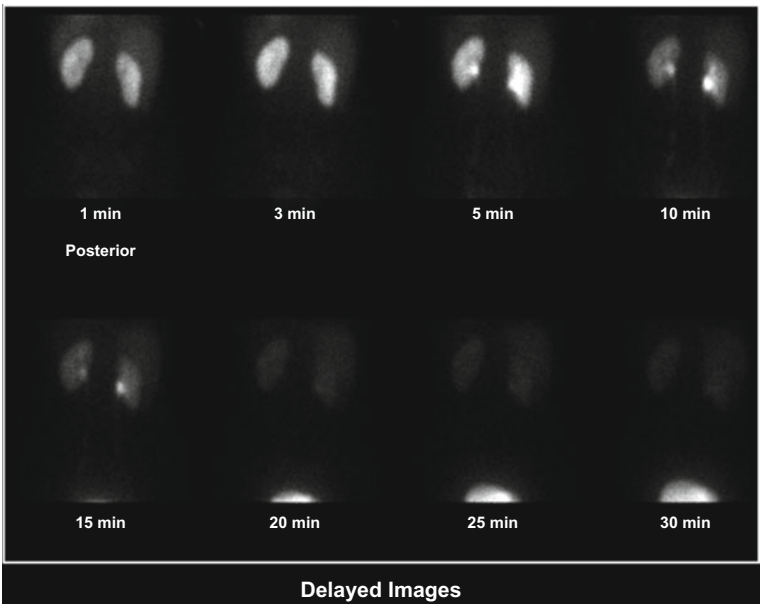

Fig. 16.15 Delayed images from a normal Renal Tubular Secretion Study with Tc-99m-MAG3. The images demonstrate the passage of tracer through the renal parenchyma, into the upper collecting system, and through the collecting system to the bladder reservoir

kidneys increases with time because the radiopharmaceutical continues to be cleared while none is excreted. Eventually, the kidney activity peaks because more activity is leaving the renal parenchyma to enter the collecting system than is being cleared and entering the renal parenchyma (Fig. 16.16).

Clearance is also quantitatively measured in both a relative and absolute fashion. Quantitation of renal clearance in a relative fashion is done by determining the percent of total renal function in each of the two kidneys from the 1 to 2 min image. This comparison is done after background correction, but without attenuation correction. Attenuation is assumed to be similar for both kidneys (see Chap. 8, Quantitation of Function: Relative Measurements). The normal range for asymmetry is given in Table 16.3 [5].

Clearance is also measured in absolute terms. Like all absolute measurements, the quantitative measurement of absolute renal clearance involves comparing the amount of activity in the kidneys, after background and attenuation correction, at an appropriate time, i.e., 1–2 min, to the amount of activity administered to the patient, i.e., dose (see Chap. 9, Quantitation of Function: Absolute Measurements). The normal range is relatively broad and decreases with age (Table 16.3).

Parenchymal transit time The formal mathematical approach to describing the parenchymal transit times through the approximately 900,000 renal nephron units is discussed in Chap. 7, Regional Transit Times: Convolution Analysis. Unfortunately, the required deconvolution analysis is not feasible in the clinical setting because it is difficult to generate an accurate time-activity curve of renal blood flow during the 30 min duration of the study.

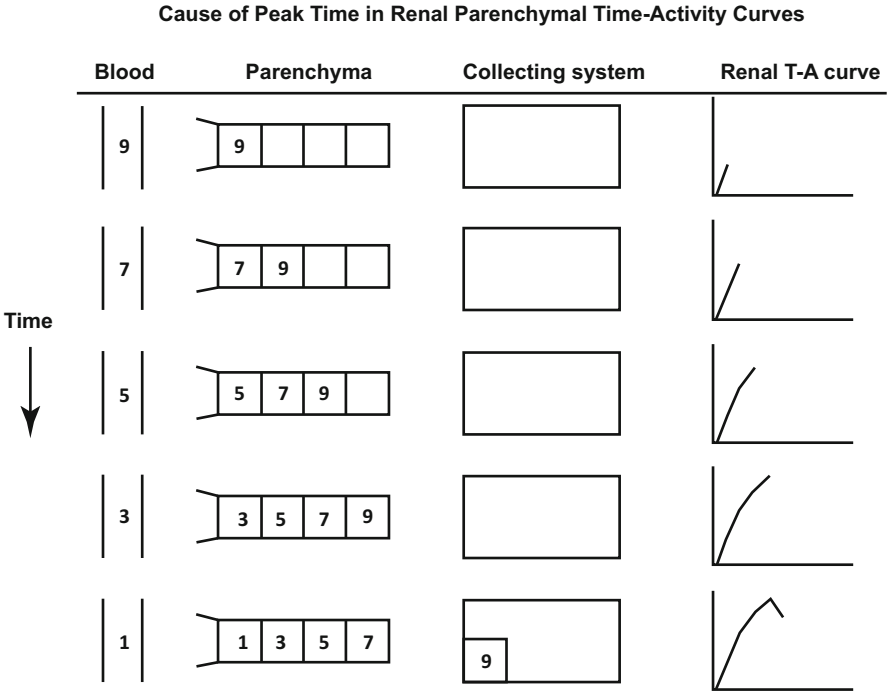

Fig. 16.16 Cause of peak time in cortical time-activity curves. The maximum concentration of activity in the blood occurs during the first circulation and then decreases exponentially thereafter as tracer is cleared from the blood. When the first activity exits the parenchyma and moves into the calyces, more activity is leaving the parenchyma than is entering the parenchyma. This causes the cortical time-activity curves to peak

Table 16.3 Renal Tubular Secretion Studies (Tc-99m-MAG3): normal ranges

Functional parameter	Normal range
Percent clearance for either kidney	42–58 %
Total renal clearance, 21–40 year	155–520 mL/min
Total renal clearance, 41–60 year	140–470 mL/min
Total renal clearance, 61–80 year	125–395 mL/min
Leading edge parenchymal transit time (cortical peak time)	≤4 min
Mean parenchymal transit time index (cortical half time from peak)	≤10 min
Time post Lasix® for activity to drop 50 % (renal time-activity curve)	≤10 min

However, the parenchymal transit time can be effectively evaluated with two indices that quantitate the leading edge transit time and mean transit time through the parenchyma. The leading edge parenchymal transit time can be visually evaluated quantitatively by noting the time at which activity first appears in the upper collecting system, which will coincide with the time of peak activity in the cortical time-activity curve (Fig. 16.16). Normally, tracer is seen in the collecting systems in either the 3 or 5 min images. In this case, it is the 5 min image.

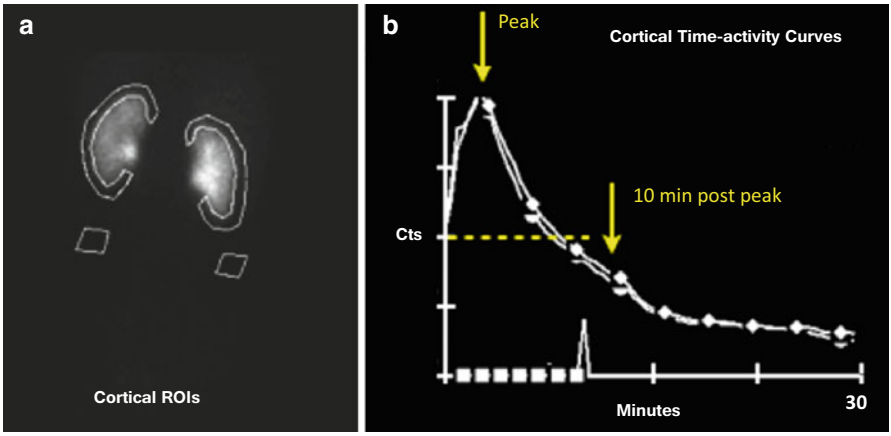

Fig. 16.17 Normal cortical time-activity curves. (**a**) ROIs over the cortices of the kidneys in 1 min image. Background ROIs are below the kidneys. (**b**) Normally the cortical time-activity curves fall by at least 50 % by 10 min after the peak

In addition, the mean transit time can be evaluated quantitatively as an index by measuring whether the activity in the renal parenchyma, as reflected in the renal cortical time-activity curves, decreases by at least one-half by 10 min after the peak of the cortical time-activity curve (Fig. 16.17).

Of note, the leading edge transit time can be normal when the mean transit time is abnormal. This is because only a minority of nephron units needs to be functioning normally to give a normal leading edge transit time while nearly all of the nephron units need to be functioning normally to give a normal mean transit time.

Excretory system Movement of urine through the excretory collecting systems is evaluated visually. Normally, the overall appearance of the collecting systems is affected by the degree of hydration and the upper collecting systems, e.g., renal pelvis, can be asymmetrical [11].

Enlarged renal pelves may be either a normal variant (patulous renal pelvis) or be caused by a ureteropelvic junction obstruction. These two etiologies can be differentiated by quantitative evaluation of washout from an enlarged renal pelves following administration of Lasix®. Normally, activity in the renal time-activity curve should decrease by at least 50 % 10 min following the time of injection of Lasix® (Fig. 16.18) [9].

Not infrequently, there is so little activity in the renal parenchyma and pelvis at 10 min that the activity cannot decrease by 50 % in the following 10 min. However, visually it is obvious that the washout is normal. In the literature, there is a wide range of recommended times for the administration of Lasix; 10 min is an intermediate choice.

The normal ranges and reproducibility for quantitative evaluation of clearance and transit time parameters are given in Table 16.3 [5] (see an example of a Tc-99m-MAG3 Renal Tubular Secretion Worksheet at the end of this chapter).

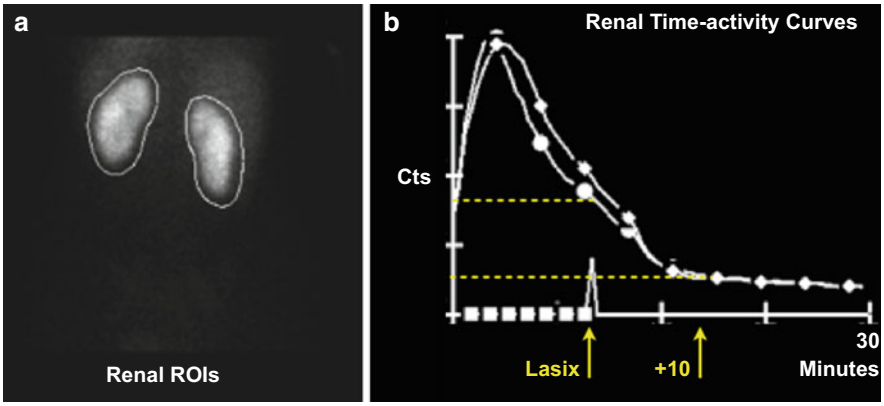

Fig. 16.18 Normal renal ROIs and time-activity curves (**a**, **b**). Lasix is given at 10 min after the injection of the radiopharmaceutical. The activity in the renal ROIs should decrease by at least 50 % by 10 min after the administration of the Lasix

Table 16.4 Interpretation of Renal Tubular Secretion Studies

1. Evaluate quality of bolus
2. Evaluate blood flow to each kidney
3. Evaluate clearance by each kidney
4. Evaluate leading edge and mean parenchymal transit times of each kidney
5. Evaluate excretion through collecting systems of each kidney
6. Evaluate anatomy of each kidney
7. Put it all together

Clinical considerations The proper approach to evaluating any nuclear medicine study is to evaluate each functional parameter individually plus anatomy, and then put the findings together to form a differential diagnosis (Table 16.4). Thus, in the Tc-99m-MAG3 Renal Tubular Secretion Study, the interpreter would begin by evaluating: the quality of the bolus, renal blood flow, clearance by tubular secretion, parenchymal transit (both leading edge and mean transit times), excretion (passage of tracer through the extra renal collecting systems), and anatomy.

Although many diseases affect nephrons differently at any given time, glomerular filtration and tubular secretion are affected in parallel in any single nephron. This phenomenon, referred to as the nephron unit theory, means that there is no advantage to studying both pathways in a single patient. Because of its higher extraction efficiency, Tc-99m-MAG3 is preferred and Tc-99m-DTPA is rarely used.

In general, regional renal blood flow changes in parallel with the associated nephron function. However, in acute tubular necrosis, blood flow is often relatively spared compared to clearance. This finding is relatively specific for acute tubular necrosis (Fig. 16.19) [12].

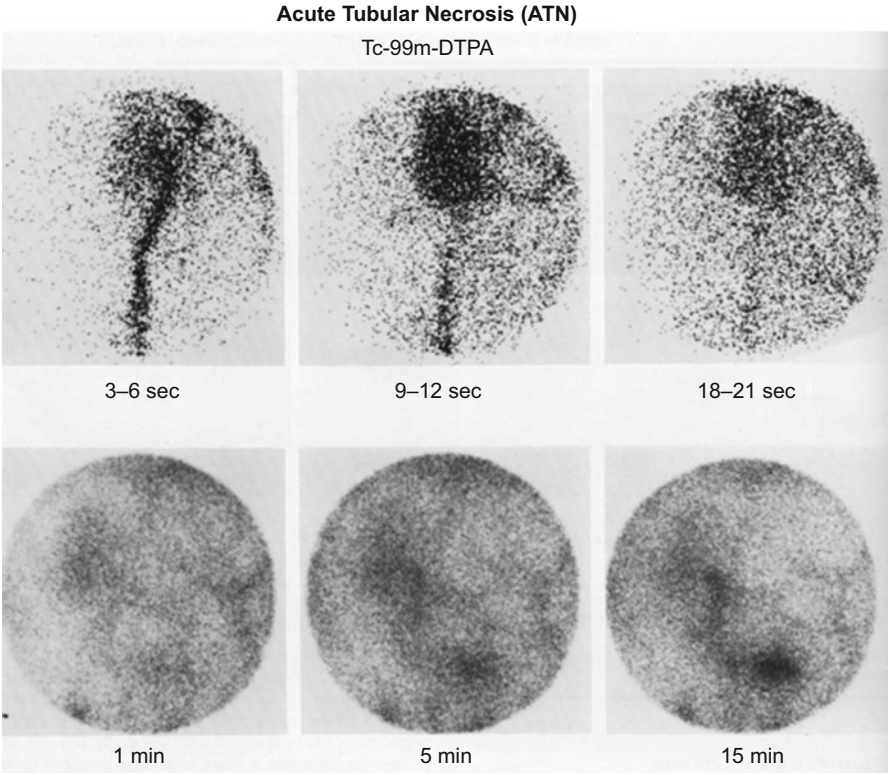

Fig. 16.19 Acute tubular necrosis in a transplanted kidney. The first circulation images (*top row*) show relatively normal blood flow. The delayed images (*bottom row*) show markedly decreased clearance. This combination is typical of acute tubular necrosis, but is not seen in all patients with acute tubular necrosis (Shanahan et al. [12])

Prolongation of the leading edge and mean parenchymal transit times tends to correspond to the acuteness of renal disease, e.g., acute tubular necrosis, and at the same time, the leading edge and mean parenchymal transit times tend to be relatively normal in chronic disease such as chronic diffuse renal disease. It may be that acute disease causes swelling of the renal parenchyma which compresses and obstructs the tubular lumens.

Examples of how the various functional parameters and anatomy can be put together to limit the diagnostic possibilities is shown in Table 16.5. Obstruction of the excretory system will invalidate the findings in the table by affecting all of the upstream functional parameters in reverse order and with increasing severity over time; this has been demonstrated experimentally in a dog model using the excretory pathway of the hepatobiliary system [13]. When the obstruction is very acute,

Table 16.5 Findings in various renal conditions

Condition	Blood flow	Clearance	Transit time	Excretion	Anatomy
Medical renal disease	Decreased	Decreased	Normal	Normal	Bilaterally small
ATN	Relatively normal	Decreased	Prolonged	Normal	Normal
Acute pyelonephritis	Decreased	Decreased	Prolonged	Normal	Regional abnormality
Chronic pyelonephritis	Decreased	Decreased	Normal	Dilatation	Cortical scarring
UPJ obstruction	Normal	Normal	Relatively normal	Delayed post Lasix	Large pelvis
RAS with ACE inhibitor	Relatively normal	Relatively normal	Prolonged	Normal	Normal

e.g., 1 day, the functional parameters appear normal because dilatation of the collecting system can accommodate urine production. Soon, thereafter, the parenchymal transit time becomes prolonged, and then renal clearance and blood flow decrease.

Renal tubular secretion clearance – Normal ranges See Table 16.3 and the Tc-99m-MAG3 Worksheet at the end of this chapter.

Renal Tubular Function Study (Tc-99m-DMSA)

Overview Tc-99m-DMSA is cleared from the blood into the renal tubular cells, but is not excreted into the urine. Thus, the Tubular Function Study with Tc-99m-DMSA depicts tubular function without interference from radioactivity in the collecting system.

Radiopharmaceutical characteristics The chemical structure Tc-99m-DMSA is shown in Fig. 16.20. The molecular weight of the Tc-99m-DMSA is 281.13.

Extraction mechanism About 75 % of Tc-99m-DMSA is protein bound. Evidence suggests that the main mechanism for clearance of Tc-99m-DMSA is glomerular filtration of the 25 % of Tc-99m-DMSA that is not protein bound followed by tubular reabsorption of most of the filtered tracer [14]. This would give an overall renal clearance rate of about 5 % in keeping with the observed relatively slow clearance of Tc-DMSA into the renal cortex.

Extraction efficiency Low, about 5 % [15].

Extraction mechanism, saturable or non-saturable There is no evidence of saturation of the renal clearance mechanism under clinical circumstances.

Interventions None.

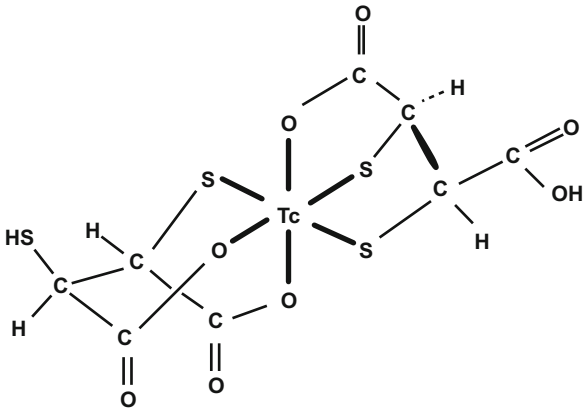

Fig. 16.20 Chemical structure for Tc-99m-DMSA (dimercaptosuccinic acid)

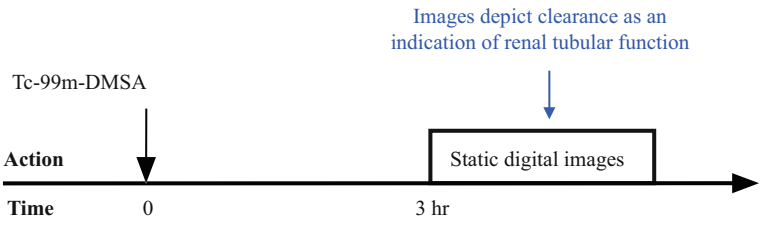

Fig. 16.21 Protocol summary diagram

Imaging Images are acquired with a dual-head gamma camera fitted with a low-energy, high-resolution, parallel-hole collimator. SPECT imaging may also be performed [16].

Protocol design Three hours following the intravenous injection of Tc-99m-DMSA planar images are obtained simultaneously in the anterior and posterior projections, the right anterior oblique and left posterior oblique projections, and in the right posterior oblique and left anterior oblique projections (Fig. 16.21).

Quantitative measurement – Renal tubular clearance Although the images are primarily used to detect cortical scarring, relative clearance between the two kidneys can be measured to determine the percent of total function in each of the two kidneys from the 3 h posterior image. This comparison is done after background correction, but without attenuation correction. Attenuation is assumed to be similar for both kidneys (see Chap. 8, Quantitation of Function: Relative Measurements). A geometric mean calculation could be used to correct for attenuation in relative terms.

Renal tubular function clearance – Normal range A suggested criterion for abnormal asymmetry is less than 45 % of total function on one side [14].

Tc-99m-MAG3 Renal Worksheet

Parameter		Patient Value		Normal Range
Renal clearance (ERPF / 1.73 m^2):				
Left kidney	=	_____	mL/min	155 - 520 mL/min: 21 - 40 yr
Right kidney	=	_____	mL/min	140 - 470 mL/min: 41 - 60 yr
Total	=	_____	mL/min	125 - 395 mL/min: 61 - 80 yr
Percent clearance / kidney:				
Percent clearance left	=	_____	%	42 - 58 %
Percent clearance right	=	_____	%	42 - 58 %
Leading edge transit time (cortical peak time):				
Left kidney	=	_____	min	≤ 4 min
Right kidney	=	_____	min	≤ 4 min
Mean parenchymal transit time (cortical half time from peak):				
Left kidney	=	_____	min	≤ 10 min
Right kidney	=	_____	min	≤ 10 min
Lasix washout - lasix at about 10 min (ROI must include renal pelvis and calyces):				
Left kidney	=	_____	min	≤ 10 min from lasix
Right kidney	=	_____	min	≤ 10 min from lasix

Klingensmith et al. [5].

References

Cystogram-Direct (Tc-99m-DTPA)

1. Mandell GA, Eggle DF, Gilday DL, et al. Procedure guideline for radionuclide cystography in children. J Nucl Med. 1997;38:1650–4.

Renal Glomerular Filtration Study (Tc-99m-DTPA)

2. Hall JE, editor. Guyton and Hall textbook of medical physiology. Philadelphia: Saunders/Elsevier; 2011.
3. Hall JE. Urine formation by the kidneys: glomerular filtration, renal blood flow, and their control. In: Guyton AC, Hall JE, editors. Textbook of medical physiology. 12th ed. Philadelphia, PA: Saunders Elsevier; 2011. p. 305.
4. Rhoades RA, Bell DR. Medical physiology: principles of clinical medicine. 4th ed. Lippincott: Williams Wilkins; 2013. Fig 22-13, p. 409.

Renal Tubular Secretion Study (Tc-99m-MAG3)

5. Klingensmith WC, Briggs DE, Smith WI. Tc-99m-MAG3 renal studies: Normal range and reproducibility of physiologic parameters as a function of age and sex. J Nucl Med. 1994;35:1612–7.
6. Shikano N, Kanai Y, Kawai K, et al. Transport of Tc-99m-MAG3 via rat organic anion transporter 1. J Nucl Med. 2004;45:80–5.
7. Itoh K. Tc-99m-MAG3: review of pharmacokinetics, clinical application to renal diseases and quantification of renal function. Ann Nucl Med. 2001;15:179–90.
8. Shikano N, Kanai Y, Kawai K, et al. Transport of T-MAG3 via rat renal organic anion transporter I. JNM. 2004;45:80–5.
9. Fine EJ. Diuretic renography and angiotensin converting enzyme inhibitor renography. Radiol Clin North Am. 2001;39:979–95.
10. Fritzberg AR, Kuni CC, Klingensmith WC, Stevens J, Whitney WP. Synthesis and biological evaluation of Tc-99m-N, N′-bis(mercaptoacetyl)-2,3-diamino-propanoate. J Nucl Med. 1982;23:592–8.
11. Klingensmith WC, Tyler HN, Marsh WC, Hanna GM, Fritzberg AR, Holt SA. The effect of hydration and dehydration on Tc-99m-CO2-DADS renal studies in normal volunteers. J Nucl Med. 1985;26:875–9.
12. Shanahan WSM, Klingensmith WC, Weil R. Tc-99m-DTPA renal studies for acute tubular necrosis: specificity of dissociation between perfusion and clearance. Am J Roentgenol. 1981;136:249–53.
13. Klingensmith WC, Whitney WP, Spitzer VM, Klintmalm GBG, Koep LM, Kuni CC. Effect of complete biliary-tract obstruction on serial hepatobiliary imaging in an experimental model. J Nucl Med. 1981;22:866–8.

Renal Tubular Function Study (Tc-99m-DMSA)

14. Piepsz A, Blaufox MD, Gordon I, et al. Consensus on renal cortical scintigraphy in children with urinary tract infection. Semin Nucl Med. 1999;29:160–74.
15. MPI DMSA kidney reagent: package insert, Medi + Physics, July, 1985.
16. Groshar D, Gorenberg M. Quantitative SPECT uptake of Tc-99m-dimercaptosuccinci acid by the kidneys in children. J Nucl Med. 1999;40:56–9.

Infection Imaging

17

White Blood Cell Activation Study (F-18-Fluorodeoxyglucose)

Overview In areas of infection and inflammation white blood cells become activated and increase their uptake of glucose [1,2]. Unlike the White Blood Cell Migration Study, the White Blood Cell Activation Study does not require white blood cells to migrate from the vascular space to the site of infection. Therefore, the White Blood Cell Activation Study is capable of detecting areas of infection and inflammation throughout the body in a relatively short period of time.

Radiopharmaceutical characteristics F-18-fluorodeoxyglucose (FDG) is an analog of glucose and exists in blood predominantly in the form of soluble FDG. Its chemical structure is shown in Fig. 17.1 and its molecular weight is 193.17.

Extraction mechanism FDG is transported across cell membranes by transmembrane glucose transporters (GLUTs), which are passive facilitative transporters. There are two main classes: glucose transporters and sodium-dependent glucose transporters (SGLTs). FDG binds mostly to GLUTs, which are not found in the renal tubular cells. This difference explains the lack of reabsorption of FDG from the tubular lumens (Fig. 17.2) [3].

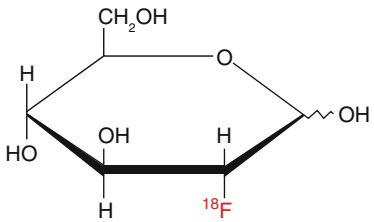

Fig. 17.1 Chemical structure of F-18-fluorodeoxyglucose (FDG). The hydroxyl group on the second carbon of glucose has been replaced by a positron-emitting fluorine-18 atom to form the radiopharmaceutical FDG

W.C. Klingensmith III, *The Mathematics and Biology of the Biodistribution of Radiopharmaceuticals-A Clinical Perspective*,
DOI 10.1007/978-3-319-26704-3_17

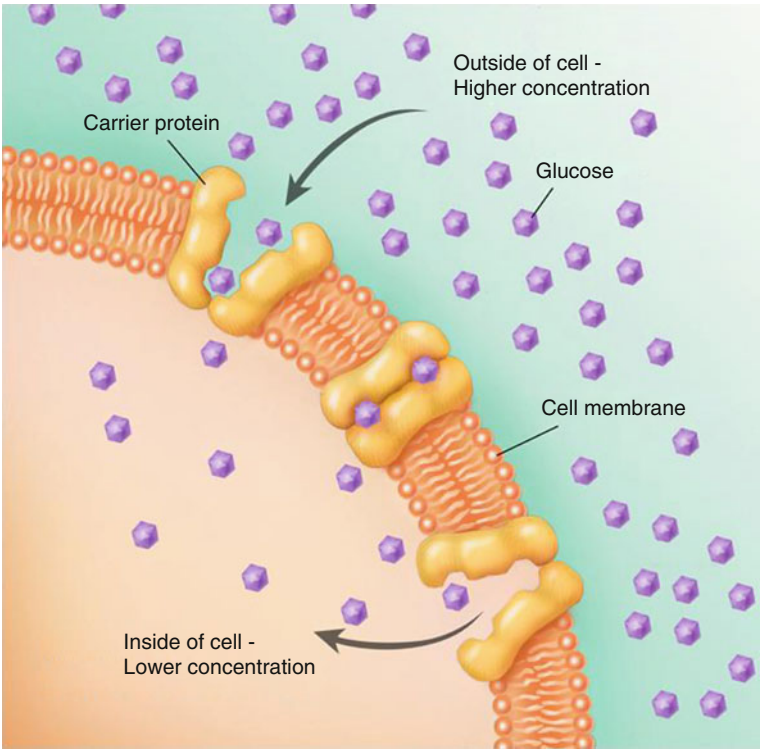

Fig. 17.2 Transport of glucose across the cell membrane by GLUT 1. GLUT transporters are an example of passive facilitative transport which is driven by the concentration gradient of glucose. The gradient is maintained by the intracellular phosphorylation of glucose. When glucose binds to the GLUT transporter, it induces a change in configuration of the transporter which in turn causes the release of the glucose molecule in the intracellular space

Once inside the cell FDG is phosphorylated by the hexokinase enzyme. The addition of a phosphate group to FDG prevents the radiopharmaceutical from diffusing out of the cell. At the same time the absence of a hydroxyl group at the second carbon position prevents phosphorylated FDG from binding to the next enzyme in the glycolytic pathway. This fact prevents FDG from being metabolized and, in turn, prevents the radiolabel, F-18, from diffusing back out of the cell into the blood (Fig. 17.3).

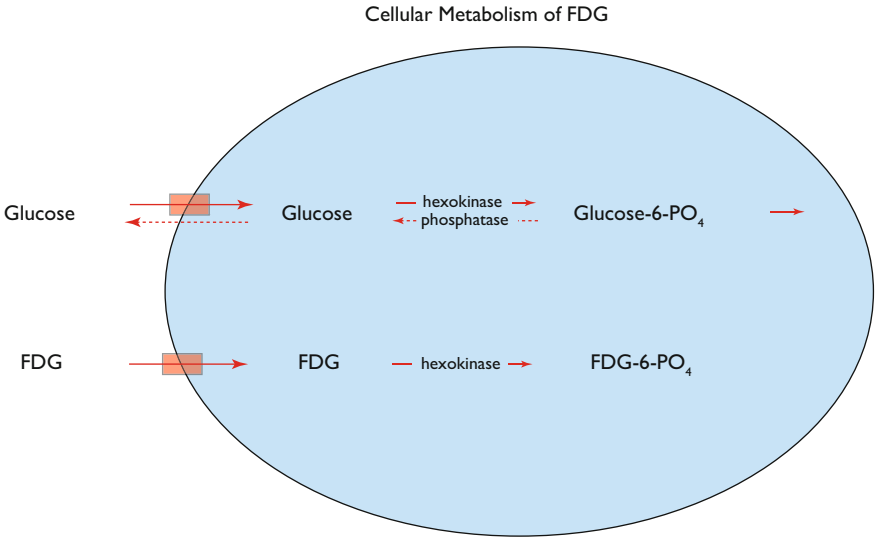

Fig. 17.3 Cellular uptake of glucose vs. FDG. Most transmembrane glucose transport proteins bind to glucose and FDG equally. In addition, the hexokinase enzyme binds to and phosphorylates glucose and FDG equally well. However, the next enzyme in the glycolytic pathway binds phosphorylated glucose, but not phosphorylated FDG

While differences in the metabolic behavior of FDG compared to native glucose make it an imperfect tracer of glucose, the differences actually improve FDG from an imaging point of view. If F-18 diffused back out of cells, the contrast between cells that clear FDG and background including blood would be decreased. In addition, if FDG were reabsorbed by the kidneys, there would be a greater amount of FDG in the blood and again the contrast between cells that clear FDG and background would be decreased.

Extraction efficiency Moderate [1].

Extraction mechanism saturable or non-saturable Saturable. Hyperglycemia increases competition for glucose receptors and decreases clearance of FDG. In addition, hyperglycemia may cause a downregulation of the GLUT receptors so that not only is there an increase in nonradioactive glucose to compete for binding to the GLUT receptors, but there are fewer receptors.

Interventions None.

Imaging F-18 is a positron emitter so imaging is done with a PET-CT scanner. Because the PET images are tomographic, there is no need for background correction. And because the CT images provide high-resolution density maps, the PET images can be readily corrected for attenuation.

Protocol design PET-CT images from the top of the head to the proximal thighs are acquired beginning at 45–60 min after administration of the FDG (Fig. 17.4).

Quantitative measurements None.

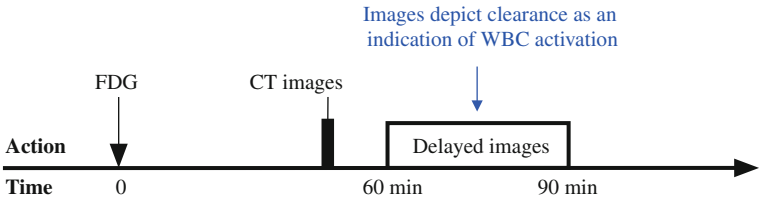

Fig. 17.4 Protocol summary diagram

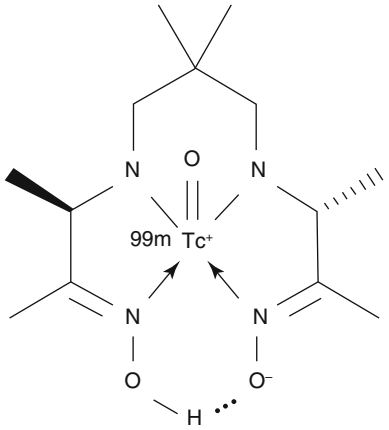

Fig. 17.5 Chemical structure of Tc-99m-HMPAO. HMPAO, a metal chelator, serves as the linker between Tc-99m, a metal, and the white blood cell

White Blood Cell Migration Study (Tc-99m-White Blood Cells)

Overview The White Blood Cell Migration Study demonstrates the distribution of labeled autologous white blood cells within the body at various times after intravenous injection. When labeled with technetium-99m, the study can be completed in 4–24 h.

Radiopharmaceutical characteristics The technetium-99m radioisotope is chelated by hexamethylpropyleneamine oxime (HMPAO), which in turn attaches to the white blood cells. The chemical structure of Tc-99m-HMPAO is shown in Fig. 17.5 and the molecular weight is 384.4. Sixty percent of white blood cells are granulocytes which have an average diameter of 14 μm.

Extraction mechanism The reinjected Tc-99m-HMPAO-white blood cells are attracted to the site of infection by chemotaxis. White blood cells already at the infection site release inflammatory cytokines that create a chemical gradient that attracts additional white blood cells [4]. Cytokines such as TNF (tumor necrosis factor) cause the nearby endothelial cells to express increased amounts of selectins, which bind to integrin on the wall of granulocytes. This causes the granulocytes to stick to the capillary wall in a process called margination (Fig. 17.6).

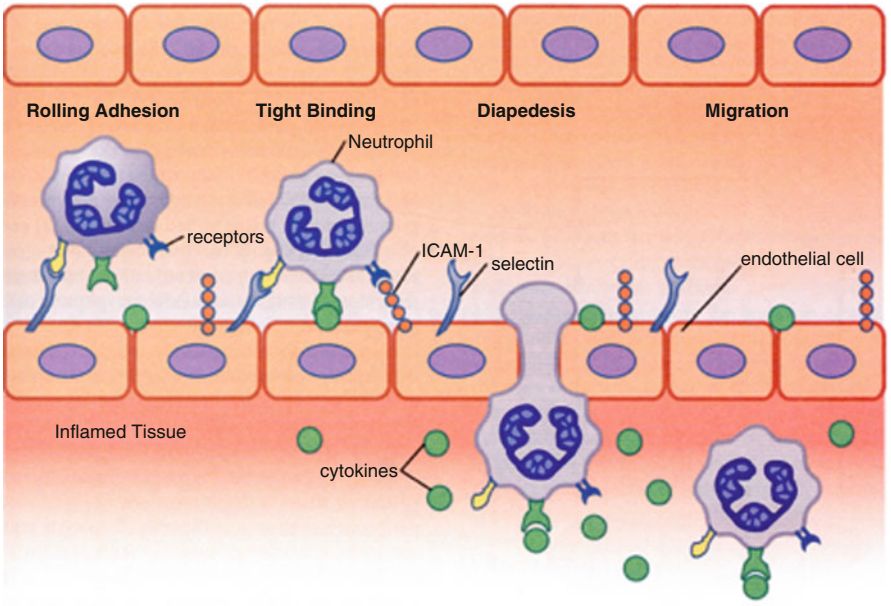

Fig. 17.6 Migration of neutrophil from blood into inflamed tissue. Cytokines of inflamed tissues cause increased expression of selectins and intracellular adhesion molecule-1 on the surface of endocytes. These adhesion molecules bind to complementary receptors on the neutrophil, causing it to adhere to the wall of the capillary or venule. The neutrophil then migrates through the vessel wall toward the site of the injury [4]

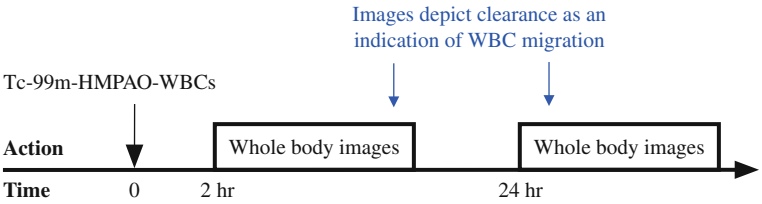

Fig. 17.7 Protocol summary diagram

Inflammatory cytokines also cause the intercellular attachments between epithelial cells to loosen so that granulocytes can move from the vascular space into the interstitial space more easily by a process known as diapedesis. In this process white blood cells undergo significant deformation in order to pass through these small openings. Migration of white blood cells from the vascular space through the capillary wall is a slow process, which is why the White Blood Cell Migration Study frequently requires 24 h to complete.

Extraction efficiency Low.
Extraction mechanism saturable or non-saturable Non-saturable.
Interventions None.
Imaging Imaging is performed with a dual-head gamma camera and a low-energy, high-resolution, parallel hole collimator.
Protocol design At 2 and 24 h after reinjection of the labeled white blood cells, anterior and posterior images from the top of the head to the proximal thighs are acquired (Fig. 17.7).
Quantitative measurement None.

References

White Blood Cell Activation Study

1. Paik JY, Lee KH, Choe YS, et al. Augmented F-18-FDG uptake in activated monocytes occurs during the priming process and involves tyrosine kinases and protein kinase C. J Nucl Med. 2004;45:124–8.
2. Sugawara Y, Gutowski TD, Fisher SJ, et al. Uptake of positron emission tomography tracers in experimental bacterial infections: A comparative biodistribution study of radiolabeled FDG, thymidine, L-methionine, Ga-67-citrate, and I-125-HSA. Eur J Nucl Med. 1999;26:333–41.
3. Ballagher BM, Fowler JS, Gutterson NI, et al. Metabolic trapping as a principle of radiopharmaceutical design: Some factors responsible for the biodistribution of [F-18] 2-deoxy-2-fluoro-D-glucose. J Nucl Med. 1978;19:1154–61.

White Blood Cell Migration Study

4. Resistance of the body to infection: In: Hall JE, editor. Guyton & Hall textbook of medical physiology, 12th ed. Philadelphia: Saunders; 2011, p. 429.

Pulmonary System

18

Lung Aerosol Study (Tc-99m-DTPA Aerosol)

Overview The images of the Lung Aerosol Study demonstrate the distribution of ventilation within the lungs in multiple projections. The quality of the study can be degraded if some of the aerosol deposits on the larger bronchi and does not reach the terminal bronchi.

Radiopharmaceutical characteristics Tc-99m-diethylenetriaminepentaacetic acid (DTPA) aerosol is produced by placing a saline solution of Tc-99-DTPA in a jet nebulizer. The particle size ranges from 1.2 to 6.9 μm [1, 2] (Fig. 18.1).

Extraction mechanism The aerosol particles are delivered to the distal bronchi of the lungs via the flow of labeled air with each breath. The aerosol particles are then cleared from the inhaled air by deposition on and adherence to the mucus of the distal bronchi including the terminal bronchi, but like other particulate matter, they do not reach the alveoli in significant amounts [3].

The delivery of the aerosol to the distal bronchi via ventilatory airflow is analogous to the delivery of intravenously injected radiopharmaceuticals to tissue via blood flow. The removal of the aerosol particles in the distal bronchi by adherence to mucus is analogous to the extraction mechanisms of intravenously injected radiopharmaceuticals in tissue (see Chap. 4, Evaluation of Clearance). The aerosol droplets are slowly eliminated from the bronchial tree by the cilia-driven movement of mucus up the bronchial tree. Table 18.1 lists the two nuclear medicine studies in which clearance of radiopharmaceuticals serves as a proxy for ventilation.

Extraction efficiency High.

Extraction mechanism, saturable or non-saturable Non-saturable.

Interventions None.

Imaging Images are acquired with a dual-head gamma camera fitted with a low-energy, high-resolution, parallel hole collimator. SPECT imaging may also be performed.

W.C. Klingensmith III, *The Mathematics and Biology of the Biodistribution of Radiopharmaceuticals-A Clinical Perspective*,
DOI 10.1007/978-3-319-26704-3_18

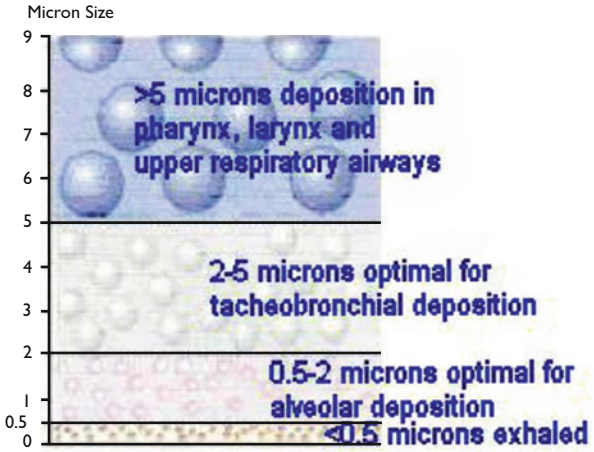

Fig. 18.1 Particle size and site of localization in the lungs. (Courtesy of Diagnostic Imaging, LTD, UK)

Table 18.1 Studies with clearance as a proxy for ventilation

Study	Radiopharmaceutical	Structure	Other parameter
Lung Aerosol Study	Tc-99m-DTPA aerosol	Lungs	None
Lung Ventilation Study	Xe-133 gas	Lungs	Air space

Protocol design Usually, a Lung Perfusion Study with Tc-99m-MAA is performed first with a relatively low dose of Tc-99m-MAA. Following acquisition of the lung perfusion images, the patient inhales the Tc-99m-DTPA aerosol until the counts from the lungs equal 3–4 times the counts at the start of the Lung Aerosol Study. Once the desired number of counts is achieved, planar images are obtained simultaneously in the anterior and posterior projections, the right anterior oblique and left posterior oblique projections, and in the right posterior oblique and left anterior oblique projections (Fig. 18.2).
Quantitative measurement Usually none.

Lung Perfusion Study (Tc-99m-MAA)

Overview The lungs have a dual blood supply, 90 % via the pulmonary arteries and 10 % via the bronchial arteries. The images of the Lung Perfusion Study with Tc-99m-MAA demonstrate the distribution of lung blood flow via the pulmonary arteries in multiple projections.
Radiopharmaceutical characteristics Ninety percent of Tc-99m-macroaggregated particles range in size from 15 to 30 μm with none over 150 μm (Fig. 18.3) [4].
Extraction mechanism Following intravenous injection, Tc-99m-MAA particles will embolize into the arterioles of the first capillary bed they encounter (see Chap. 4,

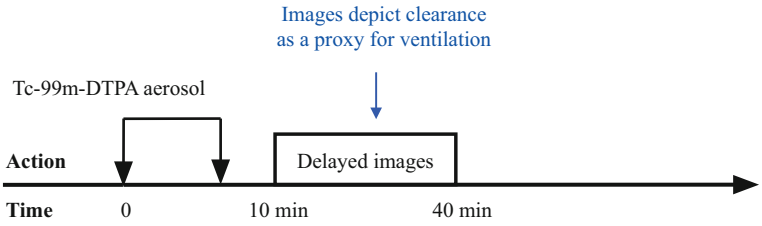

Fig. 18.2 Protocol summary diagram

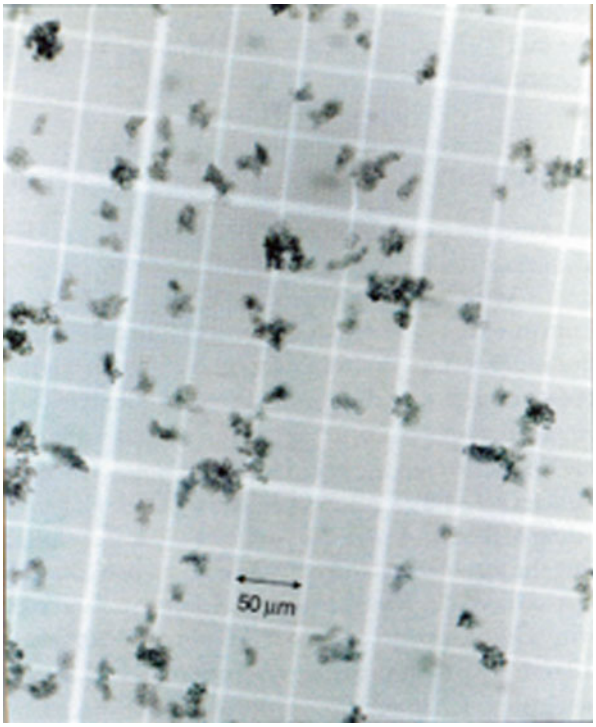

Fig. 18.3 Photomicrograph of Tc-99m-MAA [5]

Evaluation of Clearance). By the time the tracer leaves the right ventricle of the heart, it is well mixed with the blood and will distribute within the lung according to the distribution of right ventricular cardiac output. The exception that demonstrates that the extraction mechanism is related to clearance and not just blood flow is anatomic arteriovenous malformations. Anatomic arteriovenous malformations have very high pulmonary blood flow but very low clearance of Tc-99m-MAA because the extraction efficiency in these structures for Tc-99m-MAA is essentially zero.

There are roughly 350,000 MAA particles in each adult dose for a Lung Perfusion Study [4]. However, there are approximately 300 million alveoli and many billions

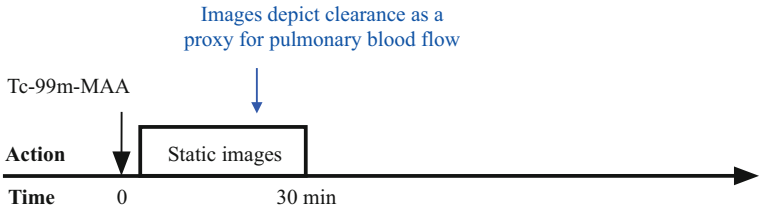

Fig. 18.4 Protocol summary diagram

of pulmonary arterioles and capillaries [6]. Thus, the MAA particles occlude fewer than 1 % of pulmonary capillaries. In addition, the MAA particles break up into smaller particles with a restoration in flow with a half time of approximately 5 h [4].
Extraction efficiency 100 %
Extraction mechanism, saturable or non-saturable Non-saturable.
Interventions None.
Imaging Images are acquired with a dual-head gamma camera fitted with a low-energy, high-resolution, parallel hole collimator. SPECT imaging may also be performed.
Protocol design Imaging may begin immediately. Planar images are obtained simultaneously in the anterior and posterior projections, the right anterior oblique and left posterior oblique projections, and in the right posterior oblique and left anterior oblique projections (Fig. 18.4).
Quantitative measurement Usually none. Occasionally, the relative blood flow in the upper, middle, and lower thirds of the lungs is calculated [7, 8]. The pulmonary relative blood flow calculation is an example of a relative quantitative measurement (see Chap. 8, Quantitation of Function: Relative Measurements).

Lung Ventilation Study (Xe-133 Gas)

Overview The Lung Ventilation Study demonstrates the distribution of ventilation, air space, and air trapping within the lungs.
Radiopharmaceutical characteristics Xenon-133 exists as an elemental and mostly inert gas. It has a molecular weight of 131.30.
Extraction mechanism The extraction mechanism is airflow into a terminal compartment. Although the Xe-133 gas is not extracted from the pulmonary airspace during the initial single breath part of the study, it is removed from the flowing air. The Xe-133 accumulates in the alveoli in a self-integrating fashion in proportion to the amount of ventilation that flows to various portions of the lungs.

This is similar to the way that Tc-99m-MAA accumulates in the arterioles and capillaries of the lungs in a self-integrating fashion in proportion to regional right ventricular cardiac output in the Lung Perfusion Study. The Tc-99m-MAA is not removed from the vascular space, but it is removed from the flowing blood.
Extraction efficiency 100 %.

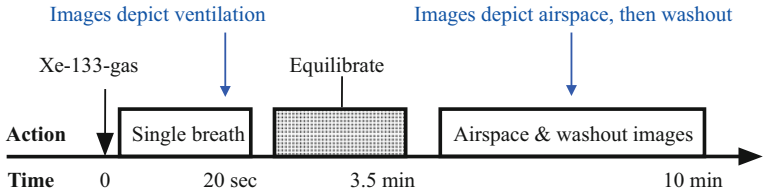

Fig. 18.5 Protocol summary diagram

Extraction mechanism, saturable or non-saturable Non-saturable.
Interventions None.
Imaging Images are acquired with a dual-head gamma camera fitted with a low-energy, high-resolution, parallel hole collimator.
Protocol design The protocol is designed to record images that show: (1) pulmonary ventilation, (2) airspace, and (3) washout (the inverse of ventilation). The patient is connected to the xenon gas delivery system with the gamma camera positioned to acquire anterior and posterior images. Initially, the valve is set so that the patient will breathe air with xenon-133 in and out in a closed system. For the first image, which will depict ventilation, the patient takes in a deep breath and holds it for as long as possible. Then the patient quietly breathes xenon-133-labeled gas in and out, for about 3 min, while the xenon-133 gas equilibrates in the pulmonary airspace. At 3 min images are obtained that reflect pulmonary airspace. At this point the valve is changed so that the patient breathes xenon-133-labeled air out and nonradioactive room air in. A sequential set of images are recorded during washout of xenon-133 from the lungs that show the inverse of ventilation.

Most pulmonary disease such as emphysema damages both alveoli and distal bronchi in parallel so that the alveoli combine and enlarge and the distal bronchi fibrose and contract. This process results in decreased ventilation for a given airspace so that the initial single breath image shows decreased activity in the diseased area, the equilibrium image shows normal air space, and the late washout images show retained activity in the diseased areas (Fig. 18.5).
Quantitative measurement Usually none [9].

References

Lung Aerosol Study

1. Silveira CM, Castiglioni MLV, Torres ICG, et al. Evaluation of two T-99m-DTPA radioaerosols with different characteristics in lung ventilation studies. Braz J Med Biol Res. 2003;36:1333–40.
2. Senden TJ, Moock KH, Gerald JF, et al. The physical and chemical nature of Technegas. J Nucl Med. 1997;38:1327–33.
3. Pulmonary ventilation: In: Hall JE, editor. Guyton & Hall textbook of medical physiology, 12th ed. Philadelphia: Saunders; 2011.

Lung Perfusion Study

4. PulmoLite product insert. Du Pont Medical Products, Billerica. Massachusetts (MA)
5. Kowalsky RJ, Falen SW. Radiopharmaceuticals in nuclear pharmacy and nuclear medicine. 3rd ed. Washington, D.C.: American Pharmacists Association; 2011. p. 189.
6. National Institutes of Health. http://www.nhlbi.nih.gov/health/health-topics/topics/ipf/lungworks.html.
7. Fukuchi K, Hayashida K, Nakanishi N, et al. Quantitative analysis of lung perfusion in patients with primary pulmonary hypertension. J Nucl Med. 2002;43:757–61.
8. Jamadar DA, Kazerooni EA, Martinez FJ, et al. Semi-quantitative ventilation/perfusion scintigraphy and single-photon emission tomography for evaluation of lung volume reduction surgery candidates: description and prediction of clinical outcome. Eur J Nucl Med. 1999;26:734–42.

Lung Ventilation Study

9. Mathews JJ, Maurer AH, Steiner RM, et al. New Xe-133 gas trapping index for quantifying severe emphysema before partial lung volume reduction. J Nucl Med. 2008;49:771–5.

Skeletal System

19

Bone Mineral Study (F-18 as Sodium Fluoride)

Overview The images of the Bone Mineral Study with F-18 as sodium fluoride depict the clearance of anionic fluoride by bone hydroxyapatite throughout the skeleton in a tomographic fashion with CT anatomic co-registration. The biodistribution of the F-18 is an approximate indicator of bone mineral metabolism [1].

Radiopharmaceutical characteristics F-18 is an anion with an atomic weight of 19.00.

Extraction mechanism Bone is composed of minute crystals of hydroxyapatite in association with collagen fibers. The extraction mechanism for fluoride is primarily chemisorption of the fluoride onto hydroxyapatite (Fig. 19.1) [1, 3]. The term chemisorption refers to the binding of anions onto the surface of bone [4]. The strength of the bond is intermediate between a chemical covalent bond and a hydrogen bond. Once absorbed F^- rapidly exchanges with OH^- in the hydroxyapatite matrix ($Ca_{10}(PO_4)6OH_2$) to form ($Ca_{10}(PO_4)6F_2$) [3].

Extraction efficiency Moderate.

Extraction mechanism, saturable or non-saturable Non-saturable.

Interventions None.

Imaging F-18 is a positron emitter so imaging is done with a PET-CT scanner. Because the PET images are tomographic, there is no need for background correction. And because the CT images provide high-resolution density maps, the images are readily corrected for attenuation.

Protocol design PET images from the top of the head to the proximal thighs are obtained beginning at 1 h after administration of the FDG (Fig. 19.2).

Quantitative measurement None.

W.C. Klingensmith III, *The Mathematics and Biology of the Biodistribution of Radiopharmaceuticals-A Clinical Perspective*,
DOI 10.1007/978-3-319-26704-3_19

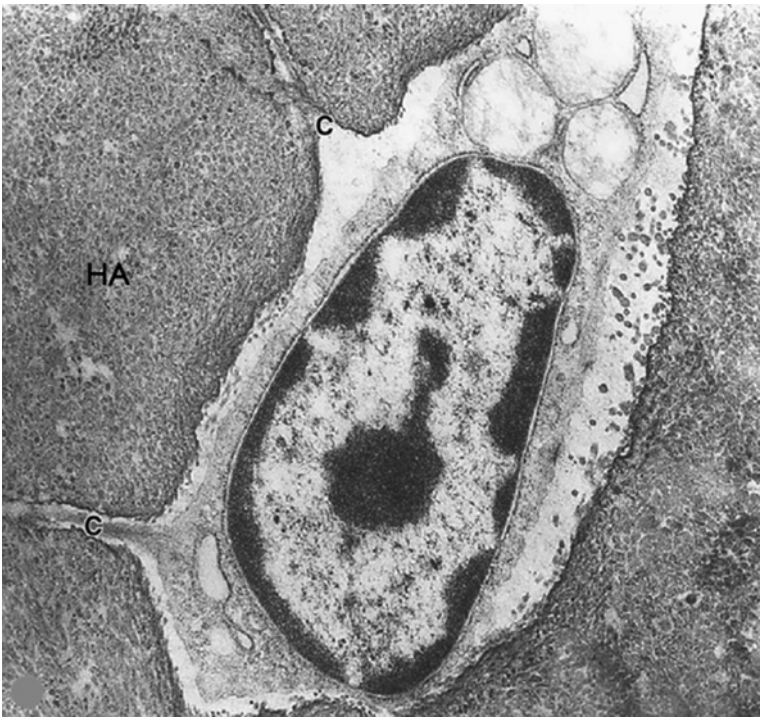

Fig. 19.1 Transmission electron micrograph. Image shows an osteocyte in a bone lacuna with two dendritic processes extending to the left into canaliculi (*C*). The processes are secreting osteoid which becomes calcium hydroxyapatite (*HA*) (Mescher [2], Fig. 8.5)

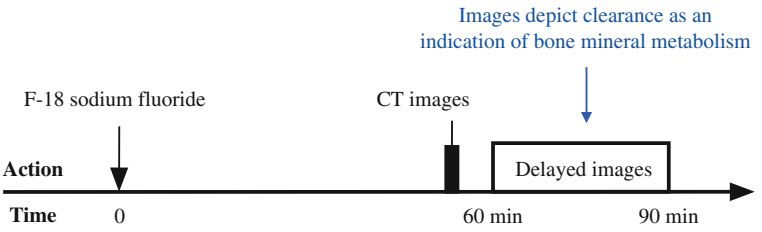

Fig. 19.2 Protocol summary diagram

Bone Mineral Study (Tc-99m-MDP)

Overview The images of the Bone Mineral Study with Tc-99m-methylenediphosphonate (MDP) depict the biodistribution of bone mineral blood flow and chemisorption throughout the skeleton [1]. When the indication is a possible lesion in an extremity, such as osteomyelitis or a stress fracture, a three-phase bone study is performed in which blood flow and extracellular space of the area in question are imaged during the first circulation of the tracer.

Radiopharmaceutical characteristics The chemical structure of Tc-99m-MDP is shown in Fig. 19.3. The molecular weight of Tc-99m-MDP is 274.92.

Extraction mechanism Bone mineral is composed of minute crystals of hydroxyapatite in association with collagen fibers. Tc-99m-MDP binds to hydroxyapatite by chemisorption (Fig. 19.1). The term chemisorption refers to the binding of anions onto the surface of bone [4]. The strength of the bond is intermediate between chemical covalent bonding and hydrogen bonding; the name chemisorption is a contraction of the two types of bonding.

Extraction efficiency Low-moderate.

Extraction mechanism, saturable or non-saturable Non-saturable [5].

Interventions None.

Imaging Imaging is performed with a dual-head gamma camera and a low-energy, high-resolution, parallel hole collimator.

Protocol design At 2–3 h after injection of the radiopharmaceutical, anterior and posterior images from the top of the head to the toes are acquired. In the three-phase version of the Bone Mineral Study with Tc-99m-MDP, rapid serial images during

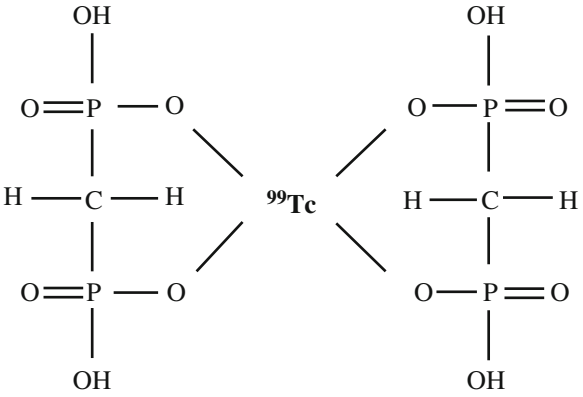

Fig. 19.3 Chemical structure of Tc-99m-MDP. Two methylene diphosphonate molecules chelate one technetium-99m atom

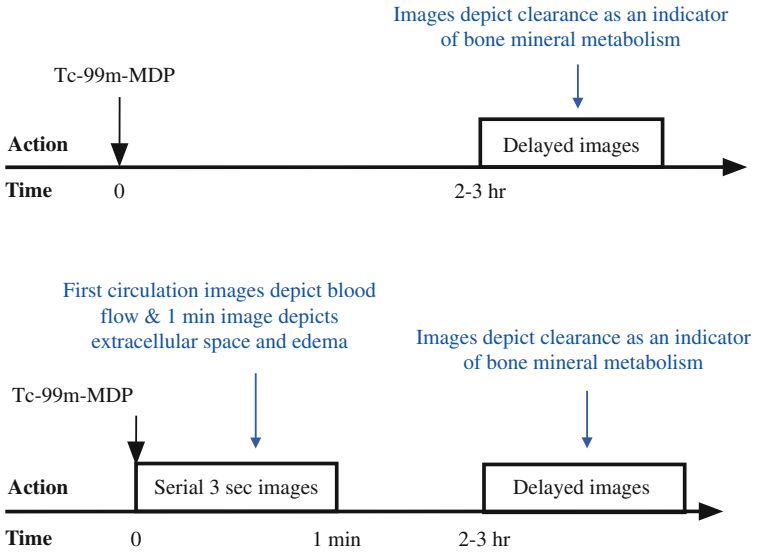

Fig. 19.4 Protocol summary diagram. The *first summary diagram* shows the protocol for the standard Bone Mineral Study with Tc-99m-MDP. The *second summary diagram* shows the protocol for the three-phase Bone Mineral Study with Tc-99m-MDP

the first circulation of the radiopharmaceutical show regional blood flow (see Chap. 6, Blood Flow: First Circulation Time-Activity Curves) (Fig. 19.4).

Quantitative measurement None.

References

Bone Mineral Study (F-18 as Sodium Fluoride)

1. Toegel S, Hoffmann O, Wadsak W, et al. Uptake of bone-seekers is solely associated with mineralisation! A study with Tc-99m-MDP, Sm-153-EDTMP and F-18-fluoride on osteoblasts. Eur J Nucl Med Mol Imaging. 2006;33:491–4.
2. Mescher AL. Junqueira's basic histology text and atlas. New York: McGraw Hill Lange; 2013.
3. Czernin J, Satyamurthy LM, Schiepers C. Molecular mechanisms of bone F-18-NaF deposition. J Nucl Med. 2010;51:1826–9.
4. Ponto JA. Mechanisms of radiopharmaceutical localization. In: Continuing education for nuclear pharmacists and nuclear medicine professionals. Vol. 16, lesson 4. University of New Mexico College of Pharmacy; Albuquerque, NM: 2012.

Bone Mineral Study (Tc-99m-MDP)

5. Carrasquillo JA, Whatley M, Dyer V, et al. Alendronate does not interfere with Tc-99m-methylene diphosphonate bone scanning. J Nucl Med. 2001;42:1359–63.

Tumor Imaging

20

B-Cell Lymphoma Imaging Study (In-111-Ibritumomab Tiuxetan [Zevalin®])

Overview In-111-ibritumomab tiuxetan is a radiolabeled chimeric murine/human monoclonal antibody that binds to CD20 antigens found on the surface of B-cell lymphoma cells and other nonspecific sites [1] (Fig. 20.1). B-cell lymphoma expresses an increased number of CD20 antigens. The chimeric monoclonal antibody ibritumomab tiuxetan binds to the CD20 antigens. When ibritumomab is labeled with the pure gamma emitter In-111, it gives diagnostic information. When it is labeled with the pure beta emitter Y-90, it gives a therapeutic dose of radiation. Notice that the linker is attached away from the antigen binding portion of the antibody so the linker will not interfere with binding of the antibody to the antigen.

Prior to treatment with Y-90-ibritumomab tiuxetan, the likely biodistribution of Y-90-ibritumomab may be determined by imaging ibritumomab tiuxetan labeled with In-111 instead of Y-90. However, in November 2011, the FDA approved treatment with Y-90-ibritumomab tiuxetan without a prior biodistribution imaging study because the incidence of altered biodistribution has been found to be less than 0.6 % [2].

Radiopharmaceutical characteristics In-111-ibritumomab tiuxetan consists of a genetically engineered chimeric murine/human antibody, ibritumomab; a linking-chelator molecule, tiuxetan; and a radioisotope, In-111 (Fig. 20.2).

The linking end of the chelating-linker molecule binds to the antibody, and the other end chelates the radioisotope. Ibritumomab is a chimeric murine/human IgG, kappa monoclonal antibody directed against CD20 antigen [1]. A humanized antibody is less antigenic than a mouse antibody when injected into humans. In-111-ibritumomab tiuxetan has a molecular weight of approximately 148,000.

W.C. Klingensmith III, *The Mathematics and Biology of the Biodistribution of Radiopharmaceuticals-A Clinical Perspective*,
DOI 10.1007/978-3-319-26704-3_20

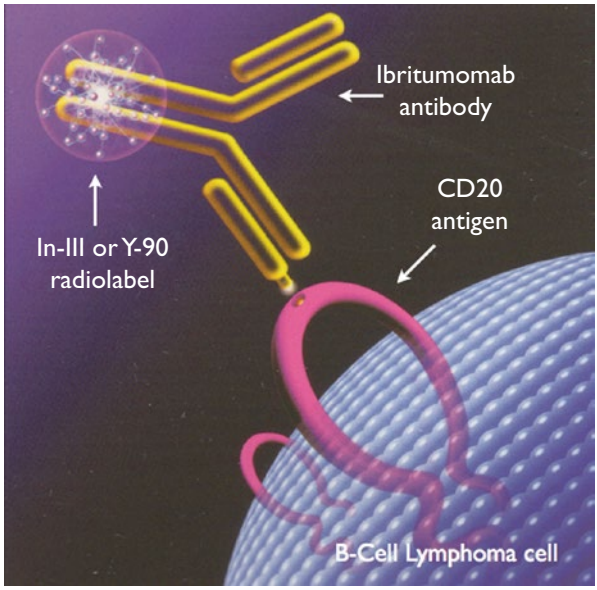

Fig. 20.1 Ibritumomab tiuxetan binding to CD20 expressed by B-cell lymphoma (Image reprinted with permission)

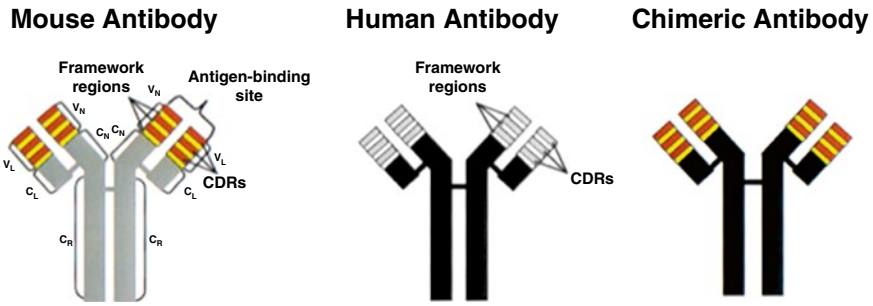

Fig. 20.2 Structure of a chimeric antibody. A chimeric antibody is formed by genetically engineering an antibody composed of the variable antigen binding region of an antibody from one species (often mouse) to the constant region of another antibody (usually human) (Image reprinted with permission)

Extraction mechanism In-111-ibritumomab tiuxetan binds to CD20 epitopes that are relatively abundant on the surface of B-cell lymphoma cells. Antibodies possess great specificity and can distinguish between proteins that differ in only one amino acid or between optical isomers of the same molecule [3]. Antibody-antigen binding is sometimes referred to as "lock and key" binding.

However, radiopharmaceuticals that are based on antibody ligands have a significant disadvantage because of their large size. Large molecules pass through the capillary walls very slowly, which results in a long time between intravenous injection and imaging. The radioisotope label must have a correspondingly long half-life, which results in a larger radiation dose to the patient.

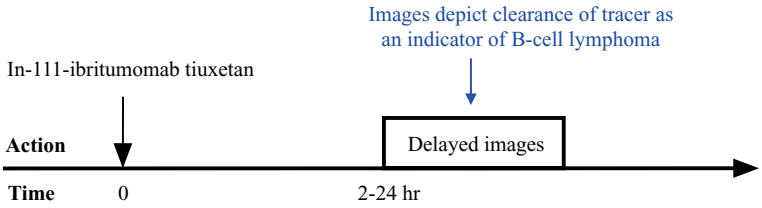

Fig. 20.3 Protocol summary diagram

Extraction efficiency Very low. The mean effective half-time for Y-90 activity in blood is 30 h [1].
Extraction mechanism saturable or non-saturable Saturable. A preliminary dose of non-labeled rituximab, a chimeric monoclonal antibody that is very similar to ibritumomab is routinely injected prior to injecting In-111-ibritumomab tiuxetan [1]. This maneuver appears to increase binding of the radiopharmaceutical to lymphoma B-cells, possibly by saturating CD20 sites on more available, nontumor cells.
Interventions None, other than pre-infusion of rituximab.
Imaging Imaging is performed with a dual-head gamma camera and a medium-energy parallel-hole collimator.
Protocol design The patient is given an infusion of rituximab within 4 h of infusion of the In-111-ibritumomab tiuxetan. The In-111-ibritumomab tiuxetan is infused over 10 min. Anterior and posterior images of the torso are obtained any time between 2 and 24 h after administration of the radiopharmaceutical (Fig. 20.3).
Quantitative measurement None.

Neuroendocrine Tumor-Somatostatin Receptor Study (In-111-Pentetreotide [Octreoscan®])

Overview The images of the Neuroendocrine Tumor-Somatostatin Receptor Study primarily identify neoplasms that arise from the embryologic neural crest and express a high density of somatostatin receptors on their cell membranes [4, 5]. These tumors are often referred to as neuroendocrine tumors because many of them secrete hormones. In-111-pentetreotide is a radiolabeled chemical analog of the naturally occurring hormone somatostatin, which suppresses growth hormone secretion.
Radiopharmaceutical characteristics The radiopharmaceutical In-111-pentetreotide is composed of the somatostatin analog octreotide connected to the metal chelating-linker DTPA. The DTPA chelates the radioisotope In-111 [5]. Somatostatin is a cyclic peptide of 14 amino acids (Fig. 20.4a). The active binding site of the hormone is the four amino acids shown in the clear circles in Fig. 20.4.

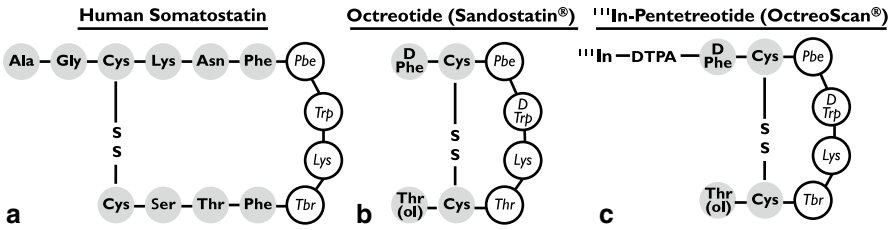

Fig. 20.4 Human somatostatin (**a**), octreotide (Sandostatin®) (**b**), and In-111-pentetreotide (Octreoscan®) (**c**). All three molecules share the four-amino-acid active site shown as clear circles. The removal of many of the other amino acids significantly increases the blood half life of the Octreotide and In-111-pentetreotide, which is necessary for their therapeutic and diagnostic efficacies, respectively (Image reprinted with permission)

Somatostatin has a very short plasma half-life of 2–3 min. In order to use the effect of somatostatin to inhibit excess secretion of hormones by neuroendocrine tumors, somatostatin was modified as shown in Fig. 20.4b. The active binding site is unchanged, but the rest of the molecule has been significantly decreased in size. The new analog of somatostatin, octreotide, has a plasma half-life of about 2 h [6]. The chemical structure of In-111-pentetreotide is shown in Fig. 20.4c at the amino acid level (with the linker and radiolabel) and in Fig. 20.5 at the atomic level (without the linker and radiolabel). The molecular weight of In-111-pentetreotide is 1,502.24 [7].

Extraction mechanism Somatostatin receptors have five subtypes, SSST1 through 5 [5, 6]. Most neuroendocrine tumors express predominantly subtype 2 and In-111-octreotide preferentially binds to subtype 2 (Table 20.1) [4, 5]. Once somatostatin or In-111-pentetreotide binds to the somatostatin receptor, the receptor-ligand complexes are internalized by endocytosis. The resultant endosomes rapidly acidify causing the ligand to dissociate from the receptor. The ligand is transported to lysosomes for processing and the receptor recycles back to the cell membrane. The polarity of the radiometabolites prevents passage across the lysosomal and cell membranes [4, 5].

Extraction efficiency Low.

Extraction mechanism saturable or non-saturable While competitive binding is possible, practically octreotide therapy does not need to be stopped before the imaging study [8, 9].

Interventions None.

Imaging Imaging is performed with a dual-head SPECT gamma camera with medium-energy parallel-hole collimators.

Protocol design Anterior and posterior images of the torso are obtained 4 and usually 24 h after administration of the radiopharmaceutical. In addition, SPECT images are usually acquired at 4 h (Fig. 20.6).

Quantitative measurement None.

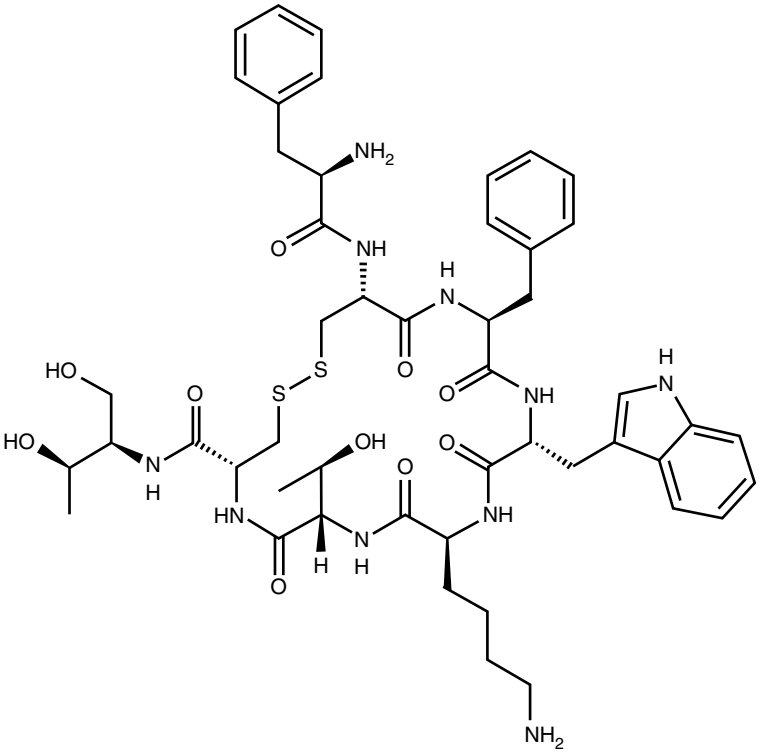

Fig. 20.5 Chemical structure of In-111-pentetreotide [OctreoScan®]

Table 20.1 Affinity profiles for 5 somatostatin receptor subtypes (SSRT)

Peptide	SSRT1	SSRT2	SSRT3	SSRT4	SSRT5
Somatostatin SS-28[a]	5.2	2.7	7.7	5.6	4.0
In-111-Penttereotide	>10,000	22	182	>1000	237

Lower number indicates higher affinity
[a]SS-28 = somatostatin – 28 amino acids

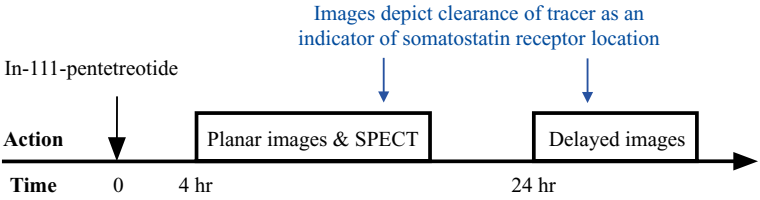

Fig. 20.6 Protocol summary diagram

Tumor Glucose Metabolism Study (F-18-Fluorodeoxyglucose)

Overview Most cancers take up and metabolize approximately five times as much glucose as normal tissues [11, 12]. The images of the Tumor Glucose Metabolism Study with F-18-fluorodeoxyglucose (FDG) are capable of demonstrating primary and metastatic cancer throughout the body.

Radiopharmaceutical characteristics FDG is an analog of glucose and exists in blood predominantly in the form of soluble FDG. It has a molecular weight of 193.17, and its chemical structure is shown in Fig. 20.7.

Extraction mechanism FDG is an analog of glucose that is taken up by cells to the same extent as glucose, but it is not metabolized [13]. FDG is transported across cell membranes by transmembrane glucose transporters. There are two main classes of glucose transporters (GLUTs) and sodium-dependent glucose transporters (SGLTs). F-18-FDG binds mostly to GLUTs, which are not found in the renal tubular cells (Fig. 20.8). This difference explains the lack of reabsorption of F-18-FDG from the tubular lumens.

Once inside the cell, FDG is phosphorylated by the hexokinase enzyme (Fig. 20.9). The addition of a phosphate group to FDG prevents the radiopharmaceutical from diffusing out of the cell. At the same time, the absence of a hydroxyl group at the second carbon position prevents phosphorylated FDG from binding to the next enzyme in the glycolytic pathway [13]. This fact prevents FDG from being metabolized and, in turn, prevents the radiolabel, F-18, from diffusing back out of the cell into the blood.

While differences in the metabolic behavior of FDG compared to native glucose make it an imperfect tracer of glucose, the differences actually improve FDG from an imaging point of view. If F-18 diffused back out of cells, the contrast between cells that clear FDG and background including blood would be decreased. In addition, if FDG were reabsorbed by the kidneys, there would be a greater amount of FDG in the blood, and again the contrast between cells that clear FDG and background would be decreased.

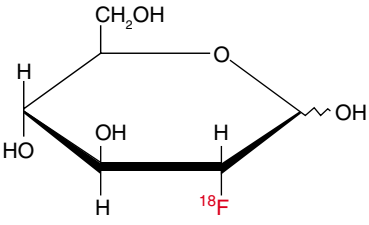

Fig. 20.7 F-18-Fluorodeoxyglucose (FDG)

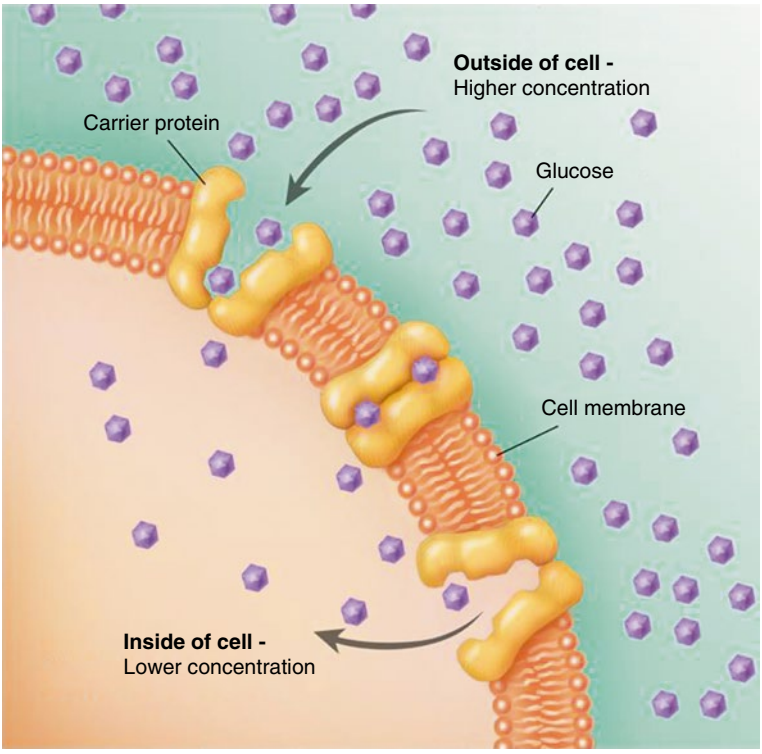

Fig. 20.8 Transport of glucose across the cell membrane by GLUT1. GLUT transporters are an example of passive facilitative transport which is driven by the concentration gradient of glucose. The gradient is maintained by the intracellular phosphorylation of glucose. When glucose binds to the GLUT transporter, it induces a change in configuration of the transporter which in turn causes the release of the glucose molecule within the intracellular space

Extraction efficiency Moderate.

Extraction mechanism saturable or non-saturable Saturable. Hyperglycemia increases competition for glucose receptors and decreases clearance of FDG. In addition, hyperglycemia may cause a downregulation of the GLUT receptors so that not only is there an increase in nonradioactive glucose to compete for binding to the GLUT receptors, but there are fewer receptors (Fig. 20.10a, b).

Interventions None.

Imaging F-18 is a positron emitter so imaging is done with a PET-CT scanner. Because the PET images are tomographic, there is no need for background correc-

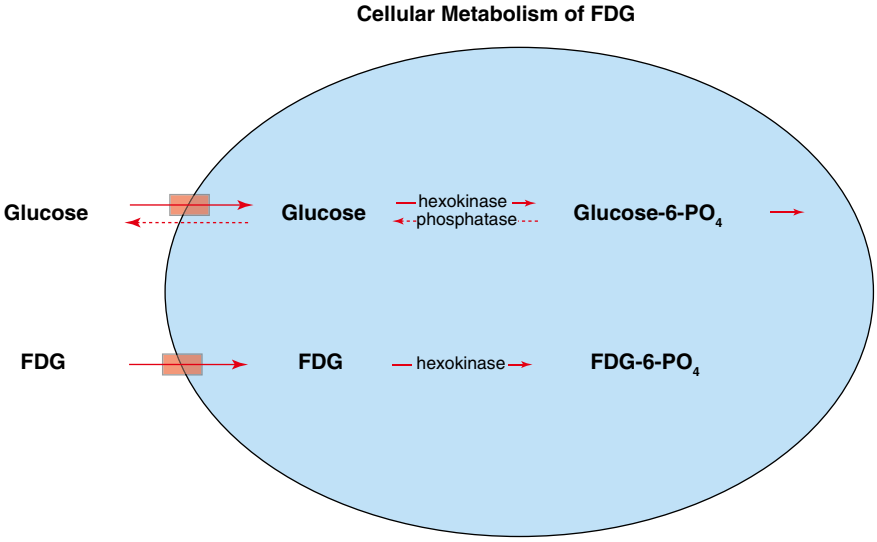

Fig. 20.9 Cellular uptake of glucose vs FDG. Most transmembrane glucose transport proteins bind to glucose and FDG equally. In addition, the hexokinase enzyme binds to and phosphorylates glucose and FDG equally well. However, the next enzyme in the glycolytic pathway binds phosphorylated glucose, but not phosphorylated FDG

tion. And because, the CT images provide high-resolution density maps, the images are routinely corrected for attenuation.

Protocol design PET-CT images from the base of the brain to the proximal thighs are obtained beginning at 60 min after administration of the FDG (Fig. 20.11).

Quantitative measurement PET-CT machines are capable of routinely calculating standard uptake values (SUV), but these quantitative measurements of the amount of injected dose in each voxel of tissue are currently used only in the Tumor Glucose Metabolism Study [14–17]. The SUV is an example of an absolute measurement as the amount of tracer in each voxel is compared to the amount of tracer that was injected. The mathematical details of the measurement are discussed in Chap. 9, Quantitation of Function: Absolute Measurements. Here we simply state the complete SUV equation rather than deriving it from the simplified SUV equation, which is usually presented,

$$\mathrm{SUV} = \frac{R(\mathrm{mCi/cpm}) * S(\mathrm{cpm/mCi}) * F(\mathrm{mL/min\text{-}g}) * \mathrm{EE} * P_{\mathrm{Nl}}/P_{\mathrm{Act}} * \int_0^T C \; \mathrm{d}t \, (\mathrm{mCi\text{-}min/mL})}{\left[D_{\mathrm{S}}(\mathrm{mCi}) - D_{\mathrm{R}}(\mathrm{mCi})\right] / \mathrm{Body\,weight}(\mathrm{g})} \tag{20.1}$$

In the numerator, "R (mCi/cts)" is a recovery factor that converts the counts recorded by the PET scanner back to millicuries, "S (cts/mCi)" is a sensitivity factor that reflects the sensitivity of the PET scanner, counts, to tissue activity, millicuries, "F (mL/min-g)" is blood flow per gram of tissue, "EE" is extraction efficiency (no units), "$P_{\mathrm{Nl}}/P_{\mathrm{Act}}$" is the ratio of the usual or normal concentration of competing molecules or substances to the actual concentration (no units), and "$\int_0^T C \, \mathrm{d}t \;\; (\mathrm{mCi\text{-}min/mL})$" is the total amount

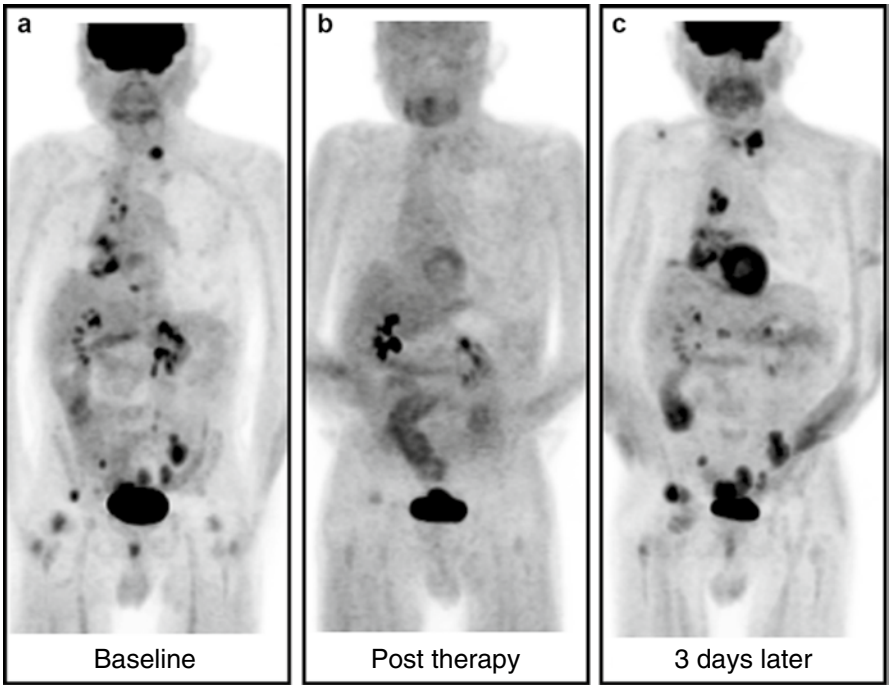

Fig. 20.10 A 76-year-old male with lung cancer. (**a**) The baseline FDG study shows widespread metastases. The blood glucose was 105 mg/dL. (**b**) Post therapy (11 weeks later), the metastases appear to have resolved. Of note, there is very little FDG uptake in the brain. The patient was not known to be a diabetic, but the blood glucose was 260 mg/dL. (**c**) The patient was sent to his physician for treatment of newly diagnosed diabetes and the FDG study was repeated 3 days later. At the time of the repeat study, his blood glucose was 76 mg/dL. In comparison to the baseline study, the repeat study demonstrates progressive metastatic disease and normal brain uptake. The elevated blood glucose level at the time of the initial post-therapy study is probably insufficient to fully explain the essentially complete lack of FDG uptake in the metastases and brain. It is postulated that, in addition to a possible competitive effect, the elevated glucose level caused a downregulation in the expression of glucose receptors

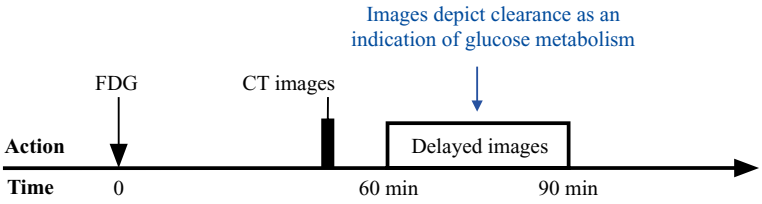

Fig. 20.11 Protocol summary diagram

of tracer in the blood that was available for clearance during the uptake time. In the denominator, D_S is the dose in the syringe and D_R is the residual dose in the syringe postinjection. The normal SUV values and their reproducibility in various organs and the implications of abnormal SUV values in various tumors have been published [14–16].

However, it is important to realize that any of the variables in Eq. 20.1, particularly the variables in the numerator, can introduce an error into the SUV measurement [17–20]. The various sources of errors in the SUV measurement are listed in Table 20.2 by: (1) category & problem, (2) explanation, (3) factor in the SUV equation (if relevant), and (4) effect on the SUV. This is an incomplete list. In addition, almost all of the "problems" listed under the categories of

Table 20.2 Causes of inaccurate SUV measurements (partial list)[a]

Category/problem	Explanation	Factor in SUV equation[a]	Effect on SUV
Technical errors			
Extravasation of dose	Decreases blood tracer concentration	$\int_0^T C\,dt$	↓
Prolonged FDG uptake time	Increases FDG available for clearance	$\int_0^T C\,dt$	↑
Dose calibrator inaccurate	Affects denominator of SUV equation	$D_S - D_R$	↑ or ↓
Dose calibrator and PET scanner clocks not synchronized	Decay correction will be inaccurate	$D_S - D_R$	↑ or ↓
Biologic factors			
Nontumorous tissue competing for blood FDG	FDG taken out of blood by normal structures, e.g., myocardium leaves less FDG for tumor	$\int_0^T C\,dt$	↓
Elevated blood glucose level	Increases competition for clearance of FDG	P_{NI}/P_{Act}	↓
Decreased extraction efficiency	Down regulation of glucose receptors secondary to elevated blood glucose level	EE	↓
Patient motion or breathing	Spreads FDG activity into greater number of pixels	S	↓
Obesity	Attenuation not fully corrected	S	↓
Competing substances	Hyperglycemia	P_{NI}/P_{Act}	↓
Inflammation	Tumors frequently contain white blood cells	EE	↑ or ↓
Physical factors			
Spatial resolution of PET scanner	Partial volume effect when lesion under 1.5 cm	S	↓
Changing blood CT contrast levels during PET scanning	Inaccurate attenuation of PET data	S	↑
Normalization method	SUV varies with method: weight, surface area, lean mass	Additional factor	↑ or ↓
ROI placement	Average SUV strongly affected by ROI size, shape, and position	Additional factor	↑ or ↓

[a]See text for definitions of symbols

"technical errors" and "biologic errors" are more likely to occur when the comparison is between the SUVs of a single tumor over two studies rather than when the comparison is between the SUVs of two different tumors within a single study.

One approach that corrects for many, but not all, of the errors in Table 20.2 is to evaluate SUVs of tumors as a ratio to a standard within the patient such as the liver. This compensates for problems that affect uptake, i.e., clearance, into the tumor and liver equally such as problems that affect the concentration of FDG in the blood, e.g., significant extravasation of FDG at the time of injection. Of note, visual evaluation of images, by way of the eye-brain complex, makes comparison of uptake in a tumor to other structures, including the liver, automatic.

References

B-Cell Lymphoma Imaging Study (In-111-Ibritumomab Tiuxetan [Zevalin®])

1. Zevalin (ibritumomab tiuxetan): package insert. IDEC Pharmaceuticals Corporation, San Diego; August 2005.
2. Conti PS, White CA, Piesolor PC, et al. The role of imaging with In-111-ibritumomab tiuxetan in the ibritumomab tiuxetan (Zevalin) regimen: results from the Zevalin imaging registry. J Nucl Med. 2005;46:1812–8.
3. The adaptive immune system. In: Alberts B, Johnson A, Lewis J, Raff M, Robert K, Walter P, editors. The molecular biology of the cell, 5th edition. New York: Garland Science; 2008. p. 1540.

Neuroendocrine Tumor – Somatostatin Receptor Study (In-111-Pentetreotide)

4. Breeman WAP, de Jong M, Kwekkeboom DJ, et al. Somatostatin receptor-mediated imaging and therapy: basic science, current knowledge, limitations and future perspectives. Eur J Nucl Med. 2001;28:1421–9.
5. Rufini V, Calcagni ML, Baum RP. Imaging of neuroendocrine tumors. Semin Nucl Med. 2006;36:228–47.
6. Sheridan MA, Kittilson JD, Slafter BJ. Structure-function relationships of the signaling system for the somatostatin peptide hormone family. Am Zool. 2000;40:269–86.
7. National Center for Biotechnology Information. PubChem Compound Database; CID=49800006, http://pubchem.ncbi.nlm.nih.gov/compound/49800006 (29 Mar 2015).
8. Bombardi E, Ambrosini V, Atolun C, et al. In-111-pentetreotide scintigraphy: procedure guidelines for tumor imaging. Eur J Nucl Med. 2010;37:1441–8.
9. Haug AR, Rominger A, Mustafa M, et al. Treatment with octreotide does not reduce tumor uptake of (68)Ga-DOTATATE as measured by PET/CT in patients with neuroendocrine tumors. J Nucl Med. 2011;52:1679–83.
10. Nocaudie-Calzada M, Huglo D, Carnaille B, et al. Comparison of somatostatin analogue and metaiodobenzylguanidine scintigraphy for the detection of carcinoid tumours. Eur J Nucl Med. 1996;23:1448–54.

Tumor Glucose Metabolism Study (F-18-Fluorodeoxyglucose)

11. Warburg O. The metabolism of tumors. New York: Richard R. Smith, Inc.; 1931. p. 129–69.
12. Plathow C, Weber WA. Tumor cell metabolism imaging. J Nucl Med. 2008;49:43S–63.
13. Ballagher BM, Fowler JS, Gutterson NI, et al. Metabolic trapping as a principle of radiopharmaceutical design: some factors responsible for the biodistribution of [F-18] 2-deoxy-2-fluoro-D-glucose. J Nucl Med. 1978;19:1154–61.
14. Boellaard R. Standards for PET image acquisition and quantitative data analysis. J Nucl Med. 2009;50:11S–20.
15. Westerterp M, Pruim J, Oyen W, et al. Quantification of FDG PET studies using standardized uptake values in multi-centre trials: effects of image reconstruction, resolution and ROI definition parameters. Eur J Nucl Med. 2007;34:392–404.
16. Wahl RL, Jacene H, Kasamon Y, et al. From RECIST to PERCIST: evolving considerations for PET response criteria in solid tumors. J Nucl Med. 2009;50:122S–50.
17. Keyes JW. SUV: standard uptake value or silly useless value? J Nucl Med. 1995;36:1836–9.
18. Paquet N, Albert A, Foidart J, et al. Within-patient variability of F-18-FDG: standardized uptake values in normal tissues. J Nucl Med. 2004;45:784–8.
19. Wang Y, Chiu E, Rosenberg J, et al. Standardization uptake value atlas: characterization of physiological 2-deoxy-2-F-18-fluoro-D-glucose uptake in normal tissues. Mol Imaging Biol. 2007;9:83–90.
20. Nahmias C, Wahl LM. Reproducibility of standardized uptake value measurements determined by F-18-FDG PET in malignant tumors. J Nucl Med. 2008;49:1804–8.

Appendix A: Nuclear Medicine Studies Covered in This Book

Appendix A lists the 39 nuclear medicine studies that are included in this book and, in particular, that are discussed in a systematic fashion in Part III, Quantitative Evaluation in Nuclear Medicine Studies. The list is a subset of the 49 diagnostic nuclear medicine studies found in the *Nuclear Medicine Procedure Manual* [1]. Nine infrequently performed nuclear medicine studies have been omitted, and the Thyroid Imaging Study with I-123 and the Thyroid Uptake Measurement with I-123 have been combined into one study.

Cardiovascular System
- Cardiac Gated Blood Pool Study at Rest (Tc-99m-red blood cells)
- Lymphoscintigraphy (Tc-99m-sulfur colloid)
- Myocardial Perfusion Study (N-13-ammonia)
- Myocardial Perfusion Study (Rb-82 as rubidium chloride)
- Myocardial Perfusion Study (Tc-99m-sestamibi, Tc-99m-tetrofosmin)
- Myocardial Perfusion and Viability Study (Tl-201-thallous chloride)
- Myocardial Viability Study (F-18-fluorodeoxyglucose)

Central Nervous System
- Brain Death Angiography Study (Tc-99m-DTPA)
- Brain Glucose Metabolism Study (F-18-fluorodeoxyglucose)
- Brain Perfusion Study (Tc-99m-HM-PAO, Tc-99m-ECD)
- Cisternography (In-111-DTPA)
- Striatal Dopamine Transporter Study (I-123-ioflupane [DaTscan])
- Ventricular Shunt Study (Tc-99m-DTPA)

Endocrine System
- Neuroectodermal / Norepinephrine Imaging (I-123-MIBG, I-131-MIBG)
- Parathyroid Study (I-123 as sodium iodide and Tc-99m-sestamibi)
- Thyroid Imaging and Uptake Study (I-123 as sodium iodide)
- Thyroid Metastases Study (I-123 as sodium iodide)

W.C. Klingensmith III, *The Mathematics and Biology of the Biodistribution of Radiopharmaceuticals-A Clinical Perspective*,
DOI 10.1007/978-3-319-26704-3

Gastrointestinal System
- Esophageal Motility Study (Tc-99m-sulfur colloid)
- Gastric Emptying Study (Tc-99m-sulfur colloid/In-111-DTPA)
- Gastrointestinal Bleeding Study (Tc-99m-red blood cells)
- Hepatic Artery Perfusion Study (Tc-99m-MAA)
- Hepatic Hemangioma Study (Tc-99m-red blood cells)
- Hepatobiliary Study (Tc-99m-trimethylbromo-IDA)
- Liver-Spleen Study (Tc-99m-sulfur colloid)
- Meckel's Diverticulum Study (Tc-99m-pertechnetate)

Genitourinary System
- Cystogram – Direct (Tc-99m-DTPA, Tc-99m-sulfur colloid)
- Renal Glomerular Filtration Study (Tc-99m-DTPA)
- Renal Tubular Function Study (Tc-99m-DMSA)
- Renal Tubular Excretion Study (Tc-99m-MAG3)

Infection Imaging
- White Blood Cell Activation Study (F-18-fluorodeoxyglucose)
- White Blood Cell Migration Study (In-111-white blood cells, Tc-99m-white blood cells)

Pulmonary System
- Lung Aerosol Ventilation Study (Tc-99m-DTPA)
- Lung Perfusion Study (Tc-99m-macroaggregated albumin)
- Lung Ventilation Study (Xe-133 gas)

Skeletal System
- Bone Mineral Study (F-18 as sodium fluoride)
- Bone Mineral Study (Tc-99m-methylene diphosphonate, Tc-99m-hydroxy methylene diphosphonate)

Tumor Imaging
- B-Cell Lymphoma Imaging Study (In-111-ibritumomab tiuxetan [Zevalin])
- Neuroendocrine Tumor – Somatostatin Receptor Study (In-111-pentetreotide)
- Tumor Glucose Metabolism Study (F-18-fluorodeoxyglucose)

Reference

1. Klingensmith WC, Eshima D, Goddard J. Nuclear medicine procedure manual 2012–14, 10th ed. Englewood: Wick Publishing; 2012.

Appendix B: Radiopharmaceuticals and Their Associated Studies

Appendix B lists all of the radiopharmaceuticals covered in this book, which in turn constitutes all of the commonly used radiopharmaceuticals. In addition, beneath each radiopharmaceutical is a sublist of the nuclear medicine studies in which the radiopharmaceutical is used.

F-18 as Sodium Fluoride
- Bone Mineral Study

F-18-Fluorodeoxyglucose (F-18-FDG)
- Brain Metabolism Study
- Myocardial Viability Study
- White Blood Cell Activation Study
- Tumor Glucose Metabolism Study

I-123 as Sodium Iodine
- Parathyroid Study
- Thyroid Imaging and Uptake Study

I-123-Iodobenzylguanidine (I-123-MIBG)
- Neuroectodermal/Norepinephrine Study

I-123-Ioflupane [DaTscan®]
- Striatal Dopamine Transporter Study

I-131 as Sodium Iodine
- Thyroid Metastases Study

In-111-DTPA
- Cisternography

In-111-Ibritumomab Tiuxetan [Zevalin®]
- B-Cell Lymphoma Imaging Study

In-111-Oxyquinoline
- White Blood Cell Migration Study

In-111-Pentetreotide
- Neuroendocrine Tumor – Somatostatin Receptor Study

N-13-Ammonia
- Myocardial Perfusion Study

Rb-82 as Rubidium Chloride
- Myocardial Perfusion Study

Tc-99m-Dimercaptosuccinic Acid (Tc-99m-DMSA)
- Renal Tubular Function Study

Tc-99m-DTPA
- Brain Death Angiography Study
- Cystogram – Direct
- Lung Aerosol Ventilation Study
- Renal Glomerular Filtration Study
- Ventricular Shunt Study

Tc-99m-Ethylene-Cysteine-Dimer (Tc-99m-ECD)
- Brain Perfusion Study

Tc-99m-Exametazine (Tc-99m-HMPAO)
- Brain Perfusion Study
- White Blood Cell Migration Study

Tc-99m-Iminodiacetates (Tc-99m-trimethylbromo-iminodiacetic acid)
- Hepatobiliary Study

Tc-99m-Macroaggregated Albumin
- Hepatic Artery Perfusion Study
- Lung Perfusion Study

Tc-99m-MAG3 (Tc-99m-mercaptoacetyltriglycine)
- Renal Tubular Excretion Study

Tc-99m-(Hydroxy)Methylenediphosphonate (Tc-99m-MDP/HMDP)
- Bone Mineral Study

Tc-99m-Pertechnetate
- Meckel's Diverticulum Study

Tc-99m-Red Blood Cells
- Cardiac Gated Blood Pool Study
- Gastrointestinal Bleeding Study
- Hemangioma Study

Tc-99m-Sestamibi
- Myocardial Perfusion Study
- Parathyroid Study

Tc-99m-Sulfur Colloid
- Gastric Emptying Study
- Liver-Spleen Study
- Lymphoscintigraphy

Tl-201 as Thallous Chloride
- Myocardial Perfusion and Viability Study

Xe-133-Gas
- Lung Ventilation Study

Appendix C: Tables of Extraction Mechanisms and Corresponding Studies

Table C.1 lists all of the different types of extraction mechanisms along with an example of one nuclear medicine study that uses each extraction mechanism. The extraction mechanisms are listed in Table C.1 in decreasing order of extraction efficiency. The following tables systematically go through each of the extraction mechanisms listed in Table C.1 and list all of the studies that utilize a given extraction mechanism. The only nuclear medicine study not listed in Tables C.1–C.13 is cisternography. The extraction mechanism for transfer of cerebrospinal fluid (CSF) from the subarachnoid space into blood, primarily by way of the subarachnoid villa, is uncertain. One hypothesis is that the cells of the arachnoid mater form a one-way valve that allows CSF to pass from the subarachnoid space into the superior sagittal sinus but not in the reverse direction [1].

Table C.1 All radiopharmaceutical extraction mechanisms from blood

Extraction mechanism category	Example study	Radiopharmaceutical	Specific extraction mechanism	Extraction efficiency	Saturable
Embolization	Pulmonary Perfusion Study	Tc-99m-macroaggregated albumin	Microembolization	100 %	No
Phagocytosis	Liver-Spleen Study	Tc-99m-sulfur colloid	Phagocytosis by sinusoidal macrophages	High	No
Passive diffusion through cell wall	Myocardial Perfusion	N-13-ammonia	Lipophilicity	High	No
Chemisorption	Bone Mineral Study	Tc-99m-MDP/HMDP	Adherence of PO_4 tracers to surface of the bone	Moderate	No
Ion exchange	Bone Mineral Study	F-18 as sodium fluoride	Exchange of F^- for OH^- in hydroxyapatite	Moderate	No
Filtration	Renal Glomerular Filtration Study	Tc-99m-DTPA	Passive filtration based on size	20 %	No
Facilitated transport	Tumor Glucose Metabolism Study	F18-fluorodeoxyglucose	GLUT glucose transporters	Moderate	Maybe
Active transport – class of molecules	Hepatobiliary Study	Tc-99m-trimethylbromo-IDA	Organic ion transport system	Moderate	Yes
Active transport – relatively specific	Thyroid Imaging Study	I-123	Na^+/I^- symporter (NIS) protein	Moderate	Yes
Cell migration	White Blood Cell Migration Study	Tc-99m-white blood cells	Migration secondary to chemotaxis	Low	No
Receptor binding (no energy input)	Somatostatin Receptor Study	In-111-pentetriotide	"Lock and key" fit	Low	Yes
Epitope binding	B-Cell Lymphoma Imaging Study	In-111-ibritumomab tiuxetan [Zevalin]	"Lock and key" fit	Low	Yes

Table C.2 Radiopharmaceutical extraction mechanisms: intravascular microembolization

Study	Radiopharmaceutical	Size	Specific extraction mechanism	Extraction efficiency	Saturable
Gastrointestinal system					
Hepatic Artery Perfusion Study	Tc-99m-macroaggregated albumin	10–80 μm	Microembolization into arterioles	Near 100 %	No
Pulmonary system					
Pulmonary Perfusion Study	Tc-99m-macroaggregated albumin	10–80 μm	Microembolization into arterioles	Near 100 %	No

Table C.3 Radiopharmaceutical extraction mechanisms: filtration

Study	Radiopharmaceutical	Size	Specific extraction mechanism	Extraction efficiency	Saturable
Genitourinary system					
Renal Glomerular Filtration Study	Tc-99m-DTPA	482.31	Renal glomerular filtration	20 %	No

Table C.4 Radiopharmaceutical extraction mechanisms: phagocytosis

Study	Radiopharmaceutical	Size	Specific extraction mechanism	Extraction efficiency	Saturable
Cardiovascular system					
Lymphangiography	Filtered Tc-99m-sulfur colloid	0.04–0.22 μm	Phagocytosis by sinusoidal macrophages	High	No
Gastrointestinal system					
Liver-Spleen Study	Tc-99m-sulfur colloid	0.4–0.8 μm	Phagocytosis by sinusoidal macrophages	High	No

Table C.5 Radiopharmaceutical extraction mechanisms: chemisorption

Study	Radiopharmaceutical	Size	Extraction mechanism	Extraction efficiency	Saturable
Skeletal system					
Bone Mineral Study	Tc-99m-MDP/HMDP	274.92	Adherence of PO_4 tracers to surface of the bone	Moderate	No

Table C.6 Radiopharmaceutical extraction mechanisms: ion exchange

Study	Radiopharmaceutical	Size	Specific extraction mechanism	Extraction efficiency	Saturable
Skeletal system					
Bone Mineral Study	F-18 as sodium fluoride	19.00	Exchange of F^- for OH^- in hydroxyapatite	Moderate	No

Table C.7 Radiopharmaceutical extraction mechanisms: passive diffusion

Study	Radiopharmaceutical	Size	Extraction mechanism	Extraction efficiency	Saturable
Cardiovascular system					
Myocardial Perfusion Study	N-13-ammonia	17.0	Lipophilicity	High	No
Myocardial Perfusion Study	Tc-99m-sestamibi	777.7	Lipophilicity	Moderate, about 38 %	No
Central nervous system					
Brain Perfusion Study	Tc-99m-HMPAO	384.3	Lipophilicity	Moderate	No
Brain Perfusion Study	Tc-99m-ECD	313.5	Lipophilicity	Moderate	No
Endocrine system					
Parathyroid Study	Tc-99m-sestamibi	777.7	Lipophilicity	Moderate, about 38 %??	No

Table C.8 Radiopharmaceutical extraction mechanisms: white blood cell migration

Study	Radiopharmaceutical	Size	Extraction mechanism	Extraction efficiency	Saturable
Infection imaging					
White Blood Cell Migration Study	Tc-99m-white blood cells	12–15 μm diameter	Migration secondary to chemotaxis	Low	No

Table C.9 Radiopharmaceutical extraction mechanisms: facilitative transport

Study	Radiopharmaceutical	Size	Extraction mechanism	Extraction efficiency	Saturable
Cardiovascular system					
Myocardial Viability Study	F18-fluorodeoxyglucose	166.17	GLUT glucose transporters	Low–moderate	Maybe
Central nervous system					
Brain Glucose Metabolism Study	F18-fluorodeoxyglucose	166.17	GLUT glucose transporters	Low–moderate	Maybe
Infection imaging					
White Blood Cell Activation Study	F18-fluorodeoxyglucose	166.17	GLUT glucose transporters	Low–moderate	Maybe
Tumor imaging					
Tumor Glucose Metabolism Study	F18-fluorodeoxyglucose	166.17	GLUT glucose transporters	Low–moderate	Maybe

Table C.10 Radiopharmaceutical extraction mechanisms: active transport – class of molecules

Study	Radiopharmaceutical	Size	Extraction mechanism	Extraction efficiency	Saturable
Cardiovascular system					
Myocardial Perfusion Study	Rb-82-rubidium chloride	85.47	Na^+/K^+ pump	High	No
Myocardial Perfusion and Viability Study	Tl-201-thallous chloride	204.38	Na^+/K^+ pump	High	No
Central nervous system					
Striatal Dopamine Transporter Study	I-123-ioflupane [DaTscan®]	407.24	Dopamine transporter receptors	Moderate	Yes
Endocrine system					
Neuroectodermal Imaging study	I-123-MIBG	193.17	Norepinephrine monoamine neurotransmitters	Mild	Yes
Thyroid Imaging Study	I-123	122.90	Na^+/I^- symporter (NIS) protein	Moderate	Yes
Thyroid Metastasis	I-123, I-131	122.90	Na^+/I^- symporter (NIS) protein	Moderate	Yes
Thyroid Uptake Measurement	I-123	122.90	Na^+/I^- symporter (NIS) protein	Moderate	Yes
Gastrointestinal system					
Hepatobiliary Study	Tc-99m-trimethylbromo-IDA	328.28	Organic ion transport system	Moderate	Yes
Meckel's Diverticulum Study	Tc-99m-pertechnetate	162.91	H^+/K^+ ATPase proton pump	Moderate	No
Genitourinary system					
Renal Tubular Function	Tc-99m-DMSA	281.13	Possibly filtration and tubular reabsorption	5 %	No
Renal Tubular Secretion Study	Tc-99m-MAG3	242.19	Organic anion transporter 1	~65 %	No

Table C.11 Radiopharmaceutical extraction mechanisms: receptor binding

Study	Radiopharmaceutical	Size	Extraction mechanism	Extraction efficiency	Saturable
Tumor imaging					
Neuroendocrine-Somatostatin Receptor Study	In-111-pentetriotide	1019.24	"Lock and key" fit	Low	Yes

Table C.12 Radiopharmaceutical extraction mechanisms: epitope binding

Study	Radiopharmaceutical	Size	Extraction mechanism	Extraction efficiency	Saturable
Tumor imaging					
B-Cell Lymphoma Imaging Study	In-111-ibritumomab tiuxetan [Zevalin]	146,000	"Lock and key" fit	Low	Yes

Table C.13 Radiopharmaceutical extraction mechanisms: none

Study	Radiopharmaceutical	Size	Extraction mechanism	Extraction efficiency	Saturable
Cardiovascular system					
Cardiac Gated Blood Pool Study	Tc-99m-red blood cells	8 × 2 μm	None	Non-applicable	Non-applicable
Central nervous system					
Brain Death Study	Tc-99m-DTPA	482.31 MW	None	Non-applicable	Non-applicable
Ventricular Shunt Study	Tc-99m-DTPA	482.31 MW	None	Non-applicable	Non-applicable
Gastrointestinal system					
Esophageal Transit Study	Tc-99m-sulfur colloid in water	0.1–2 μm	None	Non-applicable	Non-applicable
Gastric Emptying Study	Tc-99m-sulfur colloid in oatmeal	Effectively large	None	Non-applicable	Non-applicable
Gastrointestinal Bleeding Study	Tc-99m-red blood cells	8 × 2 μm	None	Non-applicable	Non-applicable
Hemangioma Study	Tc-99m-red blood cells	8 × 2 μm	None	Non-applicable	Non-applicable
Genitourinary system					
Cystogram – Direct	Tc-99m-DTPA	482.31 MW	None	Non-applicable	Non-applicable

Reference

1. Arachnoid villar reabsorption: https://en.wikipedia.org/wiki/Arachnoid_granulation.

Appendix D: Distribution of Cardiac Output in the Body at Rest

The success of both diagnostic and therapeutic procedures is fundamentally dependent on the optimal biodistribution of radiopharmaceuticals. The biodistribution of most, but not all, radiopharmaceuticals depends primarily on clearance of radiopharmaceuticals from the blood into organs, tissues, or lesions. In turn, clearance of radiopharmaceuticals depends on four factors: (1) blood flow, (2) extraction efficiency, (3) the presence of unusual amounts of competing substances, and (4) the amount of radiopharmaceutical available to be cleared from the blood from the time of injection to the end of image acquisition or therapeutic irradiation (see Chap. 4: Evaluation of Clearance).

Table D.1 below lists the amount of cardiac output that passes to each of the major organs of the body. In the case of many diagnostic nuclear medicine studies, the relevant blood flow is to a whole organ, e.g., Renal Tubular Secretion Study with Tc-99m-MAG3 and Myocardial Perfusion Study with Tc-99m-sestamibi. On the other hand, there are a number of studies in which the radiopharmaceutical localizes or clears into lesions rather whole organs, e.g., Tumor Glucose Metabolism Study with F-18-fluorodeoxyglucose and White Blood Cell Activation Study with F-18-fluorodeoxyglucose. In these studies the increased clearance of radiopharmaceutical in the lesions is often due, at least in part, to increased blood flow, but the amount of increase is hard to determine.

Table D.1 Distribution of blood in the body at rest

Organ	Percent of cardiac output (%)	Flow/organ (L/min)	Flow/100 g (mL/min-100 g)
Lungs	100	5.0	–
Brain	14	0.70	55
Heart	4	0.20	70
Liver and GI tract	27	1.35	100
Kidneys	20	1.00	400
Skeletal muscle	21	1.05	5
Skin	5	0.25	10
Bone and others	9	0.45	3

Adapted from Pearson Education, Inc., 2013

Index

Note: Page numbers with an F refer to a figure; page numbers with a T refer to a table.

W.C. Klingensmith III, *The Mathematics and Biology of the Biodistribution of Radiopharmaceuticals-A Clinical Perspective*,
DOI 10.1007/978-3-319-26704-3